

University of Nottingham

UK | CHINA | MALAYSIA

Probing the Photochemistry and Photophysics of Organic and Inorganic Chromophores

Katherine Elizabeth Anne Reynolds MSci

School of Chemistry

University of Nottingham

Thesis submitted to the University of Nottingham for the degree of Doctor of Philosophy

May 2020

This thesis is dedicated to Patricia Anne Millman *(26.03.2019)*.

Declaration

I hereby declare that this Thesis and the work presented in it are my own, unless acknowledged otheriwse.



Katherine Reynolds

December 2019

Abstract

Chapter 1

This Chapter gives an introduction to the techniques used within this Thesis. A brief outline is given on time resolved infrared (TRIR), the pump-probe method that has been utilised throughout this Thesis to investigate the photophysical, and photochemical properties of the complexes of interest.

Chapter 2

The photophysical and photochemical properties of $[Re(CO)_4(bpy)][PF_6]$ have been probed in Chapter 2, with both picosecond and nanosecond TRIR run in CH_2Cl_2 and CH_3CN at two different excitation wavelengths. $[Re(CO)_4(bpy)][PF_6]$ exhibits interesting photochemical behaviour, where a CO ligand can be easily dissociated by excitation at 355 nm. Prior to the work discussed in Chapter 2, only one time-resolved measurement had been reported in the literature, which proposed a mixed state was populated, that subsequently lead to the photodissociation of CO. However, no ultrafast studies have been conducted which could help to determine the nature of the excited states formed. The work within this Chapter probes the nature of the excited states, with time-dependent density functional theory calculations (TD-DFT) to support the assignment of the excited state. It was found that when $[Re(CO)_4(bpy)][PF_6]$ is excited at 355 nm in either CH_2Cl_2 or CH_3CN two excited states are populated si-

multaneously, with one of the states leading to the photodissociation of CO. With the experimental results and the TD-DFT calculations, it was determined that both these excited states have not only metal to ligand charge transfer (MLCT) character, but also inter ligand charge transfer (ILCT) leading to the formation of a mixed state. The MLCT character of these two mixed ILCT/MLCT excited states dictates the photodissociation of CO, as determined by the TD-DFT calculations which studied the movement of electron density throughout the molecule.

The observation of this second mixed ILCT/MLCT state has not previously been reported, and is thought to be the state responsible for the emission observed from $[Re(CO)_4(bpy)][PF_6]$. The lifetime of the two states are very different, with the emissive state decaying faster (τ = 100 ns) than the other state mixed state, which decayed (τ = 3 μs) to form a solvated photoproduct. When $[Re(CO)_4(bpy)][PF_6]$ is excited at 266 nm, only one mixed ILCT/MLCT state is observed which decayed (τ = 900 ns) to form a solvated photoproduct *via* the photodissociation of CO. The observation of two excited states following a 355 nm excitation and one excited state following a 266 nm excitation was seen for both CH_2Cl_2 and CH_3CN. Both solvated photoproducts, $[Re(CO)_3(bpy)(CH_2Cl_2)]$ and $[Re(CO)_3(bpy)(CH_3CN)][PF_6]$ were observed in the TRIR spectra, following the decay of a mixed ILCT/MLCT excited state. Preliminary spectroelectochemical investigations also found that it is possible to electrochemically induce CO loss, resulting in the formation of two stable rhenium tricarbonyl complexes, $Re(CO)_3(bpy)Cl$ and $Re(CO)_3(bpy)(CH_3CN)][PF_6]$.

Chapter 3

This Chapter probed the photophysical and photochemcial properties of $Re(CO)_4(dppz)]$ $[PF_6]$ with TRIR, to elucidate the nature of the excited states. Changing the α-diimine

ligand was also investigated to see if the photochemical properties can be altered. From the literature and work in Chapter 2, it is known that a rhenium tetracarbonyl centre coordinated to a α-diimine ligand can undergo CO loss to form a solvated photoproduct. $Re(CO)_4(dppz)][PF_6]$ was probed in CH_2Cl_2 and CH_3CN, and excited at 355 and 266 nm. When excited at 355 nm, $Re(CO)_4(dppz)][PF_6]$ formed an initial excited state that decayed away (τ = 100 ps) forming a second excited state which was a long lived mixed ILCT/MLCT state (τ = 3 μs). This mixed excited ILCT/MLCT state decayed back down to the ground state, and does not result in the formation of the solvated photoproduct in either solvent. Using TD-DFT calculations the nature of these two states was determined, with both appearing to be a mixed ILCT/MLCT excited state with varying degrees of 'Re $\longrightarrow$ phen' character.

When the excitation energy was increased to 266 nm, different photophysical properties were observed for the two solvents. In CH_2Cl_2 upon excitation a ILCT(phen) excited state was seen, which decayed (τ = 80 ps) to form a ILCT/MLCT mixed excited state. This ILCT/MLCT mixed excited state decayed (τ = 2 μs) to form a solvated photoproduct, $Re(CO)_3(dppz)(CH_2Cl_2)]$ which is not as stable as the photoproduct observed for $[Re(CO)_4(bpy)][PF_6]$. However, in CH_3CN upon excitation at 266 nm an inital excited state was populated which decayed to form a ILCT/MLCT state (τ = 55 ps). This ILCT/MLCT excited state decayed (τ = 1.4 μs) back down to the ground state, and no formation of photoproduct was observed. This suggested that the photochemical properties of $Re(CO)_4(dppz)][PF_6]$ are both solvent and wavelength dependent. Along with the photophysical and photochemcial properties, the spectroelectrochemistry was also probed. It was found that a stable tricarbonyl product was formed following the dissociation of CO. Therefore, $Re(CO)_3(dppz)Cl$ and $Re(CO)_3(bpy)(CH_3CN)][PF_6]$ can be obtained electrochemically.

Chapter 4

A group of unique rylene rotaxane handcuff complexes were investigated in Chapter 4. These rotaxane handcuff complexes are a group of PDI and NDI monomers and dimers that have been 'handcuffed' together to form non-covalently bound dimers. The photophysics of PDI monomers and covalently bound PDI dimmers have been previously reported, the photophysical properties of non-covalently bound PDI dimers remain unknown. Using ultrafast techniques, transient absorption (TA) and TRIR, we have probed, for the first time, the photophysics of a non-covalently bound handcuff PDI dimer.

The two PDI monomers were probed at 520 nm in CH_2Cl_2 and both formed ^{1}PDI excited states, with **PDI-2** being shorter lived (τ = 80 ps) than **PDI-1** (τ = 400 ps). In contrast, the NDI monomer, **NDI-1** , was excited at 380 nm which resulted in the formation of a ^{1}NDI excited state, which quickly decayed (τ = 0.6 ps) to form a $NDI^{-\bullet}$ species. This $NDI^{-\bullet}$ then decayed (τ = 20 ps) to form a long lived ^{3}NDI excited state. When the PDI monomers and NDI monomer are 'handcuffed' together there is a change to the photophysical properties. The two dimer complexes were probed at 520 nm in CH_2Cl_2, with PDI/PDI dimer handcuff complex resulting in the formation of an excimer state which has a lifetime of τ = 650 ps. The NDI/PDI dimer saw the formation of an ion pair with both a $NDI^{-\bullet}$ and $PDI^{-\bullet}$ species being populated following the decay of a ^{1}PDI excited state (τ = 2 ps). The $NDI^{-\bullet}$ species decayed away at a faster rate (τ = 220 ps) than the $PDI^{-\bullet}$ species (τ = 900 ps).

As well as these three monomers and two handucuff dimers, a PDI rotaxane was also probed. This PDI handcuff complex has a pillar-[5]-arene wheel located on the alkly chain between the end group and the PDI core. When excited at 532 nm, a

^{1}PDI excited state is formed, which undergoes a charge transfer (CT) process (τ = 10 ps) to form a $PDI^{-\bullet}$ species. Both a ^{1}PDI excited state and a $PDI^{-\bullet}$ species are observed which decay with different lifetimes. The ^{1}PDI excited state decayed faster (τ = 80 ps) than the $PDI^{-\bullet}$ species (τ = 200 ps). This illustrated that incorporating an electron rich group onto a PDI monomer can result in a charge separated state.

Chapter 5

Chapter 5 investigates the synthesis and characterisation of the fluorinated photosensitive rhenium α-diimine dye, *fac*-Re(CO)$_3$(bpy$-$R$_F{}^8$)Cl. A full spectroscopic study was conducted for *fac*-Re(CO)$_3$(bpy$-$R$_F{}^8$)Cl in range of solvents, with comparisons made to a non-fluorinated analogue; *fac*-Re(CO)$_3$(dnb)Cl. The photophysical properties of the two complexes were also investigated, in both polar and non-polar solvents. The solubilities of two perfluorinated complexes were investigated *fac*-Re(CO)$_3$(bpy$-$R$_F{}^8$)Cl and *fac*-Re(CO)$_3$(bpy$-$R$_F{}^{10}$)Cl, and it was found that *fac*-Re(CO)$_3$(bpy$-$R$_F{}^{10}$)Cl was more soluble in perfluorinated media than the shorter chain analogue. The luminescence was probed, and for *fac*-[Re(CO)$_3$(dnb)Cl] when the polarity of the solvent is decreased there is a red shift of the emission peak to higher energy, this is indicative of positive solvatochromism. However, [Re(CO)$_3$(RF$_8$(CH$_2$)$_3-$bpy)Cl] exhibited a blue shift of the emission peak to lower energy with lowering polarity, which is consistent with negative solvatochromism. When the concentration of *fac*-Re(CO)$_3$(bpy$-$R$_F{}^8$)Cl was decreased, a switch in the solvatochromism was observed, with a low concentration resulting in positive solvatochromism. This suggests that the long perfluorinated chains are aggregating in solution.

A TRIR spectroscopic investigation was carried out for *fac*-Re(CO)$_3$(bpy$-$R$_F{}^8$)Cl and *fac*-Re(CO)3(dnb)Cl in CH$_3$CN. The *ps*-TRIR and *ns*-TRIR of *fac*-Re(CO)$_3$(bpy$-$R$_F{}^8$)Cl

in acetonitrile gave a ^{3}MLCT excited state (τ = 34 ns). The *ps*-TRIR and *ns*-TRIR of $Re(CO)_3(dnb)Cl$ in CH_3CN also exhibited a ^{3}MLCT excited state (τ = 36 ns), indicating that the long perfluorinated chain on the complex is not influencing the excited state. As well as the photophysical properties, the photochemcial properties of *fac*-$Re(CO)_3(bpy{-}R_F{}^{10})Cl$ were probed at 266 nm in CH_2Cl_2 with the aim of forming a dicarbonyl species, instead a ^{3}MLCT excited state (τ = 57 ns) was seen and no formation of the dicarbonyl species was observed. This supports the theory that perfluorinated chains are aggregating in solution.

Chapter 6

The summaries and future work of the results obtained from the work in this Thesis is given in this Chapter. It discuses the implications that have arisen from these results and areas of research that could be investigated in the future.

Chapter 7

The experimental methods and spectroscopic techniques used throughout this Thesis are described in this Chapter. This includes detailed descriptions of the equipment used, along with procedures and materials used.

Acknowledgements

First and foremost, I like to thank my supervisor Professor Mike George for all his help and support throughout my PhD. He has not only been there for me academically but has also provided me with personal support when I needed it most.

I owe a tremendous amount of thanks to Dr Ashley Love, Dr Raphael Horvath, and Dr Charlotte Clark who have taught me an awful lot throughout my PhD, and have always been there to answer any question whilst always being exceptionally patient with me. A special thanks must go to Dr Xue-Zhong Sun and Dr Surajit Kayal for their help with the ultrafast time-resolved experiments in Nottingham. I am also grateful to all the staff at the ULTRA facility at Rutherford Appleton Laboratory for their help with the ultrafast time-resolved experiments.

I would also like to thank my collaborators for their help throughout this thesis, whom includes Professor Neil Champness, Dr Stephen Davies, Dr Lixu Yang, Dr Nicholas Pearce and Dr Philipp Langer at the University of Nottingham. But also Professor Keith Gordon and Joshua Sutton from the University of Otago. I would also like to acknowledge my master student James Herron whose work has contributed to this thesis.

A special thanks go to George group members, both past and present, who have made my time at Nottingham so enjoyable. In particular Ash, Raph, Beth, Xue, Dave and Jorge who I commend for putting up with me and helping to keep me sane, particularly over the past year, and always offering your help and support. Your kindness and friendship have been invaluable.

Of course, I need to thank those people who have supported me outside of the lab and have always been there at the end of the bad day, either in person or over the phone. Emily, Blanche, Emma, Jen, Alison, Pritesh, Max and Alice, there is a reason you are my best friends, I could not have done my PhD without your love and support. This year a few of you in particular have been my rock, and I will be forever grateful.

Lastly, but most importantly I have to thank my family, especially two amazing people, Valerie and Paul, also known as Mum and Dad. You constantly believe in me, always told me to shoot for the stars, and taught me to never give up. Mum, you are such an amazing role model, I am only where I am today because of you. I am eternally grateful for the love and support I have received from you both from the start of my undergraduate degree up until now. I must also thank my brother David and my sister Emily, who have always looked out for their little sister. David your support over the past year has been invaluable. Finally, I would like to thank my grandparents, who have always been proud of me and supported my dreams. Nana although you are not here to see me finish my PhD, I know you will be looking down with a proud smile on your face.

Abbreviations

Commonly used abbreviations within this report are defined below. Abbreviations that are not listed below are used too infrequently, therefore will be defined with in the body of text.

bpy	2,2-bipyridine
dmb	4,4'-dimethyl-2,2-bipyridine
dnb	4,4'-dinonyl-2,2-bipyridine
dppz	dipyrido-[3,2-a:2',3'-c]-phenazine
CT	Charge Transfer
DFT	Density Functional Theory
ES	Excited State
λ_{em}	Emission energy
GS	Ground State
ILCT	Intraligand Charge Transfer
IR	Infrared
LC	Ligand Centered
LMCT	Ligand to Metal Charge Transfer
MLCT	Metal to Ligand Charge Transfer
^{3}MLCT	Triplet Metal to ligand Charge Transfer
NDI	Naphthalene Diimides
NMR	Nuclear Magnetic Resonance
PDI	Perylene Diimides
PFMCH	Perfluoromethylcyclohexane
$R_F{}^{10}(CH_2)_3-$bpy	4,4'-bis[1H, 1H, 2H, 2H, 3H, 3H-perfluorotridecyl]-bpy
TA	Transient Absorption
TRIR	Time Resolved Infrared
UV	Ultraviolet
$\tilde{\nu}$	Vibrational energy (in cm^{-1})
$\tilde{\nu}_{abs}$	Absorption energy (in cm^{-1})
$\tilde{\nu}_{em}$	Emission energy (in cm^{-1})
τ	Excited state lifetime

Contents

Declaration **iii**

Abstract **v**

Acknowledgements **xi**

Abbreviations **xiii**

1 Introduction **1**

1.1 Excited State Intermediates 2

1.2 Time-Resolved Spectroscopy 3

1.3 Time-Resolved Infrared (TRIR) Spectroscopy 4

1.3.1 Ultrafast Time-Resolved Infrared (TRIR) Spectroscopy 5

1.4 Luminescence Spectroscopy 6

1.5 Quantum Mechanical Calculations 7

2 The Photochemical and Photophysical Properties of Rhenium Tetracarbonyl Bipyridine Complexes **9**

2.1 Introduction 9

2.1.1 Photochemistry and Photophysics of $[Re(CO)_4(diimine)]^+$ Complexes 14

2.2 Aims 26

2.3 Results . . . 27
2.3.1 Synthesis and Characterisation of $[Re(CO)_4(bpy)][PF_6]$ . . . 27
2.3.2 Time-resolved Infrared Investigation of $[Re(CO)_4(bpy)][PF_6]$ . . . 29
2.3.3 Emission of $[Re(CO)_4(bpy)][PF_6]$ . . . 58
2.3.4 Electrochemistry of $[Re(CO)_4(bpy)][PF_6]$ . . . 63
2.4 Conclusion . . . 70

3 The Photochemical and Photophysical Properties of Rhenium Tetracarbonyl Dipyridophenazine Complexes 73

3.1 Introduction . . . 73
3.1.1 Rhenium Phenanthroline Tetracarbonyl Complexes . . . 76
3.2 Aims . . . 79
3.3 Results . . . 80
3.3.1 Synthesis and Characterisation of $[Re(CO)_4(dppz)][PF_6]$ . . . 80
3.3.2 Time-resolved Infrared Investigation of $[Re(CO)_4(dppz)][PF_6]$ . . . 83
3.3.3 Electrochemistry of $[Re(CO)_4(dppz)][PF_6]$ . . . 116
3.4 Conclusion . . . 125

4 Photophysical Properties of Conjugated Perylene Diimind Handcuff Complexes 127

4.1 Introduction . . . 127
4.1.1 Photophysics of Perylene-3,4:9,10-bis(dicarboximide) Systems . . . 132
4.1.2 Photophysics of 1,4,5,8-Naphthalene Diimides Complexes . . . 142
4.2 Aims . . . 146

4.3 Results . . . 148
4.3.1 Ground State Spectra of the PDI and NDI Monomers and PDI and NDI Handcuff Complexes . . . 148
4.3.2 Time Resolved Investigation of the PDI and NDI Monomers . . . 156
4.3.3 Time Resolved Investigation of the PDI and NDI Handcuff Complexes . . . 175
4.3.4 Time Resolved Investigation of a PDI Rotaxane . . . 190
4.4 Conclusions . . . 202

5 Investigation of Rhenium Tricarbonyl Perfluorinated Bipyridine Complexes 205

5.1 Introduction . . . 205
5.1.1 Rhenium Tricarbonyl Bipyridine Complexes . . . 208
5.1.2 Perfluorinated Media . . . 214
5.2 Aims . . . 216
5.3 Results . . . 217
5.3.1 Synthesis of *fac*-Re(CO)$_3$(bpy−R$_F{}^n$)Cl Complexes . . . 217
5.3.2 Luminescence Spectroscopy of *fac*-Re(CO)$_3$(bpy−R)Cl . . . 221
5.3.3 Solubility Investigations of *fac*-Re(CO)$_3$(bpy−R$_F{}^n$)Cl . . . 226
5.3.4 Time Resolved Infrared Investigation of *fac*-Re(CO)$_3$(bpy−R)Cl . . . 231
5.4 Conclusion . . . 240

6 Conclusions and Future Work 243

6.1 Summary . . . 243
6.2 Implications and Future Work . . . 246

7 Experimental 249

7.1 Time Resolved Spectroscopic Measurements 249
7.1.1 Nottingham TRIR Apparatus 250
7.1.2 Nottingham TA Apparatus 251
7.1.3 TRIR Apparatus at the Rutherford Appleton Laboratory 252
7.1.4 TA Apparatus at the Rutherford Appleton Laboratory 253
7.1.5 TRIR and TA Data Analysis 253
7.2 Other Spectroscopic Measurements 254
7.2.1 Fourier Transform Infra-red Spectroscopy 254
7.2.2 UV/Visible Absorbance Spectroscopy 254
7.2.3 Luminescence Spectroscopy 255
7.2.4 ^{1}H NMR Spectroscopy 256
7.2.5 ^{19}F NMR Spectroscopy 256
7.2.6 Mass Spectroscopy 256
7.2.7 Electrochemistry 256
7.3 DFT Calculations 258
7.4 Materials 258
7.5 Sample Preparation 258
7.6 Synthetic Procedures 259
7.6.1 Synthesis of Diimine Ligands 259
7.6.2 Synthesis of Rhenium Carbonyl Diimine Complexes 261

Appendix A **265**

Bibliography **277**

Chapter 1

Introduction

In order to comprehensively understand the nature of chemical reactions, the mechanism and the intermediate species the reaction proceeds *via* must be understood. Time-resolved spectroscopy is a powerful tool allowing the intermediates to be probed in 'real-time' by recording spectral information over the course of the reaction. This allows the reaction mechanism and the identity of intermediate species to be studied, and depending on the timescale probed, different components of the reaction to be monitored. Kinetic information can also be obtained, which is vital for fully understanding the chemical process.[1] Time-resolved infrared (TRIR) spectroscopy is of particular interest in the study of chemical reactions, and has proved to be of great value,[2,3] as it offers structural information for the reactive species generated by probing their vibrational modes. This Thesis utilises time-resolved spectroscopy to investigate two separate topics: (i) the photochemical dissociation of rhenium diimine compounds in Chapter 2 and 3 on the picosecond and nanosecond timescale and (ii) the excited state behaviour of novel rotaxanes in Chapter 4 and transient absorption (TA) spectroscopy on the picosecond timescale. This experimental information

together with quantum mechanical calculations have been utilised to aid the characterisation of excited state and/or intermediates. Therefore, a general introduction to the spectroscopic techniques and quantum methods is given here.

1.1 Excited State Intermediates

A molecule that absorbs light to bring about a change is often called a photosensitiser and can be either inorganic or organic in nature.[4] The process following the absorption of light by a molecule can either be photophysical or photochemical. The fate of the excited state that is generated can occur by many different decay pathways illustrated in Figure 1.1. In this Thesis the nature and the different decay pathways for a range of excited states have been probed, including charge transfer, intramolecular and intermolecular energy transfer, luminescence and dissociation.

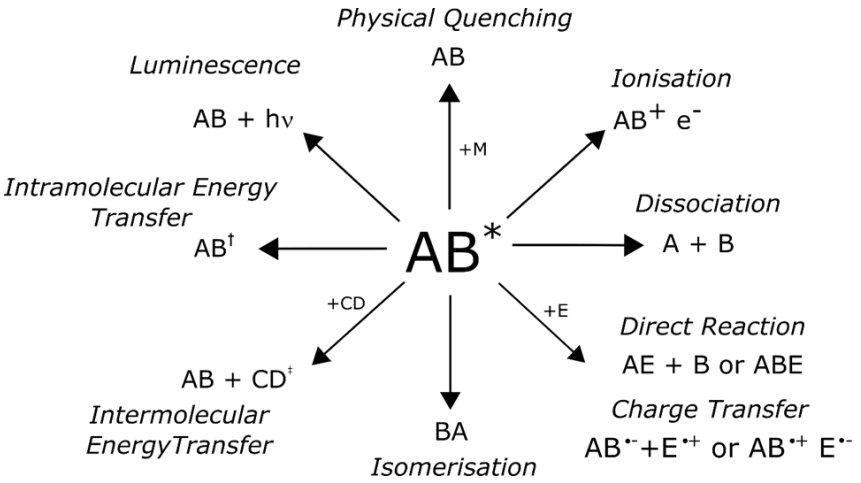


Figure 1.1: Illustrates the several routes for decay of an electronic excited state following the absorption of a photon on light my a molecule. Adapated from reference 5.

All the work discussed within this Thesis uses ultraviolet light to initiate a photochemical process or the generation of excited state intermediate species. In Chapters 2 and 3 the photolysis of rhenium diimine carbonyl complexes can result in the photodissociation of a carbonyl ligand, generating a reactive unsaturated 16-electron species which leads to the formation of a solvated product. Being able to understand the nature of the excited state that results in the photodissociation is important to further understanding the potential applications of these complexes. In Chapter 4, the irradiation of a series of perylene and naphthalene diimine rotaxanes resulted in a photophysical change rather than a photochemical one. This Chapter introduces time-resolved spectroscopy which can be used to probe both the vibrational and electronic nature of the excited state.

1.2 Time-Resolved Spectroscopy

Reaction intermediates are very short lived and are often present in low concentration due to their reactive nature, therefore spectroscopic detection can be problematic so specialised techniques are required to observe them. Time-resolved spectroscopy can be used to monitor these species and any changes that occur to gain important kinetic information about the reaction mechanism. Time-resolved spectroscopy is a pump-probe technique that involves initiating the reaction with a short pulse of light which generates these short lived intermediates which can be probed spectroscopically, Figure 1.2.

Time-resolved spectroscopy was first developed in the 1950's by Norrish and Porter who used a very high power flash lamp to photolyse the reaction,[6–8] with a lower energy light being used to probe the formation of reactive intermediates. The detection of

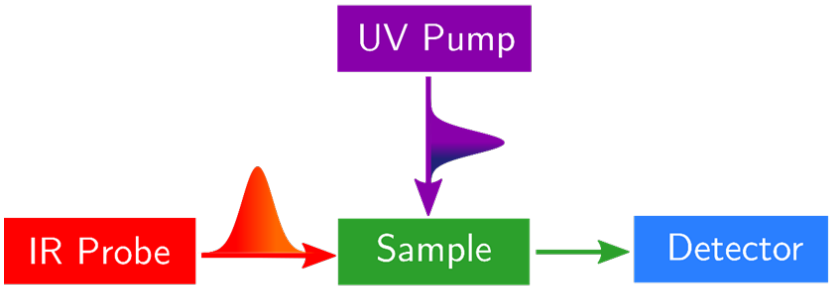


Figure 1.2: Representation of a pump probe experiment in its simplest of forms.

these reactive intermediates was obtained using a photographic plate which enabled their detection on the millisecond timescale. This initial time-resolved absorption experiment has advanced over the years with both transient absorption (TA) and TRIR experiments being able to detect the intermediates on a femtosecond timescale, through the use of ultra-fast pulsed laser systems.[9] TRIR experiments utilise an infrared probe to detect the reactive intermediate, and this Thesis will focus on TRIR spectroscopy as a spectroscopic technique.

1.3 Time-Resolved Infrared (TRIR) Spectroscopy

Time-resolved infrared spectroscopy has been widely used in the literature for the study of both organic and organometallic complexes.[10–12] Reporter ligands such as CO and CN are vibrationally sensitive to changes in electron density, this makes them the perfect tool for spectroscopically probing a changes in their vibrational frequencies as a result of the formation of a reactive intermediate. Depending on the timescale needed to probe a reaction, different TRIR methods can be used. For longer timescales rapid scan FTIR (*ms* to hr) and point-by-point TRIR (*ms* to *ns*) can be utilised,[13,14] but for shorter lived species ultrafast TRIR (*ps* to *ns*) is needed.[15–17] The work in this

Thesis uses ultrafast TRIR with a detailed experimental description being given in Chapter 6.

1.3.1 Ultrafast Time-Resolved Infrared (TRIR) Spectroscopy

This method uses an ultrafast UV pulse which pumps the samples followed by an ultrafast infrared probe pulse which reaches the sample at a chosen time delay. The time delays can be determined by changing the distance the two pulses have to travel with respects to one another, where a difference of 30 cm between the two pulses is equivalent to a difference of 1 ns. The TRIR experiments discussed within this Thesis were run at the Rutherford Appleton Laboratory, using the ULTRA line and at Nottingham University which is based on the PIRATE setup at the Rutherford Appleton Laboratory.[16] The main difference between these two experimental setups is that the ULTRA setup has a greater repetition frequency (10 kHz), a faster pulse duration (fwhm = *ca.* 80 fs) and a longer delay line.

Figure 1.3 shows the schematic outline of an ultrafast TRIR spectrometer. The heart of the system is the Ti-sapphire laser which generates a 800 nm pulse which is then split to generate two optically coupled pump and probe pulses. The seed pulse is sent to an optical parametric generator (OPG) to generate the pulse probe and an optical parametric amplifier (OPA) generating the tuneable IR probe. The IR probe pulse is then split into two further components with one sent to the mercury-cadmium-telluride (MCT) detector with the other being sent onto the sample. Once it passes through the samples, the probe pulse is sent to a MCT array detector allowing the detection of reactive intermediates. The laser systems operate on high repetition rates which can lead to degradation of the sample, therefore the samples is rastered in the x

an y direction to overcome this. In addition to the rastering, the sample is continually flowed around to refresh it.

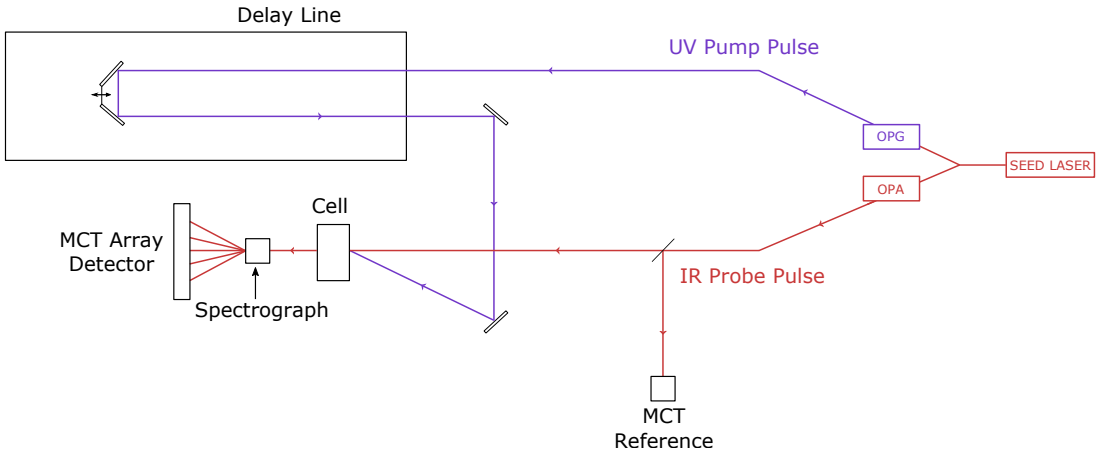


Figure 1.3: Shows a schematic diagram of an ultrafast TRIR set up similar to that used at Nottingham. The UV-pump pulse is shown in purple which is generated by a Ti-sapphire laser, this beam goes through a delay line before pumping the sample. The IR probe pulse is shown in red is also generated from the Ti-sapphire laser and is used to probe the sample.

1.4 Luminescence Spectroscopy

Luminescence spectroscopy has also been used within this thesis to probe the photophysics of rhenium diimine complexes in Chapters 2 and 3 and perylene and naphthalene diimine rotaxanes in Chapter 4. Luminescence spectroscopy allows for the detection of the emission of a complex following excitation, which can then be further probed to measure the lifetime of that emission. A xenon arc lamp provides the light source which is sent to the excitation monochromator which is set at a desired wavelength. Then passes through the sample which results in the emission of light which is then sent to the emission monochromator. The emission monochromator scans at a chosen wavelength range and the light is the detected by the photomultiplier tube

(PMT) detector. A simplified schematic of the fluorometer can be seen in Figure 1.4.

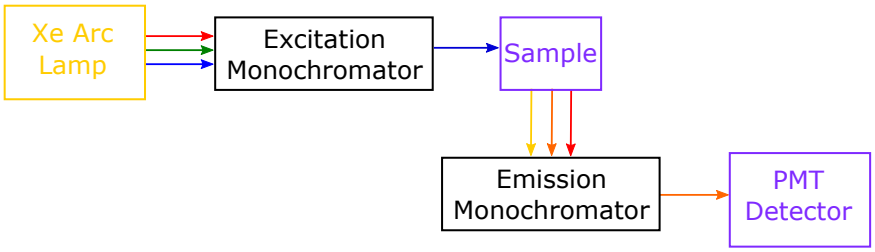


Figure 1.4: A schematic of the fluorometer used for the luminescence measurements.

1.5 Quantum Mechanical Calculations

Quantum mechanical calculations are often used alongside the study of chemical reactions and excited state experiments, as they help confirm experimental observations and give further information about the nature of the excited state and chemical reaction through optimised structures, energies and frequencies. Density functional theory (DFT) is often used for quantum mechanical calculations as it provides good results and there is not a high computational cost.[18] In this Thesis both DFT and time dependant DFT (TD-DFT) have been performed to support the work in Chapters 2 and 3 with calculations being run at both Nottingham and at The University of Otago. DFT has been widely reported in the literature,[18,19] therefore only a brief introduction is given. For DFT calculations basis sets area used, such as 6-31G, as it describes the electron density located around the nuclei which is conjunction with a functional determines the energy of a system. A very common functional used with 6-31G is B3LYP, it accounts for approximately 80% of computational chemistry.[18] For the TD-DFT calculation a CAM-B3LYP functional was used as it provides more accurate energies for calculation charge transfer excited states.

Chapter 2

The Photochemical and Photophysical Properties of Rhenium Tetracarbonyl Bipyridine Complexes

2.1 Introduction

Transition metal complexes are often utilised as a photosensitiser, owing to the fact that they can form a triplet excited state, due to metal-to-ligand charge transfer. Some transition complexes do not obey spin selection rules, resulting in the formation of emissive and long-lived triplet excited states, which give them very desirable properties. Of great interest are d^6 transition metal complexes which can act as photosensitisers for both photoinduced charge transfer and photocatalytic processes.[20–39] The photophysical and photochemical properties of d^6 transition metal complexes can

be easily influenced by the nature of the lowest excited state,[28–32,40–44] with α-diimine ligands being utilised to further tune the photophysical and photochemical properties.

One class of d^6 transition metal complex that has attracted a great deal of attention are Re(I) carbonyl complexes. They have be widely studied in the literature due to their emissive properties,[42,45–49] easy preparation and tuneable nature of the ground and excited state properties. A rhenium carbonyl species that has been at the forefront of research is the rhenium tricarbonyl species. $[Re(CO)_3(L)X]$ complexes (where L is a bidentate α-diimine ligand and X is a halogen), have been widely investigated in relation to their use as electroluminescent materials,[50] solar energy conversion,[51] and more commonly CO_2 reduction.[52–55] This has contributed to determining the fundamental properties of these complexes. These studies have demonstrated that rhenium tricarbonyl complexes exhibit solvent effects, long lived metal-to-ligand charge transfer (MLCT) excited states and can undergo physical or chemical processes,[46,56–58] illustrated in Figure 2.1. Rhenium (I) complexes offer many advantages when elucidating photophysical and photochemical properties, which makes rhenium carbonyl complexes very desirable to study.

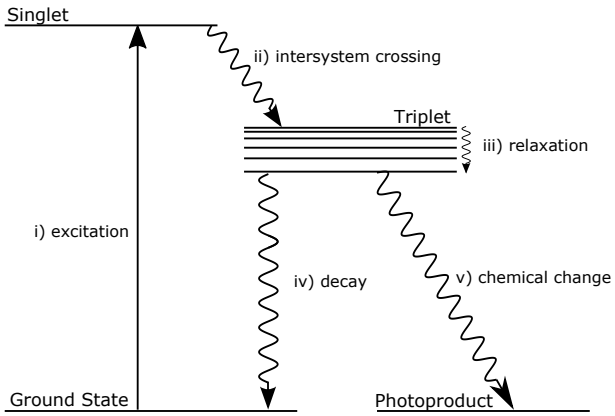


Figure 2.1: Schematic Jablonski diagram for the different photophysical processes that can occur for a [Re(CO)$_3$(α-diimine)(L)] complex following the absorption of light. These process include excitation (i), intersystem crossing (ii), relaxation (iii), decay (iv) and chemical changes (v). Adapted from reference 44.

On the picosecond, or longer timescales the excited-state properties of rhenium carbonyl α-diimine complexes are generally the result of the lowest triplet excited state, which is populated following rapid intersystem crossing and vibrational cooling.[59,60] The nature of these low-lying excited states are shown in Figure 2.2. These include the MLCT, interligand charge transfer (ILCT) or an intraligand excited state. The MLCT and ILCT character of the triplet excited states in rhenium carbonyl α-diimine complexes is different to the corresponding singlets, which is the result of the singlet-triplet splitting being larger for a IL state than a MLCT state.[44] Although the energies of ^{1}IL and ^{1}MLCT states are separated, the energies of ^{3}IL and ^{3}MLCT lie in close proximity to each other which results in the possibility of mixing of character between the lowest triplet states.[44] The mixing of triplet state character in [Re(CO)$_3$(diimine)(X)] was first reported by Stufkens,[61–63] where mixing of an MLCT and ILCT was observed resulting in excited states commonly being named MLCT/ILCT or MLLCT.[44] This demonstrates that the excited state character of Re(I) complexes can be complicated,

that fact they are highly emissions enables easier characterisation of the nature of their excited states.

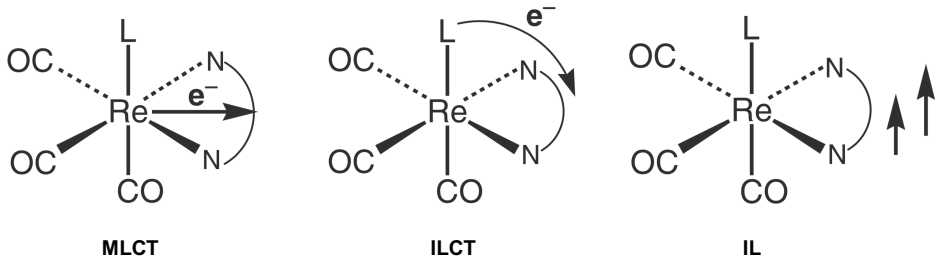


Figure 2.2: The most common low-lying triplet excited states for a $[Re(CO)_3(\alpha\text{-diimine})Cl]$ complex. These include a metal-to-ligand charge transfer (MLCT), interligand charge transfer (ILCT) and an intraligand excited state. Reproduced from reference 44.

The ^{3}MLCT excited states exhibited by rhenium carbonyl complexes are usually emissive and generally lies at a lower energy to the π-π^{**} diimine ligand-centered (LC) transition. When exciting a rhenium carbonyl complex, both the ^{1}MLCT and ^{1}LC can be populated simultaneously, however the corresponding ^{3}MLCT and ^{3}LC states vary in energy relative to one another.[64] A ^{3}LC excited state emission exhibits strong vibronic character lying around *ca.* 500 nm, whereas ^{3}MLCT excited states shows broad and structureless emission lying at *ca.* 600 nm. This difference in the emission profile allows the two excited states to be distinguishable from each other.[64] An example of the possible decay pathways for both the ^{3}MLCT and ^{3}LC excited states can be seen in Figure 2.3. A low temperature study of $[Re(CO)_3(L{-}L)(X)]$ (where L-L = bpy or phen, and X = subsituted pyridine or quiolines) found that cooling the complex to 77 K whilst measuring the emission can cause the phosphorescence to switch from a ^{3}MLCT to ^{3}LC state. This was attributed to the fact that the ^{3}MLCT state is raised or lowered energy in relation to the ^{3}LC state by temperature.[65] This temperature dependence again illustrates the complex nature of their photophysics so

being able to utilise different techniques to monitor the photophysical properties of rhenium carbonyl complexes is a vital area of research.

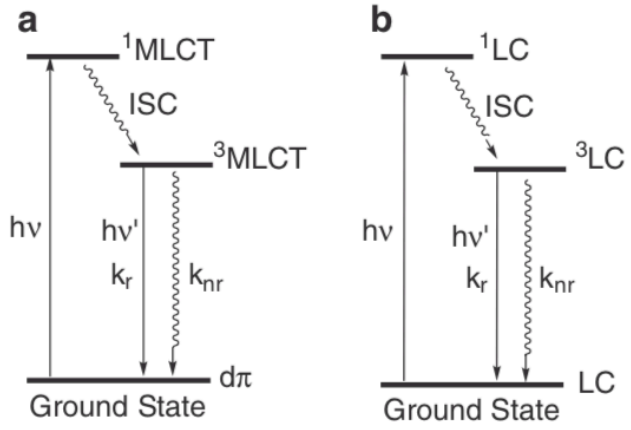


Figure 2.3: Jablonski diagram for [Re(CO)$_3$(α-diimine)(L)] complexes illustrating an MLCT excited state (a) and a LC excited state (b). Reproduced from reference 64.

It is not only the photophysical properties that are of interest, rhenium carbonyl diimine complexes can undergo photochemical ligand substitution reactions, where the photodissociation of a ligand is sometimes observed.[47,61,66] The photodissociation of CO generally occurs *via* a ^{3}LF excited state that can be thermally accessible from an excitation into a ^{3}MLCT excited state absorption.[67] The photodissociation of CO usually requires a high energy excitation (>313 nm) which has been shown to behave differently in different solvent environments.[68] Having a rhenium carbonyl complex that can readily under CO loss is desirable, leading to an interesting area of research where these complexes are utilised as photocatalysts.

2.1.1 Photochemistry and Photophysics of $[Re(CO)_4(diimine)]^+$ Complexes

A group of rhenium carbonyl complexes that has not been as widely investigated are rhenium tetracarbonyl diimine complexes, with Shaver first reporting the unusual photophysics of these complexes in 1990.[69] Shaver *et al.* reported that rhenium tetracarbonyl complexes have excited state properties that are drastically different to the excited state properties of rhenium tricarbonyl complexes.[69] There have been much fewer reports on the tetracarbonyl complexes, nevertheless, they were found to have high emission energies, long lifetimes and excited states that have powerful oxidant properties. The first rhenium tetracarbonyl diimine complex reported was $[Re(CO)_4(bpm)][CF_3SO_3]$, which contains the α-diimine ligand, 2,2'-bipyrimidine (bpm), with four nitrogen atoms, two of which are covalently bound to the rhenium centre, shown in Figure 2.4. The crystal structure showed that the Re-C(CO) bond distance for the CO groups *trans* to the bpm ligand was 1.93 Å and the Re-C(CO) bond distance of the other CO groups was 2.03 Å.[69]

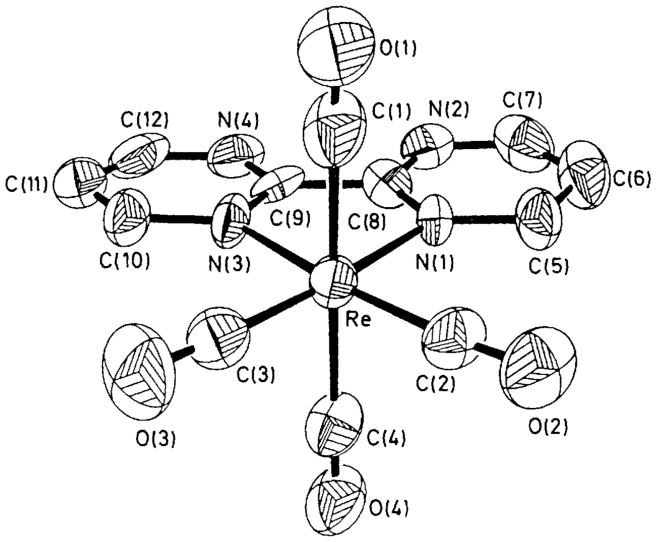


Figure 2.4: The crystal structure of the $[Re(CO)_4(bpm)]^+$ cation reported by Shaver *et al.* Reproduced from reference 69.

The absorption maxima observed for $[Re(CO)_4(bpm)]^+$ in CH_3CN are at 319 and 246 nm. $[Re(CO)_4(bpm)]^+$ emits at 543 nm when excited at 355 nm, with the emission band shown in Figure 2.5.[69] The emission band is structureless down to 77 K, which is consistent with a ^{3}MLCT excited state, with the excitation maximum seen at 325 nm. The emission lifetime of $[Re(CO)_4(bpm)]^+$ in CH_3CN was $\tau = 390$ ns. The emission of the tetracarbonyl showed a high luminescence energy and long excited state lifetimes, with the lifetime being one order of magnitude greater than the $[Re(CO)_3(bpm)Cl]$ analogue.[69] Shaver *et al.* suggested that this means the substitution of a strong field CO ligand for a chloride ligand may decrease the non-radiatve pathway thus increasing the radiative decay pathway of the complex. Having a long-lived excited state makes these tetracarbonyl complexes very interesting due to the contrasting photophysical properties to their tricarbonyl analogues.

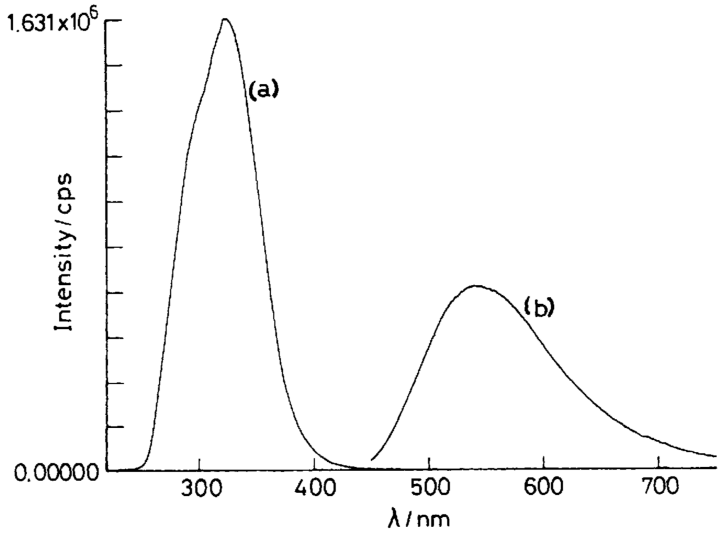


Figure 2.5: The excitation spectrum of the $[Re(CO)_4(bpm)]^+$ cation in CH_3CN λ_{em} 543 nm (a) and the emission spectrum of the $[Re(CO)_4(bpm)]^+$ in CH_3CN λ_{ex} 355 nm (b) reported by Shaver *et al.* Reproduced from reference 69.

Shaver also reported the electrochemistry of $[Re(CO)_4(bpm)]^+$ in CH_3CN.[69] This indicated the presence of one reversible reduction process with an $E_{1/2}$ of -0.87 V and a irreversible reduction process with an E_p of -1.88 V.[69] The first reduction at -0.87 V was thought to be a ligand centred reduction, with the irreversible reduction at -1.88 V being associated with the reduction of the rhenium centre, similar to tricarbonyl complexes.[69,70] The redox potential of $[Re(CO)_4(bpm)]^+$ also indicated that the excited state species is power oxidant, with a redox potential of 1.43 V allowing it to act as a reductive quencher to other molecules.[69]

Following the investigations of $[Re(CO)_4(bpm)][CF_3SO_3]$, Shaver went onto investigate another group of rhenium tetracarbonyl diimine complexes, $[Re(CO)_4(bpy)][CF_3SO_3]$, $[Re(CO)_4(dmb)][CF_3SO_3]$ and $[Re(CO)_4(phen)][CF_3SO_3]$.[71] The electronic absorption, electrochemistry and luminescence properties of these complexes were then probed. The UV-vis spectra of the complexes were measured in CH_3CN with the assignments of the $d\pi \rightarrow \pi^*$ and $\pi \rightarrow \pi^*$ transition observed compared to UV-vis

studies of $[Re(CO)_3(bpm)Cl][CF_3SO_3]$.[70,72] There is a strong contrast between the UV-vis spectrum of $[Re(CO)_4(bpm)][CF_3SO_3]$ and $[Re(CO)_4(bpy)][CF_3SO_3]$, shown in Figure 2.6. $[Re(CO)_4(bpm)][CF_3SO_3]$ exhibits a strong maximum at 260 nm, assigned to a $\pi \rightarrow \pi^*$ transition with a shoulder at 310 and 384 nm which is assigned to a $d\pi \rightarrow \pi^*$. Whereas for $[Re(CO)_4(bpy)][CF_3SO_3]$ a larger molar absorption of the $d\pi \rightarrow \pi^*$ is observed at 315 and 305 nm, as well as a $\pi \rightarrow \pi^*$ transition at 244 nm. This suggests that the photophysical properties have been just by altering the ligand coordinated to the rhenium centre.

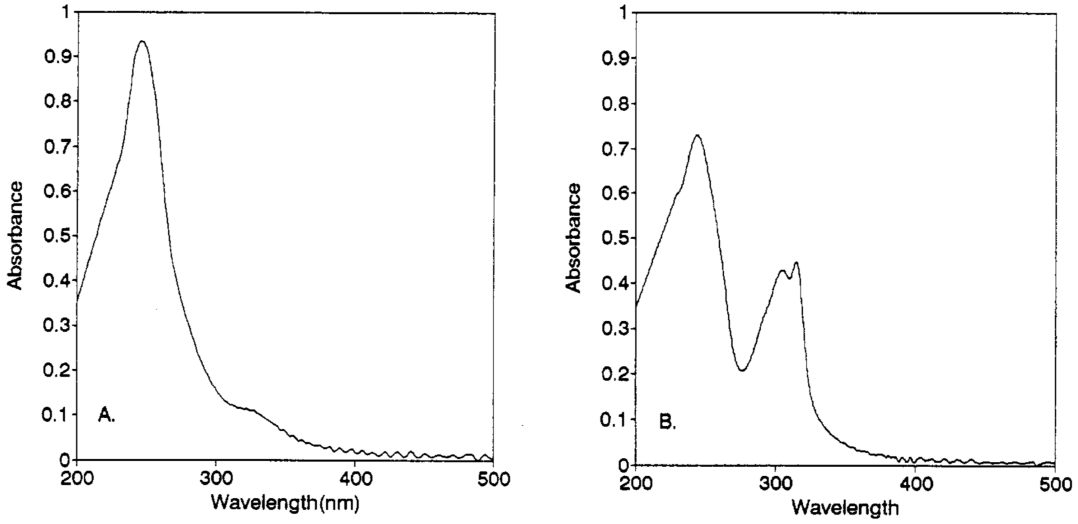


Figure 2.6: The UV-vis spectra of $[Re(CO)_4(bpm)][CF_3SO_3]$ CH_3CN (a) $[Re(CO)_4(bpy)][CF_3SO_3]$ in CH_3CN (b) reported by Shaver *et al.* Reproduced from reference 71.

The electrochemistry of the tetracarbonyl complexes exhibited a similar trend to that seen from the previous electrochemical investigations of $[Re(CO)_4(bpm)]$ $[CF_3SO_3]$, which showed that the $[Re(CO)_4(LL)][CF_3SO_3]$ complexes (where LL = bpy, dmb and phen) have a reversible reduction followed by an irreversible reduction. Shaver *et al.* reported that for $[Re(CO)_4(bpy)][CF_3SO_3]$ in CH_3CN, the first reduction was at -1.22 V, which was attributed to the reduction of the ligand, with the irreversible reduction

on the rhenium centre occurring at -1.53 V.[71] The observation of two reduction, one being irreversible and other reversible, is not commonly observed for the tricarbonyl analogue. It is clear that the change of the ligand has not altered the redox properties of the tetracarbonyl complexes.

The luminescence properties show a structured emission for all the tetracarbonyl complexes with the exception of $[Re(CO)_4(bpm)][CF_3SO_3]$, which displayed a broad and structureless emission. This change shows that the emissive nature of the complexes has be altered by a change of the ligand. The tetracarbonyl complexes were found to be unstable under steady-state excitation, therefore the emission data was collected in CH_2Cl_2 under an atmosphere of CO to prevent the photodecomposition of the complexes.[71] The structured emission of $[Re(CO)_4(bpm)][CF_3SO_3]$, seen in Figure 2.7 has emission bands at 448, 476 and 506 nm following excitation at 355 nm, with a lifetime of 4.7 μs.[71] The structured emission supports the observation of a ^{3}LC state which has been previously been reported for rhenium tricarbonyl complexes.[59,65,73–75] Comparison of the quantum yield of the steady-state emission to the quantum yield calculated for the emission lifetimes showed no strong correlation, suggesting that there may be more than one decay pathway for the excited state of $[Re(CO)_4(bpy)][CF_3SO_3]$.[71] Shaver *et al.* theorised that the photodissociation of the CO ligand could be the result of the population of a ^{3}MLCT excited state, as the oxidation of the metal centre would weaken the π bonding of the CO, resulting in CO dissociation.[71] Another thing to note is that the photodissociation of the CO is most likely to occur from an axial CO, as the higher energy of the axial CO A_1 mode (*ca.* 2150 cm^{-1}) indicates there is only weak π bonding interaction between the CO and the rhenium centre.

Previous work on the related $[M(bpy)(CO)_4]$ (M= Cr, Mo, W) complexes found that irradiating into either the LF or MLCT absorption band resulted in photochemical substitution, where the quantum yield for the photosubstitution of the MLCT state was considerably lower compared to the LF state.[76] It was concluded that the MLCT state is very weakly photoactive or that the low-lying ^{3}LF state is responsible for the longer wavelength photochemistry. In 1995 Strouse investigated the rhenium analogue, $[Re(CO)_4(bpy)][PF_6]$ and suggested that the excited state was in fact the result of a LC excited state on the bipyridine ligand or the population of an unassigned CT state, and not a LF excited state.[77] This is because $[Re(CO)_4(bpy)][PF_6]$ exhibits well resolved vibrational structure, which is typically a results of a ^{3}LC excitation and it also has characteristics arising from a CT transitions.[64]

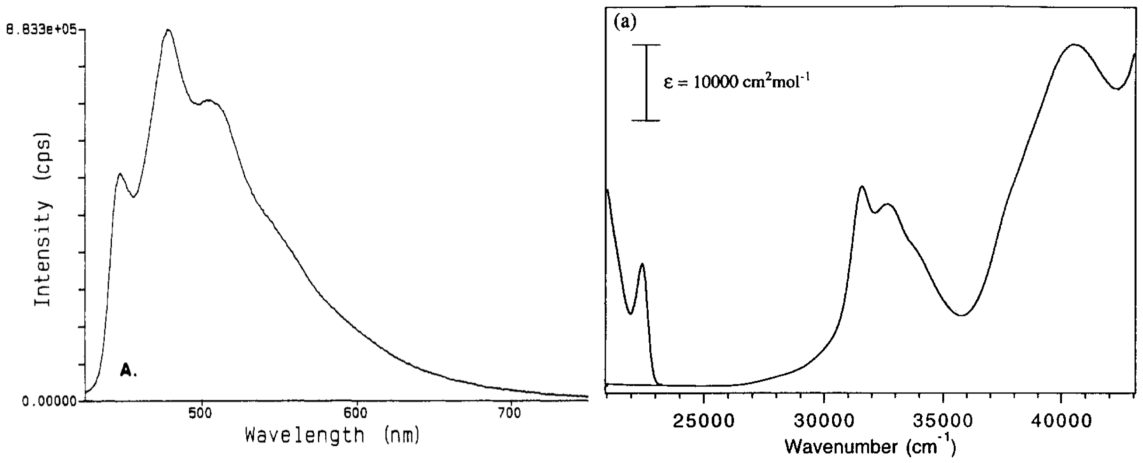


Figure 2.7: The emission spectrum of $[Re(CO)_4(bpy)][CF_3SO_3]$ in CH_2Cl_2 (left) reported by Shaver *et al.*[71] and the absorption spectrum of $[Re(CO)_4(bpy)][PF_6]$ in CH_2Cl_2 at room temperature (right) reported by Strouse *et al.* Reproduced from reference 78.

The absorption spectrum of $[Re(CO)_4(bpy)][PF_6]$ in CH_2Cl_2 is shown in Figure 2.7. The lowest maxima at *ca.* 31,500 - 34,000 cm^{-1} corresponds to a ^{1}CT transition, with the shoulder at *ca.* 26,000 and 28,000 cm^{-1} being a ^{3}CT and ^{3}LC excitation respectively.[78]. The highest maxima at *ca.* 40,500 cm^{-1} arises from a ^{1}LC excitation. These

high resolution absorption and luminescence measurements conducted by Strouse back up the observation made by Shaver *et al.*,[71] that suggested for $[Re(CO)_4(\alpha\text{-diimine})]^+$ both a ^{1}MLCT and ^{3}LC state is observed.[77,78] It was proposed the excited state is nominally an LC state with a mixture of 1-3% charge transfer character arising from the dipole mechanism for wave function mixing.

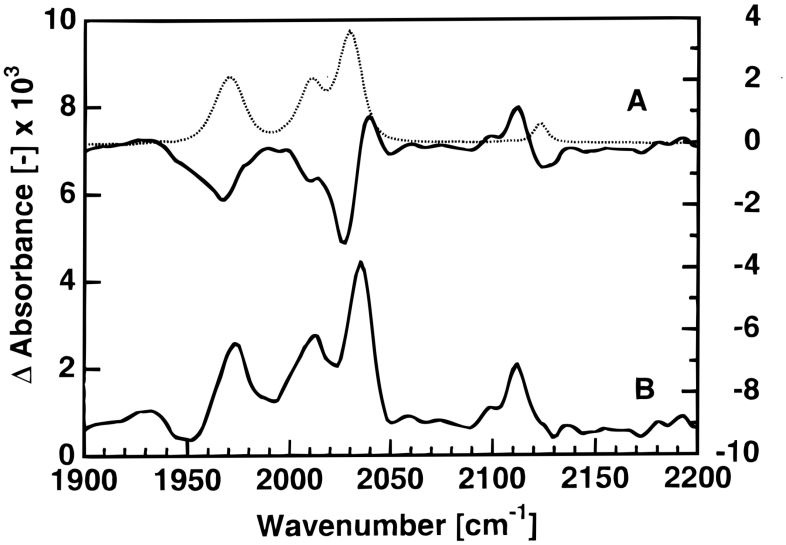


Figure 2.8: The TRIR of $[Re(CO)_4(bpy)][PF_6]$ in DCE reported by Bernhard *et al.* The ground state spectrum is shown for comparison (A, dotted line) with the calculated excited state spectrum shown as (B). Reproduced from reference 79.

The time-resolved infrared spectroscopic investigation of $[Re(CO)_4(\alpha\text{-diimine})]^+$ (α-diimine = bpy, dmbpy, phen) complexes have been reported by Bernhard *et al.* where the tetracarbonyl complex was probed at 355 nm. It found that there was a formation of a unique excited state that was assigned as a mixture of both CT character and LC excited state character, followed by the dissociation of a single carbonyl ligand to form a *fac*$-Re(CO)_3(\alpha\text{-diimine})$(solvent) complex.[79] The TRIR was run in 1,2-dichloroethane (DCE) with a 355 nm excitation wavelength, the spectrum for $[Re(CO)_4(bpy)][PF_6]$ reported by Bernhard *et al.* can be seen in Figure 2.8. The excited state TRIR showed four transient bands at 2118, 2033, 2014 and 1973 cm^{-1},

which are the a_1 ax.CO, b_1, a_1 eq.CO, and b_2 vibrational carbonyl modes. The shift of the ν(CO) bands of the excited state species do not behave the same as the excited states of other rhenium carbonyl complexes. Normally the TRIR spectrum of an ^{3}MLCT state results in a shift to higher energy of the ν(CO) bands relative to the parent bleaches (> 40 cm^{-1}), whereas a ^{3}LC state shifts to lower energy (> 10 cm^{-1}) and can be used to characterise the excited states. The excited state IR spectrum exhibited in Figure 2.8 is not consistent with this behaviour. Bernhard *et al.* reported that the bands arising from the B_1, $2A_1$, and B_2 modes shift to slightly higher energy (3 - 5 cm^{-1}), but the band arising from $1A_1$ mode shifts to lower energy (5 - 10 cm^{-1}).[79] This shift of the bands was attributed the mixed ^{3}LC and ^{3}MLCT state previously reported by Strouse *et al.*,[77] as the LC state would shift the ν(CO) to lower energy, however this is attenuated by the MLCT character shifting the bands to higher energy.

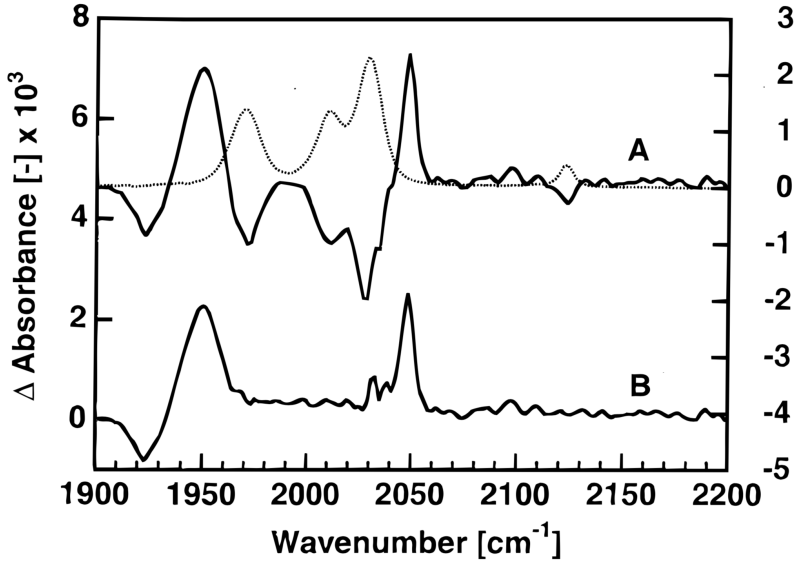


Figure 2.9: The IR spectrum of the photoproduct of [Re(CO)$_4$(phen)][PF$_6$] in DCE reported by Bernhard *et al.* The ground state spectrum is shown for comparison (A, dotted line) with the calculated photoproduct spectrum shown as (B). Reproduced from reference 79.

The mixed ^{3}LC and ^{3}MLCT excited state that was observed for all three complexes Bernhard *et al.* investigated, were all long-lived excited states that underwent photodissoiciation of a CO ligand which can been seen in Figure 2.9. It was reported that the mixed ^{3}LC and ^{3}MLCT excited state had a lifetime of *ca.* 2 μs, and that the photoproduct was formed in 100 % efficiency.[79] It was predicted that the photodissociation was most likely from a weakly active ^{3}MLCT state and not from the ^{3}LC state. The photoproduct for $[Re(CO)_4(bpy)][PF_6]$ in DCE had ν(CO) two bands at 1950 and 2048 cm^{-1}. The observation of the photodissociation of CO following 355 nm is an unprecedented result, for the tricarbonyl analogues a much higher excitation energy is needed.[68]

More recent studies have probed the electrochemistry and spectroelectrochemistry of two rhenium tetracarbonyl bipyridine in a spectroelectrochemical cell.[80] Both $[Re(CO)_4(bpy)][CF_3SO_3]$ and $[Re(CO)_4(bpy{-}^tBu)][CF_3SO_3]$ were probed in CH_3CN with 0.1 M tetrabutylammonium hexafluorophosphate, where the cyclic voltammetry (CV) indicated a small irreversible wave followed by two quasi-reversible waves. The first reduction potential matched the previous literature reports by Shaver *et al.*[71] The CV for $[Re(CO)_4(bpy)][CF_3SO_3]$ in CH_3CN shown in Figure 2.10, has three reductions at -1.15, -1.27 and -1.42 V (*vs.* SHE).

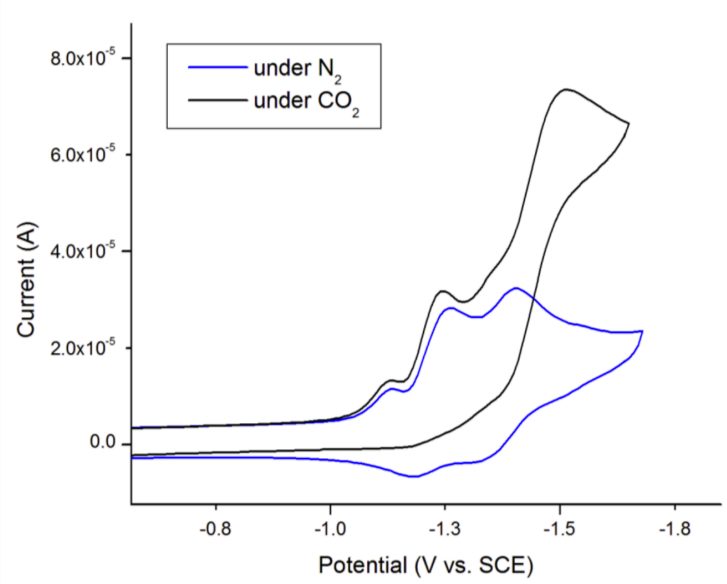


Figure 2.10: The CV of $[Re(CO)_4(bpy)][CF_3SO_3]$ under an atmosphere of N_2 shown in blue and CO_2 in black in $CH_3CN/[TBA][PF_6]$. Reproduced from reference 80.

The infrared-spectroelectrochemistry (IR-SEC) of the two tetracarbonyl complexes $[Re(CO)_4(bpy)][CF_3SO_3]$ and $[Re(CO)_4(bpy{-}^tBu)][CF_3SO_3]$ in CH_3CN were measured, where upon an applied potential the ν(CO) bands of the complexes were seen to disappear and another species was seen to grow in.[80] This species had bands that were indicative of a tricarbonyl species, which suggested the dissociation of a CO ligand. $[Re(CO)_4(bpy)][CF_3SO_3]$ had two bands that grew in at 2043 and 1939 cm^{-1}, which is consistent with the reported IR spectra for $[Re(CO)_3(bpy)(CH_3CN)]^+$,[81,82] shown in Figure 2.11. Grice *et al.* reported that the formation of the new species was in fact the result of ligand substitution reactions and not a reduction.[80]

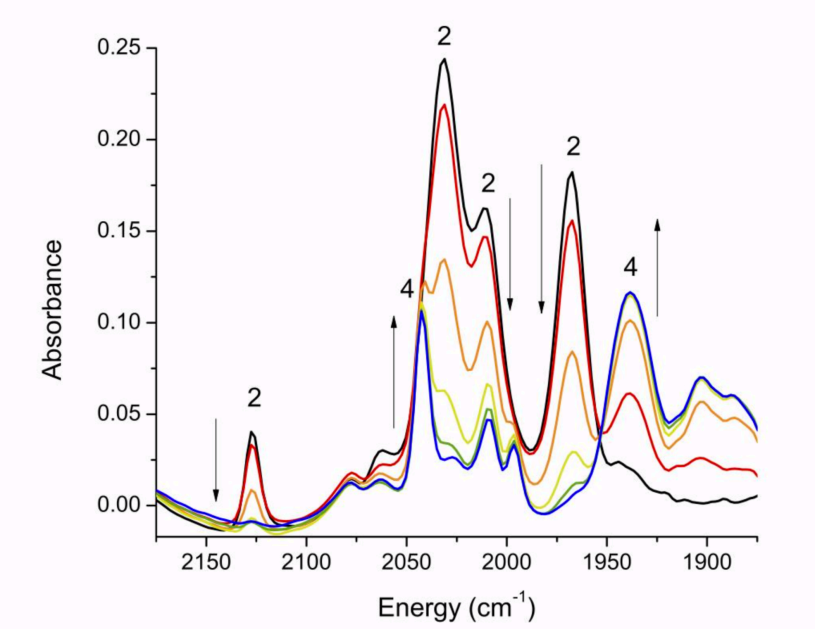


Figure 2.11: The infrared-spectrocelectrochemistry (IR-SEC) showing the decay of $[Re(CO)_4(bpy)][CF_3SO_3]$ (2) and the growth $[Re(CO)_3(bpy)(CH_3CN)][CF_3SO_3]$ (4) in $CH_3CN/[TBA][PF_6]$ following a reduction. Reproduced from reference 80.

The fact that the complex undergoes a ligand substitution reaction suggests it requires a catalytic reduction to proceed *via* this pathway. There are other literature precedents where a reduction-catalysed ligand substitution occurs for Group 7 metals and some carbonyl complexes including Group 6 $[M(bpy)(CO)_4]$ complexes.[83,84] The main difference between the reduced species of $[M(bpy)(CO)_4]^-$ and $[Re(CO)_4(bpy-R_2)]^0$ is the $[M(bpy)(CO)_4]^-$ species is stable and can be characterised by FTIR, whereas the reduced state of $[Re(CO)_4(bpy-R_2)]^0$ has not been characterised. Grice theorised that $[Re(CO)_4(bpy-R_2)]^0$ is likely to be a transient intermediate in the electron-transfer-catalysed ligand substitution of $[Re(CO)_4(bpy)][CF_3SO_3]$ and $[Re(CO)_4(bpy-^tBu)][CF_3SO_3]$.[80] Once $[Re(CO)_4(bpy-R_2)]^0$ has been formed, a ligand substitution can occur, forming $[Re(CO)_3(bpy)(CH_3CN)]^0$, which goes on to react with more of the starting material until all the starting material has undergone the ligand substitution.[80]

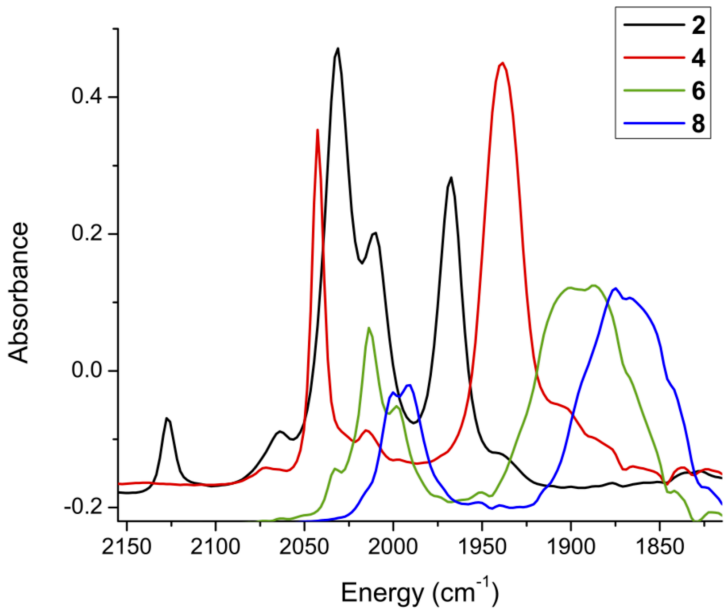


Figure 2.12: The IR-SEC spectra of $[Re(CO)_4(bpy)][CF_3SO_3]$ (2) and the resulting three reduction species $[Re(CO)_3(bpy)(CH_3CN)]^+$ (4), $[Re(CO)_3(bpy)(CH_3CN)]^0$ (6) and $[Re(CO)_3(bpy)(CH_3CN)]^-$ (8). Reproduced from reference 80.

The IR-SEC of the second reduction showed the formation of two new species for each of the complexes. The reduced species for $[Re(CO)_4(bpy)][CF_3SO_3]$ were assigned as $[Re(CO)_3(bpy)(CH_3CN)]^0$ and $[Re(CO)_3(bpy)(CH_3CN)]^-$ based on previous literature data for $[Re(CO)_3(bpy)(CH_3CN)]^+$ in a mixed THF/CH_3CN solvent.[53] The two reduced species observed for $[Re(CO)_4(bpy)][CF_3SO_3]$ were assigned to a $[Re(CO)_3(bpy)(CH_3CN)]^0$ and $[Re(CO)_3(bpy)(CH_3CN)]^-$ species, which are shown in Figure 2.12. Both these species have three $\nu(CO)$ bands. The $[Re(CO)_3(bpy)(CH_3CN)]^0$ species has bands at 2016, 1913 and 1899 cm^{-1} and $[Re(CO)_3(bpy)(CH_3CN)]^-$ has band observed at lower energies at 1992, 1875 and 1867 cm^{-1}. The results reported by Grice *et al.* have shown that being able to understand the electrochemical properties of $[Re(CO)_4(bpy)]^+$ is also important.[80] The loss of a CO ligand upon a reductive potential means the redox properties of $[Re(CO)_4(bpy)]^+$ needs to be investigated.

2.2 Aims

The aim of this Chapter is to investigate the nature of the photophysics and photochemistry of an $[Re(CO)_4(diimine)][PF_6]$ system, with particular focus on both the nature of the excited manifold, and the potential photochemical substitution of CO, which may lead to interesting coordination of weak ligands. The photophysics and photochemistry of $[Re(CO)_4(bpy)][PF_6]$ seen in Figure 2.13, was investigated in CH_2Cl_2 and CH_3CN, in order to probe whether the nature of the excited state and subsequent photochemistry was affected by the solvent.

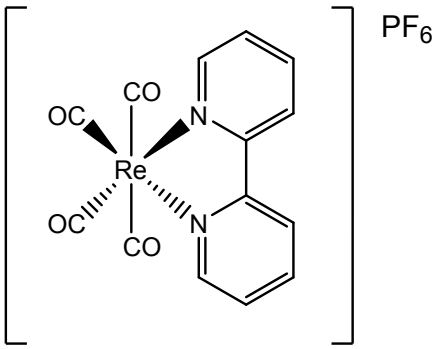


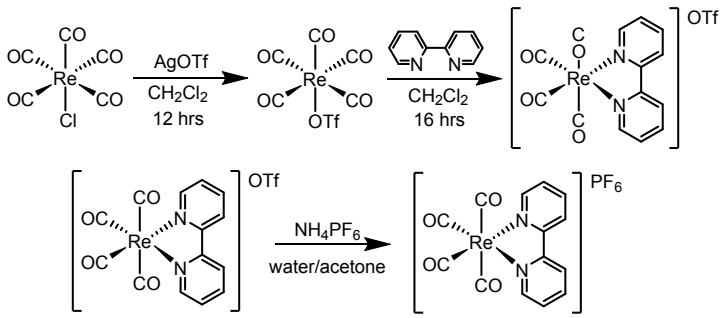
Figure 2.13: The structure of $[Re(CO)_4(bpy)][PF_6]$ which will be investigated within this Chapter.

$[Re(CO)_4(bpy)][PF_6]$ was investigated using TRIR following 266 nm and 355 nm excitation in CH_2Cl_2 and CH_3CN. This spectroscopic structural probe was used to characterise the nature and the lifetime of excited states, and subsequent formation of the solvated photoproduct. The spectroscopic results were supported with DFT calculations which were performed both in Nottingham and in collaboration with Joshua Sutton at the University of Otago in New Zealand.

2.3 Results

2.3.1 Synthesis and Characterisation of $[Re(CO)_4(bpy)][PF_6]$

The $[Re(CO)_4(bpy)][PF_6]$ complex that is reported within this Chapter was synthesised based on previous reported literature procedures.[77,85] The scheme for the synthetic procedure of $[Re(CO)_4(bpy)][PF_6]$ is shown in Scheme 2.1.[69,77,78,85] Initially the rhenium pentacaronyl triflate species was formed by stirring rhenium pentacaronyl chloride with silver triflate under an inert atmosphere for 12 hours in CH_2Cl_2. Then bipyridine was added to the rhenium pentacaronyl triflate solution which results in the formation of $[Re(CO)_4(bpy)][OTf]$. The triflate anion was exchanged *via* an anion exchange with ammonium hexafluorophosphate to give the desired $[Re(CO)_4(bpy)][PF_6]$ complex. The final product was characterised with FTIR, ^{1}H NMR, mass spectrometry and CHN analysis, which matched that reported in literature.[77,78]



Scheme 2.1: The scheme for the synthesis of $[Re(CO)_4(bpy)][PF_6]$ following literature procedures.[77,85]

$[Re(CO)_4(bpy)][PF_6]$ has a C_{2V} symmetry which exhibits four IR-active CO bands, see Figure 2.14. These bands were assigned as the symmetric (A_1 ax.CO) and antisym-

metric (B_1) stretch of the axial COs and the symmetric (A_1 ax.eq) and antisymmetric (B_2) stretch of equatorial COs. The four ν(CO) bands (2122, 2029, 2011 and 1971 cm^{-1}) in CH_2Cl_2 are consistent with previous reported by Bernhard *et al.* who reported the FTIR of $[Re(CO)_4(bpy)][PF_6]$ in 1,2-dichloroethane (DCE).[79]

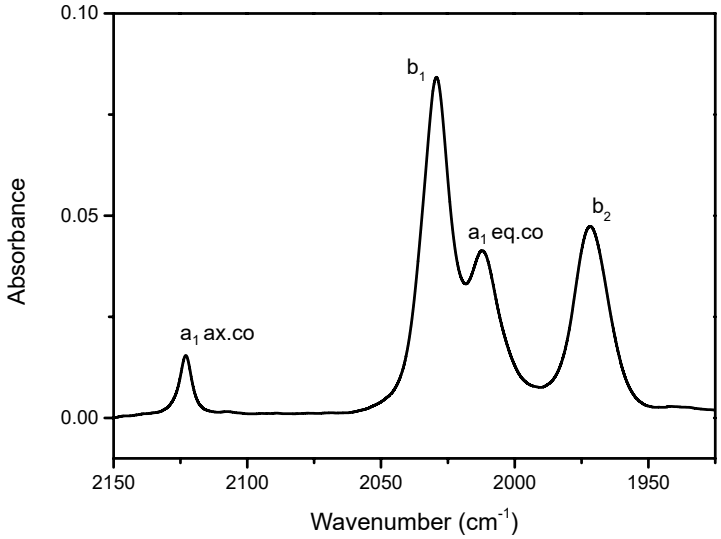


Figure 2.14: The FTIR spectra of $[Re(CO)_4(bpy)][PF_6]$ in CH_2Cl_2.

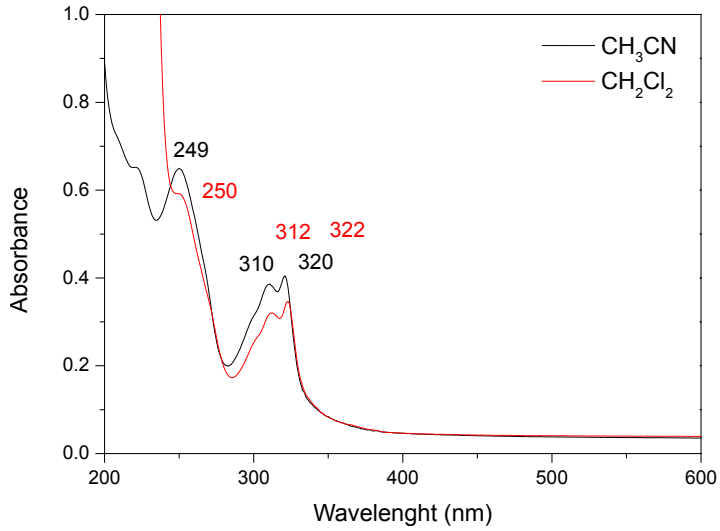


Figure 2.15: The absorption spectra of $[Re(CO)_4(bpy)][PF_6]$ in CH_2Cl_2 (red) and CH_3CN (black).

The UV-vis was investigated to help determine the electronic transitions of the complex. The absorption spectra for $[Re(CO)_4(bpy)][PF_6]$, shown in Figure 2.15 for CH_2Cl_2 and CH_3CN supports what has been reported in the literature for this complex.[71,77,78] The absorption maxima for $[Re(CO)_4(bpy)][PF_6]$ in CH_2Cl_2 has a band at 250 nm, which is thought to be a high energy ligand π-π^{**} transition. The two bands at 312 and 322 nm are ^{1}CT transitions and the shoulder at *ca.* 370 nm belongs to a ^{3}CT and a ^{3}LC transition.[78] A similar band profile is seen in CH_3CN with the only difference being a blue shift for all transitions for all transitions compared to CH_2Cl_2.

2.3.2 Time-resolved Infrared Investigation of $[Re(CO)_4(bpy)][PF_6]$

The starting point for these studies was to examine 355 nm excitation, which will excite the state reported by Bernhard *et al.* for $[Re(CO)_4(bpy)]$ $[PF_6]$ in CH_2Cl_2.

The experiment will follow on from the early experimental TRIR, which previously probed the microsecond timescale.[79] We have reinvestigated these early experiments, by performing both ps and ns-TRIR. This allowed for the monitoring of the possible formation of initial excited state on the picosecond timescale, as well as the slower formation of the photodissociation observed in the original experiments.

2.3.2.1 TRIR of $[Re(CO)_4(bpy)][PF_6]$ at 355 nm

The *ps*-TRIR spectra, of $[Re(CO)_4(bpy)][PF_6]$ after 355 nm excitation in CH_2Cl_2 are shown in Figure 2.16. The TRIR spectrum obtained after 1 ps, shows the parent bands are bleached, followed by the formation of transient species with five bands at *ca.* 2108, 2055, 2039, 1988 and 1949 cm^{-1}, assigned to an initial excited state. Over time these bands narrow and shift, with four bands seen at 2112, 2067, 2039 and 1983 cm^{-1} after 10 *ps*. This is consistent with vibrational cooling of the initially formed excited state (τ = 26 ($\pm$ 0.1) ps). The position and band profile of this initial excited state are only partially consistent with what was reported previously by Bernhard *et al.*,[79] and the band observed at 2067 cm^{-1} was not reported in the earlier study. This suggests we are observing the formation of either a different excited state, i.e a precursor state that is formed before the mixed state previously reported,[79] or two excited states populated simultaneously. This initial excited state will be assigned as State I for the the rest of this discussion.

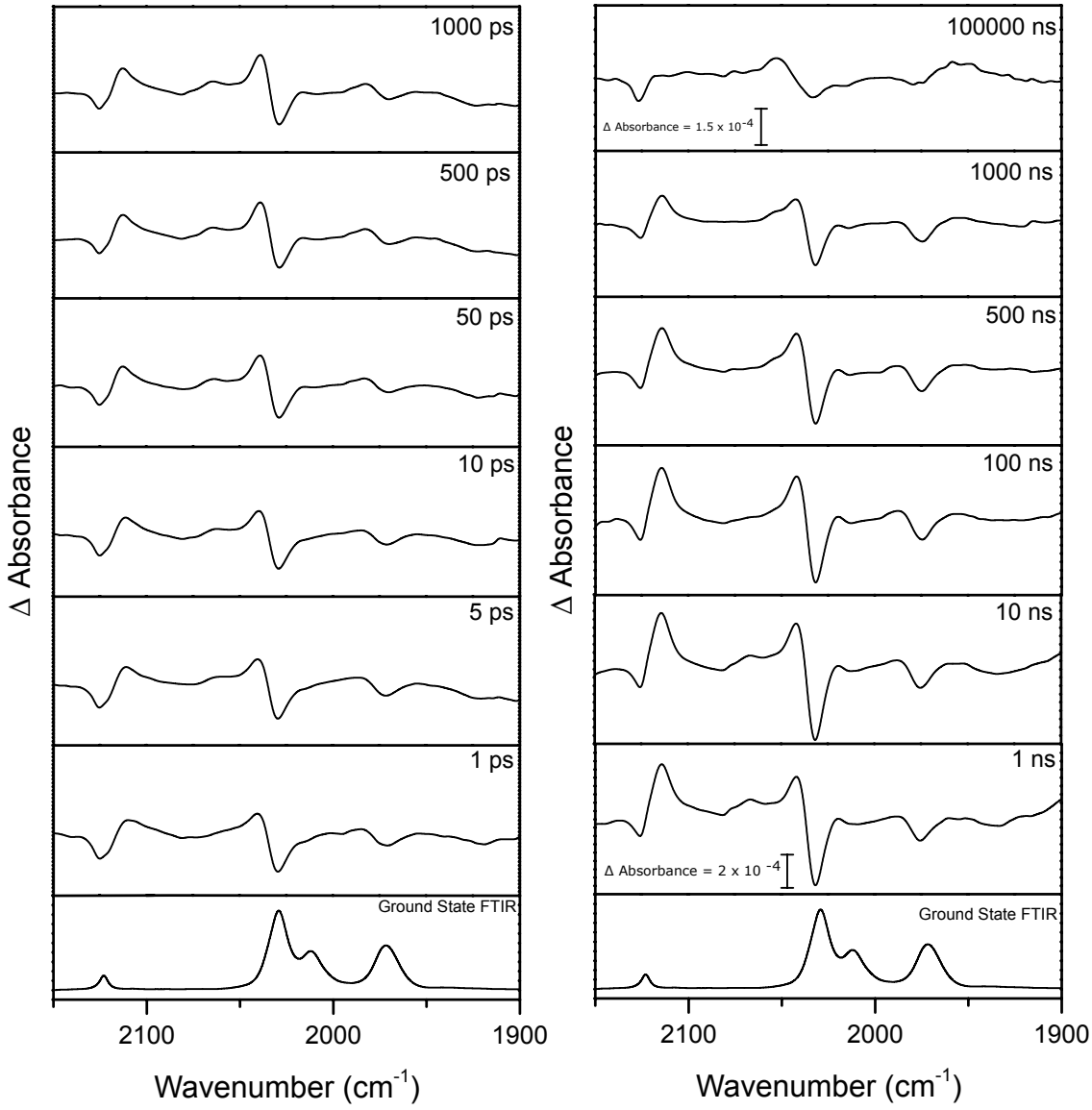


Figure 2.16: The *ps*-TRIR (left) and *ns*-TRIR spectra (right) spectra of $[Re(CO)_4(bpy)][PF_6]$ in CH_2Cl_2 following a 355 nm excitation wavelength.

The initial excited state, State I is long lived on the picosecond timescale, and is seen to decay on the nanosecond timescale. From the *ns*-TRIR spectra, shown in Figure 2.16, State I can be seen to decay (τ = 100 ($\pm$ 10) ns), by the loss of the shoulder at 2067 cm^{-1}, whilst the bands at 2113, 2040, 2019 and 1987 cm^{-1} appear to remain. These ν(CO) bands position and intensities are in agreement to those

previously reported by Bernhard *et al.*,[79] as they exhibit the same band profile and position as the reported excited state. This secondary transient is assigned to a mixed ILCT/MLCT excited state. The position of the bands for State I and the mixed ILCT/MLCT excited state are overlapped, so global analysis was undertaken on both the *ps* and *ns*-TRIR data to help further distinguish between these states. The decay of State I can be seen in Figure 2.17, and does not appear to be linked to the formation of the mixed ILCT/MLCT excited state. This suggests that both State I and the mixed ILCT/MLCT excited state are present following the cooling of the vibrationally hot state. The nature of the mixed excited state is thought to be the result of an ILCT from the bipyridine ligand onto the axial CO ligands, as well as a MLCT from the Re center onto the axial CO ligands. This is supported from new TD-DFT calculations and which will be discussed later in this Chapter. For the remainder of the discussion the mixed state will be referred too as an ILCT/MLCT excited state.

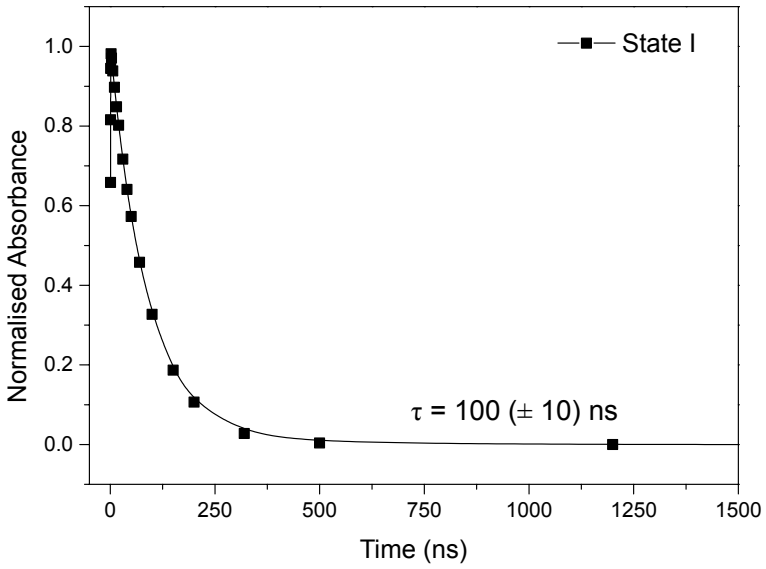


Figure 2.17: The kinetic plot generated from the global analysis for the decay of initial excited state, State I following a 355 nm excitation in CH_2Cl_2.

The mixed ILCT/MLCT excited state is long-lived on the nanosecond timescale, but does decay to form a new transient with bands at 2054 and 1955 cm^{-1}. This transient species observed on the microsecond timescale with bands at 2054 and 1955 cm^{-1} is assigned to the CO loss photoproduct, as it matched the CO loss species observed by Bernhard *et al.*[79] The kinetics for the CO loss process obtained from the global analysis can be seen in Figure 2.18. The decay of the ILCT/MLCT excited state to form the CO loss photoproduct occurs on the microsecond timescale (τ = 2.9 ($\pm$ 0.3) μs), and is consistent with the earlier reported TRIR measurements.[79] The CO photoproduct, assigned as $[Re(CO)_3(bpy)(CH_2Cl_2)]$, is long-lived and is seen to live beyond the measurement time of the TRIR experiment. The CO ligand that undergoes photodissociation is reported to be the axial ligand,[71] which is supported by TD-DFT calculations.

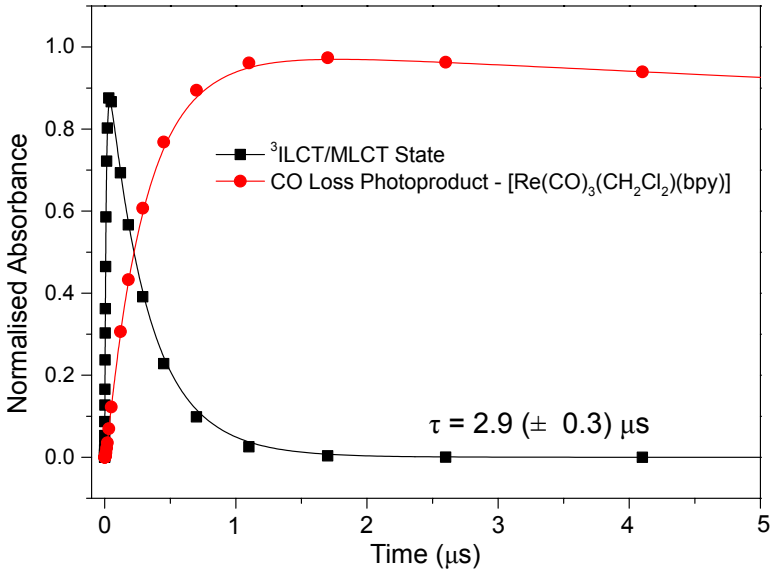


Figure 2.18: The kinetic plot generated from the global analysis for the decay of the ILCT/MLCT state and the growth of photoproduct following a 355 nm excitation in CH_2Cl_2.

Global analysis allows for the generation of the proposed excited state spectrum for the different species, as well as the kinetic information of the individual species identified within the system. This helps to distinguish the different excited states being observed. The global analysis of the both *ps* and *ns*-TRIR data produced a excited state spectra, Figure 2.19, where State I is shown in black, the ILCT/MLCT state is shown in red, and the CO loss photoproduct is shown in blue.

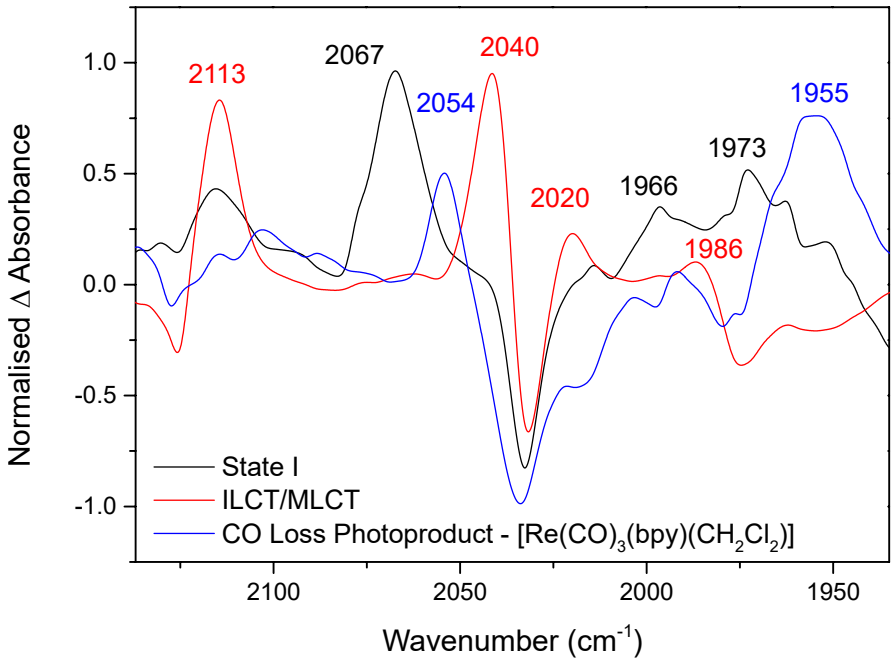


Figure 2.19: The normalised excited state spectra for State I shown in black, the ILCT/MLCT state (red) and the photoproduct (blue), following a 355 nm excitation in CH_2Cl_2.

These results shown clearly shows the bands (2061, 1966, 1973 cm^{-1}) which are assigned to State I, the ILCT/MLCT excited state (2113, 2040, 2020 and 1986 cm^{-1}) and the CO loss photoproduct (2054 and 1955 cm^{-1}).

The *ps*-TRIR spectra in CH_3CN are shown in Figure 2.20, which are similar to the experiment in CH_2Cl_2. The initial excited state is produced in a vibrational hot state at early time delays, after which a relaxed excited state can be observed with bands at 2111, 2037 and 2009 cm^{-1} following vibrational relaxation. The formation of this initial relaxed excited state occurs slightly faster in CH_3CN (τ = 10 ps) compared to CH_2Cl_2 (τ = 26 ps). The initial state has three bands at 2111, 2037 and 2009 cm^{-1}, with a shoulder band at *ca.* 2060 cm^{-1}. This is consistent with appearance of State I seen in CH_2Cl_2, thus this initial state can be assigned as State I in CH_3CN.

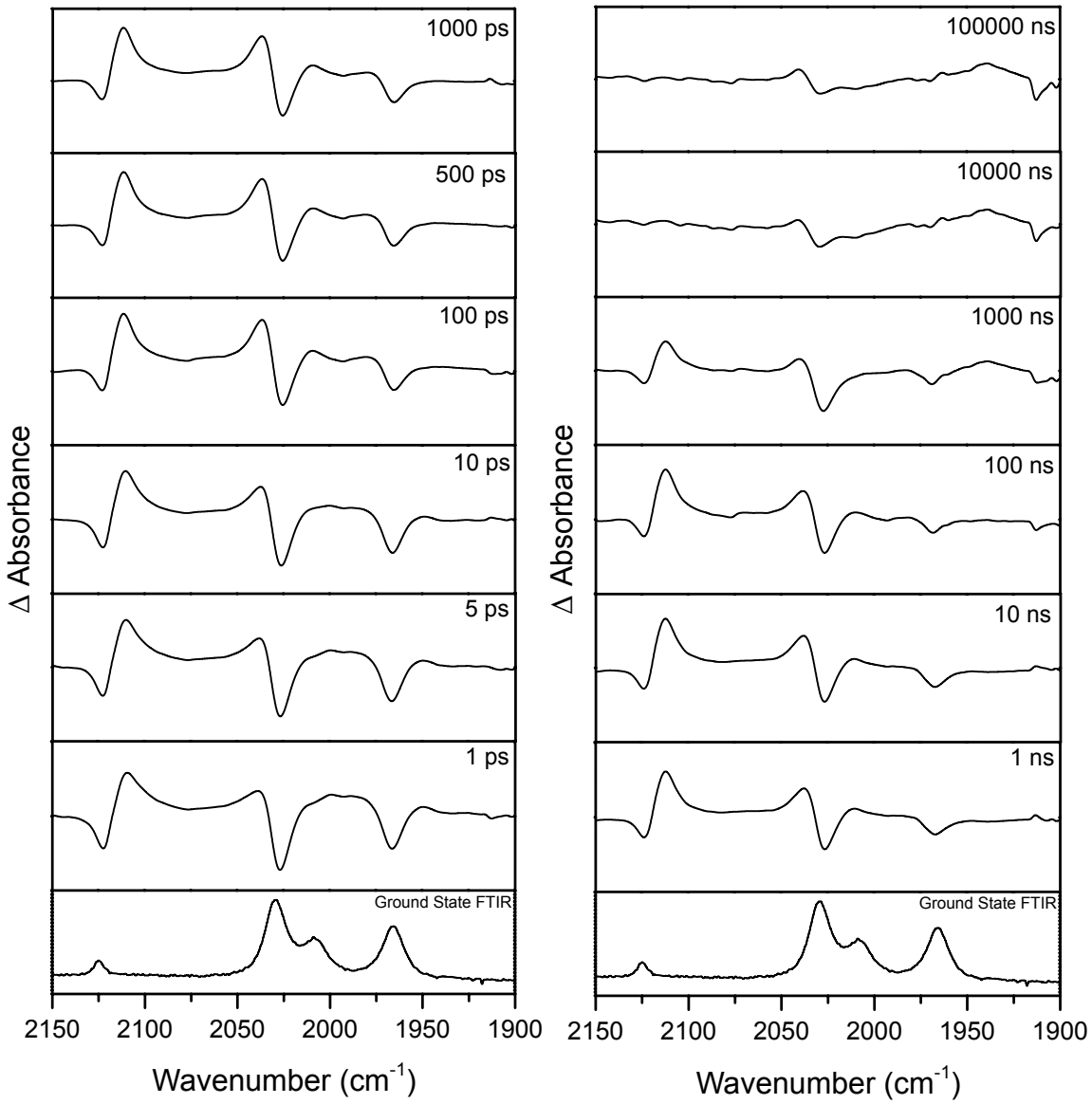


Figure 2.20: The *ps*-TRIR (left) and *ns*-TRIR spectra (right) spectra of $[Re(CO)_4(bpy)][PF_6]$ in CH_3CN, following a 355 nm excitation wavelength.

The lifetime of State I, is seen to the decay on the nanosecond timescale, with a slightly longer lifetime (τ = 160 ($\pm$ 30) ns) than that observed for CH_2Cl_2 (τ = 100 ($\pm$ 10) ns). The bands at 2112, *ca.* 2060, 2039 and 2010 cm^{-1} can assigned to State I. With the second excited state being observed at 2112, 2039, 2010 and 1983 cm^{-1}, which exhibit similar band position to the ILCT/MLCT excited state seen for CH_2Cl_2.

Therefore the second excited state can be assigned to mixed ILCT/MLCT state. The kinetic decay of State I generated by the global analysis can be seen in Figure 2.21.

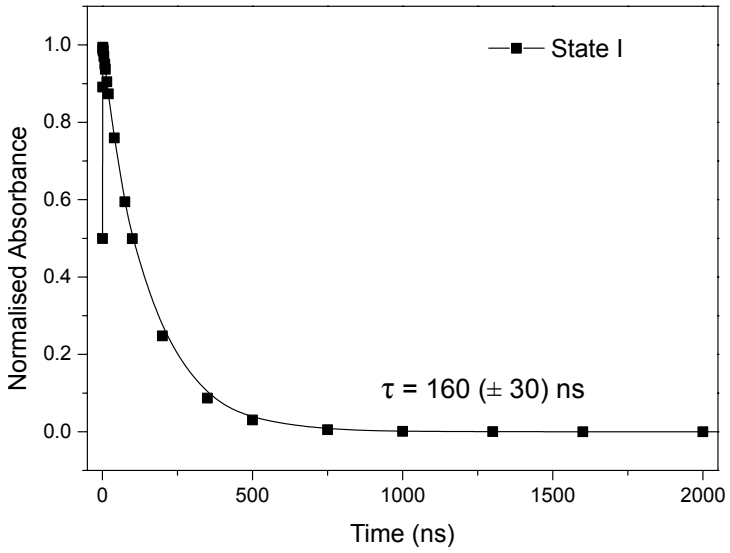


Figure 2.21: The kinetic plot generated from the global analysis for the decay of initial excited state, State I following a 355 nm excitation in CH_3CN.

As the ILCT/MLCT excited state decays, the formation of the photoproduct can be observed to grow in at 1938 cm^{-1} and 2039 cm^{-1}, which matches literature reports for a solvated $[Re(CO)_3(CH_3CN)(bpy)]^+$ complex.[80] The ILCT/MLCT excited state has a lifetime $\tau = 2.1\ (\pm\ 0.4)\ \mu s$, which is similar to the lifetime observed in CH_2Cl_2 ($\tau = 2.9\ \mu s$). The kinetic plot for the decay of the excited state and the formation of the photoproduct can be seen in Figure 2.22.

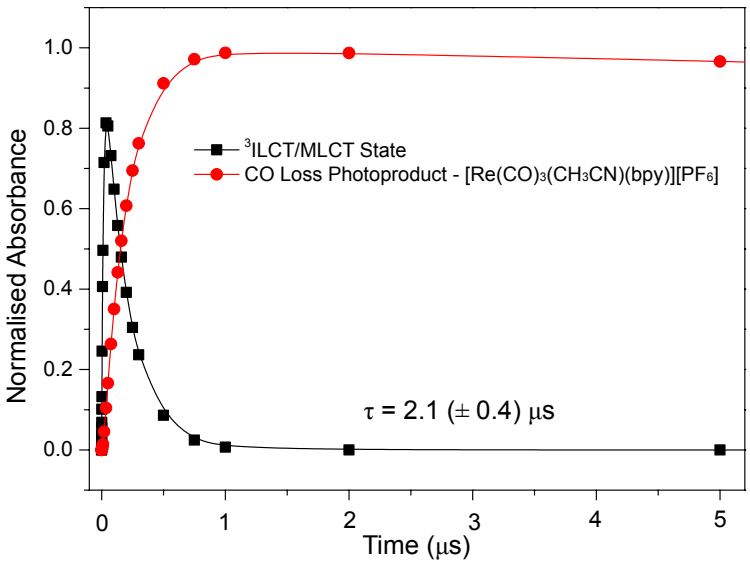


Figure 2.22: The kinetic plot generated from the global analysis for the decay of the ILCT/MLCT state and the growth of photoproduct following a 355 nm excitation in CH_3CN.

The global analysis of the nanosecond data suggests the presence of three species, which is comparable with the nanosecond data in CH_2Cl_2. Upon excitation both states, State I and the ILCT/MLCT state are formed on the picosecond timescale, with State I decaying away on the nanosecond timescale (τ = 230 ns). The mixed ILCT/MLCT excited state is seen to decay away and form the photoproduct, $[Re(CO)_3(bpy)(MeCN)]^+$. The lifetimes of all the transient species after irradiation at 355 nm are given in Table 2.1.

Table 2.1: The lifetimes of the processes observed in both the *ps* and *ns*-TRIR for $[Re(CO)_4(bpy)][PF_6]$.

Solvent	Nature of State	Band Position (cm^{-1})	τ
CH_2Cl_2	State I	2067, 1966, 1973	100 ($\pm$ 10) ns
	ILCT/MLCT	2113, 2040, 2020, 1986	2.9 ($\pm$ 0.3) μs
	$[Re(CO)_3(bpy)(CH_2Cl_2)]$	2054, 1955	-
CH_3CN	State I	2111, 2060, 2037, 2009	160 ($\pm$ 30) ns
	ILCT/MLCT	2112, 2039, 2010, 1983	2.1 ($\pm$ 0.4) μs
	$[Re(CO)_3(bpy)(CH_3CN)][PF_6]$	2039, 1938	-

The nature of the mixed excited state is known from the literature reports of absorption spectroscopy and TRIR measurements to have both ^{3}LC and ^{3}MLCT excited state character.[77–79] The luminescence spectroscopy mentioned later in the Chapter, also supported the observation of this mixed state, as it exhibits both structured (^{3}LC character) and broad (^{3}MLCT) emission bands. To further understand the nature of this mixed state, TD-DFT calculations were performed by Nottingham and in collaboration with Joshua Sutton at the University of Otago in New Zealand. These TD-DFT calculations along with electron density calculations resulted in the nature of the mixed states exhibited by $[Re(CO)_4(bpy)][PF_6]$ being further understood. The TD-DFT calculations were run in a vacuum field as well as in a CH_2Cl_2 and CH_3CN solvent field to understand the nature of the excited state in the solvent. The TD-DFT calculated different singlet and triplet excited state transitions for $[Re(CO)_4(bpy)][PF_6]$ in a vacuum, CH_2Cl_2 and CH_3CN. The change in electron density for the transition was also calculated to help determine the nature of the excited states, thus supporting the assignment the excited state being observed in the TRIR.

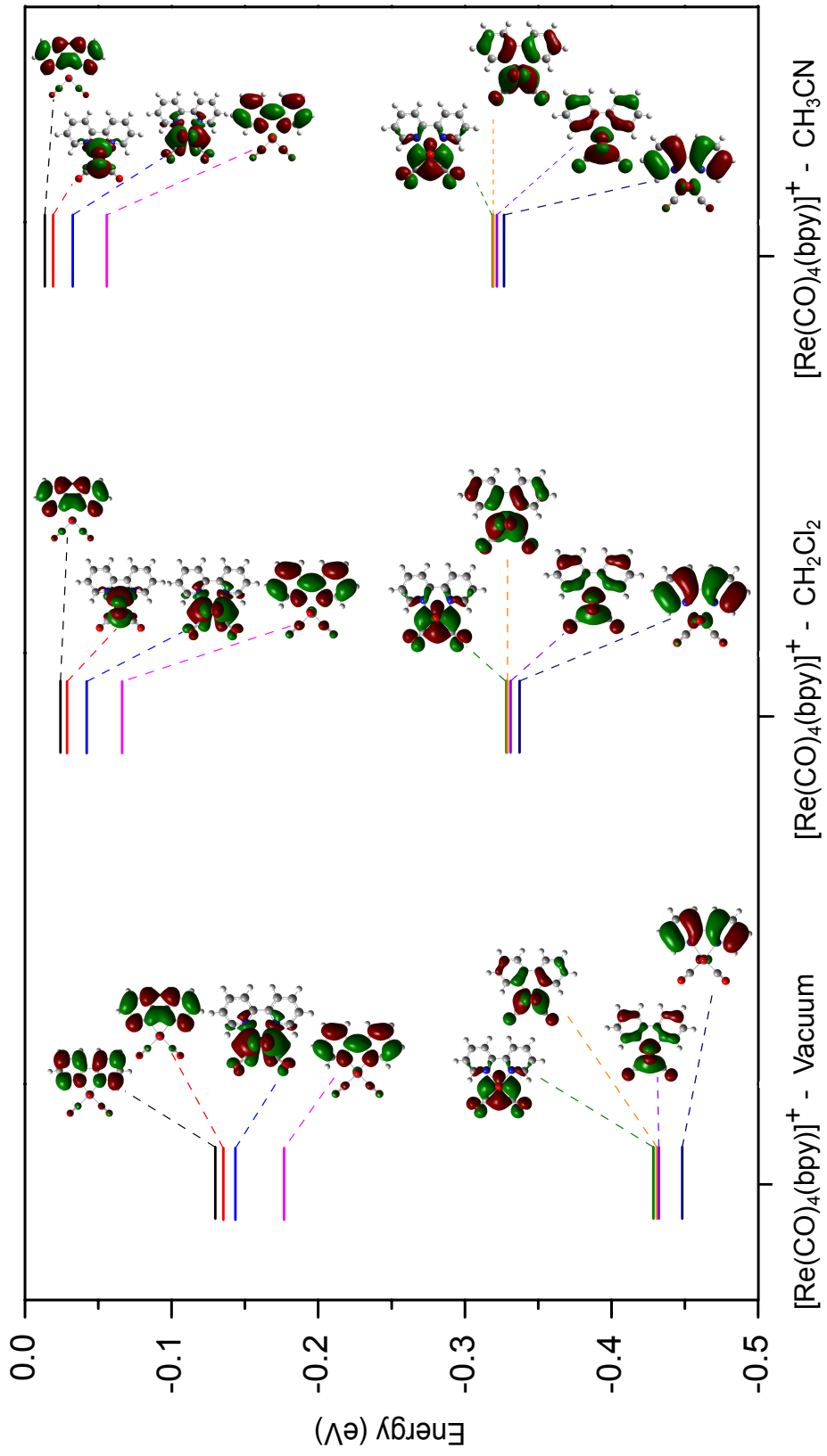


Figure 2.23: The energy of the HOMO-3 (navy), HOMO-2 (purple), HOMO-1 (orange), HOMO (green), LUMO (pink), LUMO+1 (blue), LUMO+2 (red) and the LUMO+3 (black) and the corresponding molecular orbitals calculated using TD-DFT in a vacuum field (left), CH_2Cl_2 field (middle) and a CH_3CN field (right).

The energies ranging from the HOMO -3 to LUMO -3, and the molecular orbitals calculated for a vacuum, CH_2Cl_2 and CH_3CN solvent fields can be seen in Figure 2.23. The main observation is the CH_2Cl_2 and CH_3CN MOs sit at higher energy in both solvents compared to the vacuum field. The metal based HOMO, HOMO -1 and HOMO -2 orbitals all sit at similar energy in a vacuum, with the ligand based orbital HOMO -3, sitting at lower energy. For both CH_2Cl_2 and CH_3CN the HOMO, HOMO -1 and HOMO-2 orbitals also sit at very similar energy to each other, with the ligand based orbital HOMO-3 MO lying slightly closer in energy to the metal based orbitals. As the orbitals go from HOMO to HOMO-3, more ligand character is observed, with HOMO-3 being predominately ligand based, this trend can be seen for both solvent fields and the vacuum. The energies of the LUMO to LUMO +3 sit further apart than the HOMO to HOMO -3 for all three fields. The MOs for LUMO and LUMO +1 appear to be similar for the vacuum, and the solvent fields with the LUMO being predominately ligand based and LUMO+1 being mainly metal based. The main contrast is in a vacuum, both LUMO +2 and LUMO +3 are ligand based, however in CH_2Cl_2 and CH_3CN LUMO +2 is metal based and LUMO +3 is ligand based and resembles the LUMO +2 seen in vacuum. This suggests that the solvent field has an affect of the energy of the higher energy LUMO's. Additionally the energy of the LUMO and LUMO +1 sit at slightly higher energy in CH_3CN than CH_2Cl_2. The MO's for LUMO+1 orbitals appear to have an orbital that sits between the two axial CO ligands, which could be responsible for the ^{3}ILCT/MLCT excited state that results in the loss of the CO ligand. This LUMO +1 MO is seen in the vacuum, CH_2Cl_2 and CH_3CN which suggests that the mixed ^{3}ILCT/MLCT excited state is not affected by the solvent, as supported by the observations seen the luminescence spectroscopy, and the TRIR.

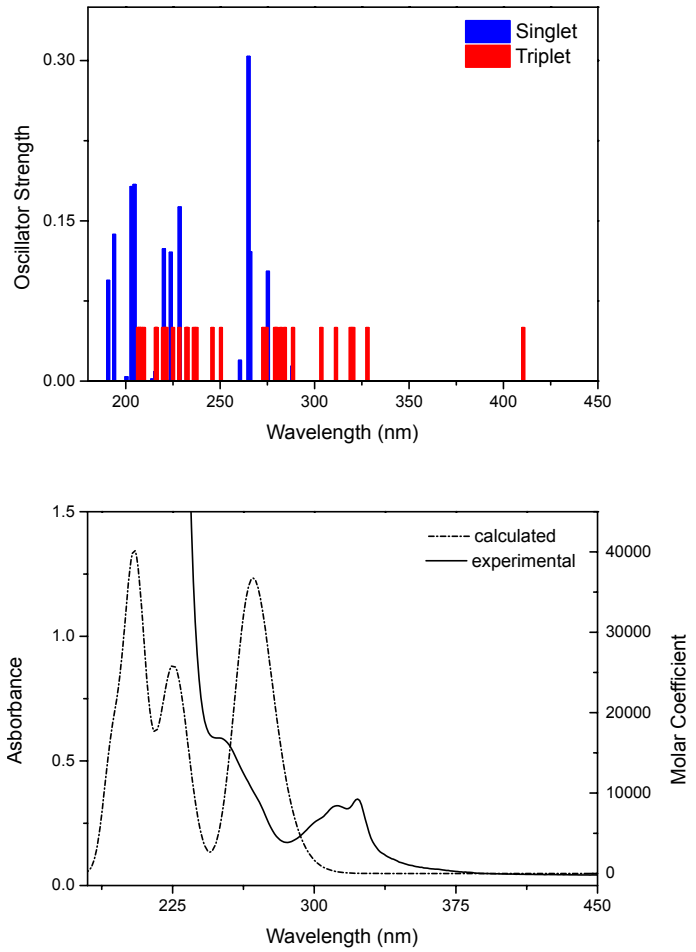


Figure 2.24: The triplet (red) and singlet (blue) excited state transitions calculated using TD-DFT in a CH_2Cl_2 field (top) and the calculated and experimental UV-vis spectra (bottom).

The TD-DFT calculated transitions for a CH_2Cl_2 solvent field can be seen in Figure 2.24. Both singlet and triplet transitions were calculated with both excited states having a range of excited state character, from being pure MLCT states, LC states to mixed ILCT/MLCT excited states. The calculated singlet excited state transitions suggest a mixture of MLCT(Re-bpy) and ILCT/MLCT states, with the strongest transition being LC in nature, with weak MLCT(Re-bpy) character. This

singlet transition can be clearly seen in the calculated UV-vis spectrum in Figure 2.24. This is the lowest energy absorption maxima and corresponds with literature reports which stated this transition had both LC and CT character.[78] The calculated UV-vis spectrum sits at higher energy than the experimental UV-vis, but it is likely that upon excitation at 355 nm it will be this singlet transition that is populated. The triplet excited state transitions are a mixture of ILCT/MLCT and MLCT excited states. There are two ILCT/MLCT excited states that sit close in energy, these sit at lower energy to the singlet excited state transition. It is likely that these mixed states are populated following the relaxation and intersystem crossing that occurs from the singlet state.

The calculated transitions and UV-vis spectrum for a CH_3CN solvent field are shown in Figure 2.25, where similar singlet and triplet excited state transitions are seen to the CH_2Cl_2 solvent field. From the HOMO and LUMO MO's energy levels, it can be seen that in a CH_3CN solvent field, the energy levels sit at higher energy than in a CH_2Cl_2 solvent field. This trend was also observed for the singlet and triplet transitions, which also sit at higher energy to the CH_2Cl_2 calculations. The nature of the singlet excited state transitions resemble the CH_2Cl_2 calculations, with MLCT(Re-bpy) and ILCT/MLCT states being observed. The strongest singlet transition, and the lowest energy absorption maxima is also LC in nature, with weak MLCT(Re-bpy) character. It can be assumed that this is also the singlet excited state that is populated following a 355 nm excitation. The nature of the triplet excited state transitions in CH_3CN were also predominately ILCT/MLCT excited states and MLCT excited states, with two close lying ILCT/MLCT excited states. The main difference between the two solvent fields is the transitions in CH_3CN sit at higher energy to those in CH_2Cl_2.

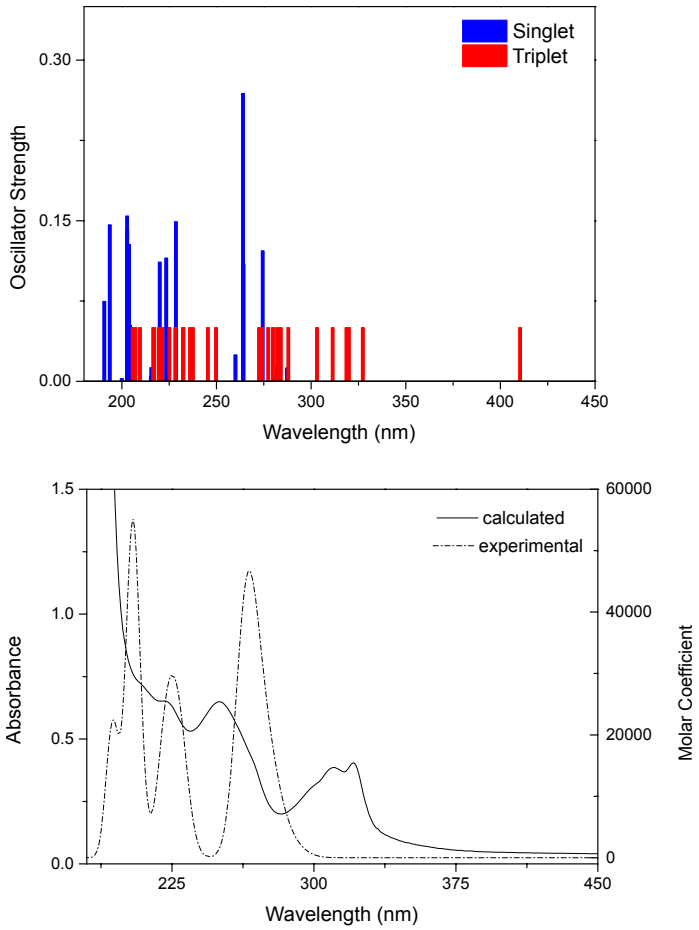


Figure 2.25: The triplet (red) and singlet (blue) excited state transitions calculated using TD-DFT in a CH_3CN field (top), with the calculated and experimental UV-vis spectra (bottom).

The TD-DFT transitions show that in a vacuum, the nature of the excited state is predominately ^{3}MLCT, whereas in CH_2Cl_2 and CH_3CN there is a greater percentage of ^{3}ILCT/MLCT. For both solvents there are two ILCT/MLCT excited states, with one sitting at lower energy to the other. These mixed ILCT/MLCT excited states are likely to be populated when $[Re(CO)_4(bpy)][PF_6]$ is excited at 355 nm. The nature of these two ILCT/MLCT excited states show slightly different charge transfer character.

The character of these ILCT/MLCT excited states was determined by looking at the distribution of their electron charge. The predicted change in the electron density can be seen in Figure 2.26, which indicates that in a vacuum the calculated excited state is mainly MLCT. There is a large proportion of the electron density going from the metal centre onto the bipyridine ligand, and some electron density moving from the CO ligands onto the bipyridine ligand. However, this change is affected when the calculations are performed in a solvent field, in both CH_2Cl_2 and CH_3CN different charge transfer character calculations indicate that the ILCT/MLCT change character. From the electron density calculations the higher energy ILCT/MLCT excited state shows an ILCT from the bipyridine ligand onto the axial CO ligand, and MLCT from the rhenium centre onto the axial CO ligand which makes up the mixed excited state, as shown in Figure 2.26. The TD-DFT calculations suggest the long-lived excited state observed in the TRIR spectrum of both solvents can be assigned as a ^{3}ILCT/MLCT excited state.

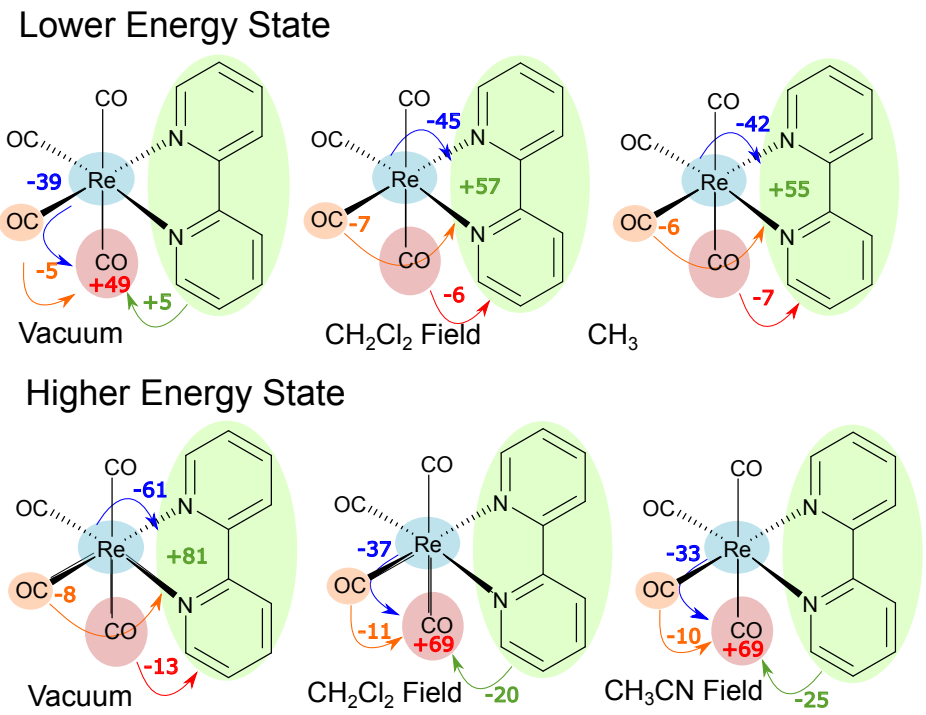


Figure 2.26: The movement of electron density that occurs for the higher energy ILCT/MLCT mixed state in a vacuum field (left), CH_2Cl_2 field (middle) and a CH_3CN field (right).

The lower energy mixed excited state appears to have slightly different charge transfer character, with the ILCT between both the axial and equatorial CO ligands to the bipyridine ligand, but also MLCT character from the rhenium center to the bipyridine ligand, as seen in Figure 2.26. The change in the MLCT character supports the observation seen for State I in the *ps* and *ns*-TRIR for both CH_2Cl_2 and CH_3CN, which shows some of the ν(CO) bands shift to higher energy which, is indicative of a metal to diimine ligand charger transfer.[79] The luminescence spectroscopy exhibited of an emissive state, which had a lifetime similar to that seen for State I in the TRIR, $\tau \approx$ 100 - 160 ns. With TD-DFT, electron density calculations, TRIR and luminescence spectroscopy the emissive excited state and State I can be assigned as mixed ILCT/MLCT excited state with different MLCT character.

From the CH_2Cl_2 and CH_3CN *ps* and *ns*-TRIR experiments, luminescence spectroscopy and TD-DFT calculations, a clear process is seen following a 355 nm excitation. The process that occurs is illustrated in Figure 2.27. Following excitation a high energy singlet is seen to decay and populate two mixed excited states, State I and the ^{3}ILCT/MLCT excited state, this is observed to occur on the picosecond timescale. State I is seen to decay on the nanosecond timescale which supports the lifetimes observed in both the TRIR and luminescence spectroscopy, thus State I is thought to be an emissive state. The TD-DFT calculations suggest this state has both ^{3}ILCT and ^{3}MLCT nature, with the ^{3}MLCT resulting from a charge transfer from the rhenium onto bipyridine ligand. The other state, the ^{3}ILCT/MLCT excited state, decays on the microsecond timescale and results in the photodissociation of a CO ligand. The TD-DFT calculations have identified that this state also has both ^{3}ILCT and ^{3}MLCT nature, however the ^{3}MLCT results from charge transfer from the rhenium onto the axial CO ligands. This long-lived mixed excited state is consistent with literature reports, where the photodissociation of CO is observed, resulting in a solvated photoproduct.[71,79] The increased intensity of the emission seen in both CH_2Cl_2 and CH_3CN under CO also supports the presence of two mixed excited states, with formation of the photoproduct being inhibited under CO, so the ^{3}ILCT/MLCT excited state decays *via* the emissive pathway, State I which is discussed later in Chapter 2.

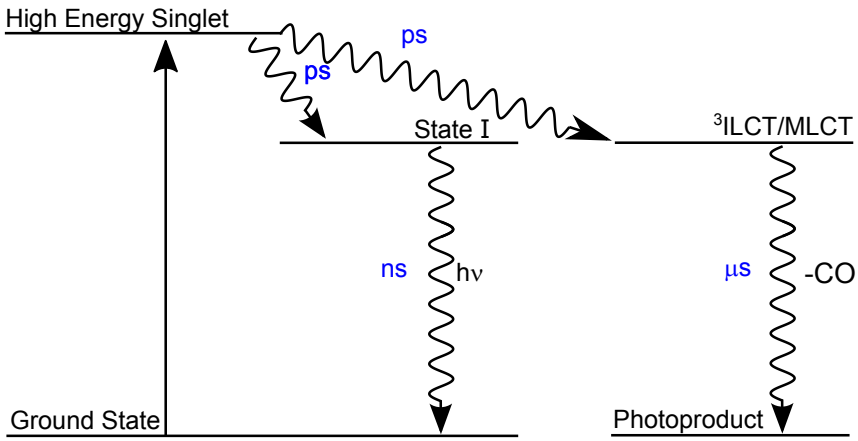


Figure 2.27: An illustration of the photophysical and photochemical processes that occur for $[Re(CO)_4(bpy)][PF_6]$ following 355 nm excitation.

2.3.2.2 TRIR of $[Re(CO)_4(bpy)][PF_6]$ at 266 nm

The investigation of $[Re(CO)_4(bpy)][PF_6]$ in CH_2Cl_2 and CH_3CN irradiating at 355 nm showed the population of two initial excited states, State I and the ^{3}ILCT/MLCT state in both CH_2Cl_2 and CH_3CN. A photoproduct was formed in both solvents, which was generated following the decay of the ^{3}ILCT/MLCT excited state. The excitation energy was increased to 266 nm to see how the photophysics and photochemistry would change. Again, both *ps* and *ns*-TRIR were used to probe $[Re(CO)_4(bpy)][PF_6]$ in CH_2Cl_2 and CH_3CN at 266 nm.

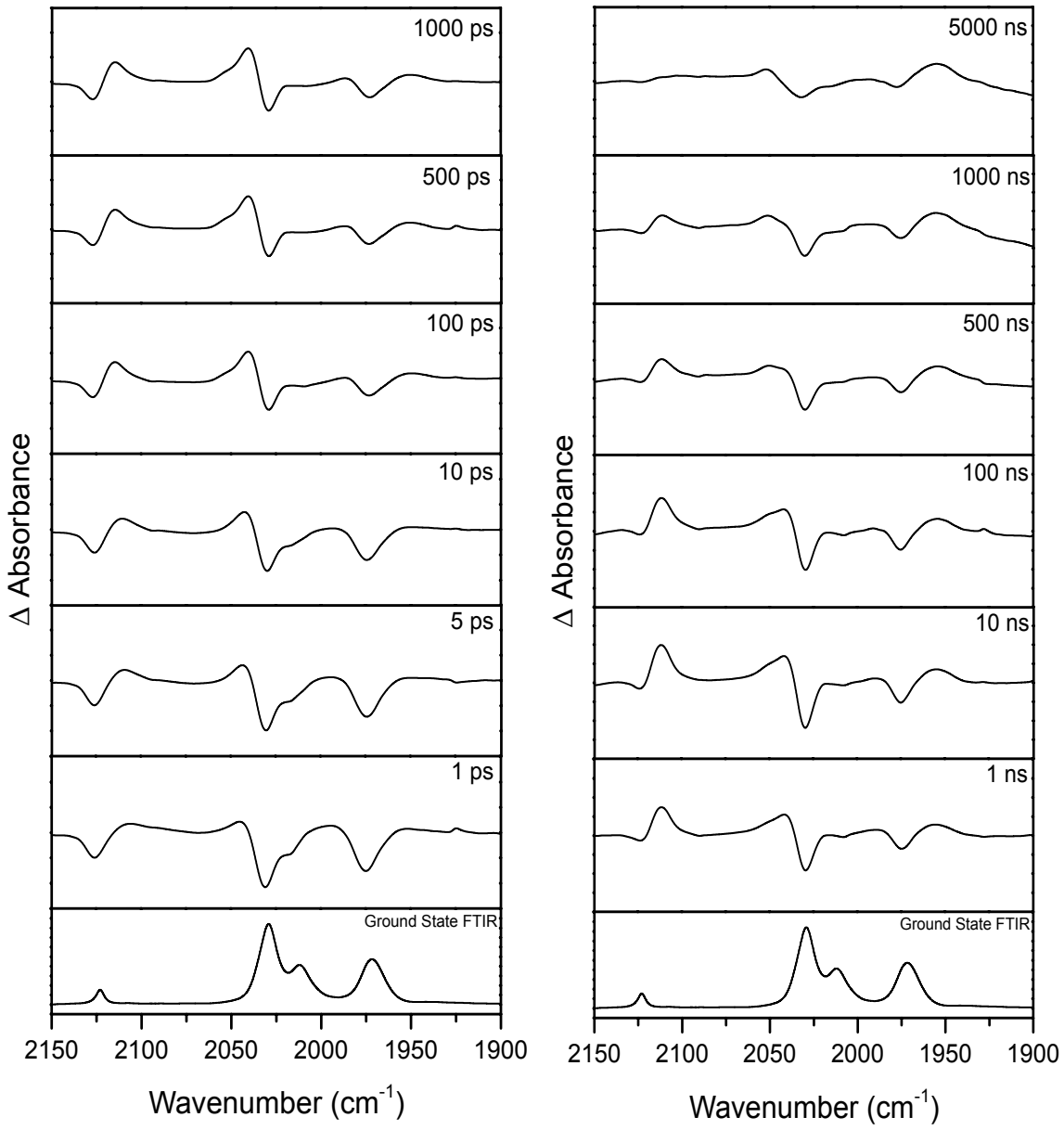


Figure 2.28: The *ps*-TRIR (left) and *ns*-TRIR spectra (right) spectra of $[Re(CO)_4(bpy)][PF_6]$ in CH_2Cl_2 following a 266 nm excitation wavelength.

The *ps*-TRIR spectra of $[Re(CO)_4(bpy)][PF_6]$ in CH_2Cl_2 following a 266 nm excitation can be seen in Figure 2.28. The parent bands are seen to bleach and transient bands grow in at 2114, 2040, 2019 and 1987 cm^{-1}, which is consistent with the formation of the mixed ^{3}ILCT/MLCT excited state. Initially the vibrational hot

mixed ^{3}ILCT/MLCT excited state can be observed, which cools (τ = 18 ps) to a ^{3}ILCT/MLCT excited state. The formation of the ^{3}ILCT/MLCT excited state is seen to grow in on the picosecond timescale, and there appears to be no formation of State I, which was seen following the 355 nm experiment. This could suggest that the higher energy excitation wavelength is directly populating a higher energy ^{3}ILCT/MLCT excited state.

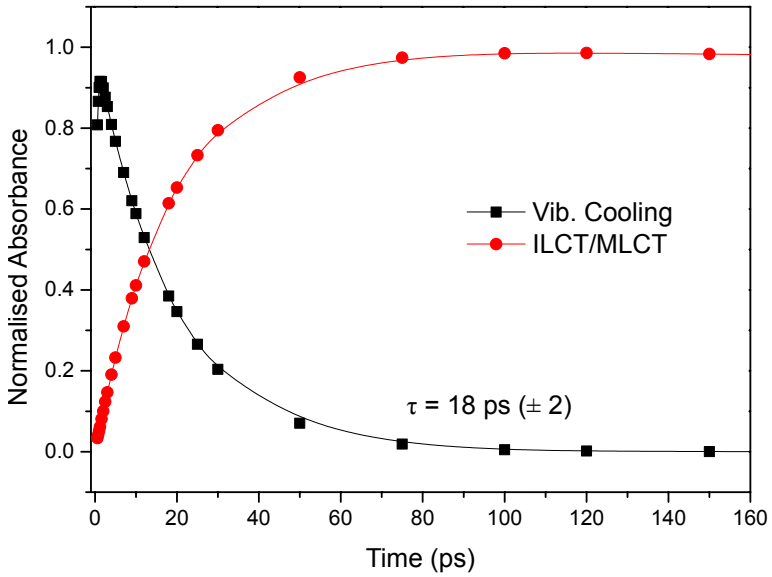


Figure 2.29: The kinetic plot generated from the global analysis for the decay of vibrational cooling and the growth the ILCT/MLCT state following a 266 nm excitation in CH_2Cl_2.

Figure 2.29 shows kinetic plot for the decay of the vibrational hot state (τ = 18 ps) and the formation of the ^{3}ILCT/MLCT excited state. The ^{3}ILCT/MLCT excited state is observed for the duration of the picosecond timescale, and is seen to decay away on the nanosecond timescale, unlike the 355 nm experiment where it was seen to live on the microsecond timescale.

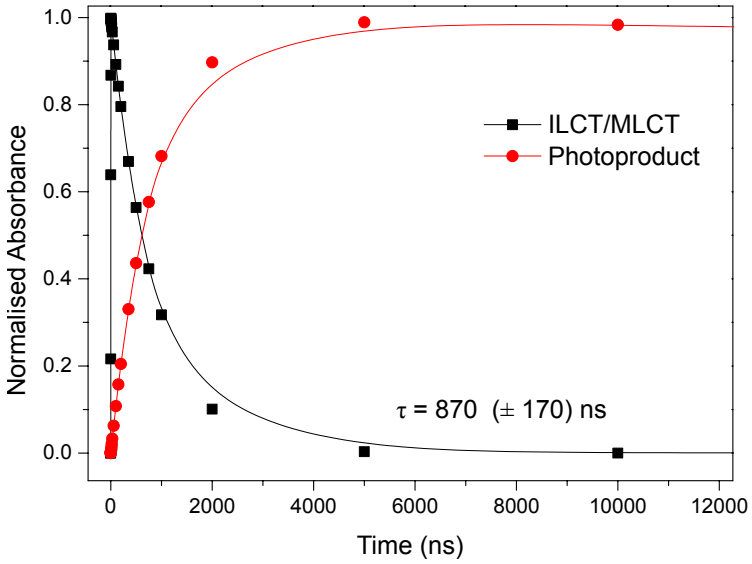


Figure 2.30: The kinetic plot generated from the global analysis for the decay of the ILCT/MLCT state and the formation of the photoproduct following a 266 nm excitation in CH_2Cl_2.

The ^{3}ILCT/MLCT excited state has a lifetime of *ca.* $\tau = 1$ μs, which is much faster than the decay of the ^{3}ILCT/MLCT excited state observed for the 355 nm experiment, where it was seen to decay away after 2.9 μs. The kinetic plot in Figure 2.29 shows the decay of the mixed ^{3}ILCT/MLCT excited state and the formation of the photoproduct. The mixed ^{3}ILCT/MLCT excited state can then be seen to decay away, resulting in the formation of the photoproduct, which can be seen to grow in with two ν(CO) bands at 2051 and 1955 cm^{-1}. The band position of the photoproduct matches the observation seen for the 355 nm experiment for the photoproduct, [Re(CO)$_3$(bpy)(CH$_2$Cl$_2$)].

The global analysis of the 266 nm data indicated only two species, which is consistent with the observations seen in both the *ps* and *ns*-TRIR. The ^{3}ILCT/MLCT excited state species is observed on both the picosecond and nanosecond data sets, with bands at 2112, 2040, 2012 and 1897 cm^{-1}. The excited state spectra for the

nanosecond data can be seen in Figure 2.31, with the ^{3}ILCT/MLCT excited state species in black and the photoproduct in red with two bands at 2052 and 1955 cm^{-1}.

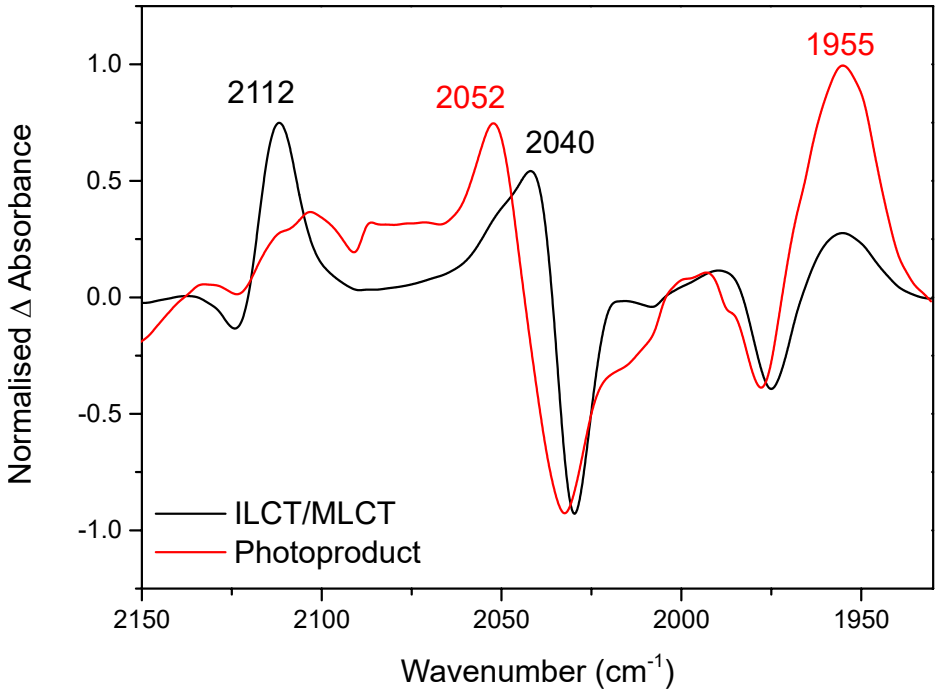


Figure 2.31: The normalised excited state spectra for ILCT/MLCT excited state shown in black and photoproduct shown in red, following a 266 nm excitation in CH_2Cl_2.

In CH_3CN no State I is observed and following vibrational cooling (τ = 17 ps) an excited state species is observed at 2113, 2040, 2010 and 1983 cm^{-1}, which is consistent with the ^{3}ILCT/MLCT excited state.

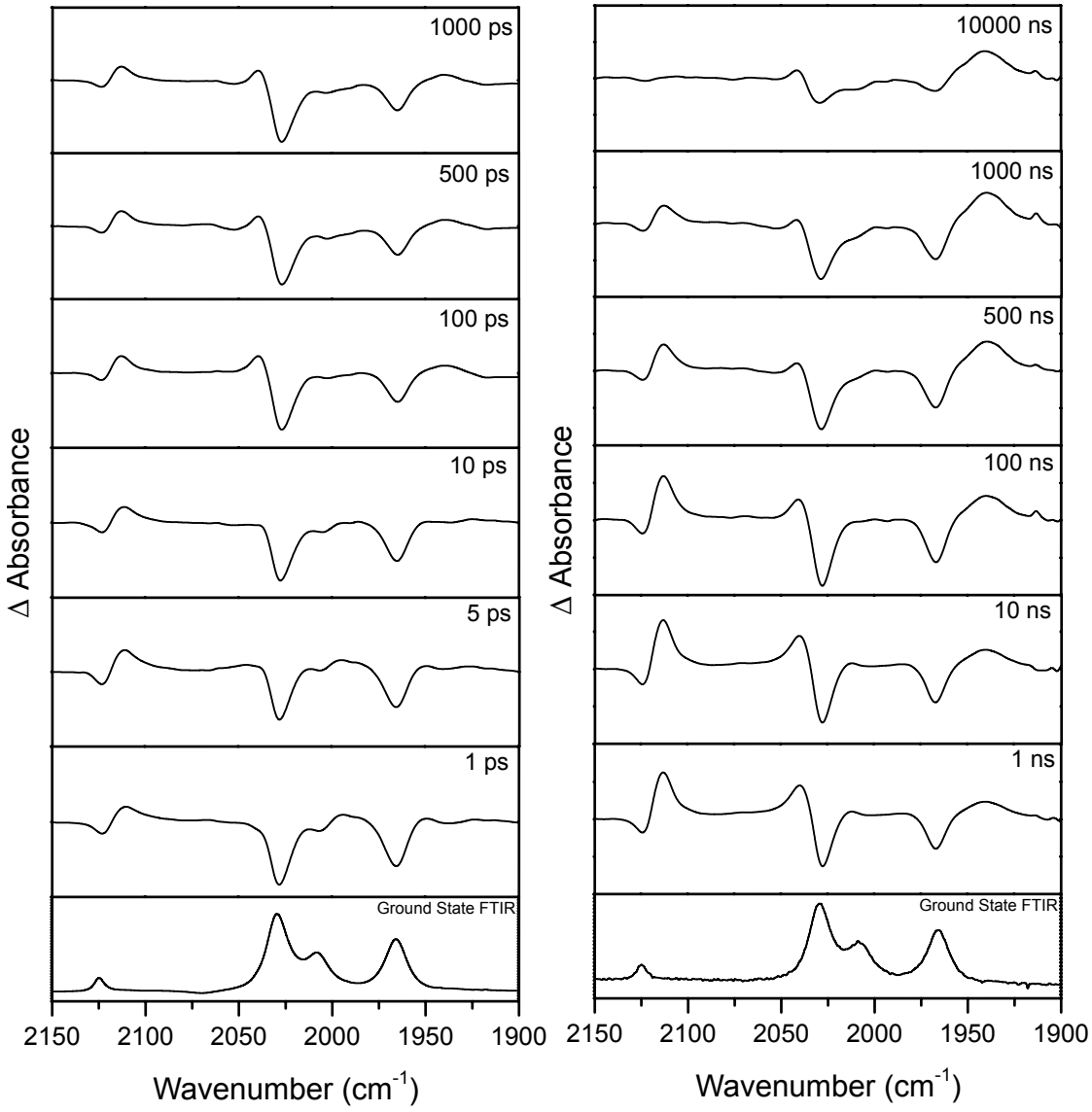


Figure 2.32: The *ps*-TRIR (left) and *ns*-TRIR spectra (right) spectra of $[Re(CO)_4(bpy)][PF_6]$ in CH_3CN following a 266 nm excitation wavelength.

Similar to the CH_2Cl_2 experiment, the ^{3}ILCT/MLCT excited state is formed on the picosecond timescale and then decays away on the nanosecond timescale. The main difference being the ^{3}ILCT/MLCT excited state is much shorter lived in CH_3CN than CH_2Cl_2, which is consistent with what was seen for the 355 nm experiments. The lifetime of the ^{3}ILCT/MLCT excited state in CH_3CN is 350 ns, which decays to form the

photoproduct. The two bands for photoproduct can be seen to grown in at 2040 and 1938 cm^{-1}, which is consistent with the formation of $[Re(CO)_3(bpy)(CH_3CN)][PF_6]$. The kinetic plot for the decay of the ^{3}ILCT/MLCT excited state and the formation of the photoproduct can be seen in Figure 2.33.

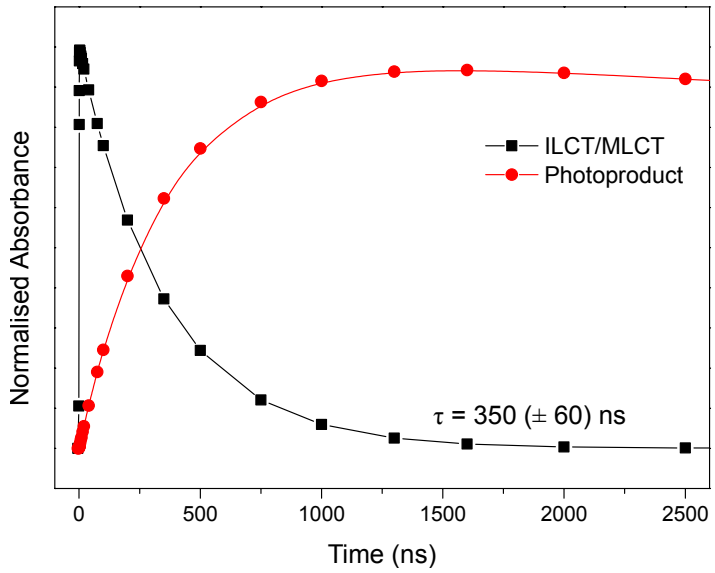


Figure 2.33: The kinetic plot generated from the global analysis for the decay of the ILCT/MLCT state and the formation of the photoproduct following a 266 nm excitation in CH_3CN.

The global analysis of the nanosecond data for the CH_3CN experiment also indicated the presence of two species, the first being the ^{3}ILCT/MLCT excited state and the second being the photoproduct. The excited state spectra for the two species can be seen in Figure 2.34, where the mixed ILCT/MLCT excited state can be seen in black, with bands at 2112, 2040, 2012 and 1987 cm^{-1}. The photoproduct can be seen in red with bands at 2040 and 1939 cm^{-1}.

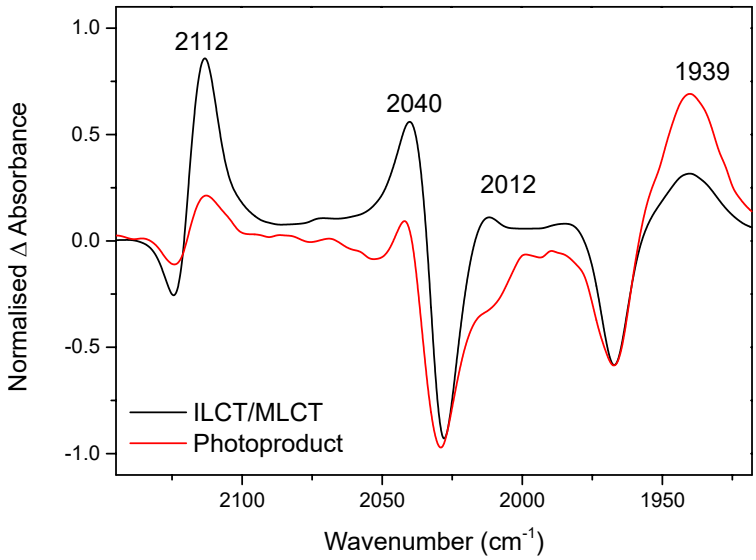


Figure 2.34: The normalised excited state spectra for ILCT/MLCT excited state shown in black and photoproduct shown in red, following a 266 nm excitation in CH_3CN.

The lifetimes observed for the 266 nm experiments are given in Table 2.2 for both the CH_2Cl_2 and CH_3CN experiments. Both the TRIR experiments saw the formation of a mixed ^{3}ILCT/MLCT excited state which decayed to form a photoproduct.

Table 2.2: The lifetimes of the processes observed in both the *ps* and *ns*-TRIR for $[Re(CO)_4(bpy)][PF_6]$ following excitation with 266 nm light.

Solvent	Nature of State	Band Position (cm^{-1})	τ (errors)
CH_2Cl_2	ILCT/MLCT	2114, 2040, 2020, 1987	870 ($\pm$ 170) ns
	$[Re(CO)_3(bpy)(CH_2Cl_2)]$	2054, 1955	-
CH_3CN	ILCT/MLCT	2112, 2040, 2012, 1983	350 ($\pm$ 60) ns
	$[Re(CO)_3(bpy)(CH_3CN)][PF_6]$	2039, 1938	-

The process observed for the 266 nm experiments is different to the processes observed for the 355 nm experiments, where a ^{3}ILCT/MLCT excited state is populated directly. The process that occurs following a 266 nm excitation can be summed up in the illustration shown in Figure 2.35.

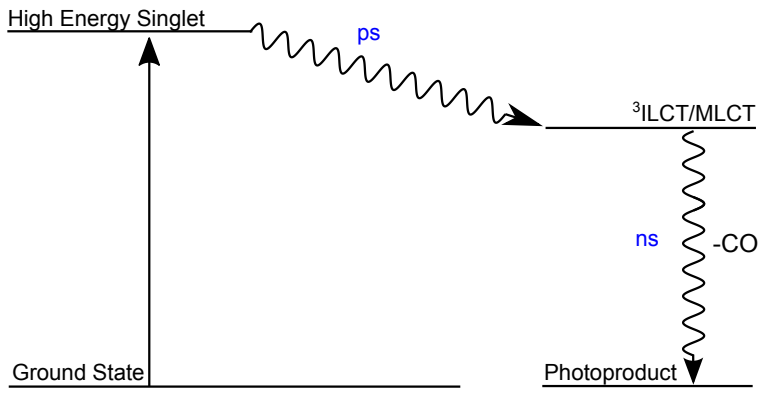


Figure 2.35: An illustration of the photophysical and photochemical processes that occurs for $[Re(CO)_4(bpy)][PF_6]$ following 266 nm excitation.

To investigate the photophysical and photochemical decay process for $[Re(CO)_4(bpy)][PF_6]$ in CH_2Cl_2 and CH_3CN the reformation of the parent bleaches was plotted to see how much recovery there was in the TRIR experiments. Figure 2.36 shows the reformation of the parents bleaches in CH_2Cl_2 and CH_3CN following a 355 and 266 nm excitation. The degree of reformation of the the parent in CH_2Cl_2 is higher than that observed for CH_3CN, suggesting that there is a reduced formation of the solvated photoproduct. The reformation in CH_2Cl_2 suggests for a 355 nm excitation there is a 26 % formation of the photoproduct and for a 266 nm excitation there is 21 % formation, which means the remaining excited state would decay back down to the ground state. In CH_3CN there is a greater formation of the photoproduct, with 40 % at 355 nm and a 36 % at 266 nm. This decreased reformation of the parent observed in CH_3CN could possibly be be due to the polar nature of the solvent, with the lone pair on the nitrogen resulting in stronger binding to the rhenium center compared to

CH_2Cl_2, which could accounts for the increased decay rates of ^{3}ILCT/MLCT excited state in CH_3CN .

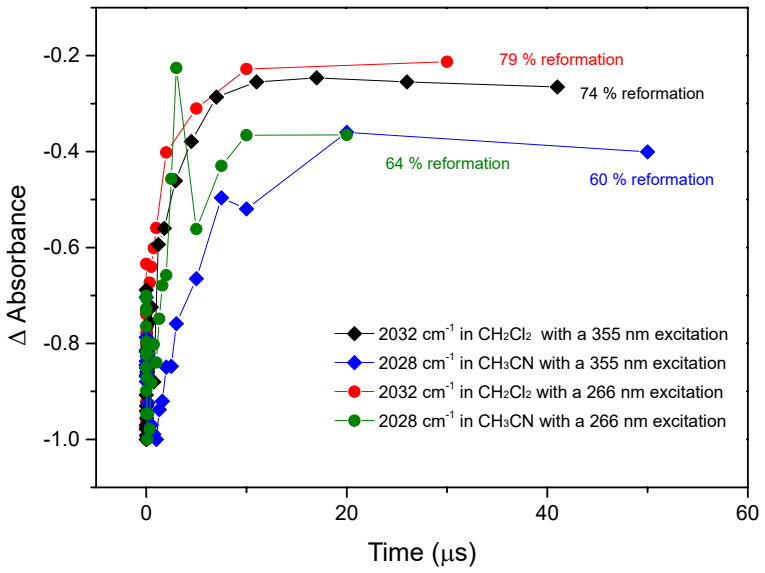


Figure 2.36: The reformation of the parent bands for $[Re(CO)_4(bpy)][PF_6]$ in CH_2Cl_2 and CH_3CN following a 355 and 266 nm excitation.

From the TRIR and TD-DFT calculations it has been shown that in CH_2Cl_2 and CH_3CN, $[Re(CO)_4(bpy)][PF_6]$ exhibits two mixed ^{3}ILCT/MLCT excited states upon excitation with 355 nm light, one decays back down to the ground state resulting in emission and the other goes on to form a photoproduct by the photodissociation of an axial ligand. However, the partial reformation of the parent suggests there is not a complete formation to photoproduct which was reported by Bernhard *et al.*[79] This can be explained by the decay of State I which is emissive. When exciting at 266 nm only one mixed state was observed, which also goes on to form a photoproduct by the dissociation of a CO ligand. This suggest that $[Re(CO)_4(bpy)][PF_6]$ is undergoing both a photophysical and photochemical decay pathway in CH_2Cl_2 and CH_3CN following an excitation at 355 or 266 nm.

2.3.3 Emission of $[Re(CO)_4(bpy)][PF_6]$

Luminescence spectroscopy was used to probe the photophysics of $[Re(CO)_4(bpy)][PF_6]$ in CH_2Cl_2 and CH_3CN to see if the complex is emissive, and determine the nature of the emissive excited state. The energy of the emission band and the structure can help shed light on the nature of the excited state. It was expected that $[Re(CO)_4(bpy)][PF_6]$ complexes have a mixed excited state that was predominately a LC excited state with mixture of 1-3 % MLCT character.[79] Therefore, if this mixed excited state is emissive the structure of the emission band will help identify the nature of the excited state. An emissive ^{3}LC excited state has strong vibronic character lying around *ca.* 500 nm, whereas a ^{3}MLCT excited state sits at lower energy and is broader and structureless.

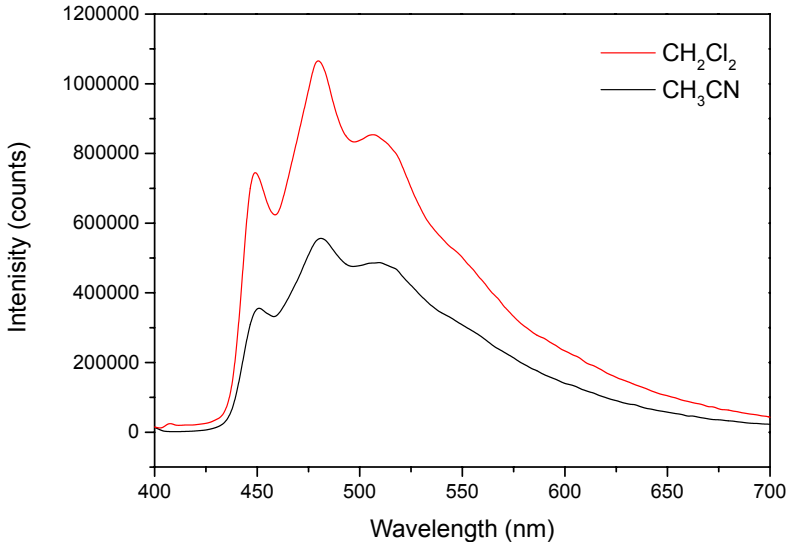


Figure 2.37: The emission spectra of $[Re(CO)_4(bpy)][PF_6]$ in CH_2Cl_2 and CH_3CN following a 355 nm excitation.

The emission of $[Re(CO)_4(bpy)][PF_6]$ was probed in CH_2Cl_2 at 355 nm shown in Figure 2.37. At higher energy there appears to be some strong vibronic character at 449 and 479 nm, which is consistent with a ^{3}LC excited state. However, at lower energy

(*ca.* 507 nm) the emission band become structureless and starts to broaden, which is indicative of the presence of a ^{3}MLCT excited state. This observation is consistent with literature reports of a mixed excited state.[79] It also supports both the solid state and solution luminescence reported in the literature,[71,77] which observed both a ^{3}LC transition as well as ^{3}MLCT excited state character. The lifetime of the emission was measured to be *ca.* 155 ns using 406 nm diode laser (Figure 2.38). This is much faster than the lifetime reported in the literature, of 4.7 μs for $[Re(CO)_4(bpy)][PF_6]$ in CH_2Cl_2.[71] The longer lifetime reported in the literature was measured using a 355 nm excitation wavelength under an atmosphere of CO to deter photodecomposition,[71] which could contribute to the contrasting lifetimes. However, the lifetime measurement was repeated under a CO atmosphere and there was no change to the lifetime. This suggests the emission being observed could be from a different excited state that sits at slightly lower energy to the mixed reported in the literature,[71,79] this emissive state being observed also has both ^{3}LC and ^{3}MLCT excited state character.

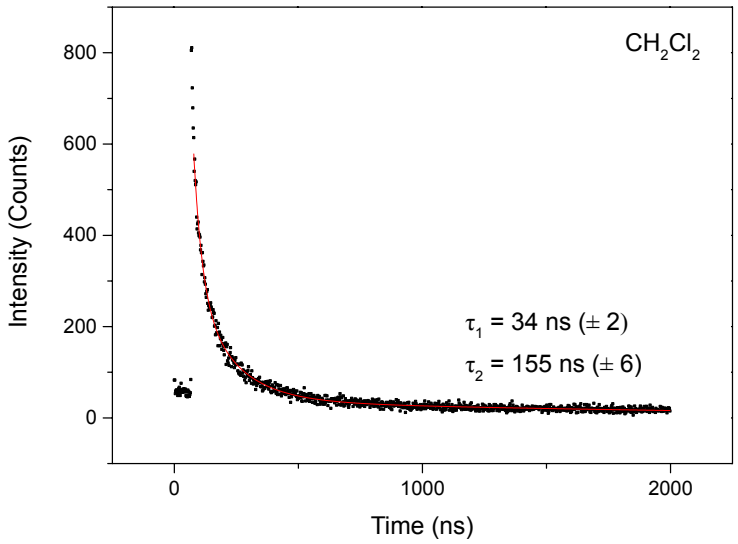


Figure 2.38: The lifetime of the emission of $[Re(CO)_4(bpy)][PF_6]$ observed in CH_2Cl_2 probed with a 406 nm diode laser.

Following this, the emission of $[Re(CO)_4(bpy)][PF_6]$ was probed in CH_3CN at 355 nm (Figure 2.37) to see how changing the solvent alters the nature of the excited state. The photophysics of $[Re(CO)_4(bpy)][PF_6]$ has only been probed in lower polarity solvent like dichloroethane and dichloromethane, it was hypothesise that increasing the polarity of the solvent might result in a change of the photophysical properties. In CH_3CN, the same strong vibronic character was observed at 451 and 482 nm, with a broader and structureless band at lower energy (*ca.* 525 nm), which is consistent with observation seen in CH_2Cl_2. The emission band observed in CH_3CN again shows both ^{3}LC and ^{3}MLCT excited state character. However, the intensity of this excited state is lower that than seen in CH_2Cl_2, with counts at *ca.* 15,000 vs 60,000 for CH_2Cl_2. The lifetime was also probed in CH_3CN with a 406 nm diode laser (Figure 2.39), where a lifetime of *ca.* 180 ns was observed. This is consistent with the lifetime measured in CH_2Cl_2, which is much faster than the mixed LC/MLCT excited state reported in the literature.[71,79] $[Re(CO)_4(bpy)][PF_6]$ has not be probed in CH_3CN before, however this reduction of the lifetime observed is probably not a result of the solvent being changed. One possible explanation for the emission being observed in CH_3CN, is the result of an emissive mixed excited state that sits at lower energy to the mixed state reported in the literature. The emission band positions for CH_2Cl_2 and CH_3CN with emission lifetimes can be seen below in Table 2.3.

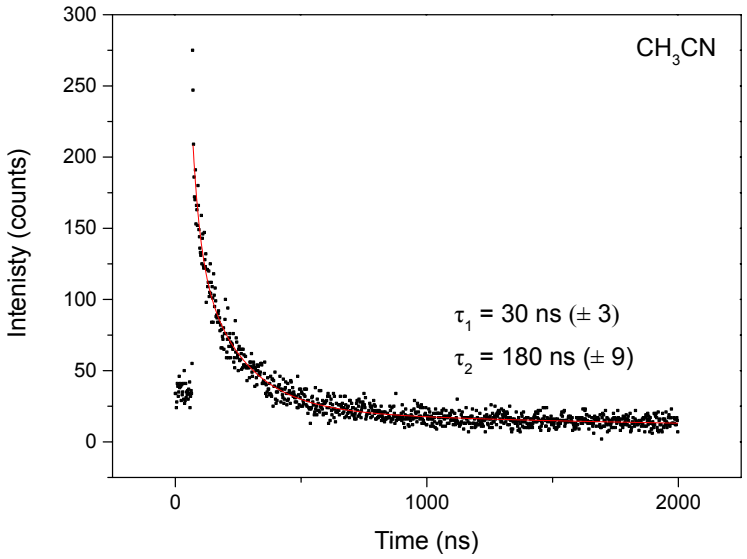


Figure 2.39: The lifetime of the emission of $[Re(CO)_4(bpy)][PF_6]$ observed in CH_3CN probed with a 406 nm diode laser.

Table 2.3: . The emission bands observed when $[Re(CO)_4(bpy)][PF_6]$ was probed at 355 nm in CH_2Cl_2 and CH_3CN.

Solvent	λ_{em} (nm)	lifetime (errors)
CH_2Cl_2	449, 479, *ca.* 507	34 (± 2) ns
		155 (± 6) ns
CH_3CN	451, 482, *ca.* 506	30 (± 3) ns
		180 (± 9) ns

The emission was repeated under a CO atmosphere to perform experiments under the conditions similar to the emission data reported in the literature.[71] The main observation of the emission experiments in the presence of CO showed an increased intensity of emission band when compared to the emission under an atmosphere of Ar. Figure 2.40 shows the emission of $[Re(CO)_4(bpy)][PF_6]$ in CH_2Cl_2 under and atmosphere of CO vs Ar, where the intensity of the emission is seen to increase by a

factor of thirty when under a CO atmosphere. This drastic increase in the intensity of the emission bands suggest the photodissociation of the excited state is being inhibited by the CO atmosphere, thus resulting in a decay of the excited state *via* an emissive pathway. This supports the observations seen for the CO experiment reported in the literature.[71] The same increased intensity of the emission band was observed for $[Re(CO)_4(bpy)][PF_6]$ in CH_3CN under and atmosphere of CO, with an increase of a factor of fifty being observed. This also supports the observation of the CO atmosphere inhibiting the photodissociation of CO, and thus decay *via* an emissive pathway. The emission bands of $[Re(CO)_4(bpy)][PF_6]$ in CH_3CN under an atmosphere of CO and Ar can be seen in Figure 2.40. The fact that the lifetime of the two emission bands was not affected when the experiment was repeated under an atmosphere of CO does suggests that the excited state being probed is different to that reported in the literature.[71] The only difference between the two lifetime experiments was the excitation wavelength, with the literature using a 355 nm excitation source.

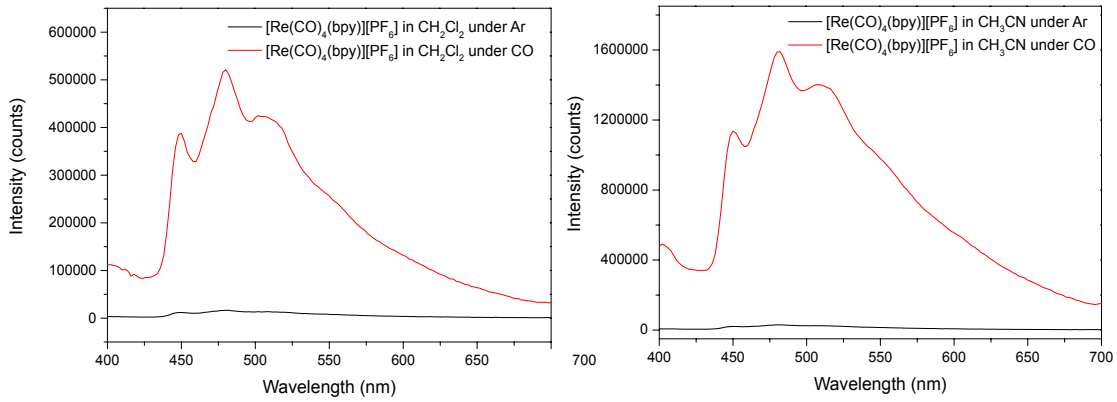


Figure 2.40: The emission of $[Re(CO)_4(bpy)][PF_6]$ observed in CH_2Cl_2 under an atmosphere of CO (left) and Ar (right). The excitation wavelength for all the measurements was 355 nm.

2.3.4 Electrochemistry of $[Re(CO)_4(bpy)][PF_6]$

A preliminary investigation of the electrochemistry and spectroelectrochemistry was conducted to probe the redox potential of $[Re(CO)_4(bpy)][PF_6]$. Being able to understand the electrochemical properties can help further understand the photophysical properties of the complex. The electrochemistry was probed in both CH_2Cl_2 and CH_3CN with the spectroelectrochemistry being monitored with FTIR and UV-vis spectroscopy. Literature reports for the electrochemistry of $[Re(CO)_4(bpy)][PF_6]$ in CH_3CN suggested that following the reduction of the complex it undergoes CO loss to form a solvated product.[80] This investigation was run in an electrochemical infrared cell, therefore a bulk reduction was performed to ensure an efficient diffusion of the electrons across the solution. The cyclic voltammetry (CV) for the reduction in CH_3CN can be seen in Figure 3.38, with the first and second reductions run at varying scan rates. The first scan was run from 0 eV to -1.27 eV and appears to have a reversible process associated with the reduction. The first reduction has two peaks at -1.0 eV and -1.20 eV suggesting there may be a reversible and a non-reversible process. The $E_{1/2}$ value of first reduction is -1.545 eV (*vs.* Fc/Fc^+).

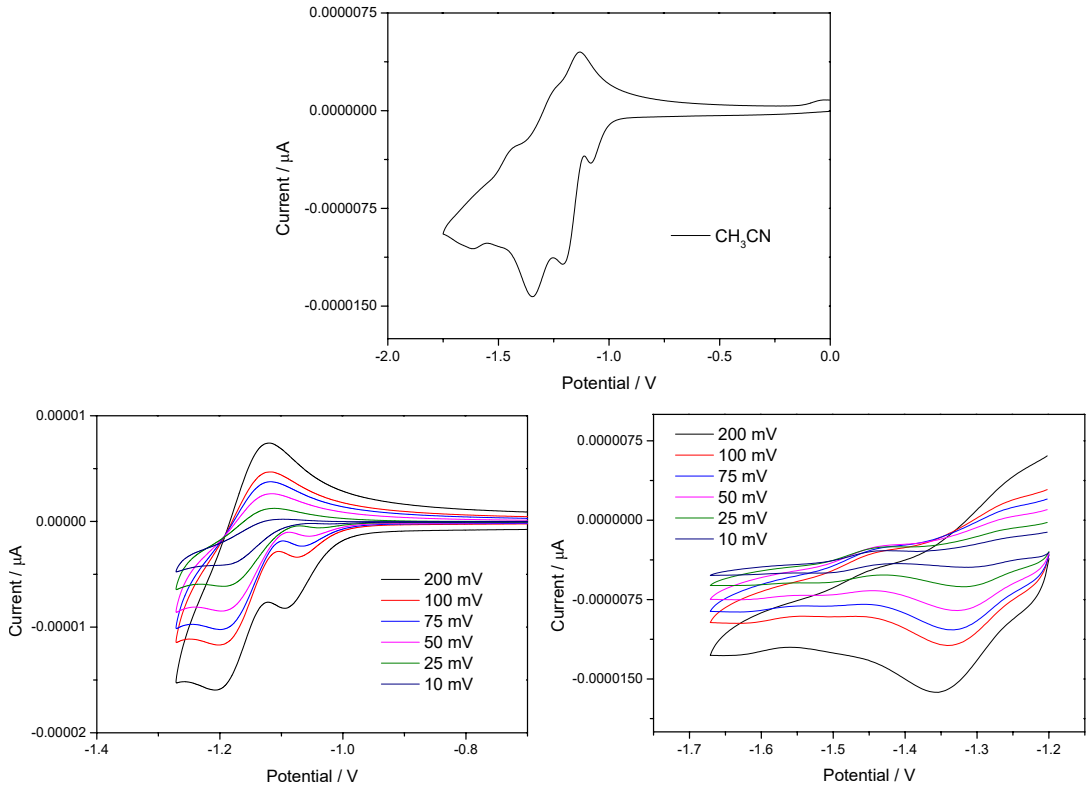


Figure 2.41: The cyclic voltammetry for the reduction $[Re(CO)_4(bpy)][PF_6]$ in $CH_3CN/[TBA][BF_4]$ with the full scan (top), first reduction (bottom left) and the second reduction (bottom right).

The second reduction was run from -1.2 eV to -1.67 eV and does not appears to be as reversible as the first reduction, with an $E_{1/2}$ value of -1.835 eV (*vs.* Fc/Fc^+). Due to the nature of the second reduction only the spectroelectrochemistry of the first reduction was probed. The FTIR of the spectroelectrochemistry can be seen in Figure 2.42, where the initial neutral spectrum can be seen at 2125, 2029, 2008 and 1965 cm^{-1}. The solution was fully reduced by holding the potential for 10 minutes at -1.28 eV and a colour change of pale yellow to a dark green was observed. The FTIR of the reduced species can be seen in red in Figure 2.42, where multiple ν(CO) bands can be observed. The five ν(CO) bands at 2013, 1997, 1913, 1884 and 1851 cm^{-1},

which are consistent with the potential formation of $[Re(CO)_3(bpy)(CH_3CN)]^0$ and $[Re(CO)_3(bpy)(CH_3CN)]^-$.[80] However, more investigation will need to be carried out to confirm this. When a CV of this reduced species was recorded, an oxidation was observed at *ca.* 0.5 eV. As a result of this, the reduced solution was oxidised at 0.5 eV for 50 minutes until the solution had been fully oxidised, resulting in a colour change from a dark green to a bright yellow. The FTIR of the oxidised species is shown in blue in Figure 2.42, with two bands at 2040 and 1934 cm^{-1}, suggesting that the complex had lost a CO ligand and formed the solvated $[Re(CO)_3(bpy)(CH_3CN)][PF_6]$ product.[80] The oxidation of the reduced species does not appear to have a full conversion to the solvated product.

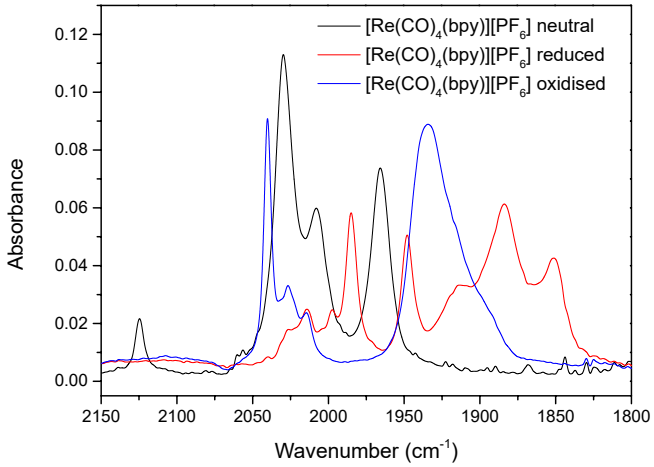


Figure 2.42: The FTIR spectra for the $[Re(CO)_4(bpy)][PF_6]$ in $CH_3CN/[TBA][BF_4]$ with neutral spectrum in black, the reduced spectrum in red and the oxidation of the reduced species in blue.

The spectroelectrochemistry was also probed with UV-vis spectroscopy which can be seen in Figure 2.43, with the three species; neutral in black, reduced in red and the oxidised species in blue. Upon the reduction, the absorption is seen to change with two low energy bands being observed at 590 and 775 nm, which is consistent with the

colour change of the solution. When the solution is oxidised the absorption spectrum changes, with broad shoulder being observed at *ca.* 365 nm, which is consistent with the formation of a tricarbonyl complex following the loss of a CO ligand.

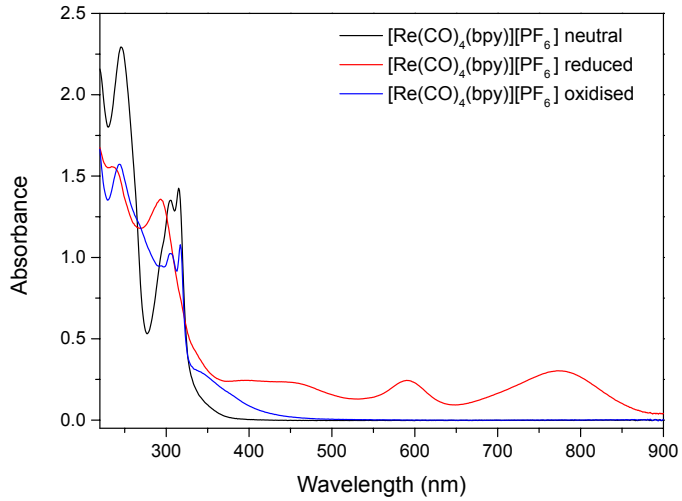


Figure 2.43: The UV-vis spectra for the $[Re(CO)_4(bpy)][PF_6]$ in CH_3CN/[TBA][BF_4]. The neutral spectrum is in black, the reduced spectrum in red and the oxidation of the reduced species in blue.

The mechanism of the reduction of $[Re(CO)_4(bpy)][PF_6]$ and the oxidation is not fully understood in CH_3CN, therefore further work will need to be carried out, but the data does show that $[Re(CO)_4(bpy)][PF_6]$ can undergo CO loss electrochemically, as well as photochemically in CH_3CN. Following this observation, the experiment was repeated in CH_2Cl_2 to also see if the loss of a CO ligand can observed electrochemically. The CV for the reduction of $[Re(CO)_4(bpy)][PF_6]$ in CH_2Cl_2 is shown in Figure 2.44, with the two reductions shown at varying scan rates. The first reduction was run from 0 ev to -1.15 eV, and a similar reduction band profile of two reductions was observed, similar to the experiment in CH_3CN. The first reduction in CH_2Cl_2 does not appear to be as reversible as the first reduction observed in CH_3CN. A small reverse wave can be seen, suggesting that the first reduction is a non-reversible one. The $E_{1/2}$ value

is -1.425 eV (*vs.* Fc/Fc^+), which sits at a lower potential than the $E_{1/2}$ in CH_3CN (-1.545 eV (*vs.* Fc/Fc^+)).

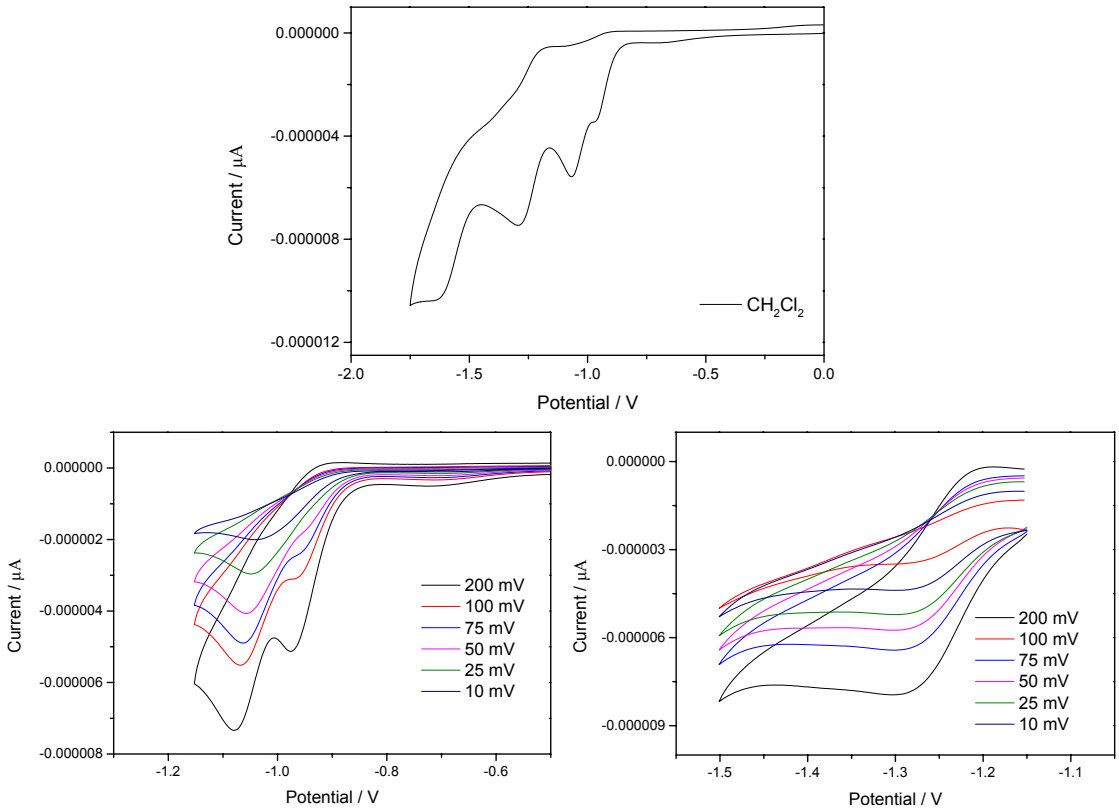


Figure 2.44: The cyclic voltammetry for the reduction $[Re(CO)_4(bpy)][PF_6]$ in $CH_2Cl_2/[TBA][BF_4]$ with the full scan (top), first reduction (bottom left) and the second reduction (bottom right).

The second reduction in CH_2Cl_2 appears to be more reversible than the second reduction seen for CH_3CN, which can be seen by the increased reverse wave. The second reduction was run from -1.14 eV to -1.5 eV, also at varying scan rates, and has an $E_{1/2}$ value of -1.675 eV (*vs.* Fc/Fc^+). The observation of a second reduction being more reversible in CH_2Cl_2 suggests there is different redox process that occurs for the two different solvents. Only the first reduction was monitored with UV-vis and FTIR spectroscopy, and further work is needed to probe the nature of the second reductive

species. The FTIR spectra in Figure 2.45, shows the neutral species in black and the reduced species in red, with the neutral species having four bands at 2122, 2028, 2010 and 1969 cm^{-1}. The potential was held at -1 eV for 30 minutes until all the solution had been fully reduced, which resulted in a colour change from a pale yellow to a bright yellow solution. The FTIR spectrum of the reduced species in Figure 2.45 has three bands at 2022, 1915 and 1898 cm^{-1}, which is consistent with loss of a CO ligand and the formation of neutral tricarbonyl complex. The position of the bands are different to the CO loss species observed in the TRIR, which were at 2054 and 1955 cm^{-1}. The reduced species has bands that sit *ca.* 30 cm^{-1} lower than the previously reported $[Re(CO)_3(bpy)(CH_2Cl_2)]^+$ species, however the position of the bands are identical to that of a $Re(CO)_3(bpy)Cl$ complex in CH_2Cl_2. DFT frequency calculations were run for a $Re(CO)_3(bpy)Cl$ and a $[Re(CO)_3(bpy)(CH_2Cl_2)]^+$ complex to help identify this reduced species. The DFT calculations showed that $[Re(CO)_3(bpy)(CH_2Cl_2)]^+$ sits at *ca.* 30 cm^{-1} higher than $Re(CO)_3(bpy)Cl$ which suggests that formation of $Re(CO)_3(bpy)Cl$ had occurred upon the reduction of $[Re(CO)_4(bpy)][PF_6]$ in CH_2Cl_2.

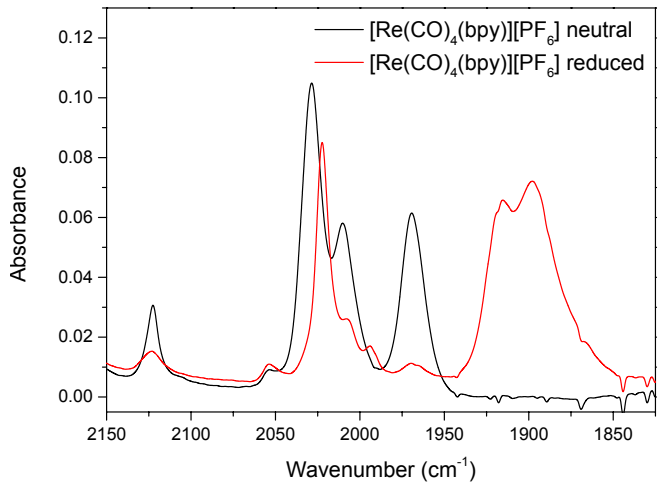


Figure 2.45: The FTIR spectra for the $[Re(CO)_4(bpy)][PF_6]$ in CH_2Cl_2/[TBA][BF_4] with neutral spectrum in black and the reduced spectrum in red.

The absorption spectra of the neutral and reduced species also supports the formation of $Re(CO)_3(bpy)Cl$, with the absorption spectrum of the reduced species, seen in Figure 2.46, resembling that of $Re(CO)_3(bpy)Cl$ with a broad MLCT absorption band at *ca.* 360 nm. The band profile of the UV-vis has also changed from the neutral to the reduced form, the main difference being the change of the characteristic ^{1}LC and ^{1}CT band seen for $[Re(CO)_4(bpy)][PF_6]$, which is no longer seen in the absorption spectrum for the reduced species.

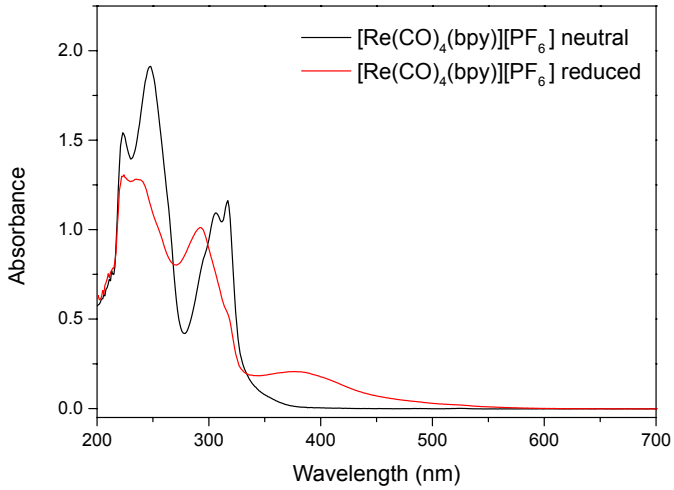


Figure 2.46: The UV-vis spectra for the $[Re(CO)_4(bpy)][PF_6]$ in CH_2Cl_2/[TBA][BF_4] with neutral spectrum in black and the reduced spectrum in red.

It is clear that a difference redox process is observed for the two solvents, with a stable $Re(CO)_3(bpy)Cl$ being formed following a reduction in CH_2Cl_2. However, in CH_3CN a solvated species is only formed following an oxidation of the reduced species. This preliminary investigation has shown that upon an applied potential $[Re(CO)_4(bpy)][PF_6]$ undergoes CO loss to form two different complexes. Further work is required to fully understand the redox mechanism of $[Re(CO)_4(bpy)][PF_6]$.

2.4 Conclusion

The photochemical and photophysical properties of $[Re(CO)_4(bpy)][PF_6]$ that have been observed from the TRIR and luminescence investigations have shown that the excited states observed for $[Re(CO)_4(bpy)][PF_6]$ are different to what has previously been reported.[79] The *ps*-TRIR has shown that upon excitation at 355 nm, two excited states are observed rather than one excited state. With the help of TD-DFT calculations it has been possible to assign the nature of these two excited states. Both are mixed ^{3}ILCT/MLCT excited states, with one state resulting in the photodissociation of CO and the other state being emissive. The emissive ^{3}ILCT/MLCT state has rhenium $\rightarrow$ bipyridine MLCT character resulting in an excited state with photophysical properties. Whereas, the other ^{3}ILCT/MLCT state has rhenium $\rightarrow$ axial CO MLCT character leading to the photodissociation of CO which results in an excited state with photochemical properties. $[Re(CO)_4(bpy)][PF_6]$ was probed at 355 nm in CH_2Cl_2 and CH_3CN, where both ^{3}ILCT/MLCT excited states were observed which is supported by a structured emission being observed for both solvents and the formation of the photoproduct in the TRIR spectra. These results show that $[Re(CO)_4(bpy)][PF_6]$ has two different decay pathways when excited at 355 nm, which backs up the hypothesis by Shaver *et al.* in 1992. The two processes decay at a different rate, with the emissive ^{3}ILCT/MLCT state have a lifetime on the nanosecond timescale and the photoactive ^{3}ILCT/MLCT state having a lifetime on the microsecond timescale.

When $[Re(CO)_4(bpy)][PF_6]$ was probed at 266 nm, a different decay pathway was seen to the 355 nm experiments. Upon an excitation at 266 nm only one excited state was observed, exhibiting similar ν(CO) band positions to the 355 nm experiment, so is assigned to a ^{3}ILCT/MLCT state. The ^{3}ILCT/MLCT state is directly populated

upon excitation and is seen to decay *via* the photodissociation of CO, resulting in the solvated photoproduct. This singular ^{3}ILCT/MLCT excited state is observed in both CH_2Cl_2 and CH_3CN, along with the formation of the photoproduct. The nature of this state is therefore thought to have rhenium $\rightarrow$ axial CO MLCT character due to the observation of the photoproduct. The lifetime of the photoactive ^{3}ILCT/MLCT excited state observed is on the nanosecond timescale which is faster than the lifetime observed at 355 nm. This is probably due to the fact the populated ^{3}ILCT/MLCT state sits at higher energy and therefore is more likely to decay faster, which is in accordance with the energy gap law.[86]

The electrochemical properties of $[Re(CO)_4(bpy)][PF_6]$ were also probed in CH_2Cl_2 and CH_3CN and indicated that upon an applied negative potential the loss of a CO ligand. The electrochemical properties differed in the two solvents, with $[Re(CO)_3(bpy)Cl]$ being formed upon the reduction in CH_2Cl_2, whereas in CH_3CN the reduced species were observed following the induced CO loss. The solvated product $[Re(CO)_3(bpy)(CH_3CN)][PF_6]$ was obtained upon the oxidation of the reduced species in CH_3CN. This shows that $[Re(CO)_4(bpy)][PF_6]$ has powerful oxidative properties, which supports observations previously reported for $[Re(CO)_4(bpm)][PF_6]$,[69] but the solvent clearly has an effect on the electrochemical properties.

The investigations of $[Re(CO)_4(bpy)][PF_6]$ have shown that it has very desirable photophysical, photochemical and electrochemical properties. The loss of a CO ligand can easily be achieved by either applying a negative potential or exciting at 355 nm, which has not be observed for the tricarbonyl anlogue. These observation open up future application for $[Re(CO)_4(bpy)][PF_6]$ as a catalyst in both photochemical and electrochemical processes.

Chapter 3

The Photochemical and Photophysical Properties of Rhenium Tetracarbonyl Dipyridophenazine Complexes

3.1 Introduction

As outlined in Chapter 2, transition metal polypyridyl complexes have been widely reported with respect to their applications in solar energy systems,[87,88] molecular electronics,[89] and biological probes.[90–94] The ability to influence the excited manifold of polypyridyl ligand has led to tuneable photoinduced and electron transfer processes with include both CO_2 reduction,[95–97] and water oxidation.[98–101] The complexes at the forefront of these investigations have been Ru(II), Rh(III) and Cu(I) with polypyridyl ligands such as 1,10-phenanthroline (phen) and dipyridophenazine (dppz).[102,103] Par-

ticular focus have been on the dppz ligand,[10,104–109] as coordination to the metal centre results in an excited state manifold which is more complex, making them interesting to investigate. An example of this is, some metal dipyridophenazine complexes have been found to be DNA probes, which is a result of their diverse electrochemical and photophysical properties they exhibit. One complex that has been extensively reported is $[Ru(phen)_2(dppz)]^{2+}$, which has been termed a molecular 'light switch' for DNA.[110] This is due to the fact it is non-emissive in an aqueous solution but when intercalated into DNA it is emissive. This 'light switch' phenomenon is a direct result of the planar dppz ligand stacking into the double helix of the DNA,[111? –114] it also shows that the complex is affected by the local solvent environment.[115] This solvent effect has been shown by the interplay of two MLCT excited states which arise from the distribution of charge on the dppz ligand framework. The dppz ligand is comprised of a two ring systems illustrated in Figure 3.1: a phenathroline (phen) system (blue) and a phenazine (phz) system (purple).[116]

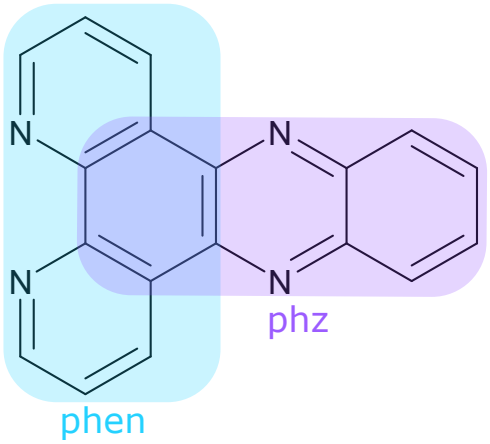


Figure 3.1: The structure of dipyridophenazine (dppz), with the two low lying units phenanthroline (blue) and phenazine (purple).

Theoretical calculations on the dppz ligand suggested that the two different ring systems result in three close lying LUMOs, which can be assigned to those localised on the 'phen' unit and those localised on the 'phz' unit.[116] Therefore, when the complex is excited the electron can either populate a 'phen' or 'phz' based MO giving rise to two MLCT excited states that were observed experimentally. These two MLCT excited states are known as MLCT(phen) or MLCT(phz), and the deactivation pathway of these two states differs depending on the local solvent environment.[115,117] The 'light switch' phenomenon is the result of the MLCT(phen) being emissive and the MLCT(phz) being a dark non-emissive state.[115] This emission switch of $[Ru(phen)_2(dppz)]^{2+}$ is thought to be governed by a state reversal where the emissive MLCT(phen) state is the lowest lying excited state in organic solvents which result in $[Ru(phen)_2(dppz)]^{2+}$ exhibiting luminescence. In aqueous solvents the non-emissive MLCT(phz) is the lowest lying excited state which results in the luminescence being quenched,[118,119] thus 'switching off' the emission. The 'light switch' behaviour can be attributed to competition between energetic factors favouring the MLCT(phz), dark state, and entropic factors favouring the MLCT(phen), emissive state.[118,119] The population of these two states can be altered by either the temperature or the solvent.

The photophysics of rhenium dipyridophenazine complexes has not been reported as much in literature as their ruthenium analogues. However, they have attracted attention due to rhenium tricarbonyl α-diimine complexes exhibiting strong luminescent ^{3}MLCT excited states which are the lowest lying state.[73,116,120–124] By including a dppz ligand and probing $[Re(CO)_3(dppz)Cl]$, a more complex excited state manifold was reported, with the lowest lying excited state either being a ^{3}IL(π-π^{**}), ^{3}MLCT(phen) or ^{3}MLCT(phz) state.[116,121,123–129] Kuimova *et al.*utilised TRIR as a spectroscopic tool for probing the nature of the excited states of $[Re(CO)_3(dppz)Cl]$ to help distinguish between ^{3}IL(π-π^{**}) and ^{3}MLCT excited states.[107] The shift of the ν(CO) bands to

lower wavenumber is characteristic of the formation of a ^{3}IL(π-π^{**}) excited state, whereas a shift to higher wavenumber is indicative of the formation of a ^{3}MLCT excited state. The formation of a ^{3}MLCT(phen) or ^{3}MLCT(phz) excited state can also be identified, as a ^{3}MLCT(phz) excited state shifts to a higher wavenumber compared to ^{3}MLCT(phen).[2,104]

3.1.1 Rhenium Phenanthroline Tetracarbonyl Complexes

As mentioned in Chapter 2, rhenium tetracarbonyl diimine complexes have not been reported much in the literature in comparison to their tricarbonyl analogues. For example, there have been no reports of rhenium tetracarbonyl dipyridophenazine complexes in literature, but rhenium phenanthroline tetracarbonyl complexes have been reported.[71,78,79] The dppz ligand is made up of two unit, phen and phz, so understanding the nature of $[Re(CO)_4(phen)][PF_6]$ and the photophysical and photochemical properties is important. The first literature report of $[Re(CO)_4(phen)][CF_3SO_3]$ was by Shaver *et al.* in 1992,[71] where a range of rhenium tetracarbonyl diimine complexes, including $[Re(CO)_4(phen)][CF_3SO_3]$, were investigated. The luminescence, photosubstitution and electronic absorption properties of these complexes were probed. The luminescence properties of $[Re(CO)_4(phen)][CF_3SO_3]$ were similar to that of $[Re(CO)_4(bpy)][CF_3SO_3]$, where the emission band was seen to be structured with emission maxima at 459, 489 and 525 nm which sits at lower energy in comparision to those of $[Re(CO)_4(bpy)][CF_3SO_3]$. The structured emission spectrum is indicative of a ^{3}LC emitter state.[74] The lifetime of the emission was reported to be 3.8 μs, which is faster than the lifetime reported for $[Re(CO)_4(bpy)][CF_3SO_3]$ (4.7 μs).[71]

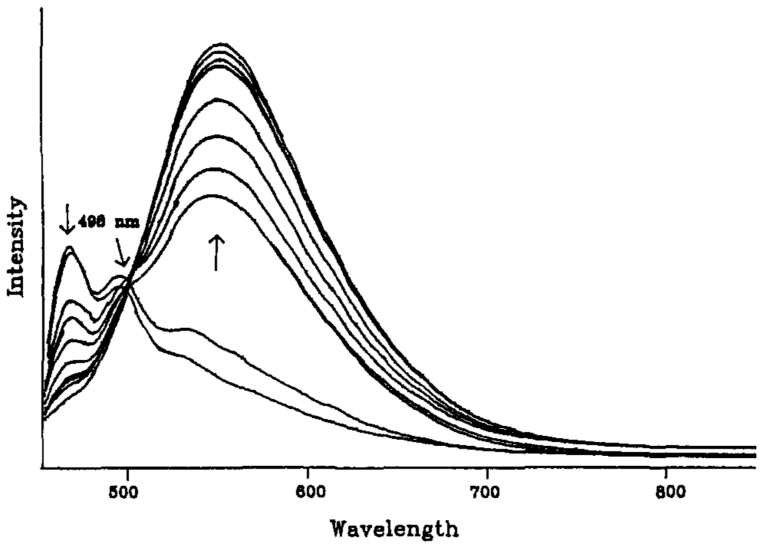


Figure 3.2: The steady-state photolysis of $[Re(CO)_4(phen)][CF_3SO_3]$ in CH_2Cl_2 following excitation at 355 nm reported by Shaver *et al.* Reproduced from reference 71.

The photosubstitution investigations of $[Re(CO)_4(phen)][CF_3SO_3]$ found that upon steady-state excitation the complexes were unstable and underwent photosubstitution. The steady-state excitation of $[Re(CO)_4(phen)][CF_3SO_3]$ in CH_2Cl_2 at 355 nm can be seen in Figure 3.2. During the steady-state excitation, the emission maxima at 460 nm is seen to decrease, with a new maxima at *ca.* 550 nm with a much higher intensity being observed. The photosubstitution process occurring was reported as $[Re(CO)_4(phen)][CF_3SO_3]$ undergoing CO loss, and the $[CF_3SO_3]^-$ binding to the vacant site to form $[Re(CO)_3(phen)(CF_3SO_3)]$. This was backed up by independently synthesising $[Re(CO)_3(phen)(CF_3SO_3)]$ which was seen to have an emission maxima at 565 nm when excited at 355 nm. It was proposed that upon steady-state excitation of all the diimine complexes, a CO was displaced resulting in $[CF_3SO_3]^-$ binding. The quantum yield of the photosubstitution was probed for all the complexes, with $[Re(CO)_4(phen)][CF_3SO_3]$ having the lowest quantum yield of ϕ 0.05, which is much lower than the quantum yield reported for $[Re(CO)_4(bpy)][CF_3SO_3]$, $[Re(CO)_4(dmb)][CF_3SO_3]$ and $[Re(CO)_4(bpm)][CF_3SO_3]$.[71] The ability of the com-

plex to dissociate CO in favour of $[CF_3SO_3]^-$ indicated that the photolability of the rhenium tetracarbonyl diimine complexes followed the order of $[Re(CO)_4(dmb)]^+$ > $[Re(CO)_4(bpm)]^+$ > $[Re(CO)_4(bpy)]^+$ > $[Re(CO)_4(phen)]^+$.[71] This suggests that $[Re(CO)_4(phen)]^+$ does not as readily dissociate CO in comparison to the other complexes.

The photophysics and photochemistry of rhenium tetracarbonyl bipyridine and phenanthroline complexes are very similar. The main thing to mention is the difference between $[Re(CO)_4(bpy)][PF_6]$ and $[Re(CO)_4(phen)][PF_6]$ is that the absorption spectra of the $[Re(CO)_4(phen)][PF_6]$. The ^{1}LC of $[Re(CO)_4(phen)][PF_6]$ is observed at a high energy and exhibits a stronger absorption band than that of $[Re(CO)_4(bpy)][PF_6]$. The position of the ^{3}CT and ^{1}CT are also sat at higher energy to $[Re(CO)_4(bpy)][PF_6]$, with a lower absorption intensity observed.[78] The luminescence behaviour of $[Re(CO)_4$ $(phen)][PF_6]$ was also found to have a significant temperature dependence compared to $[Re(CO)_4$ $(bpy)][PF_6]$.[71,78]

3.2 Aims

The aim of this Chapter is to investigate the nature of the photophysics and photochemistry of two $[Re(CO)_4(dppz)][PF_6]$ systems to further understand the photophysical processes that result in the photochemical substitution of CO to form a solvated photoproduct. The photophysics and photochemistry of $[Re(CO)_4(dppz)][PF_6]$, seen in Figure 3.3, was investigated in CH_2Cl_2 and CH_3CN, in order to probe whether the nature of the excited state and subsequent photochemistry was affected by the solvent.

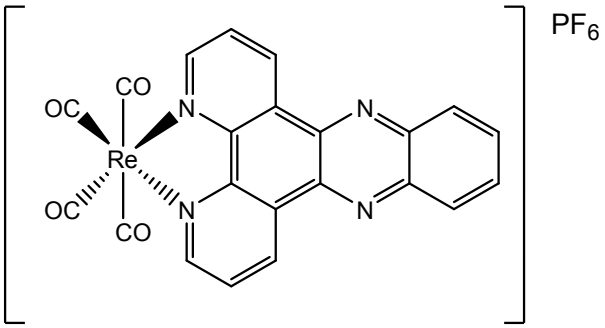


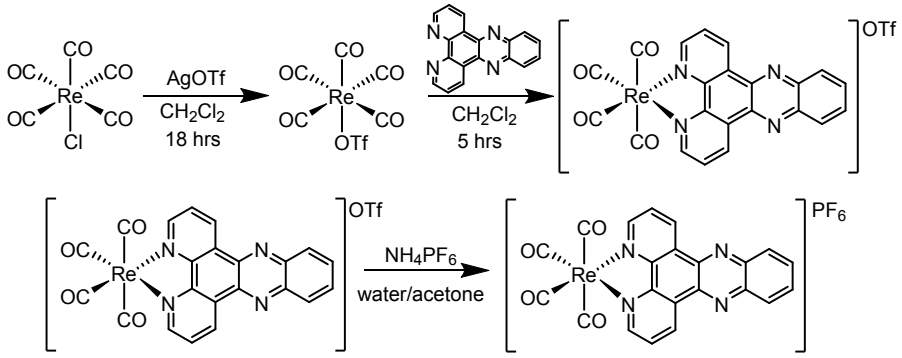
Figure 3.3: The structure of $[Re(CO)_4(dppz)][PF_6]$ which will be investigated within this Chapter.

$[Re(CO)_4(dppz)][PF_6]$ was probed with both *ps*-TRIR and *ns*-TRIR at 266 and 355 nm in CH_2Cl_2 and CH_3CN. This spectroscopic structural probe was used to characterise the nature and lifetime of excited states and subsequent formation of the solvated photoproduct. The spectroscopic results were again supported with DFT calculations which were again performed both in Nottingham and by Joshua Sutton at the University of Otago in New Zealand.

3.3 Results

3.3.1 Synthesis and Characterisation of $[Re(CO)_4(dppz)][PF_6]$

The synthesis of $[Re(CO)_4(dppz)][PF_6]$ was adapted from literature procedures,[77,85] with adaptation of the bipyrdine ligand being swapped for a dipyridophenazine ligand. The adapted synthetic scheme can be seen in Scheme 3.1. Reaction times differ between the two synthetic procedures following the addition of the α-diimine ligand, 23 *vs.* 28 hours in total.



Scheme 3.1: The scheme for the synthesis of $[Re(CO)_4(dppz)][PF_6]$ following literature procedures.[77,85]

The FTIR of $[Re(CO)_4(dppz)][PF_6]$, shown in Figure 3.4, exhibits four ν(CO) bands, which is consistent with the reports for $[Re(CO)_4(bpy)][PF_6]$ and $[Re(CO)_4(phen)][PF_6]$.[71,79] The four band at 2124, 2030, 2014 and 1974 cm^{-1} are shifted in relation to $[Re(CO)_4(bpy)]$ $[PF_6]$, but are similar to the reported position for $[Re(CO)_4(phen)][PF_6]$ which is to be expected as the dppz ligand consists of a phen unit. The successful synthesis can further be supported with characterisation by mass spectrometry, ^{1}H NMR and elemental analysis.

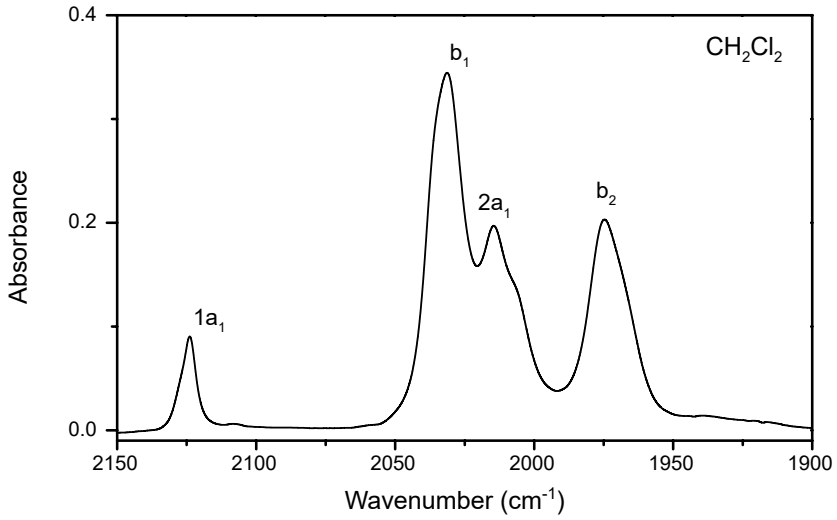


Figure 3.4: The FTIR of $[Re(CO)_4(dppz)][PF_6]$ in CH_2Cl_2.

$[Re(CO)_4(dppz)][PF_6]$ has C_{2V} symmetry and shows four IR-active bands ($1a_1$, b_1, $2a_2$ and b_2). The UV-vis spectra for $[Re(CO)_4(dppz)][PF_6]$ in CH_2Cl_2 and CH_3CN can be seen in Figure 3.5, which has a band profile again similar to $[Re(CO)_4(bpy)][PF_6]$ and $[Re(CO)_4(phen)][PF_6]$.[78] The lower energy transitions (*ca.* 380 - 350 nm) which were assigned as ^{3}CT and ^{1}CT transition for both $[Re(CO)_4(bpy)][PF_6]$ and $[Re(CO)_4(phen)][PF_6]$ can be seen.[71,78] The main difference is the UV-vis spectra for $[Re(CO)_4(dppz)[PF_6]$ is shifted to higher energy. The same trend was seen for $[Re(CO)_4(phen)][PF_6]$ in relation to $[Re(CO)_4(bpy)][PF_6]$.[71,78] A higher energy transition can also be observed at *ca.* 260 nm which exhibits different band profiles for the two solvents. This could suggest, the higher energy transitions are affected by the solvent. For both $[Re(CO)_4(bpy)][PF_6]$ and $[Re(CO)_4(phen)][PF_6]$ this transition was assigned to a ^{1}LC state.

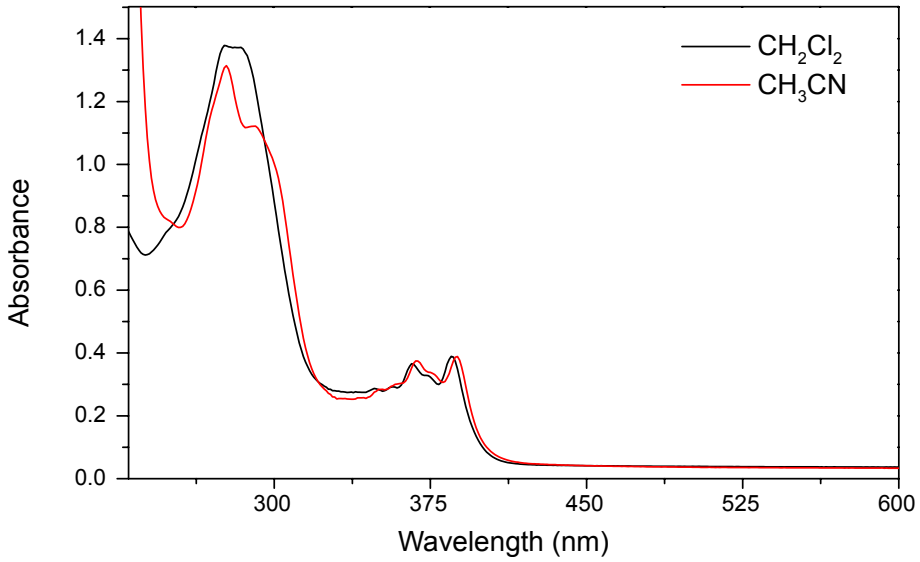


Figure 3.5: The UV-vis spectra of $[Re(CO)_4(dppz)][PF_6]$ in CH_2Cl_2 and CH_3CN.

The luminescence spectra were recorded for $[Re(CO)_4(dppz)][PF_6]$ in CH_2Cl_2 and CH_3CN and the emission bands can be seen in Figure 3.6. In both solvents $[Re(CO)_4(dppz)][PF_6]$ exhibits some structured emission and broad emission. For CH_2Cl_2 the band positions of the emission are observed at 399 and 429 nm. The position of the emission bands for $[Re(CO)_4(dppz)][PF_6]$ sit at higher energy compared to $[Re(CO)_4(bpy)][PF_6]$ and $[Re(CO)_4(phen)][PF_6]$ (*ca.* 50 nm and 60 nm respectivley).[71] There is also a difference between the two solvents, with the emission band for CH_3CN shifted to higher energy than CH_2Cl_2 with bands at 387, 398 and 421 nm. This shift to higher energy could be the result of a solvent effect, however further investigations are required to support this theory. The band profile for both solvents is similar to that of $[Re(CO)_4(bpy)][PF_6]$ and $[Re(CO)_4(phen)][PF_6]$, where both structured and broad bands were observed. This may suggest the excited state being observed is a mixed MLCT/ILCT state, similar to that seen for $[Re(CO)_4(bpy)][PF_6]$. The lifetime of the emission in both CH_3CN and CH_2Cl_2 was found to be very short, decaying with the laser pulse.

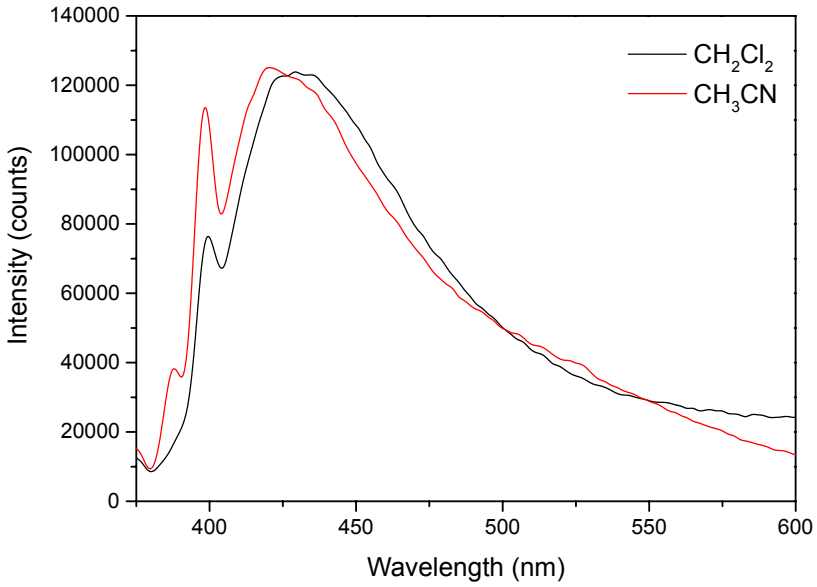


Figure 3.6: The emission spectra of $[Re(CO)_4(dppz)][PF_6]$ in CH_2Cl_2 and CH_3CN following a 355 nm excitation.

3.3.2 Time-resolved Infrared Investigation of $[Re(CO)_4(dppz)][PF_6]$

The starting point for the investigation of $[Re(CO)_4(dppz)][PF_6]$ was to examine the complex in CH_2Cl_2 with a 355 nm excitation wavelength, which are the same reaction conditions as the bipyridine analogue and the phenanthroline analogue reported by Bernhard *et al.*,[79] and the results described in Chapter 2. The excitation of $[Re(CO)_4(dppz)][PF_6]$ could result in the formation of different excited states, with the dppz ligand affecting both the photophysical and photochemical properties of the complex. Both *ps* and *ns*-TRIR were used to probe the early formation of initial excited states, with the hope of observing the photoproduct, as seen for the bipyridine analogue.

3.3.2.1 TRIR of $[Re(CO)_4(dppz)][PF_6]$ at 355 nm

The *ps*-TRIR for $[Re(CO)_4(dppz)][PF_6]$ in CH_2Cl_2 can be seen in Figure 3.7, where following excitation the bleach of the parents bands at 2126, 2031, 2013 and 1975 cm^{-1} are observed. The initial transient species can be seen at 2118, 1999 and 1959 cm^{-1} following the cooling of the vibrationally hot state (τ = 16 ps). The position of the transient bands sit at slightly lower energy to the parents bands, which suggests this initial excited state has some π-π^* character. The band positions are similar to that seen for $[Re(CO)_4(phen)][PF_6]$,[79] suggesting this initial excited state could be a mixed ILCT/MLCT state with some 'phen' character. This initial state can then be seen to decay away on the picosecond timescale (τ = 108 ($\pm$ 9) ps), with a second excited state growing in at 2118, 2021, 2007 and 1967 cm^{-1}. The position of some bands for the second excited state have shifted slightly to higher energy with the exception of the highest energy band at 2118 cm^{-1}. This slight increase in energy of the bands could be a result of another ^{3}ILCT/MLCT state. One possibility is that the shift to higher energy could be the result of a MLCT with 'phz' character, however such a change in MLCT character can not be confirmed from just this small blue shift. The complex exhibited emission which is consistent with population of an emissive MLCT(phen) state, and the emission lifetime recorded was very short lived. Due to the this, for the remainder of this discussion the initial will be assigned as a State I with the second state being assigned to a ^{3}ILCT/MLCT state.

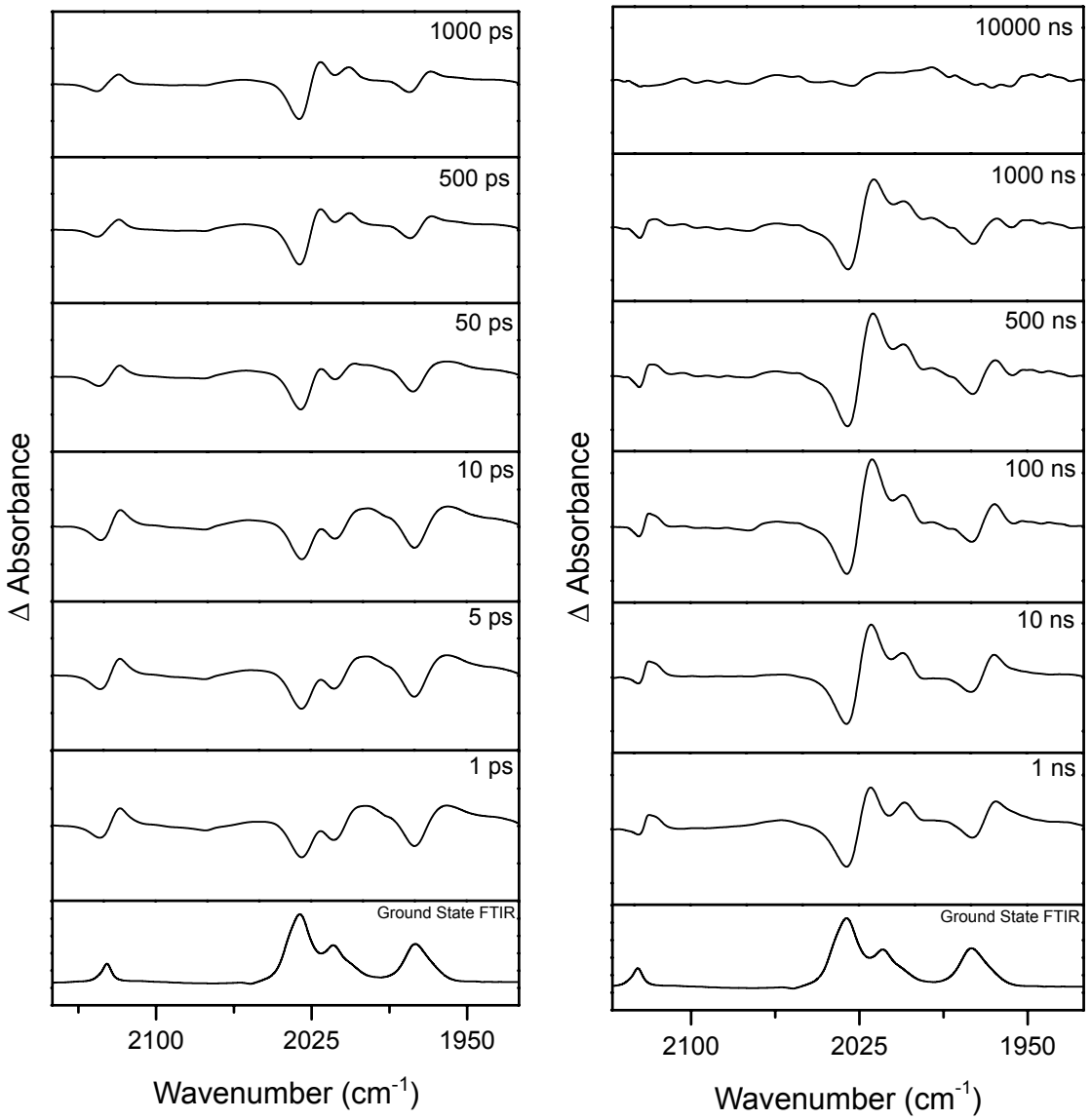


Figure 3.7: The *ps*-TRIR (left) and *ns*-TRIR spectra (right) spectra of $[Re(CO)_4(dppz)][PF_6]$ in CH_2Cl_2 following a 355 nm excitation wavelength.

Global analysis was used to examine the picosecond data to help distinguish between the states and generate the kinetics for those states. The initial excited state is seen to grow and decay on the picosecond timescale, with a lifetime of $\tau = 108$ ps. As this initial excited state decays away, the second excited state is seen to grow in, the kinetic plot for this can be seen in Figure 3.8.

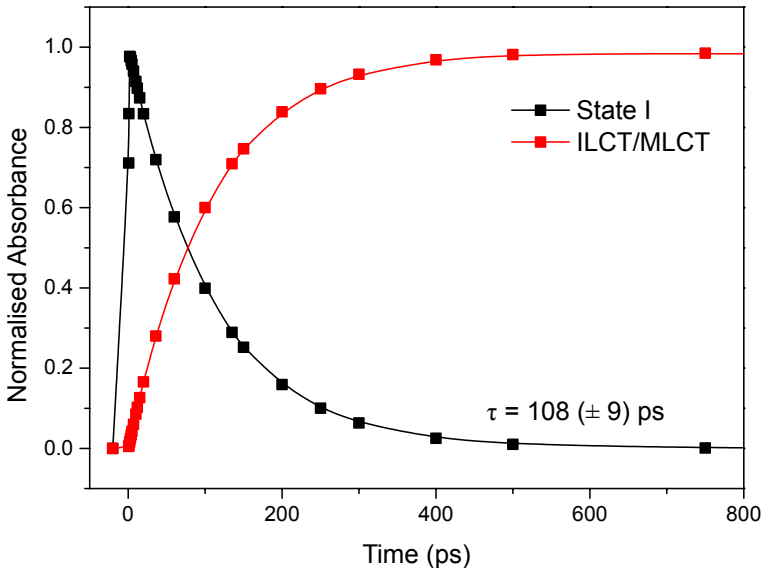


Figure 3.8: The kinetic plot generated from the global analysis for the decay of State I and the growth the ^{3}ILCT/MLCT state following a 355 nm excitation in CH_2Cl_2.

The global analysis of the data supports the observations seen in the *ps*-TRIR, which suggests the formation of two excited states. The excited state spectra generated from the global analysis, seen in Figure 3.9, shows the two different excited states species. The initial excited state, State I is show in black, with the second excited state shown in red which is thought to be ^{3}ILCT/MLCT state. This second excited state is seen to live onto the nanosecond timescale.

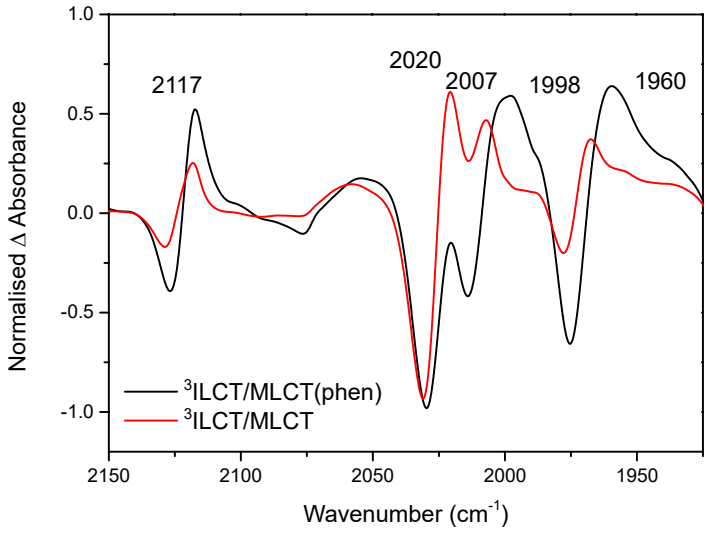


Figure 3.9: The normalised excited state spectra generated from the global analysis for State I and the ^{3}ILCT/MLCT state following a 355 nm excitation in CH_2Cl_2.

The *ns*-TRIR, Figure 3.7, shows the ^{3}ILCT/MLCT excited state that is seen to grow in on the picosecond timescale. The ^{3}ILCT/MLCT excited state is long lived on the nanosecond timescale and is seen to decay back down to the ground state. There does not appear to be the formation of a solvated photoproduct following the decay of this excited state. This suggests that this ^{3}ILCT/MLCT excited state that is being populated does not decay *via* the same photodissociation process as the bipyridine analogue. The ^{3}ILCT/MLCT excited state is seen to decay away with a lifetime of τ = 3.7 ($\pm$ 0.4) μs, which can be seen in the kinetic plot shown in Figure 3.10. The lifetime of the mixed ^{3}ILCT/MLCT excited state seen for $[Re(CO)_4(dppz)][PF_6]$ is comparable with the lifetime observed for $[Re(CO)_4(bpy)][PF_6]$ (2.1 μs), however the decay of the ^{3}ILCT/MLCT state does not results in the formation of a photoproduct.

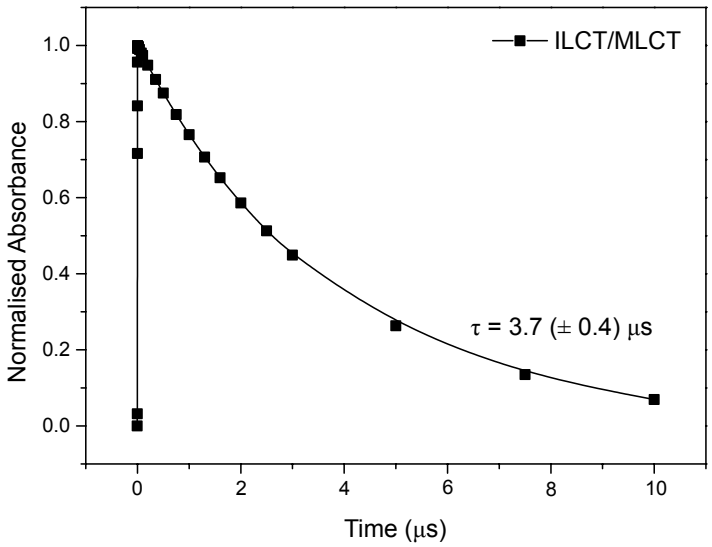


Figure 3.10: The kinetic plot generated from the global analysis for the decay of the ^{3}ILCT/MLCT excited state after a 355 nm excitation in CH_2Cl_2.

The global analysis of the nanosecond data also only suggested the presence of one species, thus supporting the observation of no photoproduct being formed following the decay of the ^{3}ILCT/MLCT mixed excited state. The excited state spectrum generated from the global analysis, seen in Figure 3.11, shows that only one species is observed on the nanosecond timescale. The excited state spectrum shows the excited state species observed on the nanosecond timescale data, which is consistent with ^{3}ILCT/MLCT excited state seen in the TRIR spectra.

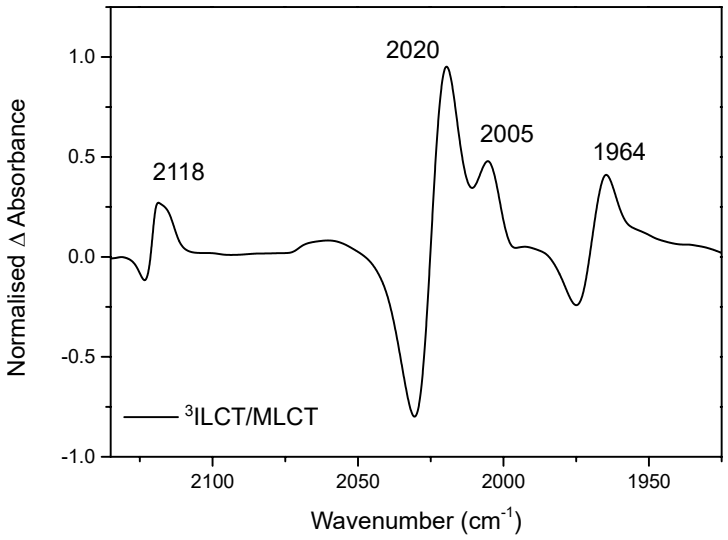


Figure 3.11: The normalised excited state spectra generated from the global analysis for the ^{3}ILCT/MLCT state following a 355 nm excitation in CH_2Cl_2.

The *ps*-TRIR spectra for the 355 nm experiment in CH_3CN can be seen in Figure 3.12, where the formation of an initial excited state is observed at 2117, 2005 and 1963 cm^{-1}. The parent bleaches at 2126, 2035 and 1973 cm^{-1} can be seen following excitation. The position of the initial transient excited state is similar to that of State I seen in CH_2Cl_2. This initial excited state is seen to decay away (τ = 114 ps) and the second excited state grows in. The second transient species has bands at 2121, 2025, 2005 and 1963 cm^{-1}, with some of the bands shifting to higher energy than the initial excited state. The blue shift of the bands could be the result of another ^{3}ILCT/MLCT state with 'phz' character, similar to that seen for CH_2Cl_2, however the MLCT nature of the second state again can not conclusively be known. Therefore, the initial excited state will be assigned as State I, with the second state being a ^{3}ILCT/MLCT state for the sake of ease.

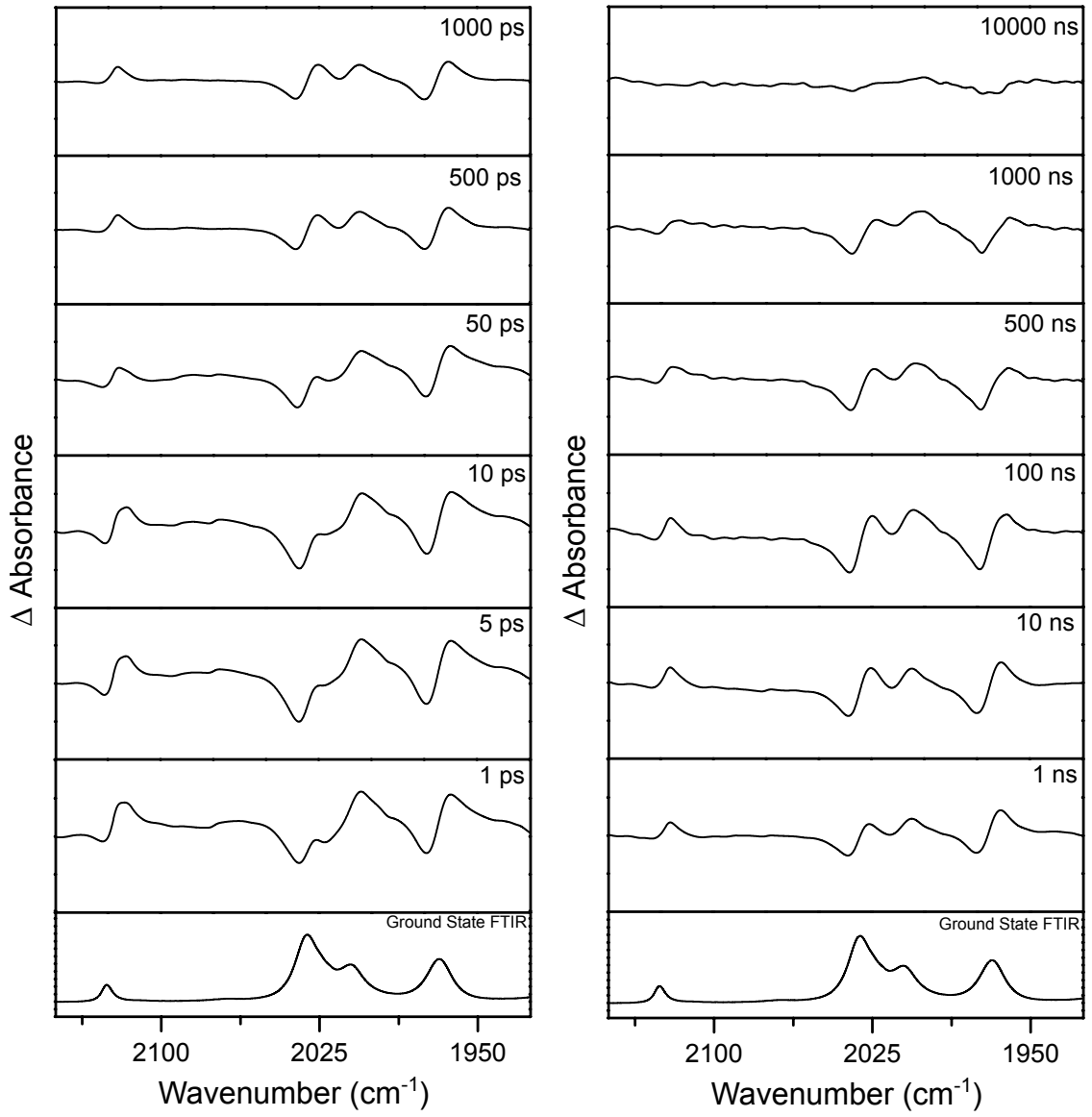


Figure 3.12: The *ps*-TRIR (left) and *ns*-TRIR spectra (right) spectra of $[Re(CO)_4(dppz)][PF_6]$ in CH_3CN following a 355 nm excitation wavelength.

State I is seen to decay away with a lifetime of $\tau = 114$ ps as the ^{3}ILCT/MLCT state grows in. The kinetic plot for this can be seen in Figure 3.13, which clearly shows the decay and growth of the two excited states observed on the picosecond timescale. The kinetic information was obtained by global analysis of the data set and two different species were identified which supports the *ps*-TRIR observations. State I

state observed in CH_3CN has a similar lifetime to State I seen for CH_2Cl_2 experiment. Like the CH_2Cl_2 results the ^{3}ILCT/MLCT state is seen to live onto the nanosecond timescale.

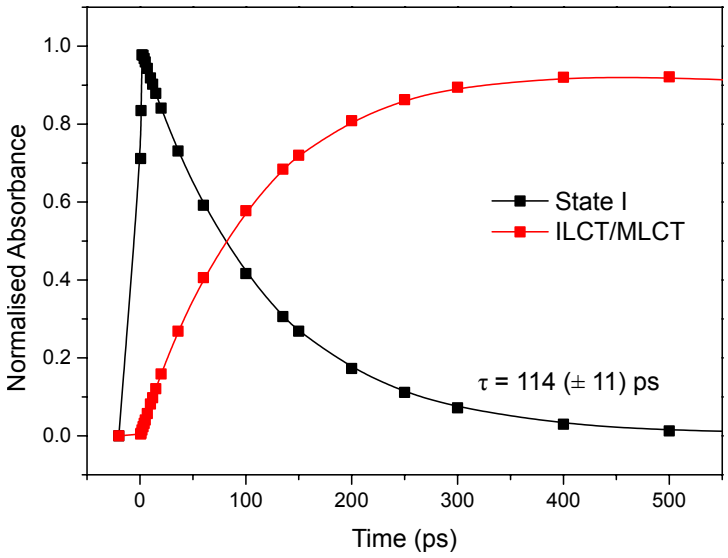


Figure 3.13: The kinetic plot generated from the global analysis for the decay of the ^{3}ILCT/MLCT(phen) and the growth the ^{3}ILCT/MLCT state following a 355 nm excitation in CH_3CN ·

The excited state spectra generated from the global analysis showing the two excited species identified can be seen in Figure 3.14. The initial state, State I, shown in black with the second state, the ^{3}ILCT/MLCT state, shown in red. The two excited state species identified from the global analysis supports the *ps*-TRIR.

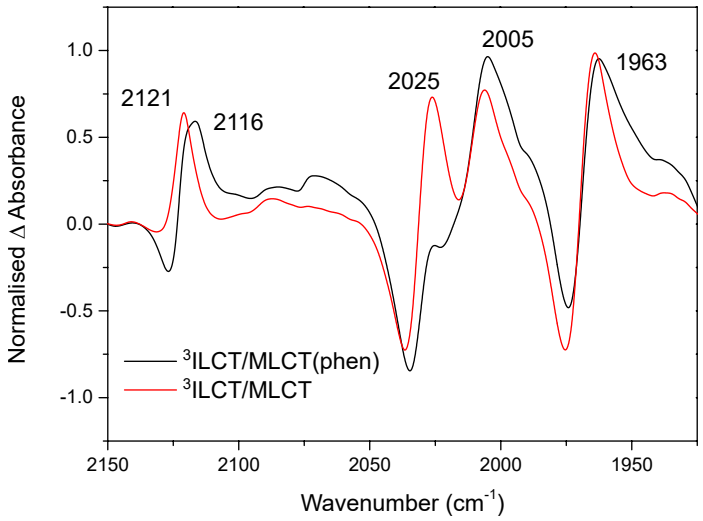


Figure 3.14: The normalised excited state spectra generated from the global analysis for State I and the ^{3}ILCT/MLCT state following a 355 nm excitation in CH_3CN.

The ^{3}ILCT/MLCT state that grows in on the picosecond timescale can be seen in the *ns*-TRIR spectra, Figure 3.12, with bands at 2120, 2025, 2005 and 1963 cm^{-1}. The ^{3}ILCT/MLCT state appears to be long lived on the nanosecond timescale, where it is seen to decay(τ = 1.3 ($\pm$ 0.14) μs). Following the decay of the ^{3}ILCT/MLCT excited state, only the reformation of the parent is seen. This is in line with the *ns*-TRIR in CH_2Cl_2 where the ^{3}ILCT/MLCT excited state decayed to ground state and not *via* the photodissociation of a CO.

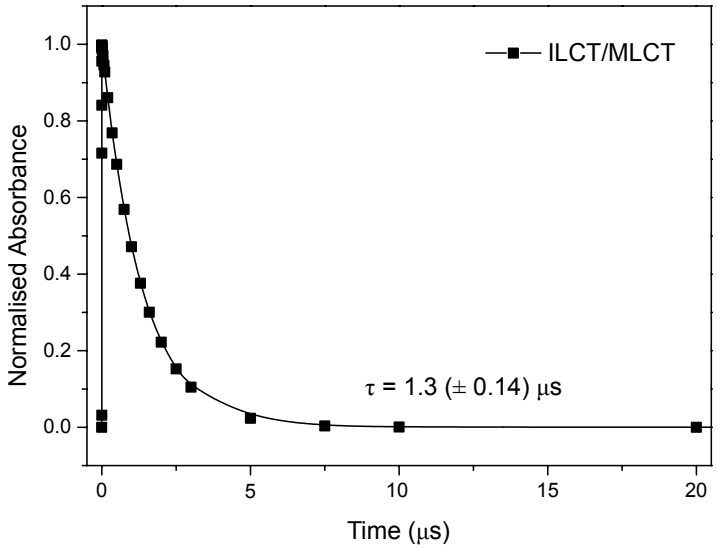


Figure 3.15: The kinetic plot generated from the global analysis for the decay of the ^{3}ILCT/MLCT excited state after a 355 nm excitation in CH_3CN.

The kinetic plot for the decay of the ^{3}ILCT/MLCT excited state can be seen in Figure 3.15, which was generated from the global analysis of the data set. The decay of the ^{3}ILCT/MLCT excited state has a lifetime of $\tau = 1.3$ μs, which is shorter lived than the lifetime in CH_2Cl_2. The global analysis also did not identify the formation of a photoproduct following the decay of the excited state. The excited state spectrum for the ^{3}ILCT/MLCT state observed on the nanosecond timescale is shown in Figure 3.16, and clearly shows bands that are consistent with the ^{3}ILCT/MLCT state see in the TRIR spectra.

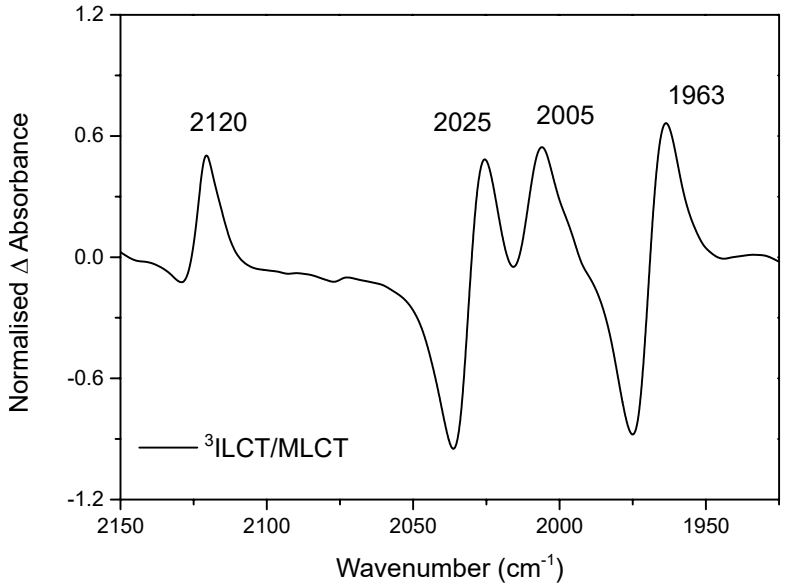


Figure 3.16: The normalised excited state spectra generated from the global analysis for the ^{3}ILCT/MLCT state following a 355 nm excitation in CH_3CN.

The TRIR of $[Re(CO)_4(dppz)][PF_6]$ in CH_2Cl_2 and CH_3CN showed that following a 355 nm light excitation, an initial excited state, State I was formed. State I was seen to decay and form a second excited state, a ^{3}ILCT/MLCT state. This ^{3}ILCT/MLCT excited state is then seen to decay, however no formation of the photoproduct was observed for either solvent. Table 3.1 shows the lifetimes observed for the excited states observed for both CH_2Cl_2 and CH_3CN.

Table 3.1: The lifetimes of the processes observed in both the *ps* and *ns*-TRIR for $[Re(CO)_4(dppz)][PF_6]$ following a 355 nm excitation.

Solvent	Nature of State	Band Position (cm^{-1})	τ ($\pm$ errors)
CH_2Cl_2	State I	2117, 1998, 1960	108 (9) ps
	^{3}ILCT/MLCT	2117, 2020, 2007, 1964	3.7 (0.4) μs
CH_3CN	State I	2116, 2005, 1963	114 (11) ps
	^{3}ILCT/MLCT	2121, 2025, 2005, 1963	1.3 (0.14) μs

The nature of the excited states observed in the TRIR experiments have been assigned based on the investigation $[Re(CO)_4(phen)][PF_6]$ and previous reported photophysics for $[Re(CO)_3(dppz)(Cl]$ complexes.[107] To help support the observations and assignments of the TRIR experiments in CH_2Cl_2 and CH_3CN TD-DFT calculations were also performed on $[Re(CO)_4(dppz)]^+$ by Joshua Sutton at the University of Otago in New Zealand. The TD-DFT calculations were calculated within a vacuum and in both a CH_2Cl_2 and CH_3CN solvent field. From the TD-DFT calculations information about the LUMO and HOMO energies and MOs were obtained along with the nature of the different electronic transitions and how the electron density is distributed for those transitions.

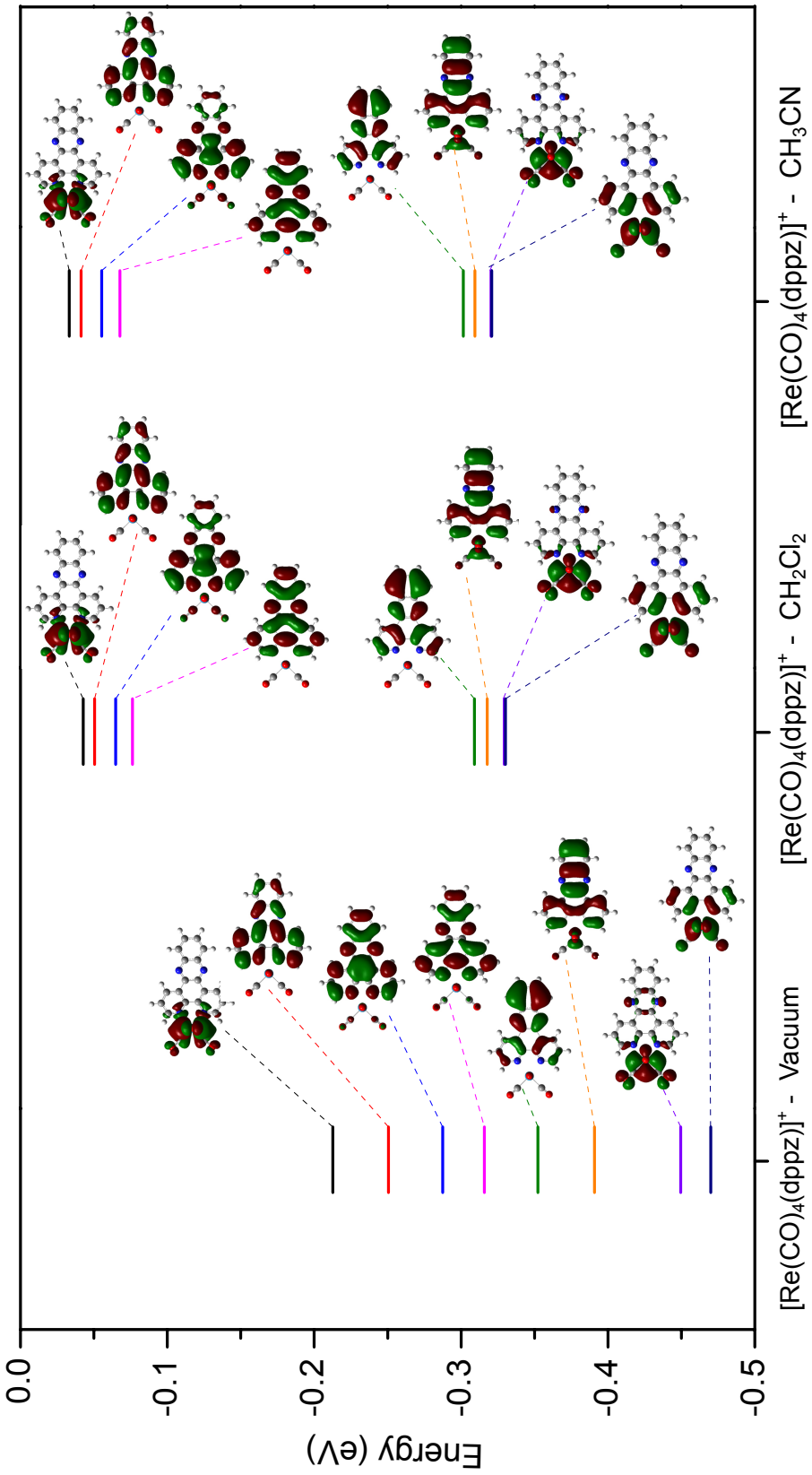


Figure 3.17: The energy of the HOMO-3 (navy), HOMO-2 (purple), HOMO-1 (orange), HOMO (green), LUMO (pink), LUMO+1 (blue), LUMO+2 (red) and the LUMO+3 (black) and the corresponding molecular orbitals of $[Re(CO)_4(dppz)][PF_6]$ calculated using TD-DFT in a vacuum field (left), CH_2Cl_2 field (middle) and a CH_3CN field (right).

The HOMO and LUMO energies for $[Re(CO)_4(dppz)]^+$ in a vacuum, CH_2Cl_2 and CH_3CN can be seen in Figure 3.17. The energies between the HOMOs and LUMOs in a vacuum are not spilt to higher and lower energy like expected, however this spilt is seen for CH_2Cl_2 and CH_3CN. The HOMO and LUMO for both the solvents are sat at very similar energy, with CH_3CN sitting at higher energy compared to CH_2Cl_2. The MO's for the different HOMOs and LUMOs are also very similar for both solvents. The MO character for both CH_2Cl_2 and CH_3CN appear to show both phen based character (LUMO +1) and phz based character (LUMO +2), with metal based character being observed for the higher of the LUMOs shown (LUMO +3). The HOMO MO character for both CH_3CN and CH_2Cl_2 again is very similar, with ligand based character being observed for the two higher energy HOMOs (HOMO and HOMO -1) and more metal based character being seen for the two lower energy MOs (HOMO -2 and HOMO -3). Even though the splitting between the HOMOs and LUMOs within a vacuum does not appear to be standard, the character of the MOs is very consistent with that observed for the solvent fields.

The calculated singlet and triplet transitions for a CH_2Cl_2 solvent field can be seen in Figure 3.18, along with the calculated and experimental UV-vis spectra. The singlet transition with a high oscillator strength that sits lowest in energy (*ca.* 311 nm) is likely to be the transition populated upon excitation at 355 nm. The nature of this singlet transition is ILCT/MLCT state, with the MLCT being 'phen' in nature. This supports the observations seen in the emission and TRIR for the first initial excited state, State I. It is possible that State I is a ILCT/MLCT(phen) based state. The calculated UV-vis spectrum for CH_2Cl_2 exhibits a band profile similar to the experimental spectrum, with the main difference being that it has been shifted to higher energy. The splitting of the lower energy band is also not observed, however it has only been calculated using the calculated singlet transitions, but there are triplet

transitions situated at that energy. This is consistent with these transitions having ^{1}CT and ^{3}CT character.[71,78] The higher energy transition (*ca.* 256 nm) has singlet ILCT character, which supports the assignment of ^{1}LC character.[78]

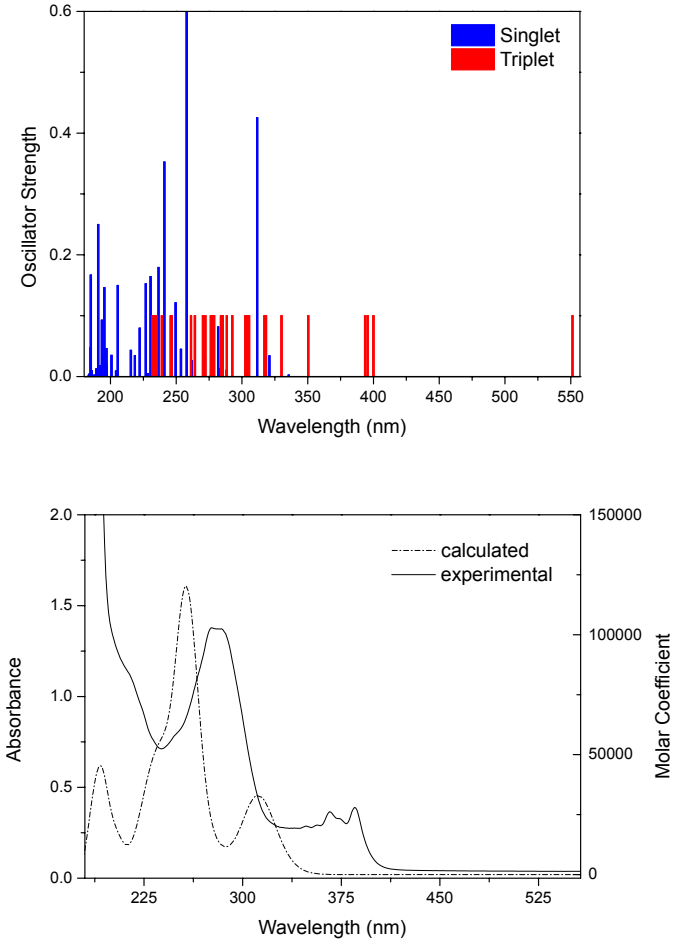


Figure 3.18: The calculated triplet (red) and singlet (blue) excited state transitions for [Re(CO)$_4$(dppz)][PF$_6$] calculated using TD-DFT in a CH_2Cl_2 field (top) and the calculated and experimental UV-vis spectra (bottom).

A very similar calculated UV-vis spectrum is observed for CH_3CN to that seen for CH_2Cl_2 except it is shifted to higher energy which was also observed for the HOMO and LUMO energies. The calculated singlet and triplet transitions are also very similar

in position. The nature of the lower energy transitions in CH_3CN appear to be mainly CT character, with the singlet transition with the highest oscillator strength (*ca.* 310 nm) being both ILCT and MLCT in nature. The nature of the MLCT for this transition is 'phen' based which was also observed in the CH_2Cl_2 calculations. This also supports the observations seen in the TRIR and luminescence. The higher energy band (*ca.* 254 nm) seen in the calculated UV-vis has ILCT character which appears to be 'phen' in nature. These TD-DFT calculations can be supported by the reported assignment of a high energy ^{1}LC and lower energy ^{1}CT and ^{3}CT character.[71,78]

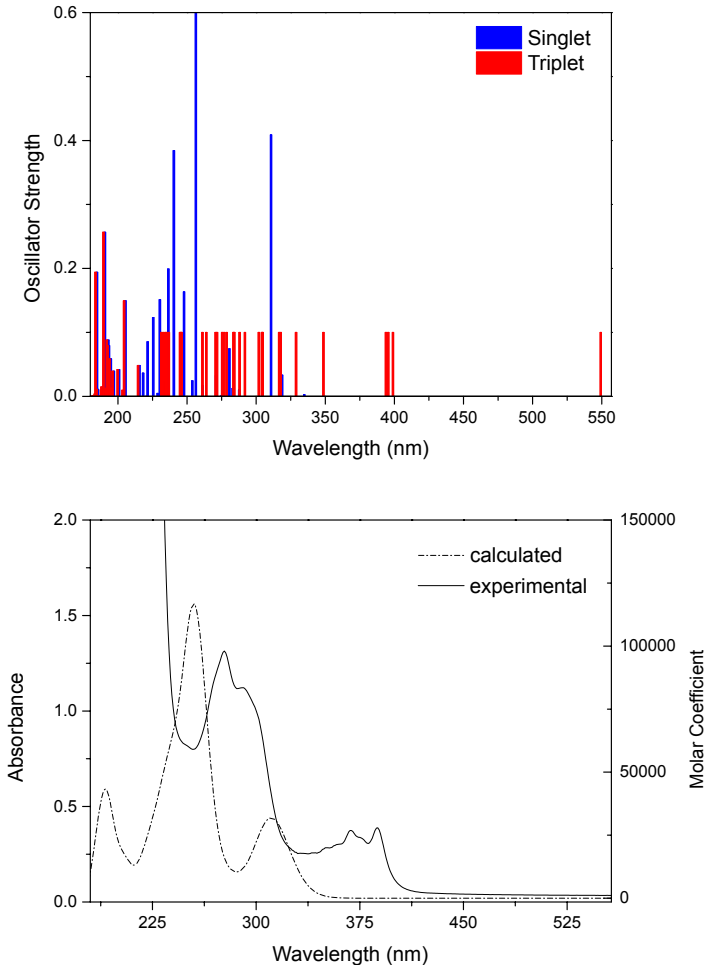


Figure 3.19: The calculated triplet (red) and singlet (blue) excited state transitions for $[Re(CO)_4(dppz)][PF_6]$ calculated using TD-DFT in a CH_3CN field (top) and the calculated and experimental UV-vis spectra (bottom).

The calculated electron density for the lowest energy singlet transition, that is the state that is most likely being populated at 355 nm, can be seen in Figure 3.20. The nature of these states shows that in CH_2Cl_2 and CH_3CN there is movement of electron density from both the metal and the ligands resulting in a mixed ILCT/MLCT excited state. This state appears to have a greater contribution from MLCT character which is 'phen' in nature than the ligand contribution. The CH_2Cl_2 state has slightly

higher ligand contribution than the state calculated for CH_3CN. The fact the MLCT character for both these states is rhenium to phen could explain why CO loss is not observed for the 355 nm TRIR experiments.

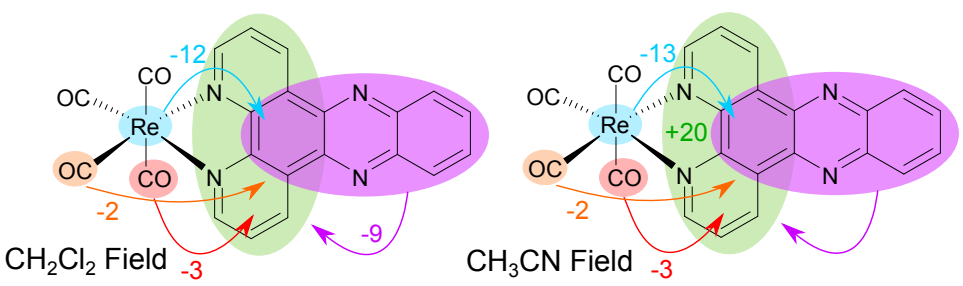


Figure 3.20: The calculated movement of electron density that occurs for State I populated upon 355 nm excitation in a CH_2Cl_2 (left) and a CH_3CN solvent (right) field.

It is clear from the 355 nm TRIR investigations that in both CH_2Cl_2 and CH_3CN the formation of a solvated photoproduct is not observed for $[Re(CO)_4(dppz)][PF_6]$ following the decay of the ^{3}ILCT/MLCT excited state. From the luminescence, TRIR and TD-DFT results it is possible that State I is ^{3}ILCT/MLCT excited state that is MLCT(phen) based, decaying to another ^{3}ILCT/MLCT excited state. This is illustrated in Figure 3.21. By changing the α-diimine ligand to dppz, the photochemical process that has been observed for other $[Re(CO)_4(\alpha\text{-diimine})][PF_6]$ has been 'switched off' and only photophysical processes are occurring. This could be due to the fact that the transitional states that are most likely populated with 355 nm light do not exhibit the 'rhenium $\rightarrow$ axial CO' or 'α-diimine $\rightarrow$ axial CO' character that is observed for $[Re(CO)_4(bpy)][PF_6]$.

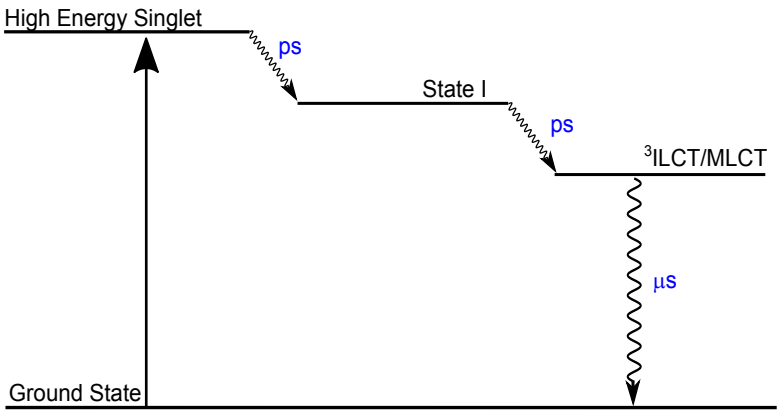


Figure 3.21: An illustration of the photophysical processes that occur for $[Re(CO)_4(dppz)][PF_6]$ following 355 nm excitation.

3.3.2.2 TRIR of $[Re(CO)_4(dppz)][PF_6]$ at 266 nm

To investigate if it was possible for $[Re(CO)_4(dppz)][PF_6]$ to form a solvated photoproduct a higher energy excitation, 266 nm, was investigated. Both the *ps* and *ns*-TRIR were probed at 266 nm in CH_2Cl_2 and CH_3CN. The *ps*-TRIR spectra in CH_2Cl_2 can be seen in Figure 3.22, where the formation of an excited state can be seen, along with the bleach of the parent. The parent bleaches can be seen at 2123, 2031 and 1976 cm^{-1} with an initial excited state at 2112, 1995 and 1956 cm^{-1}. The position of the bands appears to have a shifted to lower energy compared to the initial state observed for the 355 nm experiment. It is known from the TD-DFT that there is a high energy ^{1}LC state, so it is possible the state being observed, the red shift of the bands in relation to the parent, is consistent with a π-π^*(phen) based excited state. This initial excited state is seen to decay away (τ = 82 ps) and the formation of a second excited state is observed to grow in with bands at 2118, 2022, 2010 and 1986 cm^{-1}. The band positions are similar to the ^{3}ILCT/MLCT state observed for the 355 nm experiment, although they appear to be slightly more blue shifted. With

the TD-DFT calculations and the observation seen in the TRIR spectra, the initial state is assigned to a ^{3}ILCT(phen) excited state and the second state is assigned to a ^{3}ILCT/MLCT state.

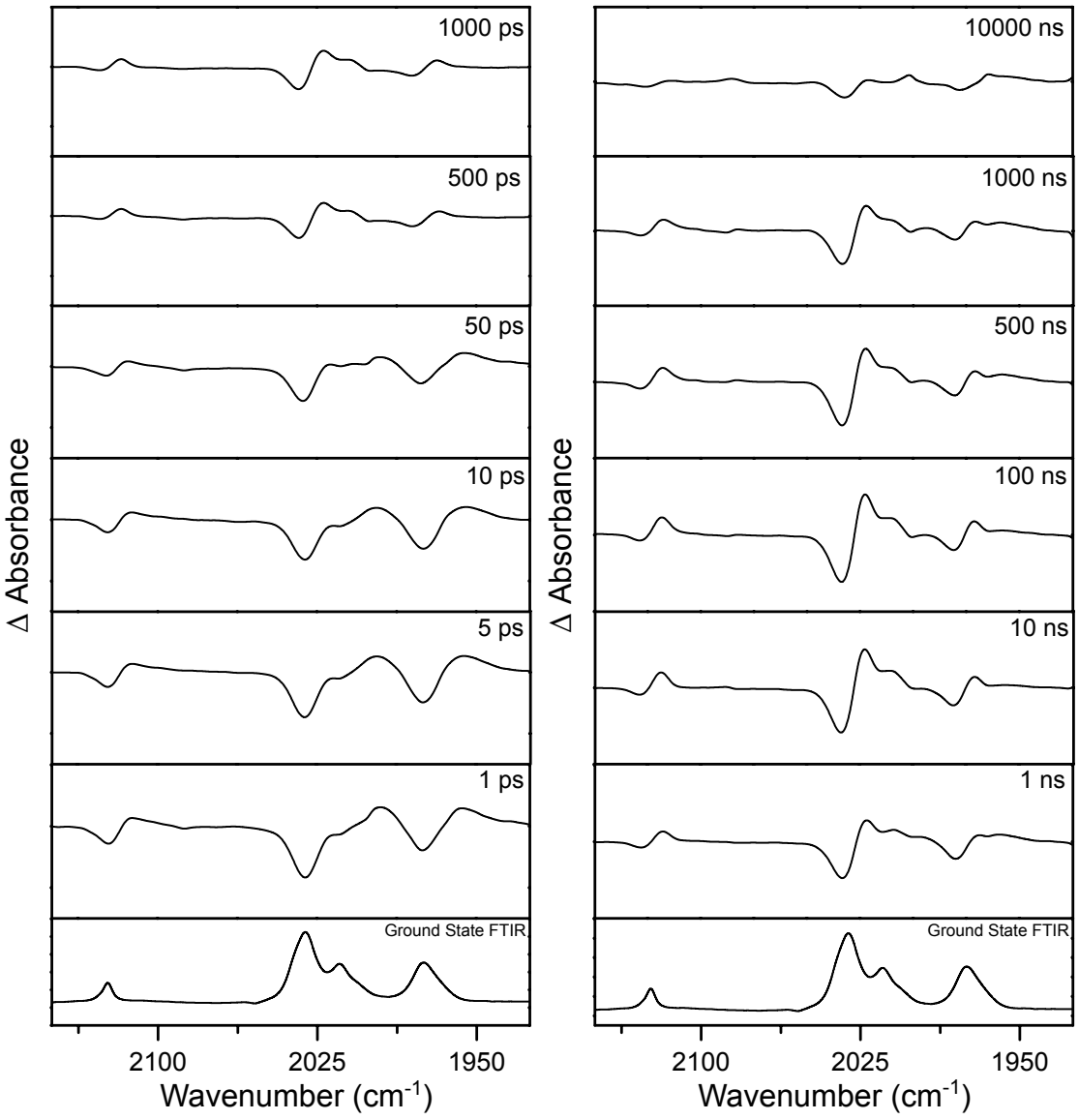


Figure 3.22: The *ps*-TRIR (left) and *ns*-TRIR spectra (right) spectra of $[Re(CO)_4(dppz)][PF_6]$ in CH_2Cl_2 following a 266 nm excitation wavelength.

The decay of the ^{3}ILCT(phen) excited state and the growth of the ILCT/MLCT excited state can be seen in Figure 2.29, where the ^{3}ILCT(phen) excited state is seen

to decay with a lifetime of $\tau = 82\ (\pm\ 7\ )$ ps. The global analysis indicated the presence of two excited species on the picosecond timescale, which supports observations seen in the *ps*-TRIR spectra. The ^{3}ILCT/MLCT excited state that is observed to grow in on the picosecond timescale lives onto the nanosecond timescale.

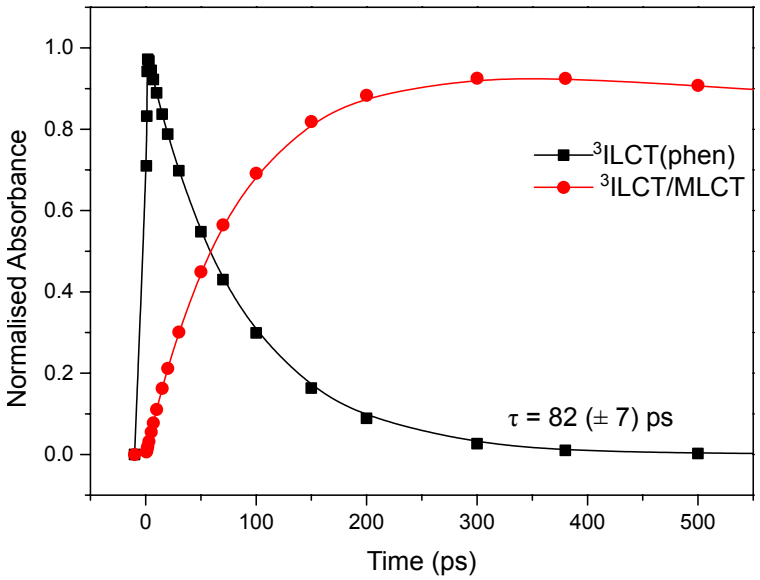


Figure 3.23: The kinetic plot generated from the global analysis for the decay of the ^{3}ILCT(phen) and the growth the ^{3}ILCT/MLCT state following a 266 nm excitation in CH_2Cl_2.

The excited state spectra generated from the global analysis, Figure 3.24, indicated the presence of two excited state species, with are consistent with the ^{3}ILCT(phen) and ILCT/MLCT excited states observed in the TRIR spectra. The ^{3}ILCT(phen) excited state is shown in black and the ^{3}ILCT/MLCT excited state is shown in red. The blue shift of the ^{3}ILCT/MLCT excited state can clearly been seen in Figure 3.24, which is likely to be the result of the MLCT character in the mixed state.

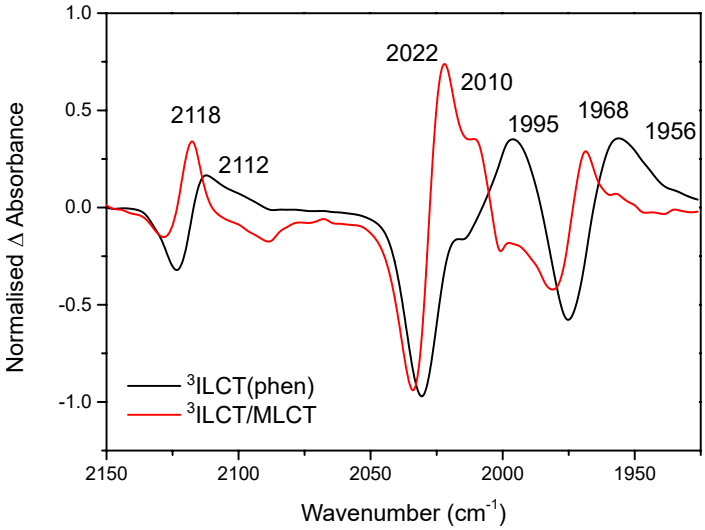


Figure 3.24: The normalised excited state spectra generated from the global analysis for the ^{3}ILCT(phen) and the ^{3}ILCT/MLCT state following a 266 nm excitation in CH_2Cl_2.

The ^{3}ILCT/MLCT excited can be seen in the *ns*-TRIR with bands at 2118, 2022, 2010 and 1968 cm^{-1} and parent bleaches at 2123, 2031 and 1975 cm^{-1}. The ^{3}ILCT/MLCT excited state is long lived on the nanosecond timescale, as is seen to decay away at later time delays. As the ^{3}ILCT/MLCT excited state starts to decay, the growth of another species can be observed, growing in at *ca.* 2050 and 1955 cm^{-1}. The position of this species is consistent with the formation of a solvated species, so it is possible there is the formation of the photodissociation product. The absorbance of these bands is very small, and there also appears to be some residual bands associated with the ^{3}ILCT/MLCT excited state. It is possible that there is not full conversion of the mixed ^{3}ILCT/MLCT excited state to the photoproduct, with the decay of the excited state back down to the ground state also being observed.

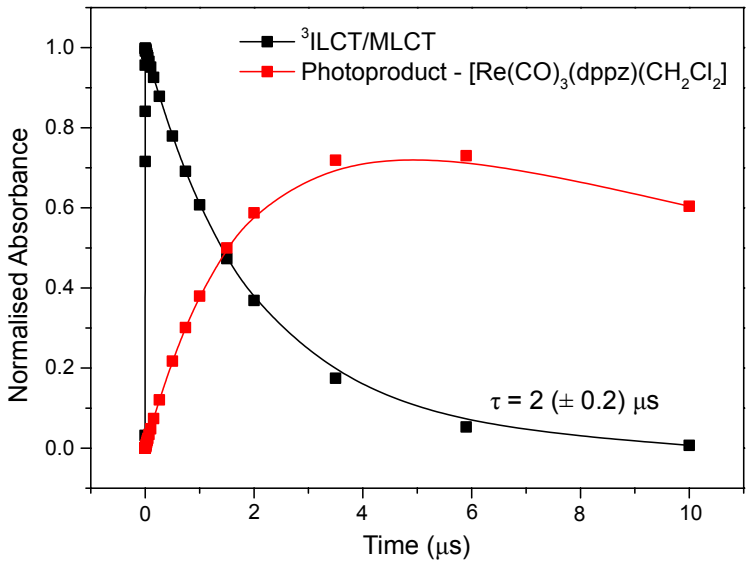


Figure 3.25: The kinetic plot generated from the global analysis for the decay of the ^{3}ILCT/MLCT excited state and the formation of the solvated photoproduct after a 266 nm excitation in CH_2Cl_2.

The global analysis for the nanosecond data calculated the kinetic information for the *ns*-TRIR spectra and indicated the two species, the ^{3}ILCT/MCLT and the species that is thought to be the solved photoproduct. The ^{3}ILCT/MLCT excited state is seen decay with a lifetime of $\tau = 2\ (\pm\ 0.2)\ \mu$s. The photoproduct is seen to grow in as the ^{3}ILCT/MLCT state decays, which can be seen in Figure 3.25. Following the decay of the ^{3}ILCT/MLCT, growth of the photoproduct can be seen, however the photoproduct starts to decay away suggesting it is not as stable as the photoproduct observed for the bipyridine analogue. The excited state spectra generated from the global analysis can be seen in Figure 3.26, where the two species are observed, with the ^{3}ILCT/MLCT excited state shown in black and the photoproduct shown in red. The two bands associated with the photoproduct can be seen at 1958 cm^{-1} and the tail of a band at 2049 cm^{-1} which is most likely being obscured by the parent bleach.

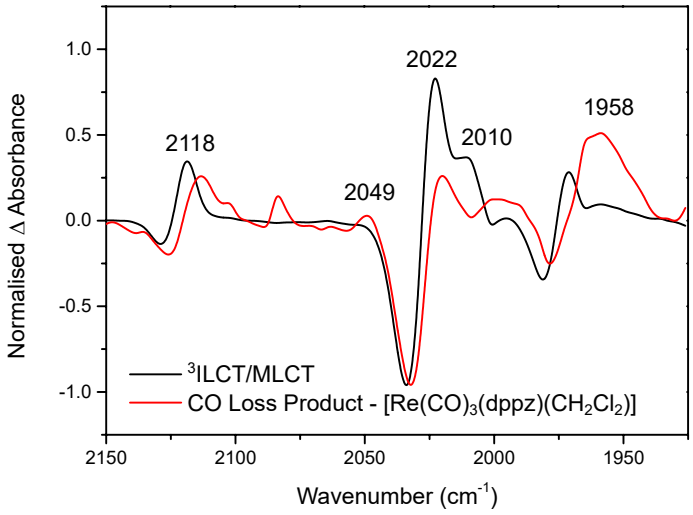


Figure 3.26: The normalised excited state spectra generated from the global analysis for the ^{3}ILCT/MLCT excited state and the solvated photoproduct after a 266 nm excitation in CH_2Cl_2.

The *ns*-TRIR spectra for the 266 nm experiment in CH_2Cl_2 has indicated a different result to that seen for the 355 nm experiment. Following irradiation with a 266 nm light, an initial ^{3}ILCT(phen) excited state is observed followed by a mixed ^{3}ILCT/MLCT excited state, which appears to decay away to form the photoproduct. The formation of the photoproduct was not observed in the 355 nm experiment, which suggests the mixed state that was populated with the 266 nm light could be different to the state populated with the 355 nm light. Following the observation seen in CH_2Cl_2, the 266 nm experiment was repeated in CH_3CN to see if changing the solvent would also result in the formation of a photoproduct following the decay of the mixed ^{3}ILCT/MLCT excited state. The *ps*-TRIR spectra for $[Re(CO)_4(dppz)][PF_6]$ in CH_3CN can be seen in Figure 3.27.

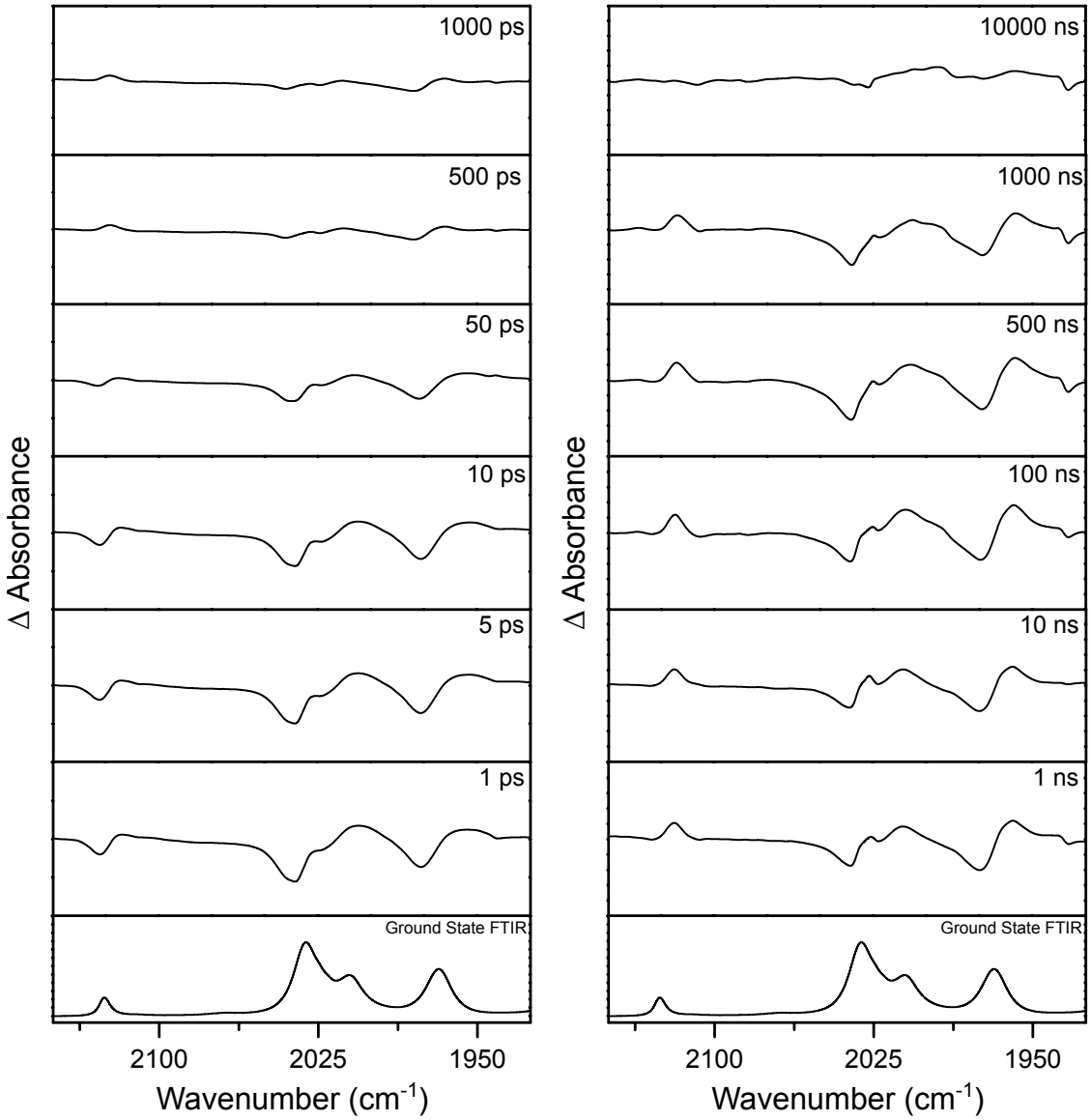


Figure 3.27: The *ps*-TRIR (left) and *ns*-TRIR spectra (right) spectra of $[Re(CO)_4(dppz)][PF_6]$ in CH_3CN following a 266 nm excitation wavelength.

The *ps*-TRIR spectra shows the bleach of the parents at 2127, 2036, 2023 and 1976 cm^{-1} with an initial excited state seen at 2116, 2005 and 1954 cm^{-1}. These are consistent with the initial excited state seen in the 355 nm experiment. This inital excited state is then seen to decay away (τ = 55 ($\pm$ 6) ps) as a second state grows in, with bands which have blue shifted relative to the initial excited state. The second

excited state has bands at 2119, 2026, 2011 and 1960 cm^{-1}, which are similar to the second excited state observed in the 355 nm experiment. Due to the band position, which is similar to the 355 nm experiment, and the TD-DFT calculations, this initial excited state can also be assigned as State I, with the second state being another mixed ^{3}ILCT/MLCT state. The main difference is the decay of State I has a lifetime of τ = 55 ps, which is faster than the lifetime seen for the 355 nm experiment which had a lifetime of τ = 114 ps. This change is likely to be a concentration effect as the 266 nm experiments had to be run at a much lower concentration due to the fact that the solution is more absorbing at 266 nm compared to 355 nm. The kinetic plot for the decay of State I and the growth of the ^{3}ILCT/MLCT excited state can be seen in Figure 3.28.

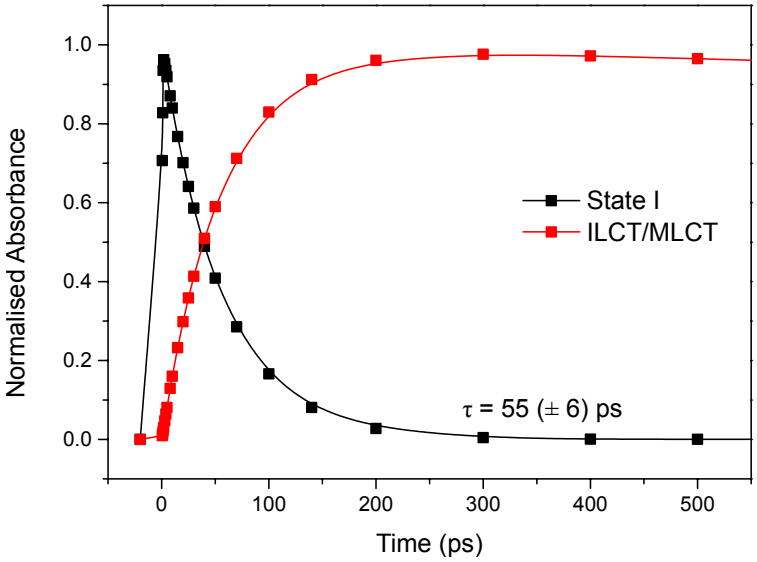


Figure 3.28: The kinetic plot generated from the global analysis for the decay of State I and the growth the ^{3}ILCT/MLCT state following a 266 nm excitation in CH_3CN.

The global analysis indicated that there were two excited state species, matching what is seen in the *ps*-TRIR. The two species identified from the global analysis can

be seen in the excited state spectra, Figure 3.29. The positions of these bands are in agreement with State I, shown in black, with the ^{3}ILCT/MLCT state species shown in red. This ^{3}ILCT/MLCT excited state is seen to grown in on the picosecond timescale and is seen to live onto the nanosecond timescale.

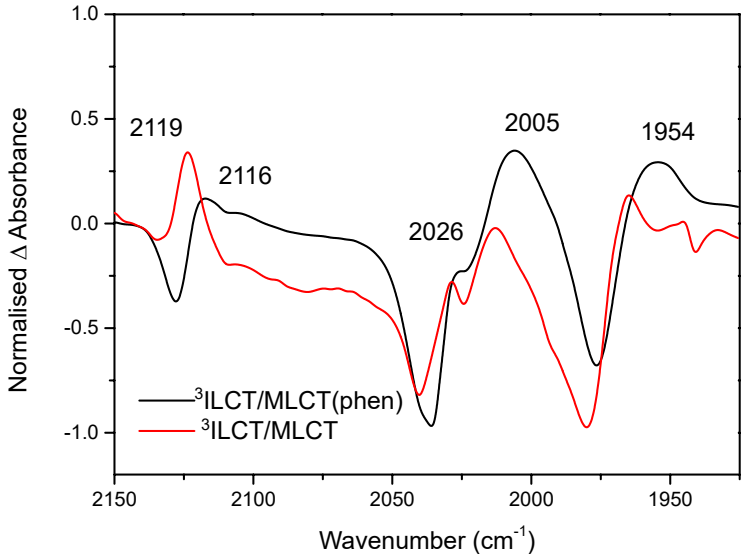


Figure 3.29: The normalised excited state spectra generated from the global analysis for State I and the ^{3}ILCT/MLCT state following a 266 nm excitation in CH_3CN.

The *ns*-TRIR spectra shows the ^{3}ILCT/MLCT excited state with bands at 2119, 2026, 2011 and 1960 cm^{-1}. This ^{3}ILCT/MLCT excited state is seen to be long lived on the duration of the nanosecond timescale, with the decay seen at later time delays. Following the decay of the ^{3}ILCT/MLCT excited state there appears to be no formation of a photoproduct, which was observed in the CH_2Cl_2 experiment. The recovery of the parents can be observed as the ILCT/MLCT excited state decays. The decay of the ^{3}ILCT/MLCT has a lifetime of $\tau = 1.4\ (\pm\ 0.2)\ \mu$s which is comparable with the lifetime seen for the 355 nm experiment in CH_3CN. The global analysis of the data also only identified the presence of one species on the nanosecond timescale

which supports the observation of no photoproduct being seen following the decay of the ^{3}ILCT/MLCT excited state. The kinetic decay of the ^{3}ILCT/MLCT excited state can be seen in Figure 3.30.

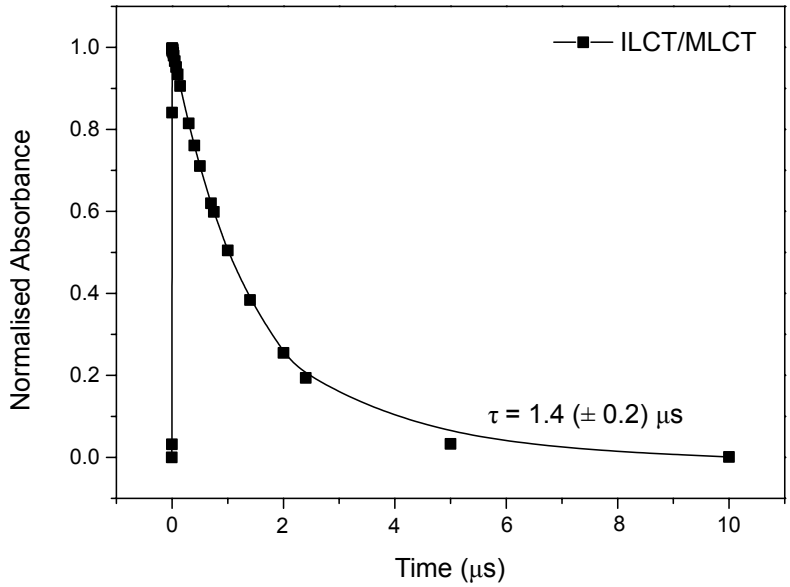


Figure 3.30: The kinetic plot generated from the global analysis for the decay of the ^{3}ILCT/MLCT excited state after a 266 nm excitation in CH_3CN.

Figure 3.31 shows the spectrum of an excited state species, generated from global analysis, which matches the observation in the *ns*-TRIR. This spectrum also supports what was seen for the 355 nm experiment where the decay of the ^{3}ILCT/MLCT also did not result in the formation of the photoproduct. It is clear that the second excited state assigned as the ^{3}ILCT/MLCT does not decay *via* the same excited state pathway as that seen for the 266 nm experiment in CH_2Cl_2.

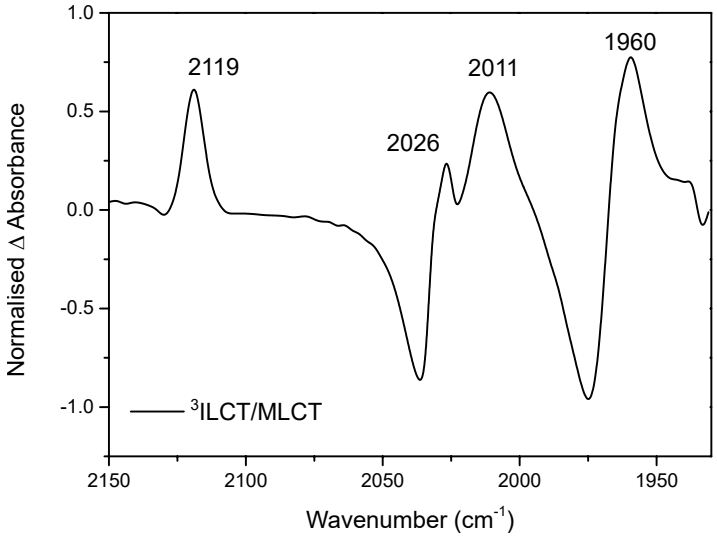


Figure 3.31: The normalised excited state spectra generated from the global analysis for the ^{3}ILCT/MLCT state following a 266 nm excitation in CH_3CN.

The 266 nm experiments conducted in CH_2Cl_2 and CH_3CN have shown two completely different results, with a photoproduct being observed in CH_2Cl_2 and no photoproduct is seen in CH_3CN. The lifetimes seen for the two different solvents shows that in CH_2Cl_2 an initial ^{3}ILCT(phen) excited state is seen to decay to a ^{3}ILCT/MLCT state, whereas State I is seen to decay followed by the formation of another ^{3}ILCT/MLCT state. Table 3.2 shows the lifetimes observed for $[Re(CO)_4(bpy)][PF_6]$ following an 266 nm light excitation.

Table 3.2: The lifetimes of the processes observed in both the *ps* and *ns*-TRIR for $[Re(CO)_4(dppz)][PF_6]$ following a 266 nm excitation.

Solvent	Nature of State	Band Position (cm^{-1})	τ ($\pm$ errors)
CH_2Cl_2	^{3}ILCT(phen)	2112, 1995, 1956	82 (7) ps
	^{3}ILCT/MLCT	2118, 2022, 2010, 1968	2.0 (0.2) μs
	$[Re(CO)_3(dppz)(CH_2Cl_2)]$	2049, 1958	-
CH_3CN	State I	2116, 2005, 1954	55 (6) ps
	^{3}ILCT/MLCT	2119, 2026, 2011, 1960	1.4 (0.2) μs

It is apparent that the solvent has a far great effect on the formation of a photoproduct for $[Re(CO)_4(dppz)][PF_6]$ along with the excitation wavelength used than it does for $[Re(CO)_4(bpy)][PF_6]$. It has been shown that the lower energy states for $[Re(CO)_4(dppz)][PF_6]$ are predominately ILCT/MLCT based, with the MLCT being 'phen' in nature. The higher energy states appear to be more LC in nature, but there are also some ILCT/MLCT states with MLCT(phen) based character. The UV-vis spectra for CH_2Cl_2 and CH_3CN were different for the higher energy band, which could explain why two different results are being observed for the 266 nm experiment. It is possible that in CH_2Cl_2 the higher energy ILCT(phen) is favoured, whereas in CH_3CN the population of State I is favoured. To confirm this more investigations are required. One thing to note is that from the TD-DFT calculations some other ILCT/MLCT states can be observed that have MLCT character that is 'metal $\rightarrow$ axial CO' in nature, illustrated in Figure 3.32. For both CH_2Cl_2 and CH_3CN these sit at higher energy than the state that is thought to be populated at 355 nm, however they sit at lower energy to the state that is thought to be populated at 266 nm. It is plausible this is why photodissociation is observed for the 266 nm experiment in

CH_2Cl_2. Another factor to notes is that $[Re(CO)_4(dppz)][PF_6]$ less soluble in CH_3CN which could be obscuring the results.

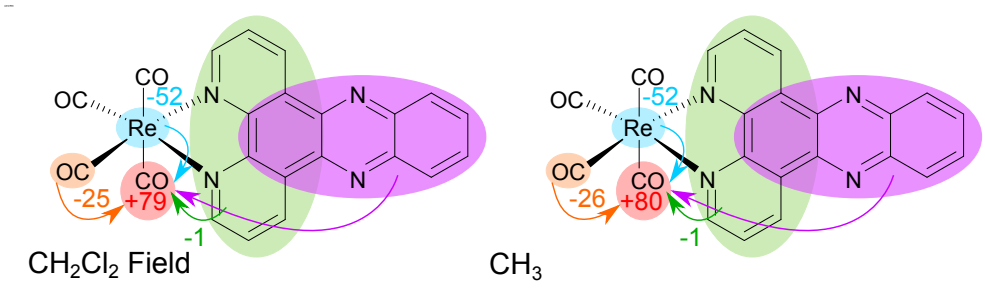


Figure 3.32: The calculated movement of electron density that occurs for the ^{3}ILCT/MLCT mixed state that has 'metal → axial CO' character that could be populated following a 266 nm excitation. The two solvent fields can be seen with CH_2Cl_2 on the left and a CH_3CN on the right.

From the results obtained from the TD-DFT and the 266 nm TRIR experiments it appears that two separate processes are occurring. In CH_2Cl_2 a different initial excited state is observed, this state is red shifted the most and is thought to be ILCT(phen) in nature. Upon the decay of this state, a ^{3}ILCT/MLCT mixed state is then populated, which appears to have different MLCT character than the other ^{3}ILCT/MLCT states observed, it has 'metal → axial CO' character. This state results in the photodissociation of CO. The decay process that occurs for $[Re(CO)_4(dppz)][PF_6]$ in CH_2Cl_2 following a 266 nm excitation can be seen in Figure 3.33. The process that is observed in CH_3CN following 266 nm excitation is similar to that observed for the 355 nm experiments, shown in Figure 3.21.

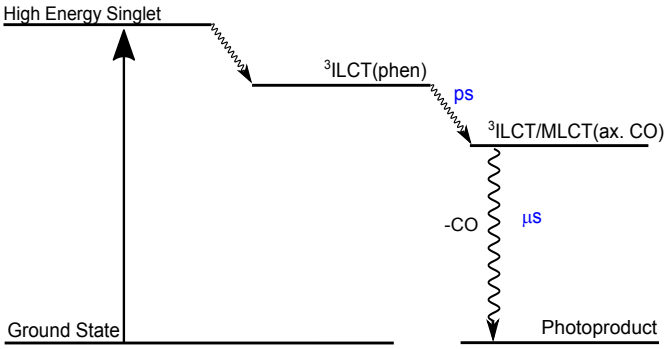


Figure 3.33: An illustration of the photophysical processes that occurs for $[Re(CO)_4(dppz)][PF_6]$ in CH_2Cl_2 following a 266 nm excitation.

If the change in absorbance of the parent bleaches is plotted against the time of the experiment, the percentage recovery of the parent can be calculated, this is shown in Figure 3.34. There is nearly full recovery of the parent for both 355 nm experiments which supports the observation of no photoproduct formation. For the 266 nm CH_2Cl_2 experiment, a 77% reformation is seen which supports the observation of a photoproduct. The one anomaly is the reformation of the parent in CH_3CN with a 266 nm excitation, which suggests there is only a 68% reformation. There was no evidence for the formation of a photoproduct from either of the TRIR spectra, so this could be due to the low solubility in CH_3CN or could suggest degradation of the sample.

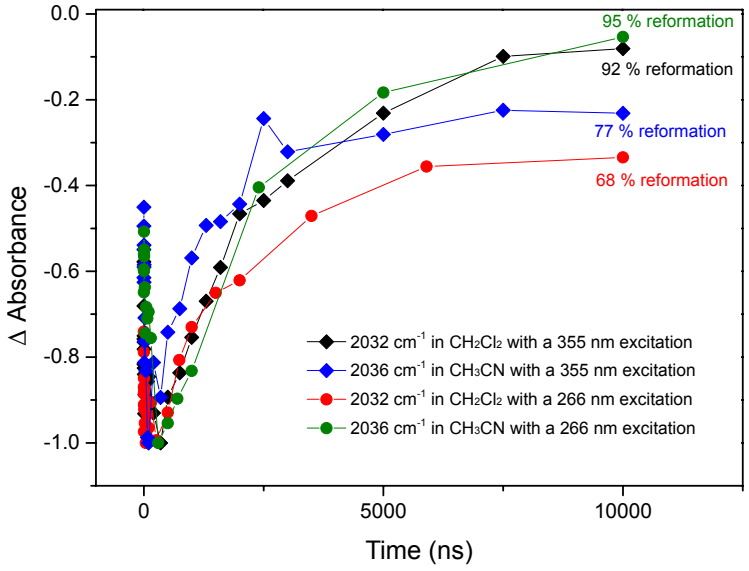


Figure 3.34: The reformation of the parent bands for $[Re(CO)_4(dppz)][PF_6]$ in CH_2Cl_2 and CH_3CN following a 355 and 266 nm excitation.

3.3.3 Electrochemistry of $[Re(CO)_4(dppz)][PF_6]$

The electrochemical properties of $[Re(CO)_4(dppz)][PF_6]$ were also probed in a preliminary investigation. Both the electrochemistry and spectroelectrochemistry was probed in CH_2Cl_2 and CH_3CN. The CV for the electrochemistry for $[Re(CO)_4(dppz)][PF_6]$ in CH_2Cl_2 with $[TBA][BF_4]$ as the chosen electrolyte is shown in Figure 3.35.

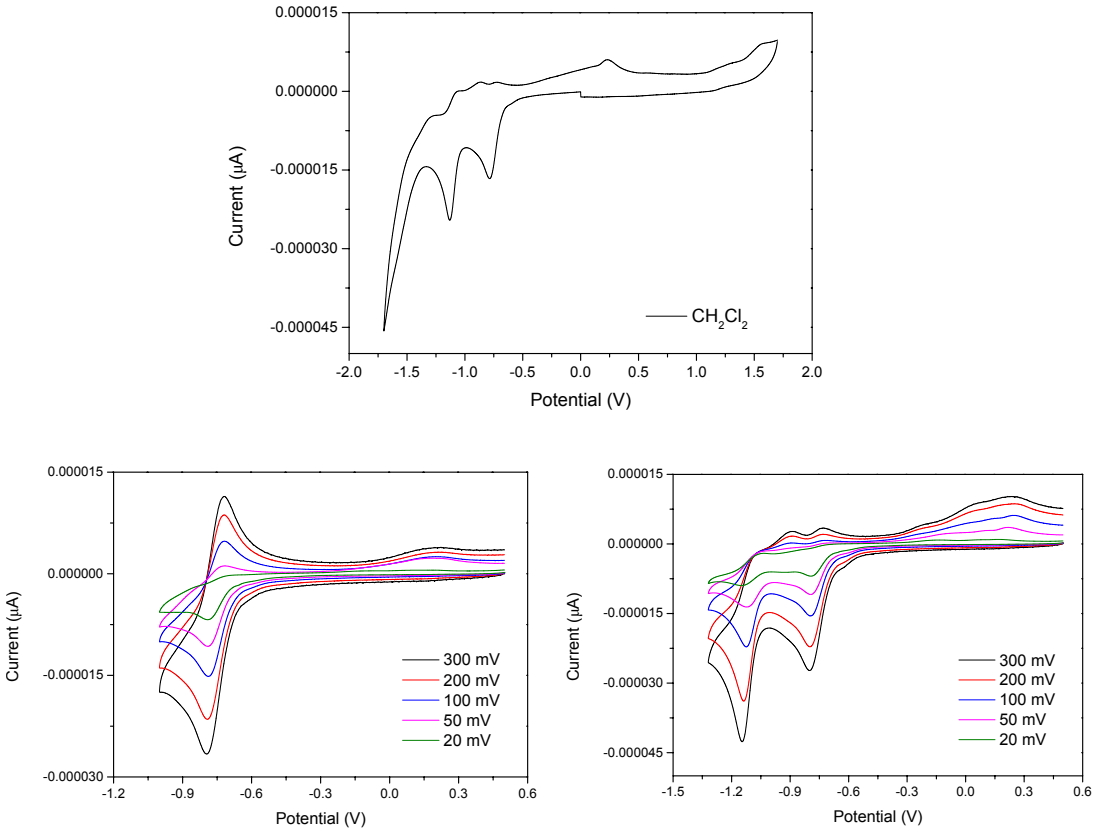


Figure 3.35: The cyclic voltammetry for the reduction $[Re(CO)_4(dppz)][PF_6]$ in CH_2Cl_2/[TBA][BF_4] with with the full scan (top), the first reduction (bottom left) and the second reduction (bottom right).

The full scan can be observed which shows there are two reductions occurring at *ca.* -0.7 and -1.19 eV. The first reduction appears be be reversible and has an $E_{1/2}$ of -1.512 eV (*vs.* Fc/Fc^+). A oxidation band grows in at 0.3 eV at higher scan rates for the first reduction process. The second reduction process was probe which appeared to be dependent on the first reduction. This second reduction does not appear to be reversible, and following the second reduction the oxidation band at 0.3 eV get more pronounced pronounced.

Following this, the spectroelectrochemistry was probed to help identify the processes that were observer in the CV. A bulk reduction was done for the spectroelectrochemistry at a potential of -0.94 eV, which was run for 20 minutes, after which the solution was fully reduced. The FTIR for the reduced species can be seen in Figure 3.36, and shows two bands at 2010 and 1900 cm^{-1}. The observation of two ν(CO) bands suggests there has been a change in symmetry from C_{2V}, which could suggest the complex has undergone CO loss. The position of these bands is consistent with a reduced species of $Re(CO)_3(dppz)Cl$.[107] The solution was then oxidised for 20 minutes at 0.5 eV, which corresponds to the oxidation peak that was seen to grow in CV. The oxidised spectrum also shows two ν(CO) bands, with the lower energy band potentially being two ν(CO) bands over lapped. The position of the observed bands at 2024, 1920 and 1904 cm^{-1} are the exact band positions for the neutral $Re(CO)_3(dppz)Cl$ species further suggesting upon a negative potential the complex has undergone CO loss.

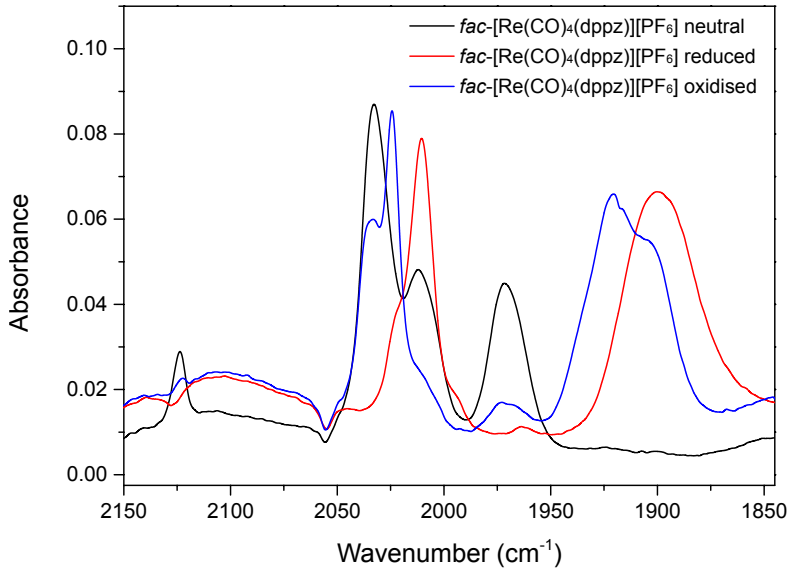


Figure 3.36: The FTIR spectra for the *fac*-$[Re(CO)_4(dppz)][PF_6]$ in CH_2Cl_2/[TBA][BF_4] with neutral spectrum in black, the reduced spectrum in red and the oxidised spectrum in blue.

The UV-vis from the spectroelectrochemistry can be seen in Figure 3.37, where the reduced species is shown in red and the oxidised species shown in blue. The reduced species has bands that are very similar to that of the reduced species of $Re(CO)_3(dppz)Cl$, with a distinctive lower energy bands at *ca.* 560 nm. There are also some higher energy bands at *ca.* 230, 300 and 390 nm, which are also consistent with the reduced form of $Re(CO)_3(dppz)Cl$.[107] The oxidised species has very similar absorption bands to the neutral species of $Re(CO)_3(dppz)Cl$, with bands at *ca.* 280, 320 and 395 which are consistent with the absorption bands reported in the literature.[107] The spectroelectrochemistry results for both the FTIR and UV-vis are in agreement with each other. Further investigations will be needed to confirm these observations, but what this results do suggest is that the dissociation of CO can be achieved electrochemically.

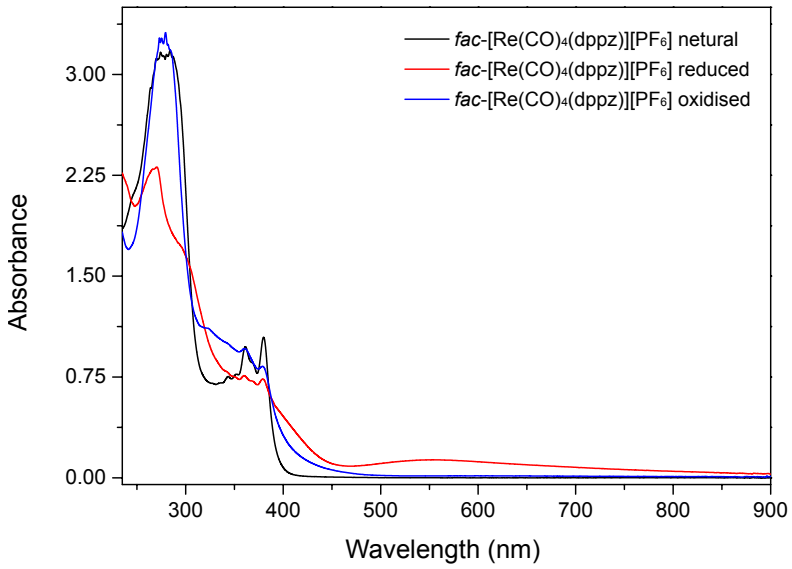


Figure 3.37: The UV-vis spectra for the *fac*-$[Re(CO)_4(bpy)][PF_6]$ in $CH_2Cl_2/[TBA][BF_4]$ with the neutral spectrum in black, the reduced spectrum in red and the oxidised spectrum in blue.

The electrochemistry was then probed in CH_3CN to see if a similar ligand dissociation process occurs. The CV for $[Re(CO)_4(dppz)][PF_6]$ in CH_3CN/[TBA][BF_4] can is shown in Figure 3.38. The full scan clearly shows there are two defined reductions similar to the CH_2Cl_2 experiment, followed by less defined reductions at a lower potential. Due to the fact that these were preliminary investigation, the discussion will only on the first reduction to see if ligand dissociation could be induced electrochemically in CH_3CN. The CV for first reduction at -0.91 eV appears to be a reversible process, and like the CH_2Cl_2 experiment oxidation peak, can be observed forming at *ca.* 0.1 eV. The first reduction has an $E_{1/2}$ of -1.512 eV (*vs.* Fc/Fc^+), which sits at a lower potential to the first reduction observed in CH_2Cl_2.

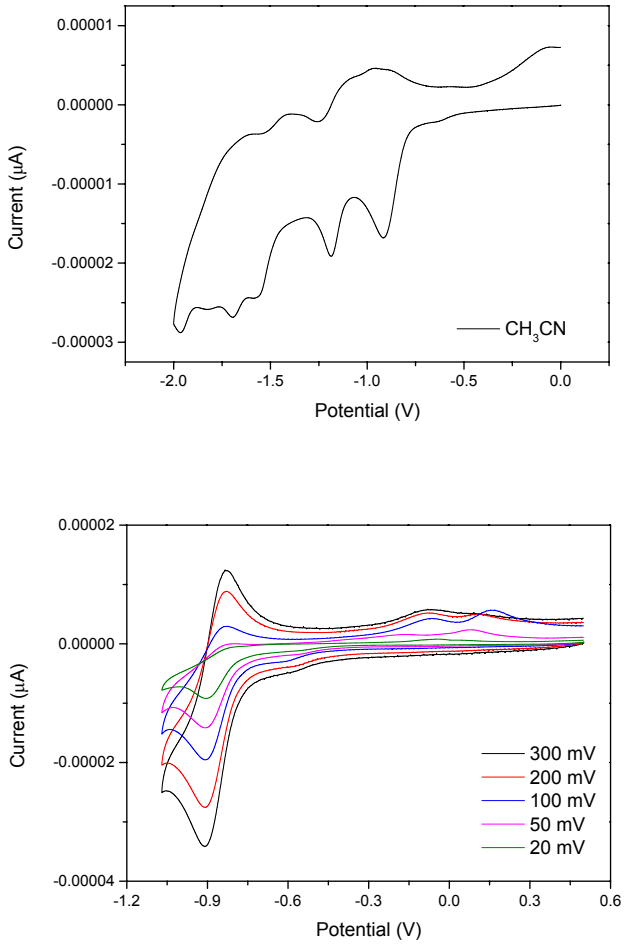


Figure 3.38: The cyclic voltammetry for the reduction $[Re(CO)_4(dppz)][PF_6]$ in $CH_3CN/[TBA][BF_4]$ with the full scan (top) and the first reduction (bottom).

For the bulk reduction, the $[Re(CO)_4(dppz)][PF_6]$ in $CH_3CN/[TBA][BF_4]$ was held at a potential of -1.00 eV for 8 minutes by which time there was a complete reduction of the solution. The FTIR of the reduced species can be seen as the blue spectrum in Figure 3.39, which has two ν(CO) bands at 2010 and 1903 cm^{-1}, with two other bands growing in at the same position as the oxidised species. The change in symmetry observed is consistent with a $[Re(CO)_3(dppz)(py)]^+$ species with C_{3V}, which suggests the species has undergone CO loss. However, the electrochemistry of the reduced form of $[Re(CO)_3(dppz)(CH_3CN)]$ has not been reported in the literature, so it difficult to

assign this species. There was a colour change in the solution from pale yellow to a deep purple/black colour which known for reduced dppz complexes. This could suggest that the species being observed is the reduced species of $[Re(CO)_3(dppz)(CH_3CN)]^+$. Upon the oxidation of the solution there was a colour change from purple/black to bright yellow which, is indicative of a$[Re(CO)_3(dppz)(L)]^{+/0}$ complex. The solution was fully oxidised to a potential of +0.5 eV. The oxidised species also exhibited two ν(CO) bands at 2041 and 1933 cm^{-1} which sit at a higher wavenumber than the reduced species. A mass spec was recorded of the oxidised solution and the mass of 594.06 g/mol was detected, which suggests that upon the oxidation of the sample a stable $[Re(CO)_3(dppz)(CH_3CN)][PF_6]$ has formed. Although, further investigations need to be carried out to confirm this.

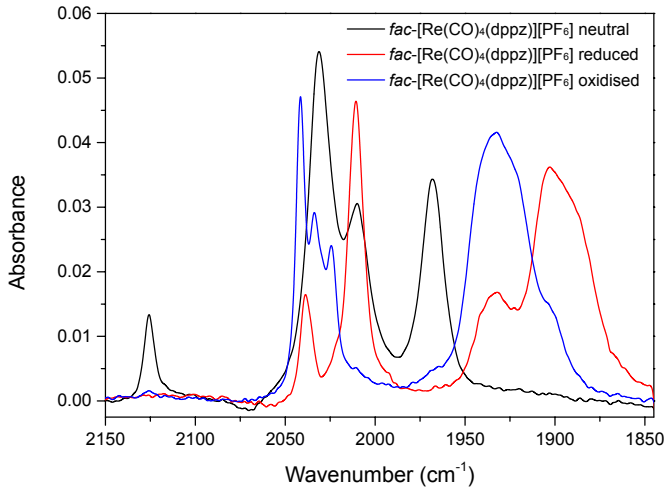


Figure 3.39: The FTIR spectra for the *fac*-$[Re(CO)_4(dppz)][PF_6]$ in CH_3CN/[TBA][BF_4] with neutral spectrum in black, the reduced spectrum in red and the oxidised spectrum in blue.

The UV-vis of the reduced and oxidised species can be seen in Figure 3.40, with the reduced species in red and the oxidised species in blue. For the reduced species, a band at *ca.* 590 nm is seen which was also observed for the CH_2Cl_2 experiment.

This could suggest the formation of a reduced $[Re(CO)_3(dppz)(CH_3CN)]^+$ species, but again without other literature reports or further investigations it is difficult to confirm. The oxidised species has the presence of a new shoulder at *ca.* 330 nm, which was also seen for the CH_2Cl_2 experiment. The mass spec results of this species does support the assignment of it being $[Re(CO)_3(dppz)(CH_3CN)][PF_6]$, however again further work needs to be done to confirm this.

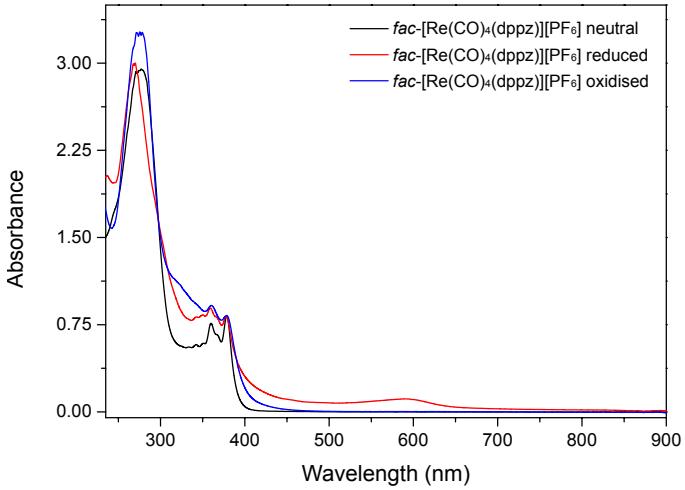


Figure 3.40: The UV-vis spectra for the *fac*-$[Re(CO)_4(dppz)][PF_6]$ in $CH_3CN/[TBA][BF_4]$ with the neutral spectrum in black, the reduced spectrum in red and the oxidised spectrum in blue.

The main result to draw from the preliminary electrochemical and spectroelectrochemical results is that upon an applied negative potential, the complex appears to undergo a chemical change which involves ligand dissociation. The electrochemical and spectroelectrochemical properties observed for $[Re(CO)_4(dppz)][PF_6]$ appear to be slightly different than those observed for $[Re(CO)_4(bpy)][PF_6]$. Upon an applied negative potential for $[Re(CO)_4(bpy)][PF_6]$ in CH_2Cl_2, the formation of the stable tricarbonyl analogue is observed, but in CH_3CN a reduced species is observed which has to be reoxidised to form the tricarbonyl analogue. The result for $[Re(CO)_4(bpy)][PF_6]$

in CH_3CN is very similar to the observation seen for $[Re(CO)_4(dppz)][PF_6]$, however the formation of the reduced species followed by the stable tricarbonyl analogue appears to be more efficient for $[Re(CO)_4(dppz)][PF_6]$. This opens up potential future applications for $[Re(CO)_4(dppz)][PF_6]$ as a catalyst, as it can easily undergo CO electrochemically.

3.4 Conclusion

Previous to the work within this Chapter, the photophysical and photochemical properties of $[Re(CO)_4(dppz)][PF_6]$ had not be investigated, this also included the electrochemical properties of the complex. With the use of TRIR, TD-DFT, electrochemistry and spectroelectrochemistry an idea of the properties of $[Re(CO)_4(dppz)][PF_6]$ has been gained. When $[Re(CO)_4(dppz)][PF_6]$ was probed at 355 nm in CH_2Cl_2 and CH_3CN the desirable photochemical properties seen for $[Re(CO)_4(bpy)][PF_6]$ were not observed. Instead, an initial state was observed, State I, which is thought to have MLCT(phen) character from both the TD-DFT calculations and the emission observed for the complex. State I is short lived and decays to a ^{3}ILCT/MLCT excited state, which is a long-lived state with a microsecond lifetime. This ^{3}ILCT/MLCT excited state decayed back to the ground state and the formation of a photoproduct was not observed. The TD-DFT calculations indicated there were some ILCT/MLCT states with 'rhenium $\rightarrow$ axial CO character' however, these were at higher energy to the state being populated with 355 nm excitation. This showed that by simply changing the α-diimine ligand the photochemical properties were completely changed.

The TRIR investigation with a 266 nm excitation wavelength highlighted that a photochemical decay processes was possible for $[Re(CO)_4(dppz)][PF_6]$ in CH_2Cl_2, however this was not observed for CH_3CN. From the TRIR and TD-DFT calculations it was found that in CH_2Cl_2 a ^{3}ILCT(phen) state is populated which decays to a ^{3}ILCT/MLCT states thats has a MLCT with rhenium $\rightarrow$ axial CO character. The lifetime of the ^{3}ILCT(phen) state is on the picosecond timescale with the ^{3}ILCT/MLCT(ax.CO) states decaying away on the microsecond timescale. The decay of the ^{3}ILCT/MLCT(ax.CO) results in the dissociation of CO, and the formation of a

photoproduct is observed. Although the photoproduct does not appear to be stable, it has demonstrated that in CH_2Cl_2 $[Re(CO)_4(dppz)][PF_6]$ exhibits both photophysical and photochemical properties. In contrast, the TRIR for $[Re(CO)_4(dppz)][PF_6]$ in CH_3CN showed that following a 266 nm excitation a very similar decay process to the 355 nm experiment is observed. The first excited state observed State I, decaying on the picosecond timescale to a ^{3}ILCT/MLCT excited state which is seen to decay back down to the ground state after a microsecond. By probing $[Re(CO)_4(dppz)][PF_6]$ at 266 nm in CH_2Cl_2 and CH_3CN, it is clear that the complex can exhibit some photochemical properties as well as photophysical properties.

Finally, probing the electrochemistry and spectroelectrochemistry in CH_2Cl_2 and CH_3CN highlighted that $[Re(CO)_4(dppz)][PF_6]$ readily undergoes an electrochemical process that results in the loss of a CO ligand. It is observed that for both solvents upon a bulk reduction with a negative potential, $[Re(CO)_4(dppz)][PF_6]$ readily undergoes CO loss and forms a reduced species of the product. When a bulk oxidation is conducted, the neutral species is formed, resulting in a stable tricarbonyl species. This results indicates that $[Re(CO)_4(dppz)][PF_6]$ acts very well as a catalyst when reduced.

Chapter 4

Photophysical Properties of Conjugated Perylene Diimind Handcuff Complexes

4.1 Introduction

There has been considerable interest in supramolecular molecules particularly due to many desirable properties resulting in them having applications for organic light-emitting diodes,[130–134] photovoltaics,[135–147] light harvesting materials,[148–153] and photoinduced charge transfer and electron transfer studies.[154–157,157–161] In the area of supramolecular photochemistry a large amount of research has focused on the construction of large covalently bound structures, which are capable of intramolecular photoinduced charge separation.[162–171] The synthesis of these large covalently bound structures is problematic and alternatives for these photofunctional materials are non-covalent self-assembly materials.[172–178] The ability to understand the interactions be-

tween the individual components of a non-covalent system is desirable for realising the full potential many application.

One class of chromophores that has gained attention in recent years are perylene-3,4:9,10-bis(dicarboximide) (PDI) complexes.[139,158–160,165,166,179–197] PDI systems have been shown to be both photochemically and thermally stable and exhibit high fluorescence quantum yields, low triplet yields and strong electron accepting character.[196,198–201] PDI complexes also exhibit an affinity for self-assembly in both solution and solid state, facilitated by π-π stacking interactions.[158,160,188,189,192,194,198,202]

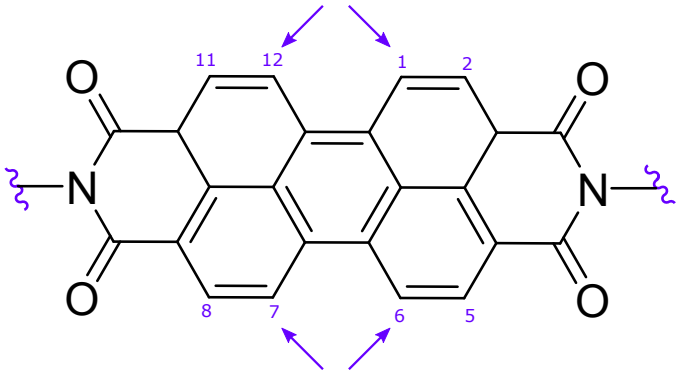


Figure 4.1: The structure of a perylene-3,4:9,10-bis(dicarboximide) (PDI) complex. A PDI complex can be modified at either the imide nitrogen position or the 1, 6, 7 and 12 position.

PDI systems can easily be modified at either the imide nitrogen position or the 1, 6, 7 and 12 positions on the PDI core,[203] shown in Figure 4.1. There have been photophysical investigations into monomer PDI derivatives with different substituent groups either bound to the imide nitrogen position or the bay positions on the main PDI core, which can alter the nature of the electron and energy transfer properties.[200] The addition of electron rich substituent groups may have an effect on their electronic and photochemical properties, with alkoxyphenyl group being known to decrease the

quantum yield to <5%, due to a self quenching effects.[196,198] The presence of a electron donor substituent groups has been shown to exhibit charge transfer from the donor to the PDI core,[204] including aryl donor groups which are substituted directly to the core imide position.[198,200,205,206]

Whilst the PDI core has been modified, the investigation of PDI dimers has been limited to either PDI aggregates or covalently bound dimers. A unique non-covalently bound group of PDI dimers have been reported recently by Yang *et al.*This study explores handcuff rotaxane complexes,[173] where two rylene diimides are positioned in a co-facial arrangement without the use of covalent or coordination bonds. A rotaxane is a supramolecular complex where a rod-like molecule is threaded through a wheel-like macrocyclic component, which is then 'locked' into place by bulky end groups which are located on the end of the rod-like component.[207] Yang *et al.* utilised the robust interaction bewteen a pilar-[5]-arene and an imidazolium group to provided a reliable method for forming a pseudo-rotaxane, resulting in the formation of a unique non-covalently bound dimer.[173] These non-covalently bound dimer are essentially 'handcuffed' in place by the interaction between the pilar-[5]-arene and the imidazolium end group, which is shown in Figure 4.2.

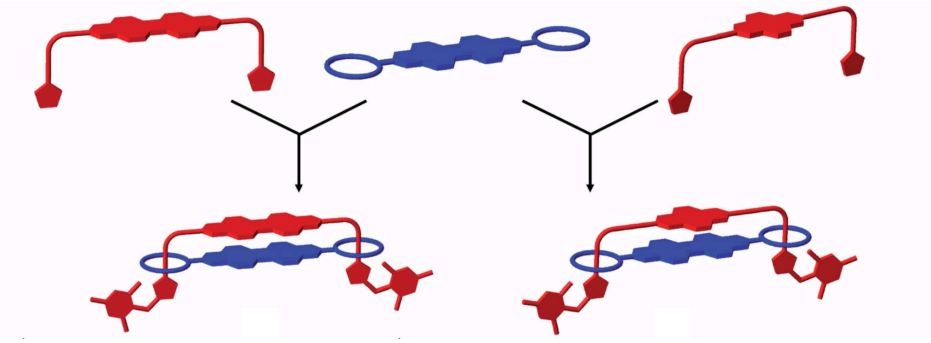


Figure 4.2: An illustration of the formation of the unique non-covalently bonded dimers that are handcuffed *via* a pseudo-rotaxane system. Reproduced from reference 173.

The synthesis of these non-covalently bound, handcuff complexes opened up an area of research that has yet to explored in the literature. The anionic and dianionic nature of these unique handcuff complexes was probed by Yang *et al.* using spectroelectrochemistry.[173] The monomer components and the two handcuff dimers were probed to determine both the UV-vis and the IR features for the anionic and dianionic specices. Being able to identify the spectroscopic features of the anionic and dianionic species is particularly helpful when investigating the photophysical properties. The IR spectra of the anionic and dianionic specices for the PDI monomer components and PDI handcuff dimer can be seen in Figure 4.3, with IR bands at *ca.* 1640, 1585 and 1530 cm^{-1} which are observed in all three of the complexes. The position of these IR bands for the $PDI^{-\bullet}$ species is comparable with other reports in the literature.[208]

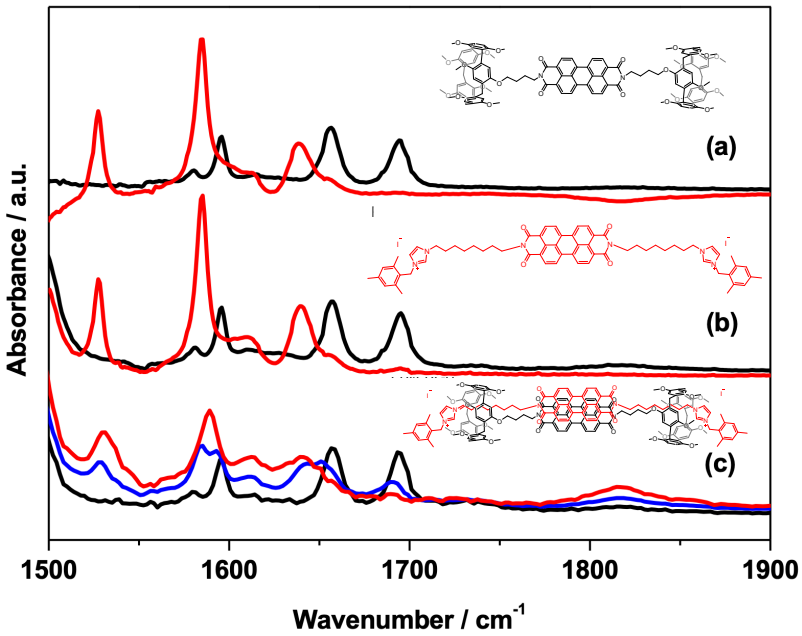


Figure 4.3: The IR spectra for the redox species of the two PDI monomer components (A & B) and PDI handcuff dimer (C) gained from the spectroelectrochemical investigations. The neutral spectrum is shown in black, the anionic species is shown in red and the dianionic species is shown in blue. Adapted from reference 173.

As well as the IR features, the UV-vis bands of the anionic and dianionic species were also determined using spectroelectrochemistry. The UV-vis band for the two PDI monomers clearly showed an absorption band at *ca.* 713 nm for the $PDI^{-\bullet}$ species, which exhibits a similar absorption to other PDI monomers.[196,209] The reported UV-vis of two unique handcuff complexes saw slightly different anionic and dianionic absorption bands than the monomeric components. The anionic and dianionic species of the two handcuff complexes can be seen in the UV-vis spectra in Figure 4.4, where for the PDI/PDI handcuff a broad band at *ca.* 615 nm is observed for the anionic species. The NDI/PDI handcuff has slightly different absorption bands, with the dianionic species exhibiting two broad band at *ca.* 470 and 610 -700 nm, which suggests there is both $PDI^{-\bullet}$ and $NDI^{-\bullet}$ character.[173] A dimer consisting of both a PDI and NDI unit has not be reported in the literature, therefore these spectroelectrochemical properties of this novel NDI/PDI handcuff prove very valuable for further photophyscial investigations.

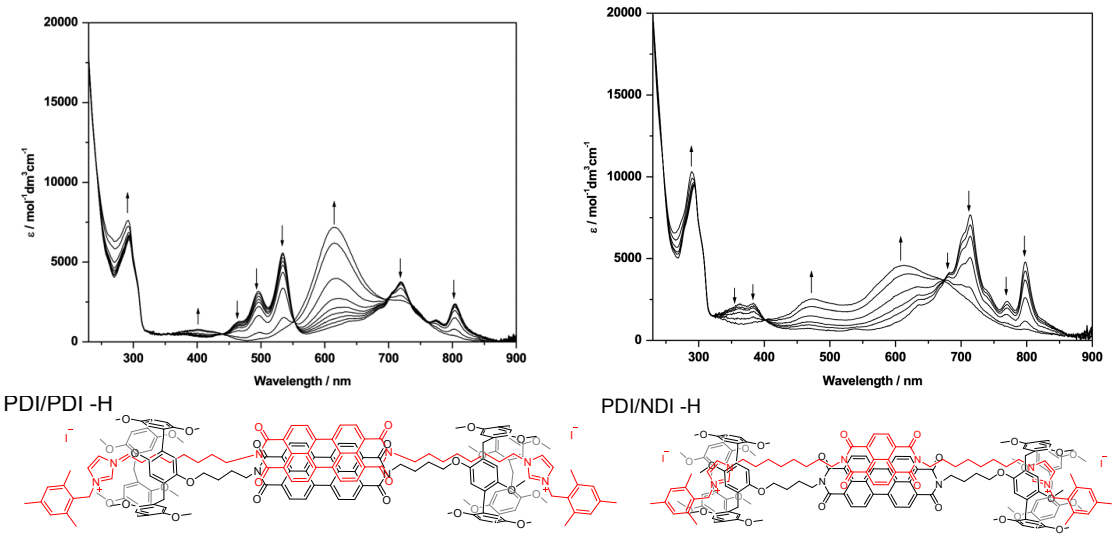


Figure 4.4: The UV-vis spectra for the redox species of the PDI/PDI handcuff complex (left) and PDI/NDI handcuff complex (right) gained from the spectroelectrochemical investigations. The left spectra shows the transition from the anionic to the dianionic species of the PDI/PDI handcuff complex. The right spectra shows the transition from the anionic to the dianionic species of PDI/NDI handcuff complex. Adapted from reference 173.

DFT calculations were also reported by Yang *et al.* for the monomer components and the two handcuff dimers. The DFT calculations investigated both the molecular dynamics and the calculated UV-vis spectra for the two handcuff complexes. The DFT calculations gave an insight into the nature of the transitions and the structural orientation. The reported nature of the dianionic tranisition of the PDI/PDI dimer indicated the broad band at 615 nm is the result of the dianionic species adopting a state in which an unpaired electron on each PDI unit, and the spin density is spread across both molecules.[173] Along with the DFT calculations and the spectroelectrochemistry, luminescence spectroscopy was conducted, which helped to identify the nature of this broad band observed in the UV-visible. The fluorescence measurement suggests that the broad band at an 615 nm for the PDI/PDI dimer was an excimer like state.[173,210] The DFT calculations for the dianionic tranisition of PDI/NDI dimer suggested that there is an unpaired electron located on both the PDI and the NDI unit, which sup-

ports the reported UV-vis spectra.[173] It was found that the two handcuff complexes are able to interact with one another but are not restricted in their geometries unlike other dimers which are held in place by the rigid covalent linkers.[173]

4.1.1 Photophysics of Perylene-3,4:9,10-bis(dicarboximide) Systems

More recently, PDI dimer molecules have been investigations with the aim of observing either singlet fission, excimer formation and charge transfer states which could potentially be used in photovoltaic devices.[165,166,204,211–213] The PDI dimer molecules that are most commonly reported in the literature are covalently linked cofacial stacked dimers linked at just one end of the molecule,[188,189,201,214,215] or less frequently being linked at both ends of the molecule.[179,212] PDI dimers and aggregates are known to have a low-lying electronic state, which is the result of the excitation energy being delocalised over multiple moieties of the PDI. This state is thought to localise on two PDIs resulting in the formation of an excimer state.[165,195,204,214,216,217] The formation of the excimer is very dependant on the stacking distance between the two PDI molecule including displacement both transversely and longitudinally.[165] One example of *ps*-TA spectroscopy being used to probe the formation of an excimer state was reported by Lefler *et al.*, where a slip-stacked dimer and the monomer component were probed.[166] Both the monomer and dimer complex were excited at 532 nm, where for the monomer complex a ^{1}PDI excited state was formed directly following excitation.[166] This ^{1}PDI excited state was seen to decay (τ = 3.7 ps) to form a long lived PDI$^{-\bullet}$ species with a sharp transient band located at *ca.* 700 nm, which is characteristics of a PDI$^{-\bullet}$ species.[196,209] The TA spectra for the monomer and the dimer can been seen in Figure 4.5. In contrast, the TA spectra for the dimer showed a broad tranisent band at

ca. 600 - 800 nm. Although a transient band which is thought to be ^{1}PDI excited state is observed at early time delays, it is seen to broaden by 60 ps. This broad ^{1}PDI excited state is indicative of cofacial dimers.[189,191,214,218] The long lived state observed does not show any clear indication of the formation of a $PDI^{-\bullet}$ species, instead the lifetime of this state (τ = 28 ns) correspond well with the time-resolved fluorsecence where an excimer like state was observed.[166]

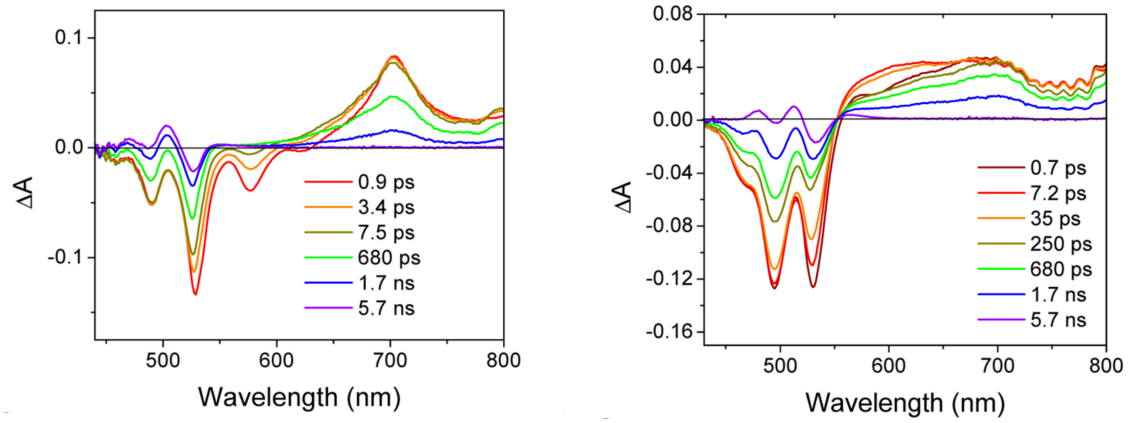


Figure 4.5: The TA spectra for a PDI monomer (left) and a slip-stacked PDI dimer (right) probed at 532 nm in CH_2Cl_2 reported by Lefler *et al.* which illustrates the formation of a $PDI^{-\bullet}$ species for the monomer and an excimer like state for the dimer. Reproduced from reference 166.

The excimer state of slip-stacked dimers has also been reported by Margulies *et al.* in which two different PDI dimers were probed, one of which is the slip-stacked dimer (Figure 4.7).[165] The authors investigated how the distance between the two PDI units affect the rate of formation of an excimer. Both dimers were probed following excitation at 530 nm in CH_2Cl_2, and was reported that following excitation of both dimers a ^{1}PDI excited state was populated, followed by the formation of an excimer state. Along with the formation the kinetic traces indicated that the excimer undergoes structural relaxation (τ = 24 ps),[165] which was in agreement with other excimer studies.[219] It was reported that the structural difference between the two dimers gave

rise to notable changes in the formation of the observed excimer state. The slip-stacked dimer, where there was a 4.3 Å shift along the PDI transition dipole axis, resulted in a slower formation of the excimer which was attributed to a decreased electronic coupling between the two PDI units.[165] The excimers formed had at a lifetime of 12 ns for the non slip-stacked dimer and 24 ns for the slip-stacked dimer respectively. These results indicated that PDI aggregates have a higher propensity to form an excimer state, thus inhibiting other excited state processes such as triplet formation or singlet fission.

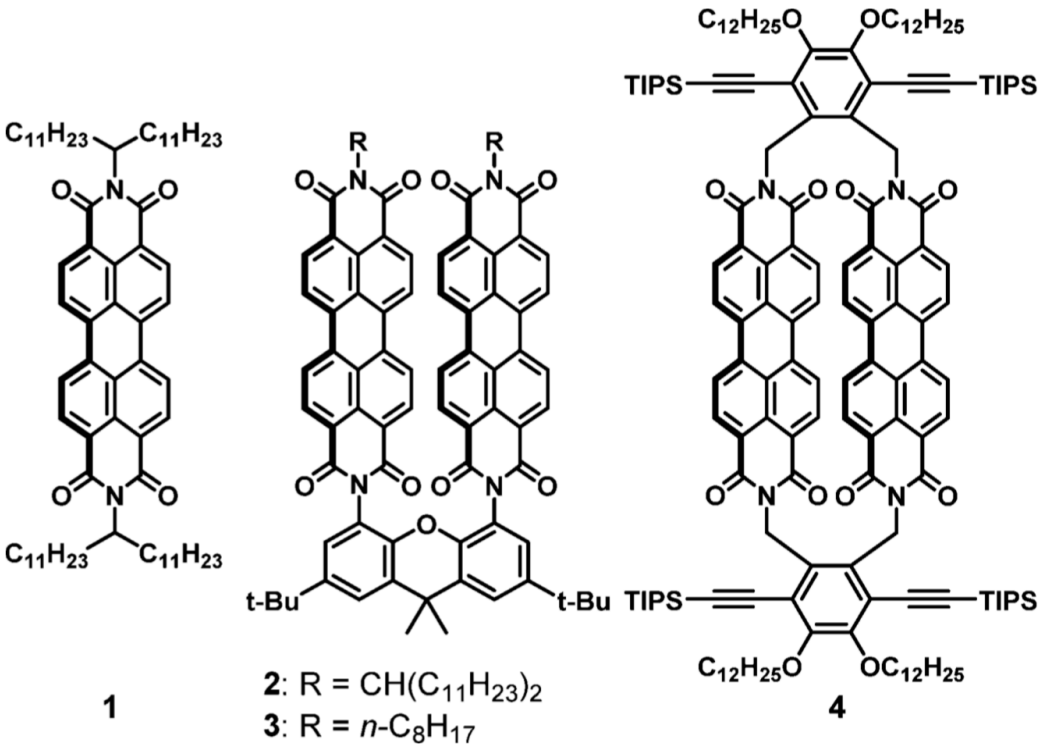


Figure 4.6: The structure of the PDI complexes Brown *et al.* reported which shows the varying rigidity of the PDI dimers probed at 525 nm. Reproduced from reference 212.

The formation of an excimer state of three different PDI dimers with varying rigidity was probed to see how the formation of the excimer is altered by the covalent bound nature of the dimer. Brown *et al.* looked at three dimers, two less rigid dimers

which were covalently bound at one end and one rigid dimer covalently bound at both ends,[212] as shown in Figure 4.6. All the dimer complexes were probed with *ps*-TA at 525 nm in toluene. The formation of an excimer was observed for all three dimers. The kinetic analysis of the three dimers provided information about the nature of the excimer formed. The rigid dimer that was covalently bound at both ends was significantly shorter lived, ($\tau = 2.5$ ns), compared to the other two dimers which had lifetimes of $\tau = 29$ ns and $\tau = 9$ ns respectively. It was proposed that the short lifetime of the rigid dimer was the result of destabilisation of the ground state, which resulted in enhanced internal conversion decreasing the excimer lifetime.[212] The two-step formation mechanism of the relaxed excimer, which has been reported previously,[165,219] was observed for both the dimers which are covalently bound at one end. The short rise component ($\tau = 2$ ps) was assigned to the initial formation of the excimer state, with the second component ($\tau = 14$ ps) being assigned to subsequent structural rearrangement of the excimer state.[212] Interestingly, for the rigid dimer only a monoexponential rise was observed. This suggested the population of the excimer state occurred during the experiment response time, and the short *ca.* 3-6 ps component observed is the result of the small degree of conformational relaxation required for the desired excimer geometry. The rigid nature of the dimer means that the PDI units are locked in an ideal geometry for excimer formation, therefore structural rearrangement is prohibited following the excimer formation.[212] The literature report of excimer formation in PDI dimers has predominately been probed using TA spectroscopy, which has shown that the position of the PDI units within the dimer, and the flexibility of the dimer can drastically alter the nature of the excimer formed.

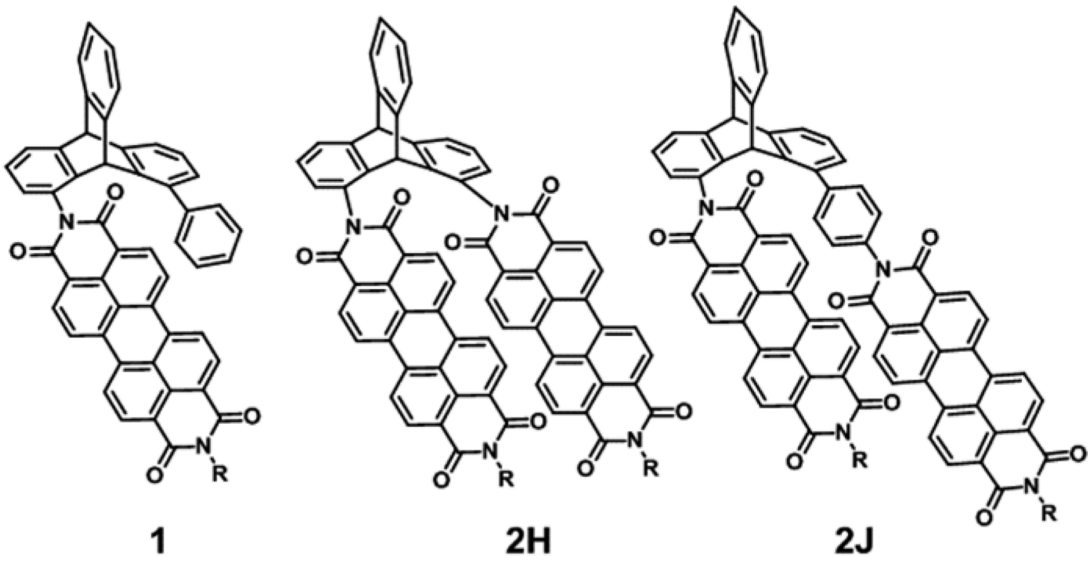


Figure 4.7: The structure of a PDI monomer (1), a PDI dimer (2H) and a slip-stacked dimer (2J) probed at 530 nm by Mauck *et al.* Reproduced from reference 211.

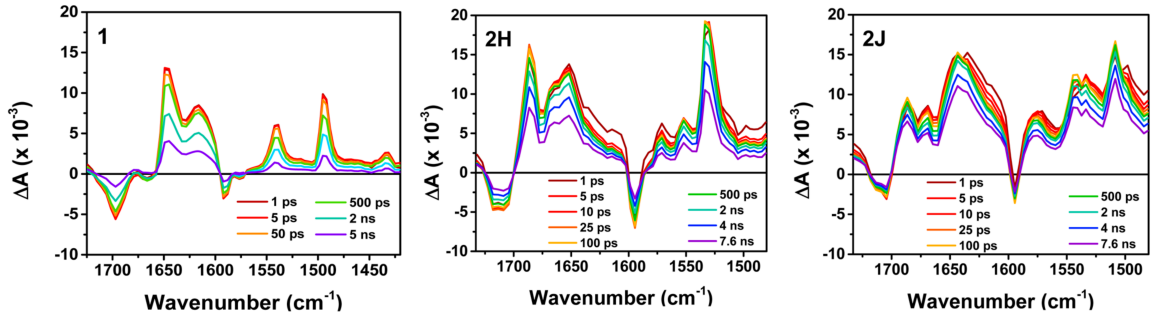


Figure 4.8: The TRIR spectra for a PDI monomer (1), a PDI dimer (2H) and a slip-stacked PDI dimer (2J) probed at 530 nm in CD_2Cl_2 reported by Mauck *et al.* which illustrates the formation of a ^{1}PDI excited state for the monomer (1) and an excimer like state for the dimers (2H and 2J). Reproduced from reference 211.

In more recent years, TRIR spectroscopy has been used to probe the photophysical properties of PDI monomers, dimers and PDI aggregates. The first TRIR investigation into the characterisation of excimer formation was reported in 2017 by Mauck *et al.*, where TRIR was used to probe a monomer and two PDI dimers,[211] which can be seen in Figure 4.7. The TA of these complexes was conducted by Margulies *et al.*

which has been discussed above.[165] The TRIR spectra for the three complexes is shown in Figure 4.8. For the PDI monomer (1), upon excitation transient bands at 1645, 1616, 1538, 1495 and 1433 cm^{-1} are observed and were assigned to the formation of a ^{1}PDI excited state, which was backed up by DFT calculations ^{1}PDI spectra.[211] The spectra for the two dimers (2H and 2J) indicated that the transient bands observed following excitation appear to be broader and shifted to higher energy in comparison to the spectra for the monomer. Global analysis of associated spectra is shown in Figure 4.9, where the blue shift of the transient bands of the dimers can be observed. The broadening of the C=O bands and the blue shift of the C=C bands are assigned to the formation of an excimer like state. The initial state is assigned to the hot unrelaxed excimer, with the second state being assigned to the relaxed excimer state. The lifetime of excimer observed for 2H (12 ns) and 2J (24 ns) supports the excimer lifetimes observed for the TA investigations of these complexes.[165]

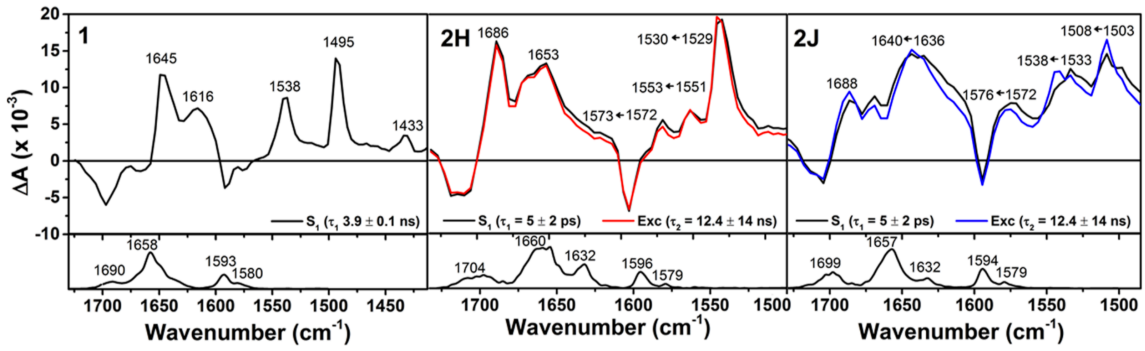


Figure 4.9: The species-associated spectra generated from global analysis of the TRIR data for the monomer (1), a PDI dimer (2H) and a slip-stacked PDI dimer (2J) excited at 530 nm reported by Mauck *et al.* Reproduced from reference 211.

Another TRIR investigation into the formation of excimer states in PDIs was reported by Kennehan *et al.*,[210] where the aggregation of PDI units was investigated by varying the concentration of the PDI monomers in solution. In crystalline films

PDI molecules can form strong π-π interaction can generally result in the formation of localised excimer states.[220–223] However, the excimer formation can be controlled by the geometric arrangements of the PDI molecules.[224,225] Kennehan *et al.* reported that by increasing the concentration of PDI monomers in solution from 0.5 mM to 95 mM excimer formation was observed. The photoluminescence was conducted at the varying concentration and can be seen in Figure 4.10. The emission band at low concentration is structured which broadened and red shifts as the concentration is increased. This shift and broadening in the emission band has been associated with excimer formation in PDI monomers.[166,214,226–228]

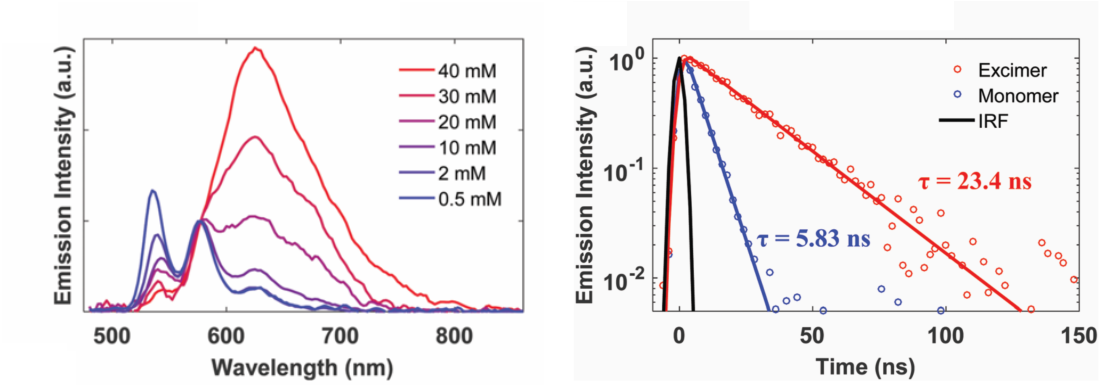


Figure 4.10: The photoluminescence spectra for a PDI monomer in chloroform at varying concentrations (left) and the photoluminescence decay of the monomer and excimer species. Reproduced from reference 210.

The TRIR spectra was probed at the varying concentrations, with the low concentration spectra (2 mM) exhibiting transient bands at 1645, 1502 and 1550 cm^{-1} that have a similar band profile and positions which are characteristic of a ^{1}PDI excited state.[211] In the higher concentration spectra (30 mM) two new vibrational features appear on the nanosecond timescale, which are assigned to the formation of an excimer state.[210] The vibrational features at 1525 and 1580 cm^{-1} do not appear in the 2 mM spectra but are observed in the 30 mM spectra, shown in Figure 4.11. This illustrated

that as the concentration is increased, the observation of an excimer is seen which matches the photoluminescence results.

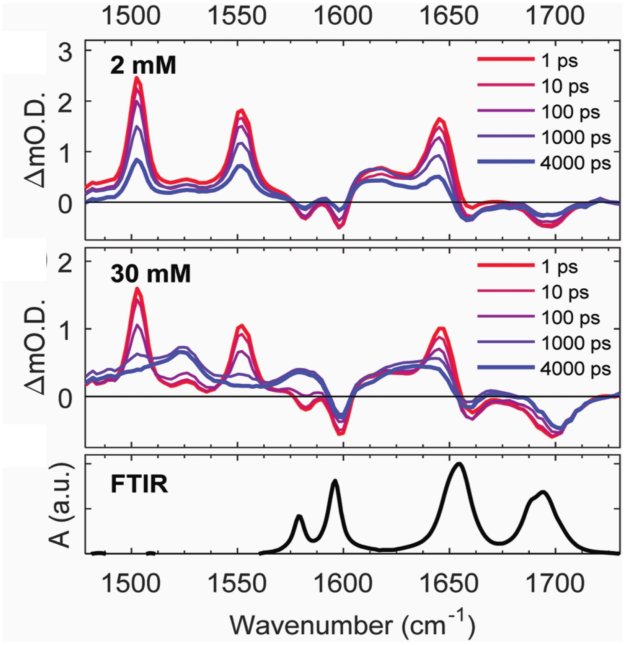


Figure 4.11: The TRIR spectra for a PDI monomer in chloroform at a low concentrations (top) and a higher concentration (middle). The FTIR spectrum of the PDI molecule in chloroform is shown for reference (bottom). Reproduced from reference 210.

The excimer formation at an increased concentration can be further supported by focusing on the vibrational feature at 1525 cm^{-1}. The concentration dependence of the band at 1525 cm^{-1} at varying concentrations of 2 mM to 40 mM is shown in Figure 4.12. There is no observation of a dimer excited state in the 2 mM spectra, only the monomeric excited state at 1502 and 1550 cm^{-1}. However, when the concentration is increased to 40 mM the dimer excited state assigned to the excimer is observed at 1525 cm^{-1}. The decay of the 1502 cm^{-1} band can be linked to the growth of the excimer band at 1525 cm^{-1} as the concentration is increased.

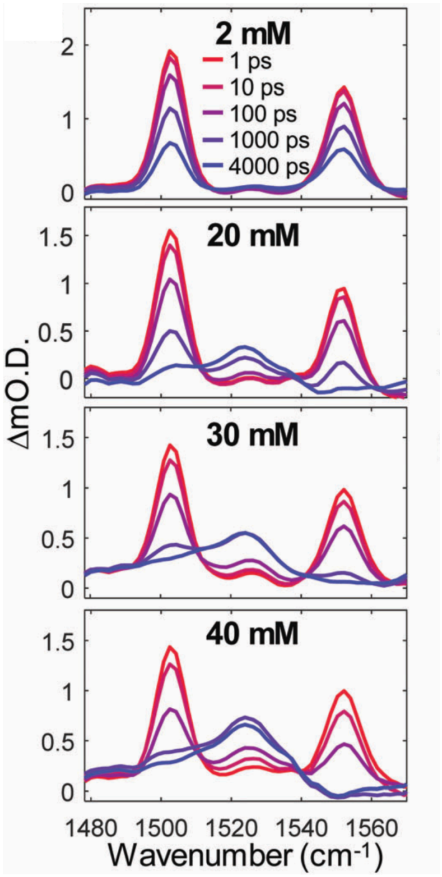


Figure 4.12: The TRIR spectra of the C=C mode of PDI monomer in chloroform at varying concentrations from 2 nM to 40 nM, which shows the growth of the excimer excited state at 1525 cm^{-1}. Reproduced from reference 210.

The formation of an excimer state is not the only photophysical property of PDI dimers and aggregates that has been reported in the literature. The observation of charge separation states following charge transfer (CT) has also been reported.[196,208] It has been shown that if an electron rich group is substituted directly onto the PDI core, CT is observed from the electron rich substituent onto the PDI core. Rybtchinski *et al.* reported that upon excitation at 400 nm, a ^{1}PDI excited state is formed which is seen to decay following CT to form a $PDI^{-\bullet}$ species.[196] The formation of the charge separated state was very fast, > 1ps, with the transient absorption of a $PDI^{-\bullet}$ species observed in the TA spectra.[196] This quenching of a ^{1}PDI excited state by CT transfer

has also be reported by Brown *et al.* where both TA and femtosecond stimulated raman spectroscopy (FSRS) was used to probe the charge separated state.[208] It was reported that when a PDI monomer with an electron rich substituent was excited at 525 nm, an initial ^{1}PDI excited state was also observed. This ^{1}PDI excited state was quenched by CT from the electron rich substituent, to form a charge separated state within 6 ps. Both the TA and the FSRS of the charged separated species indicated the formation of a $PDI^{-\bullet}$ species, with raman bands at 1544 and 1588 cm^{-1} which are unique to the radical anion of $PDI^{-\bullet}$.[208]

The literature reports of PDI monomers, dimers and aggregates have shown that by probing the photophysical properties with a range of time-resolved techniques can help identify the different formation decay pathways of the excited state.

4.1.2 Photophysics of 1,4,5,8-Naphthalene Diimides Complexes

Another group of chromophores which has attracted attention in the literature is derivatives of 1,4,5,8-naphthalene diimides (NDIs).[229–233] NDIs have been utilised for the studies of electron-transfer processes,[234–238] fluorescent dyes,[239–244] molecular probes and supramolecular assemblies.[245–249] The photophysical and electrochemical properties of NDIs have been reported in the literature,[250–254] which has focused on the excited-state nature of the NDI radical anions.[209] A study by Green *et al.* focused on investigating the photophysical properties by measuring the fluorescence and phosphorescence.[255] The authors attempted to calculate both the singlet and triplet energy levels from the fluorescence and phosphorescence, however the fluorescence was too short to be measured by the equipment and therefore attributed to a short lived singlet that undergoes fast depopulation *via* intersystem crossing with a lifetime of $<$20 ps.[255]

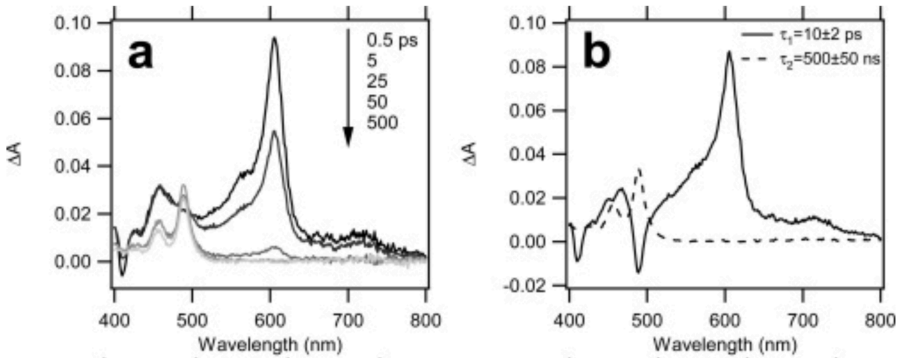


Figure 4.13: The time-resolved *fs*-TA spectra (a) and the decay associated difference spectra (b) of a NDI derivative reported by Ganesan *et al.* illustrating the formation of a ^{1}NDI excited state. Reproduced from reference 254.

Despite the fact the triplet state and radical anion formation of NDIs complex had been thoroughly reported,[209,250,255,256] prior to 2007 the singlet state dynamics of NDIs had not been observed, other than the fact it had been measured to be <20 ps.[255] Ganesan *et al.* used femtosecond time-resolved techniques to probe the singlet state dynamics of NDIs.[254] Using femtosecond TA spectroscopy, the absorption spectra and lifetime (10 ps) of the electronically excited singlet state was determined, as shown in Figure 4.13.[254] Ganesan *et al.* studied three different NDI derivatives, and found for a symmetrically substituted NDI, the excited singlet state absorption was observed at *ca.* 600 nm with a lifetime of 10 (± 2) ps. This singlet excited state was seen to decay to the ground state *via* efficient intersystem crossing.[254] The other NDI derivatives that had different subsituents on the imide nitrogen resulted in a different decay pathway, shown in Figure 4.14, where the decay of the ^{1}NDI to the ^{3}NDI went *via* a intramolecular CT state. The population of this CT state drastically reduced the lifetime of the ^{1}NDI excited state from 10 ps to *ca.* 0.4 ps.[254] This demonstrates how the photophysical properties of an NDI complex can be tuned by simply altering the subsituents on the imide nitrogen position.

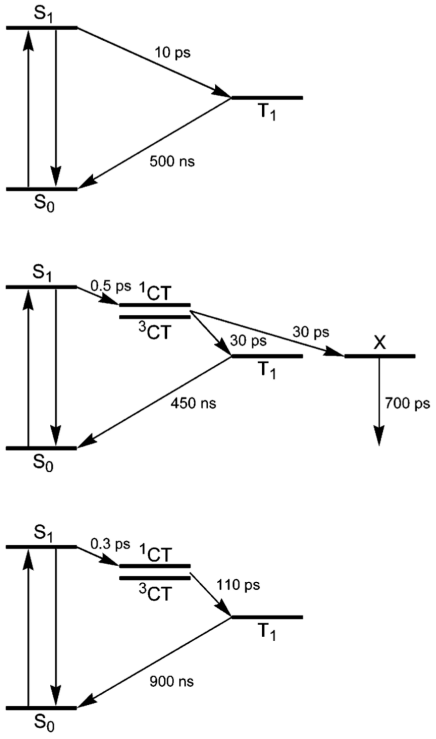


Figure 4.14: The energy level diagrams proposed for the excited state dynamics of three NDI derivatives reported by Ganesan *et al.* where upon changing the subsituent can alter the decay pathway of the ^{1}NDI excited state. Reproduced from reference 254.

As well as TA spectroscopy, TRIR spectroscopy has also been utilised to probe a NDI unit. A study by Sazanovich *et al.* reported the first IR signature bands of a ^{3}NDI state as well as the IR bands for a ^{1}NDI species.[257] The study focused on a NDI unit bound to a Pt(II) diimine complex, and it was shown that upon excitation at 395 nm, both the excited state on the Pt(II) centre and the NDI unit were observed in the *ps*-TRIR and *ps*-TA spectra. Upon excitation the ^{1}NDI excited state was populated, with transient absorption bands at *ca.* 470 and 600 nm being observed with a lifetime of 0.9 ps. The band position is indicative of a ^{1}NDI excited state.[254] This ^{1}NDI excited state was also observed in the *ps*-TRIR spectra with bands within the region of 1500 to 1680 cm^{-1}, however this region was also over lapped with the excitation of the ^{1}MLCT state so it was difficult to assign exact IR bands for the ^{1}NDI excited state.

This ^{1}NDI excited state was then seen to undergo inter-system crossing to form a ^{3}NDI excited state, where two unique IR tranisent bands were observed in the *ps*-TRIR spectra at 1607 and 1647 cm^{-1}. This was the first reported observation of a ^{3}NDI excited state using TRIR spectroscopy, which shows how utilising both TA and TRIR spectroscopy is important when probing the photophysical properties of these NDI systems. The investigations conducted by Sazanovich *et al.* and Ganesan *et al.* highlight that the decay process of an ^{1}NDI excited state can be altered depending on the bound substituents which further supports the need for both TA and TRIR spectroscopy.

4.2 Aims

The aims for this Chapter is to investigate the nature of the excited states of some novel perylene diimide (PDI) and naphthalene diimide (NDI) complexes to further understand their photophysical properties. The work within this Chapter focuses on PDI and NDI momomers, two unique non-covalently bound PDI/PDI and PDI/NDI dimers, and a PDI rotaxane complex. The complexes that will be discussed can be seen in Figure 4.15. All the complexes discussed within this Chapter were synthesised and characterised by members of the Champness group here in Nottingham.

The complexes of particular interest are the two non-covalently bound PDI/PDI and PDI/NDI dimers, and the PDI rotaxane complex. The PDI/PDI and PDI/NDI dimers utilises a rotaxanes structure where each end of dimer is 'handcuffed' in position by two different substituent groups on the PDI molecules. It is this interaction between the two different substituent which holds the two units in place forming a non-covalently bound dimer. The other PDI rotaxane complex is a more traditional rotaxane structure with a pillar-[5]-arene 'wheel' situatiated on the alkyl chain 'rod' which sits between the PDI core and the end imidizole substituent which 'locks' in place. Using transient absorption (TA) and time resolved infrared (TRIR) on the picosecond timescale, the photophysics of these unique complexes has been investigated. The electrochemistry, spectroelectrochemistry and photoluminescence were run on these complexes by Dr Stephen Davies and Dr Philipp Langer here at Nottingham, which will be mentioned to help support the observations seen in both the TRIR and TA spectra.[173]

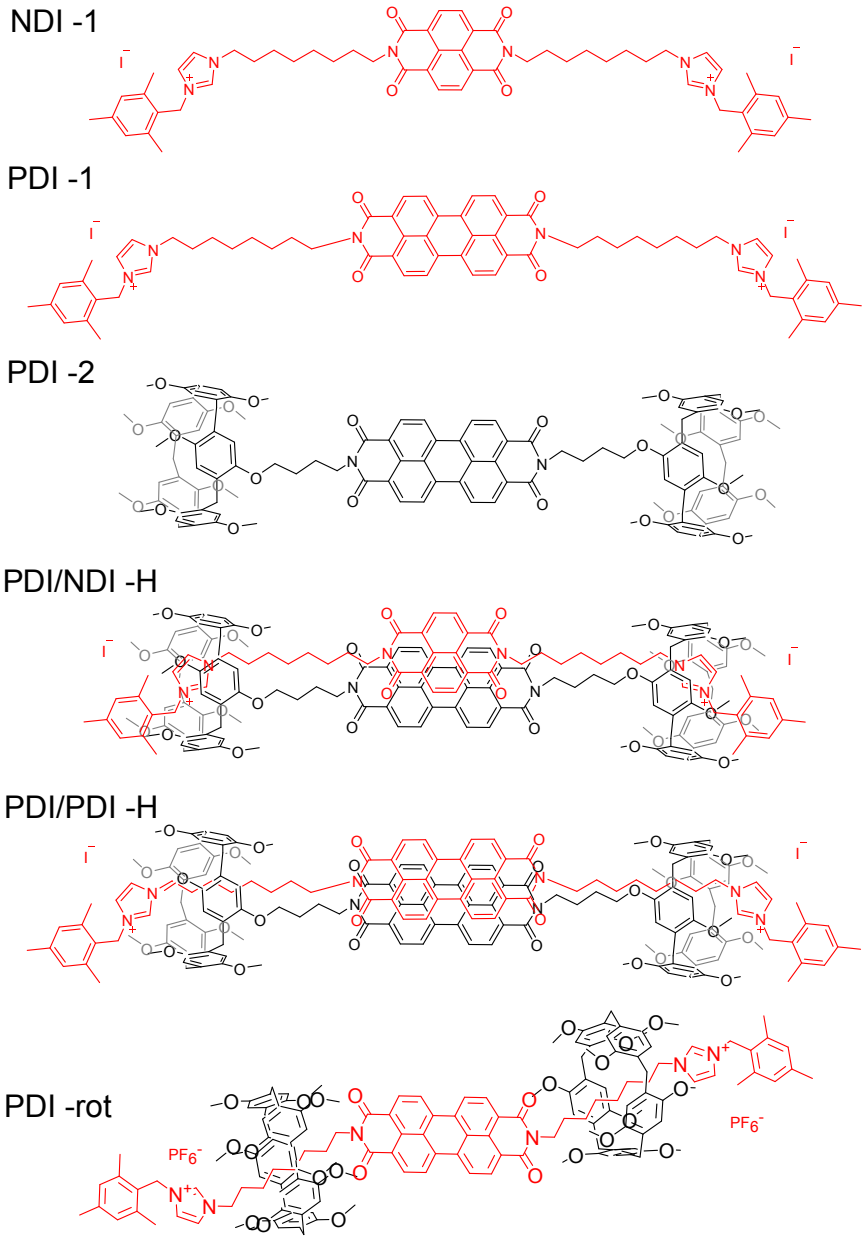


Figure 4.15: The structure of a complexes that are investiagted within this Chapter where PDI-1, PDI-2, NDI-1 are the monomers, PDIPDI-H and PDI/NDI-H are the unbound dimer handcuff complexes and PDI-rot is the rotaxane complex.

4.3 Results

This Chapter will investigates the photophysics and photochemistry of previously unreported PDI and NDI monomers, two unique PDI/PDI and PDI/NDI non-covalently bound dimers, which are 'handcuffed' together and a PDI rotaxane molecule. The synthesis of the PDI and NDI monomers and the 'handcuff' complexes was conducted by Lixu Yang and Philipp Langer. This Chapter will focus on the photophysics of these complexes which has been probed using both *ps*-TRIR and *ps*-TA.

4.3.1 Ground State Spectra of the PDI and NDI Monomers and PDI and NDI Handcuff Complexes

The ground state spectra for PDI and NDI monomers was investigated initially followed by the non-covalently bound handcuff complexes. The absorption spectra for both **PDI-1** and **PDI-2**, show that the lowest energy vibronic transition (0-0) is at 525 nm with the higher energy transitions (0-1) and (0-2) at 488 and 457 nm respectively. The absorption spectra for **PDI-1** and **PDI-2**, shown in Figure 4.16, is consistent with previous reports in the literature for similar monomeric PDI complexes.[165,166,200,212]

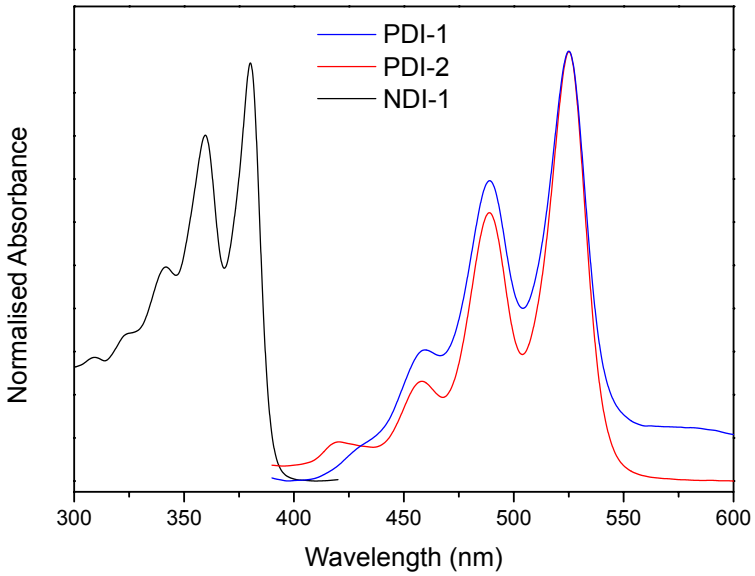


Figure 4.16: The absorption spectra for **PDI-1** (blue), **PDI-2** (red) and **NDI-1** in CH_2Cl_2.

The transitions for **NDI-1** sit at higher energy compared to **PDI-1** and **PDI-2**, shown in Figure 4.16. The absorption spectrum observed for the NDI monomer is comparable with what is reported in the literature,[247,254,258,259] with the lowest energy vibronic transition (0-0) at 380 nm, the higher energy transitions (0-1) and (0-2) at 360 and 340 nm respectively. From the ground state absorption spectra for **NDI-1**, **PDI-1** and **PDI-2** it can be clearly seen that different excitation wavelengths are needed to excite into the PDI unit and the NDI unit. With this in mind, the PDI monomers were excited at 520 nm and the NDI monomer was excited with a 380 nm excitation wavelength.

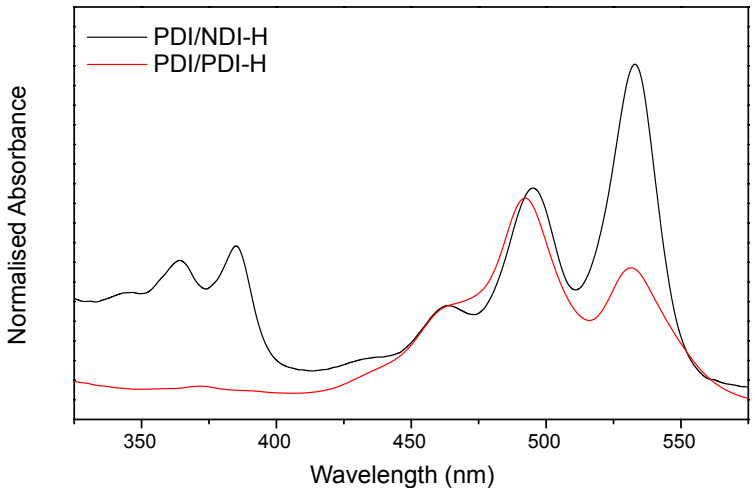


Figure 4.17: The absorption spectra for **PDI/NDI-H** and **PDI/PDI-H** in CH_2Cl_2.

The absorption spectrum for **PDI/PDI-H** can be seen in Figure 4.17, where the enhanced electronic coupling of **PDI/PDI-H** leads to a slight red shift in energy as well as a change in the vibronic band-intensity relative to **PDI-1** and **PDI-2**. This observed red shift shows a change of the vibrational bands to 531, 491 and 462 nm, which is consistent with **PDI/PDI-H** having an in-line transition dipole.[260] As well as an in-line dipole, the inversion of the (0-0) and (0-1) intensities was also observed, which is consistent with what has previously been observed for other PDI dimers.[213] The inversion of the (0-0) and (0-1) intensities has been shown using high level electronic-structure calculations, where the inversion of the (0-0) and (0-1) band ratio is a result of electronic distortions due to strong π overlap of the two PDI cores and contributions from charger transfer states.[224] The absorption spectrum for **PDI/NDI-H** does not show the inversion of the (0-0) and (0-1) intensities, which is most likely due to the fact there is not a strong π overlap between the NDI and PDI cores. The absorption spectrum for **PDI/NDI-H** shows both the transitions for the PDI and NDI cores with the PDI core at 533, 495 and 462 nm and the NDI core at 384, 364 and 343 nm. The transitions observed for **PDI/NDI-H** have also red

shifted relative to the monomers **NDI-1** and **PDI-2**, suggesting there is an in-line dipole which is expected considering it is a dimer.[260]

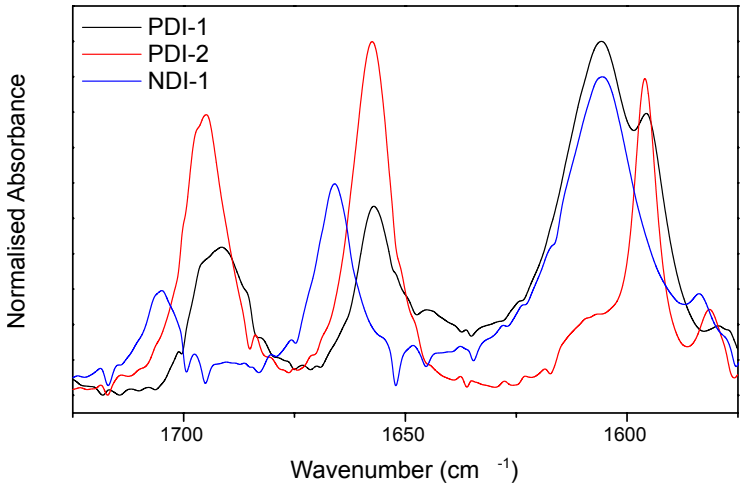


Figure 4.18: The FTIR spectrum for **PDI-1**, **PDI-2** and **NDI-1** in CH_2Cl_2.

The FTIR for the three monomers **PDI-1**, **PDI-2** and **NDI-1** can be seen in Figure 4.18. The C=O stretching frequencies for **PDI-1** and **PDI-2** are comparable with one another considering they both are carbonyl groups on a PDI unit, with the C=O stretching frequencies for **NDI-1** sitting at lower energy. The C=C stretching frequencies for **PDI-1**, **PDI-2** and **NDI-1** show more unique differences which can help distinguish them. The broad band at 1606 cm^{-1} can be seen for **PDI-1** and **NDI-1** but not for **PDI-2**, which suggests this band could be the C=C stretches from the imidazole substituent.

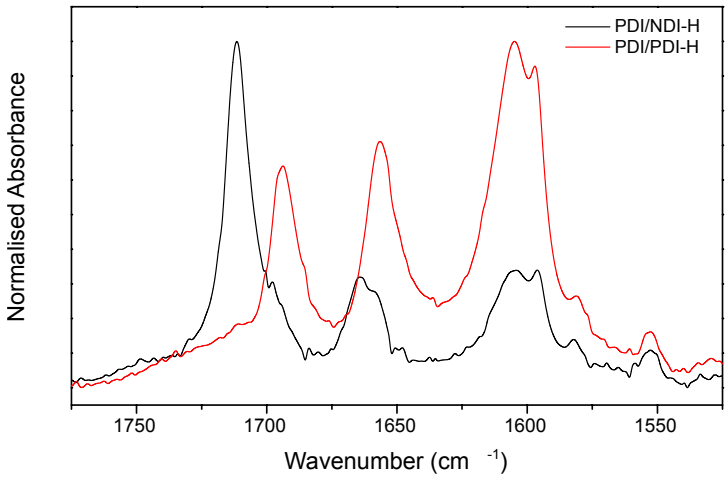


Figure 4.19: The ground state FTIR spectrum for **PDI/NDI-H** and **PDI/PDI-H** in CH_2Cl_2.

The FTIR of the **PDI/NDI-H** and **PDI/PDI-H** handcuff complexes still have the characteristic C=O stretches observed from the monomer PDI and NDI counterparts. There is a slight difference in the band position from **PDI/NDI-H** and **PDI/PDI-H** which is expected as the **PDI/NDI-H** has both C=O stretches from both the NDI and PDI unit. The C=C stretches also show similarities to the monomers, the broad band at *ca.* 1600 cm^{-1} observed for **PDI-1** and **NDI-1** and the sharper band at *ca.* 1580 cm^{-1} indicative of the **PDI-2** monomer.

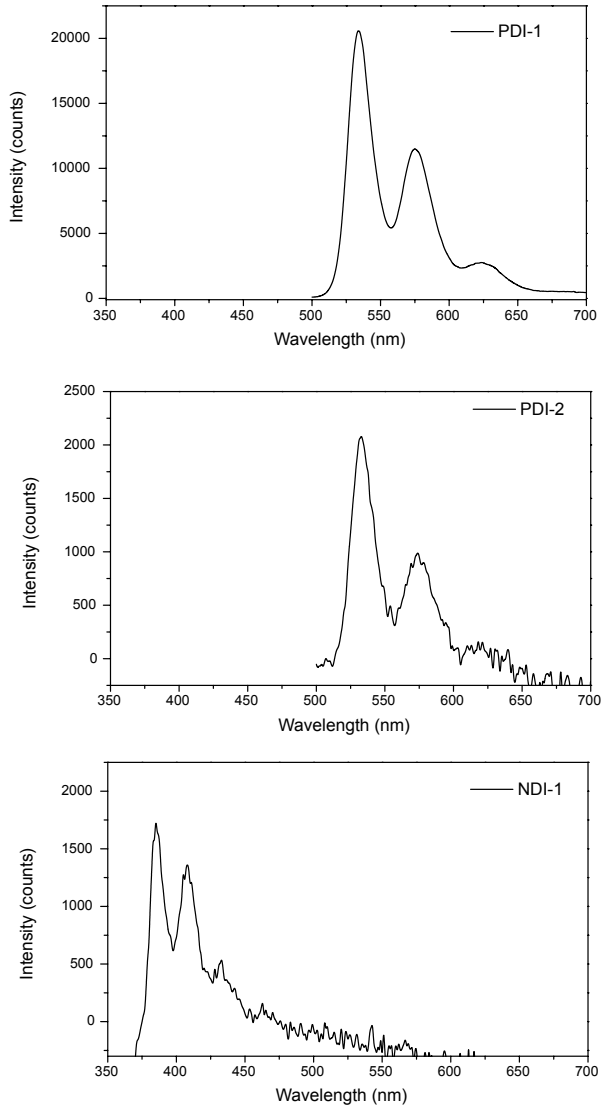


Figure 4.20: The emission spectra of **PDI-1**(top), **PDI-2** (middle) and **NDI-1** (bottom) in $CHCl_3$. The compounds were excited at λ_{em} 490, 485 and 360 nm respectively.

The photoluminescence for all the complexes was run by Dr Stephen Davies, and showed that the monomers, **PDI-1**, **PDI-2** and **NDI-1**, all exhibited structured emission which is consistent for PDI and NDI monomers.[210,254] The emission for the three monomers is shown in Figure 4.20. The most intense emission was seen for **PDI-1**, with a quenched emission being observed for **PDI-2** which could be a result of the

substituents on the PDI monomers. The emission band for **NDI-1** has a weak intensity but shows the correct band profile that is expected for a NDI monomer.[254] A strong emission is not expected for NDI monomers due to the efficient triplet quenching process that can occur.[261]

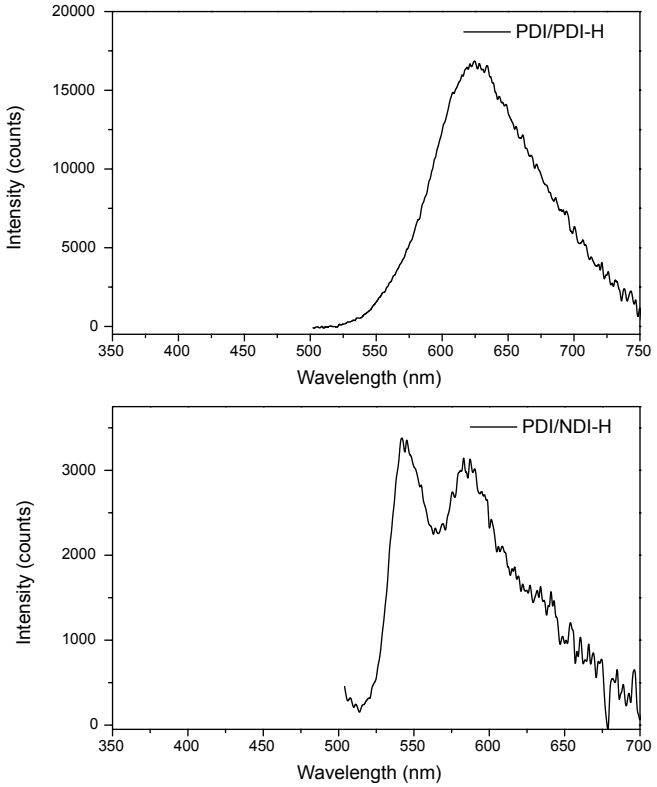


Figure 4.21: The emission spectrum for **PDI/PDI-H** (top) and **PDI/NDI-H** (bottom) excited at 490 nm in CH_2Cl_2.

The photoluminescence for the non-covalently bound handcuff complexes, **PDI/PDI-H** and **PDI/NDI-H**, showed very different emissive behaviour. The emission for **PDI/PDI-H** is broad, whereas the emission for **PDI/NDI-H** is structured. The observation of a PDI giving a broad emission has been reported by Kennehan *et al.*,[210] where close lying PDI units that pack together exhibit the formation of an excimer. The photoluminescence of this excimer was broad and sat at lower energy compared

to the structure emission of non-packed PDI.[210] This broad emission band observed for **PDI/PDI-H** is consistent with the formation of an excimer. In contrast, the emission for **PDI/NDI-H** is structured and appears to have a similar emission to the PDI monomers, suggesting the excited state is based on the PDI unit rather than spread across both unit like seen for **PDI/PDI-H**.

4.3.2 Time Resolved Investigation of the PDI and NDI Monomers

The PDI and NDI monomers were probed with *ps*-TRIR and *ps*-TA to help elucidate their photophysical properties. All the experiments mentioned in this section were run at Rutherford Appleton Laboratories. The monomer complexes were probed at 520 or 380 nm depending on the core unit of the complexes. The PDI based complexes were excited at 520 nm, with **NDI-1** being excited at 380 nm.

4.3.2.1 Time Resolved Study of a PDI-1 at 520 nm

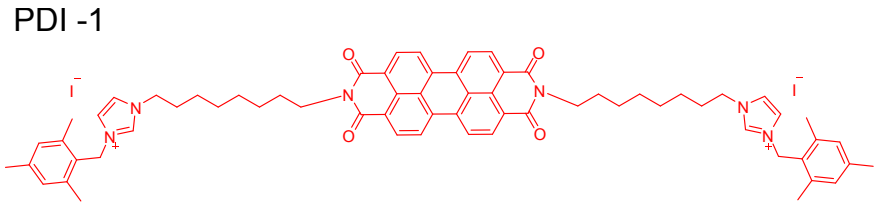


Figure 4.22: The structure of **PDI-1** which was probe at 520 nm in CH_2Cl_2 with *ps*-TRIR and *ps*-TA.

The first PDI monomer that was proved was **PDI-1**, which can be seen in Figure 4.22. The *ps*-TRIR spectra of **PDI-1** is shown in Figure 4.23, where parent bleaches are observed at 1696, 1660 and 1597 cm^{-1}, with transient peaks growing in at 1647, 1623, 1550 and 1505 cm^{-1} following excitation. The position of the transient bands are consistent with a singlet excited state on the PDI unit, resulting in the formation of a ^{1}PDI, which correspond with what has been reported for a PDI monomer.[211,262] The transient bands are long-lived on the picosecond timescale, with bands still observed at 500 ps.

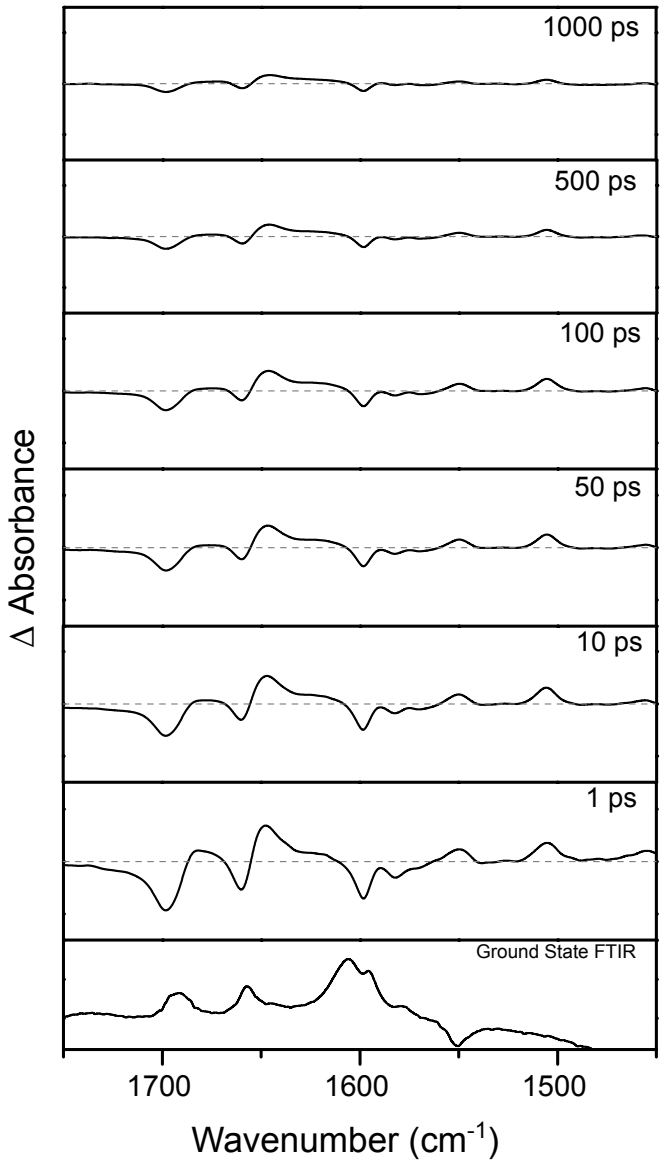


Figure 4.23: The *ps*-TRIR spectra of **PDI-1** in CH_2Cl_2 at a number of time-delays after photoexcitation at 520 nm.

The kinetic information obtained from the *ps*-TRIR showed two processes occurring, the first was a shorted lived (τ_1 = 7 ps) and the second was longer lived (*ca.* τ_2 = 390 ps) and is seen to decay away by the end of the experiment. The first process

can be assigned as vibrational cooling of the hot state following the initial excitation, and the second process is assigned as the decay of the ^{1}PDI excited state. The kinetic plot for the decay of the ^{1}PDI excited state of **PDI-1** in Figure 4.24 shows the decay of the ^{1}PDI excited state and the recovery of the parent bands. The lifetime of ^{1}PDI excited state is much shorter than other PDI monomers reported in literature (τ = 2 ns).[262] This decrease in lifetime could be attributed to the nature of the charged imidazole substituent on the monomer, which is quenching the ^{1}PDI excited state of the monomer resulting in a shortened ^{1}PDI excited state lifetime.

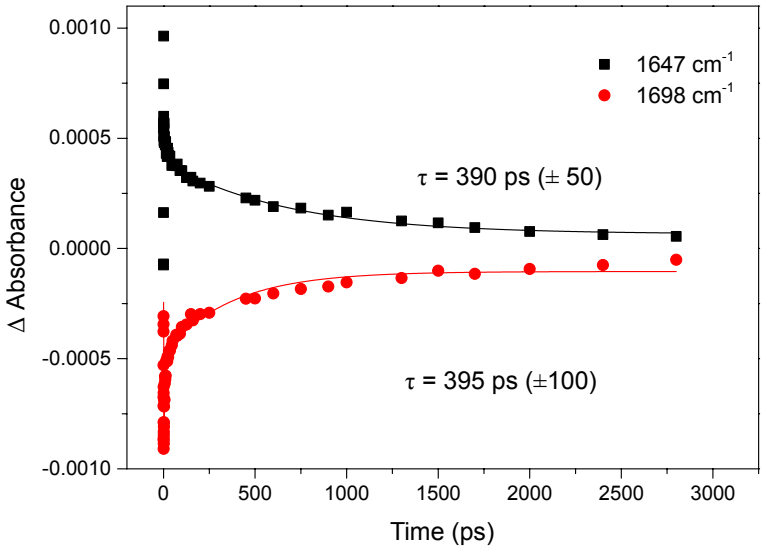


Figure 4.24: The kinetic plot for the decay of the ^{1}PDI excited state of **PDI-1** which was generated following the photoexcitation at 520 nm in CH_2Cl_2.

The *ps*-TA spectra for monomer **PDI-1** is shown in Figure 4.25, where the bleach of the ground state is observed at 534 and 464 nm, and the photoinduced excited state at 752 and 942 nm. The photoinduced excited state bands observed for **PDI-1** are very similar to a ^{1}PDI excited states reported in the literature.[165,166,203–206,212,263] The excited state band in the visible region is narrow, which is characteristic of the

formation of a ^{1}PDI excited state.[165,166,212] The small band in the NIR at *ca.* 940 nm is also indicative of a ^{1}PDI excited state.[212] The formation of a ^{1}PDI excited state is consistent with the observations seen in the *ps*-TRIR for **PDI-1**.

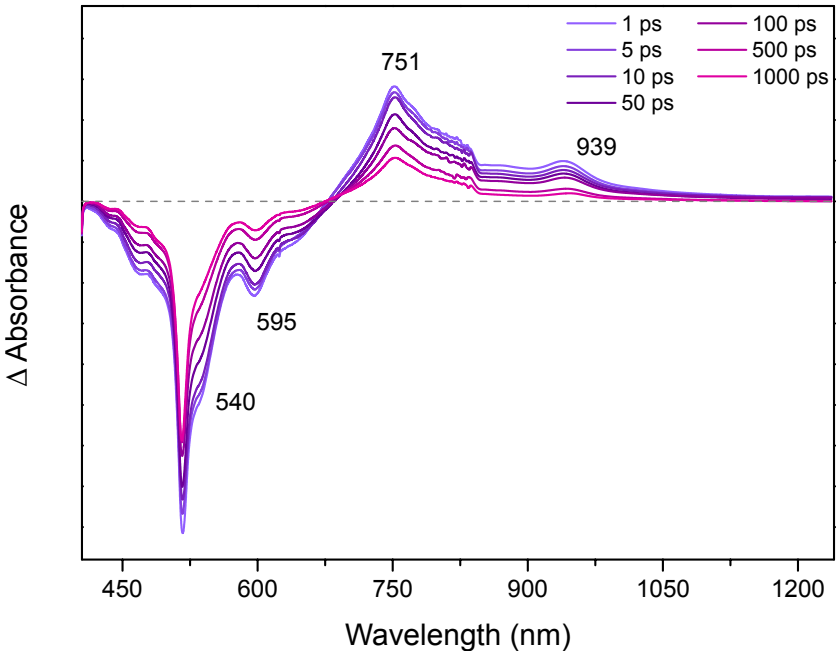


Figure 4.25: The picosecond transient absorption spectra of **PDI-1** in CH_2Cl_2 at a number of time delays after photoexcitation at 520 nm.

The kinetic fits of the bands at 752 and 942 nm indicate that there are two processes occurring. The first process, which has been attributed to a solvent relaxation, occurs with a lifetime of τ_1 = 19 ps (± 9),[206] while the second is the decay of the ^{1}PDI excited state, with τ_2 = 625 ps (± 65). The excited state of **PDI-1** is significantly longer lived than that PDI monomer reported in the literature,[165,166,203–206,212,263] with this trend also being observed in the *ps*-TRIR. The charged nature of the imidazolium group could be having an affect on the excited state of **PDI-1**, as it is shorter lived than other reported PDI monomers.[166,204,206,212] Electron rich substituents have been

reported to quench an excited state,[196,198] therefore it is feasible the imidazolium group is having a similar effect.

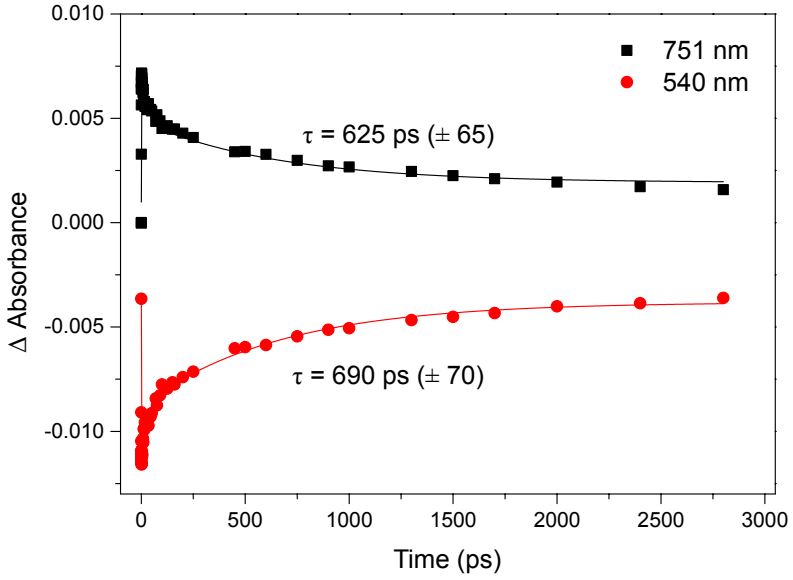


Figure 4.26: The kinetic plot for the decay of the ^{1}PDI excited state of **PDI-1** which was generated following the photoexcitation at 520 nm in CH_2Cl_2.

4.3.2.2 Time Resolved Study of a PDI-2 at 520 nm

The next monomer that was probed was **PDI-2**, which comprises of the same backbone as **PDI-1** with the only difference being the substituent on the end of the alkyl chain being a pilar-[5]-arene ring instead of a imidazolium group. The structure of **PDI-2** can be seen in Figure 4.27.

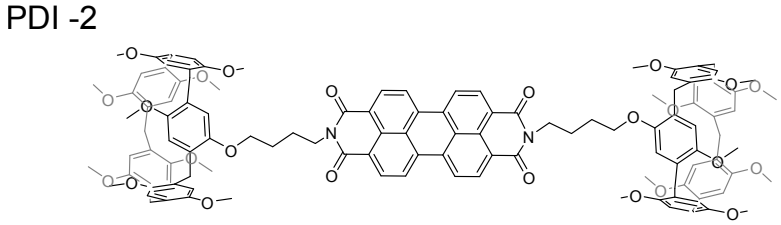


Figure 4.27: The structure of **PDI-2** which was probe at 520 nm in CH_2Cl_2 with *ps*-TRIR and *ps*-TA.

The *ps*-TRIR spectra for **PDI-2** can be seen in Figure 4.28, with parents bleaches at 1698, 1660 and 1598 cm^{-1}. The transient bands for the excited state are observed at 1645, 1619, 1550 and 1504 cm^{-1}, which are also consistent with a PDI monomer reported in literature,[211,262] with addition peaks at 1587, 1529 and 1456 cm^{-1}, which have not previously been observed for an excited state of a PDI monomer. The position of these bands are however consistent with the $PDI^{-\bullet}$ species of this complex,[173] however this can not be confirmed from just the *ps*-TRIR spectra. It is possible that these peaks are a result of the pillar-[5]-arene substituent on the monomer, which are contributing to the excited state spectra. The position of the excited bands are consistent with a ^{1}PDI excited state, similar to **PDI-1**. From the 500 ps time delay in the *ps*-TRIR spectra of **PDI-2**, its is clear the ^{1}PDI excited state has fully decayed and the parent has recovered, suggesting the ^{1}PDI excited state of **PDI-2** is shorter lived than for **PDI-1**.

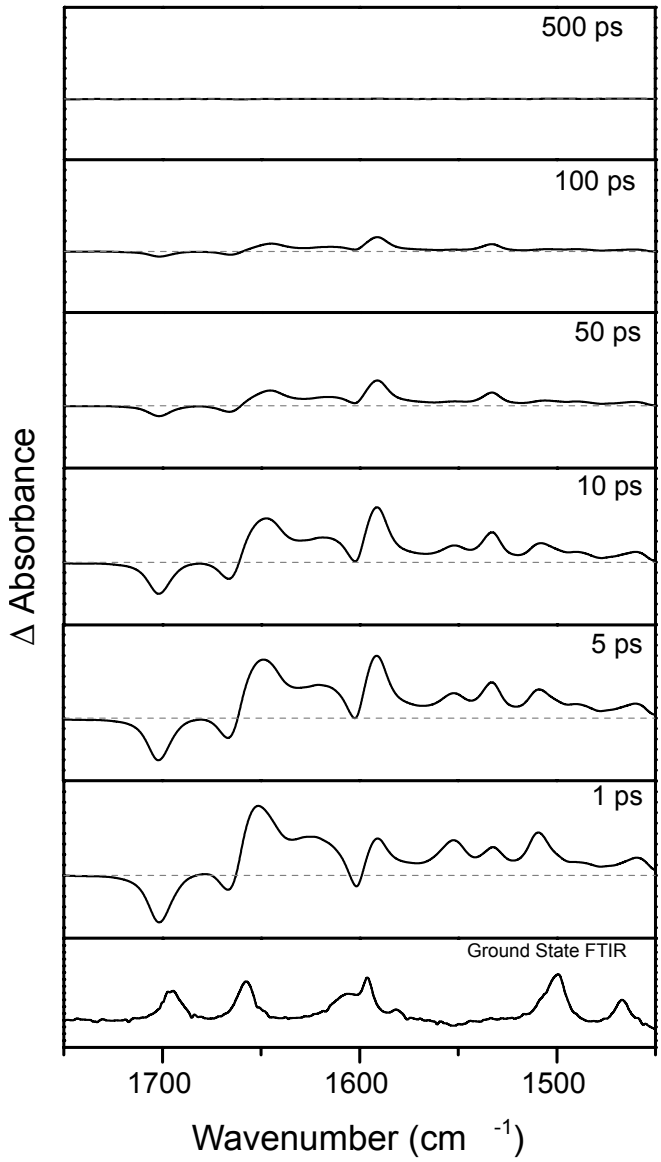


Figure 4.28: The *ps*-TRIR spectra of **PDI-2** in CH_2Cl_2 at a number of time-delays after photoexcitation at 520 nm.

When kinetics are fitted, a two state process it observed, similar to the *ps*-TA for **PDI-2**, with lifetimes of τ_1 = 16 ps (± 6) and τ_2 = 70 ps (± 20). The first state observed can be assigned to the cooling of the vibrationally hot state, with the

second longer lived state being a short lived ^{1}PDI excited state. The excited state of **PDI-2** is shorter lived than the excited state of **PDI-1**, and is much shorter lived compared to what is usually observed for a PDI monomer.[262] It has been reported that the presence of an electron rich substituent, like alkoxyphenyl, can decrease the quantum yield to <5 %,[196,198] thus the pillar-[5]-arene substituent could be responsible for this shortened lifetime being observed. This quenching effect was also seen in the photoluminescence experiments for this complex, where a less intense emission was observed in comparison to **PDI-1**.

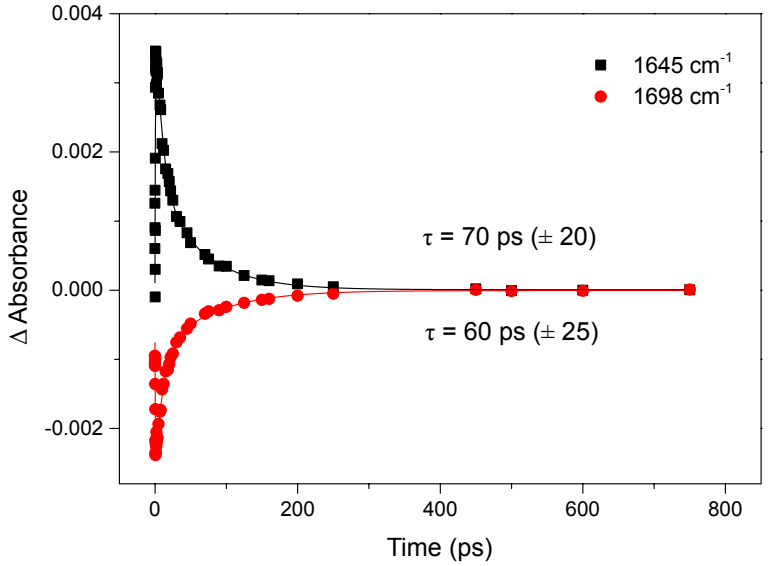


Figure 4.29: The kinetic plot for the decay of the ^{1}PDI excited state of **PDI-2** which was generated following the photoexcitation at 520 nm in CH_2Cl_2.

The *ps*-TA for monomer **PDI-2**, shown in Figure 4.30, exhibited a bleach of the ground state at 528 and 464 nm, with photoinduced excited states at 752 and 950 nm. The position and shape of the transient bands are similar to reported PDI monomers and the *ps*-TA for **PDI-1**. The position of this band at 752 nm is does not match the absorption band observed for $PDI^{-\bullet}$ species of this complex (713 nm),[173] suggesting

a ^{1}PDI excited state is formed.[165,166,212] Therefore the extra bands observed in the *ps*-TRIR must be from the pillar-[5]-arene ring. The lifetime of the ^{1}PDI excited state is considerably shorter than **PDI-1** ($\tau_2 = 625$ ps) and other reported PDI monomers ($\tau = 1 - 4$ ns).[166,204,206,212] This reduction in the lifetime when compared to **PDI-1** is also supported by the lifetimes observed from the *ps*-TRIR investigation. It is likley that the pillar-[5]-arene substituent group on the alkyl chain is quenching the excited state, which is supported by similar observations reported in the literature.[206] The lifetime from the *ps*-TA is comparable with the observed lifetimes from the *ps*-TRIR experiment.

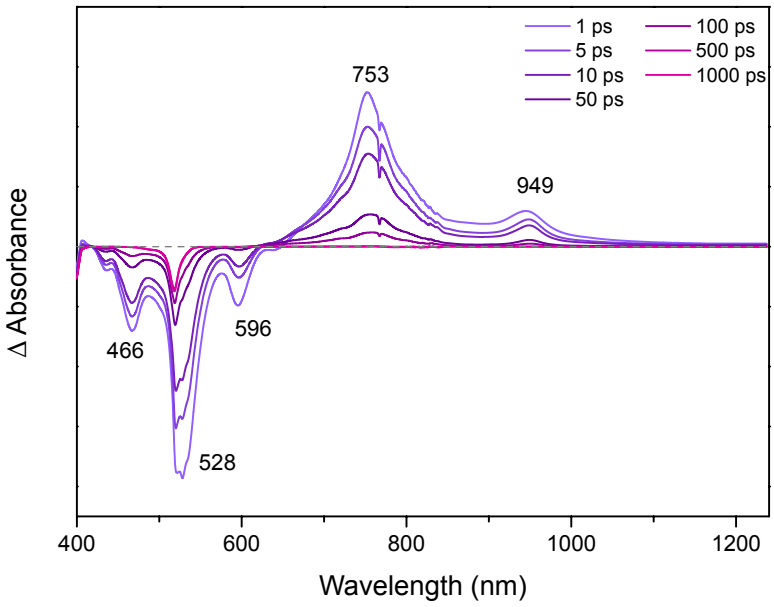


Figure 4.30: The picsosecond transient absorption spectra of **PDI-2** in CH_2Cl_2 at a number of time-delays after photoexcitation at 520 nm.

From the kinetic data of the ^{1}PDI excited state bands at 752 and 950 nm indicate that there are two processes occurring, the first being similar to a previously reported fast solvent relaxation process,[206] and the second being the decay of the singlet excited

state, ^{1}PDI, with $\tau_1 = 8$ ps ($\pm$ 4) and $\tau_2 = 55$ ps ($\pm$ 15) respectively. The kinetics plot for the *ps*-TA of **PDI-2** is shown in Figure 4.31.

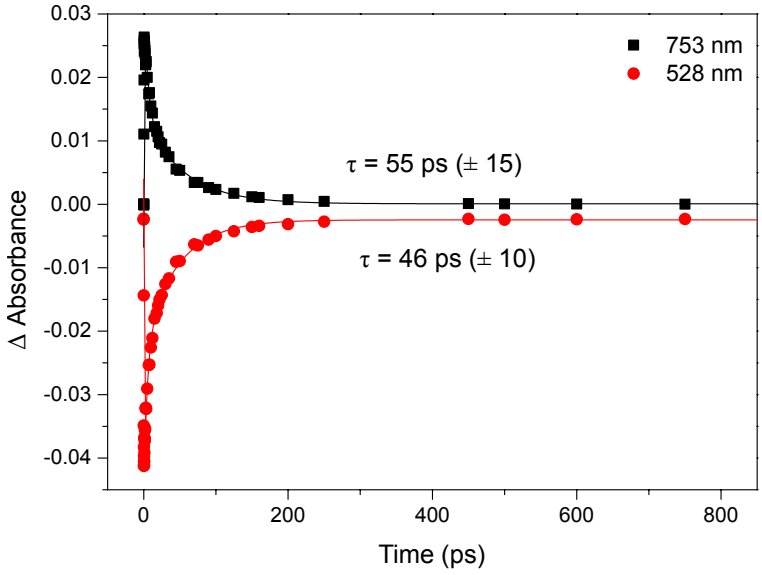


Figure 4.31: The kinetic plot for the decay of the ^{1}PDI excited state of **PDI-2** which was generated following the photoexcitation at 520 nm in CH_2Cl_2.

4.3.2.3 Time Resolved Study of a NDI-1 at 380 nm

The final monomer to be probed was **NDI-1** which can be seen in Figure 4.32, where the NDI core is connected to a imidazole group *via* an alkyl chain, similar to **PDI-1**. Due the nature of the NDI core, a higher energy excitation was required, therefore **NDI-1** was probed at 380 nm rather than 520 nm like the other two monomers.

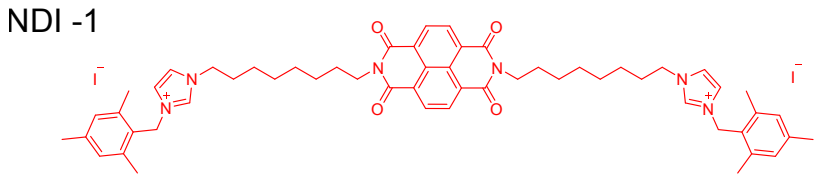


Figure 4.32: The structure of **NDI-1** which was probe at 380 nm in CH_2Cl_2 with *ps*-TRIR and *ps*-TA.

The *ps*-TRIR spectra of **NDI-1** is shown in Figure 4.33, with the parent bleaches at 1706 and 1666 cm^{-1}. The third parent bleach at 1605 cm^{-1} is not observed, most likely due to an overlapping transient band in the same position. Following an excitation at 380 nm, an initial transient species is observed at 1624 and 1516 cm^{-1}. These two bands at 1624 and 1516 cm^{-1} are seen to decay away, with two new bands growing in at 1643 and 1605 cm^{-1}. The two bands at 1643 and 1605 cm^{-1} are long lived on the picosecond timescale, still observed at later time delays. The position of these bands at 1643 and 1605 cm^{-1} is consistent with the formation of a ^{3}NDI matching what has been reported in literature for a ^{3}NDI.[257,261] This suggests the first initial state at 1624 and 1516 cm^{-1} is either a ^{1}NDI state or a $NDI^{-\bullet}$, either of which can be populated following excitation. Ganesan *et al.* reported two potential decay pathways for substituted NDI monomers,[254] one of which goes *via* ^{1}NDI excited state that decays directly to the ^{3}NDI excited state, with the other pathway doing *via* charge transfer (CT) state, $NDI^{-\bullet}$. From the observations seen in *ps*-TRIR it is hard to conclude whether **NDI-1** goes *via* the CT state. To help distinguish between the two processes, global analysis was carried out on the *ps*-TRIR data to help aid the assignments of the states. Observation made in the literature suggest the lifetime of a ^{3}NDI excited state is long lived, with some substituted NDI complexes having a

lifetime on the μs timescale,[257,261,264] and more simple NDI monomers having a lifetime on the nanosecond timescale.[254]

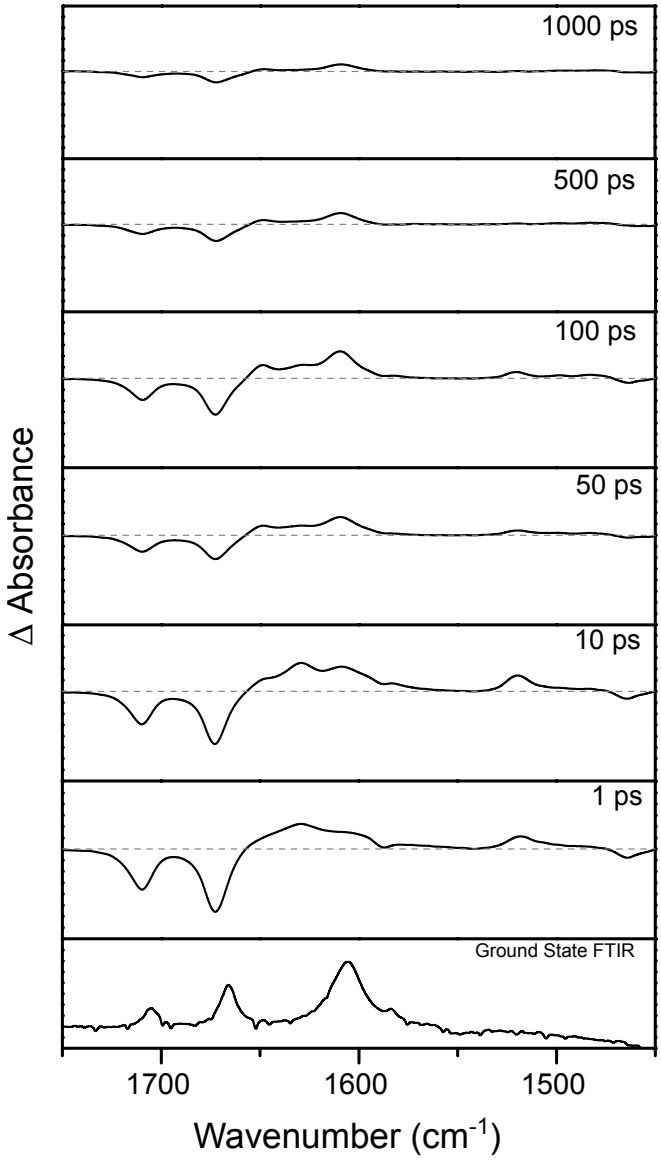


Figure 4.33: The *ps*-TRIR spectra of **NDI-1** in CH_2Cl_2 at a number of time-delays after photoexcitation at 380 nm.

The global analysis was run on the *ps*-TRIR data to help distinguish between the excited states observed, where the kinetic information along with an exited state spectra was generated. The global analysis indicated three processes, suggesting the formation of the ^{1}NDI excited state (τ_1 = 0.6 ps), followed by the CT state NDI$^{-\bullet}$ (τ_2 = 25 ps) resulting in the ^{3}NDI excited state. The initial lifetime of the ^{1}NDI excited state was fixed due to instrument response times. It has been reported in the literature that the initial ^{1}NDI excited state is difficult to assign on the *ps*-TRIR,[257] so the fast lifetime from the *ps*-TA was used for the global analysis fit. The excited state spectra for the three different species can be seen in Figure 4.34, where the fast ^{1}NDI species (0.6 ps) is indicated by the black line. The second species, seen in red has three bands at 1629, 1600 and 1518 cm^{-1}, which has been reported to be the CT species NDI$^{-\bullet}$.[257] This observation also supports observations made in the spectroelectrochemistry.[173] The final species, seen in blue, corresponds to the ^{3}NDI excited state, with a band at 1648 and 1609 cm^{-1}, which supports observation reported in the literature for a ^{3}NDI excited state.[257,261]

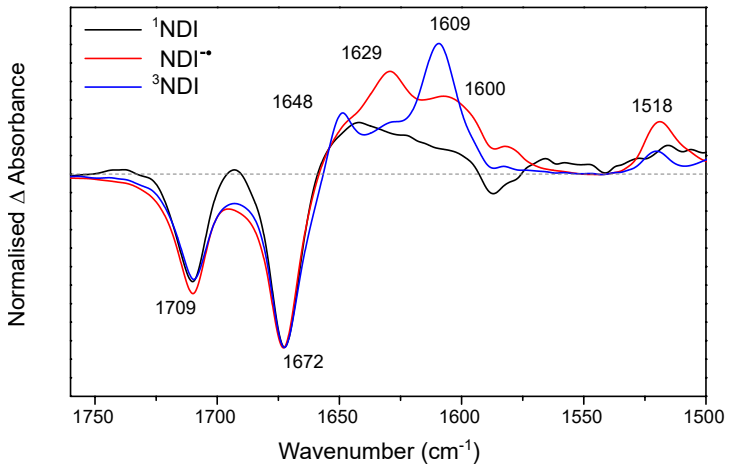


Figure 4.34: The normalised excited state spectra for the ^{1}NDI and ^{3}NDI excited state of **NDI-1**. This was a result of the global analysis of the *ps*-TRIR data set.

The kinetic plot for the decay of the ^{1}NDI excited state ($\tau_1 = 0.6$ ps) to the NDI$^{-\bullet}$ ($\tau_2 = 25$ ps), which then decays ^{3}NDI excited state can be seen in Figure 4.35. It is clear from the global analysis kinetic plot that the lifetime of the ^{3}NDI excited state is shorter lived than what has been previously reported in the literature. The ^{3}NDI excited state is seen to decay away after 800 ps. The kinetics seen in the global analysis support other NDI monomer systems that have seen the formation of the NDI$^{-\bullet}$ following the decay of the ^{1}NDI excited state.[209,254,257]

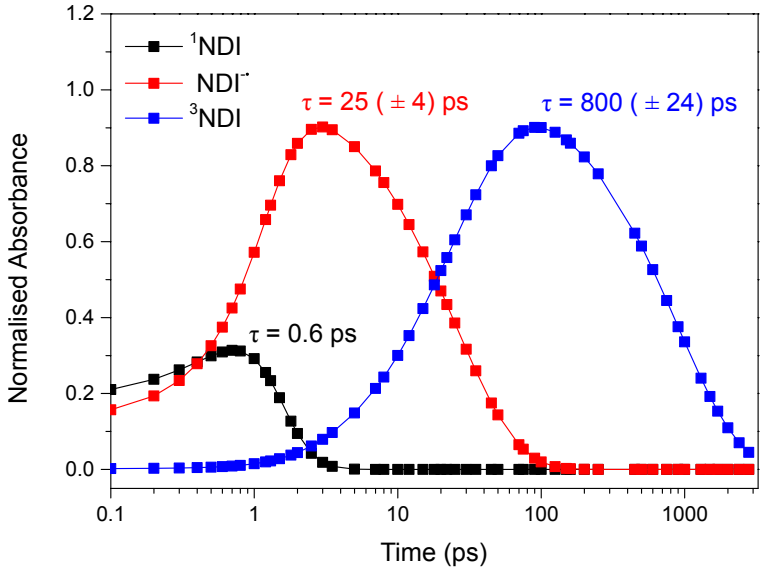


Figure 4.35: The kinetic plot for the decay of the ^{1}NDI excited state of **NDI-1** which was generated following the photoexcitation at 380 nm in CH_2Cl_2.

The *ps*-TA of the final monomer, **NDI-1** can be seen in Figure 4.36. The parent bleaches are not observed due to the 380 nm excitation pump band obscuring them. The only parent bleach being observed at 403 nm. The transient bands observed are seen at 464, 631, 960 and 1143 nm. The bands at 1143 and 631 nm are seen to decay away initially, with the bands at 464 and 960 nm growing in at later time delays. As the band at 631 nm decays, a shoulder can be seen at *ca.* 550 nm, which

is then seen to decay at later time delays. There is a switch in the intensity of the two bands at 464 nm and 631 nm, with the 464 nm band being more intense at later time delays. This could suggest the formation of several species, which supports the observations made in the *ps*-TRIR for this complex. The initial ^{1}NDI state is most likely the bands at 631 and 1143 nm, which quickly decay to the NDI$^{-\bullet}$. The NDI$^{-\bullet}$ like state has three bands at *ca.* 460, 530 and 631 nm,[264] which is also supported by the spectroelectrochemistry.[173] In addition, the two sharp bands at 464 and 631 nm are very indicative of a NDI$^{-\bullet}$ state.[257] The final state has a sharp band at 464 nm which has also been seen for other NDI complexes exhibiting a ^{3}NDI excited state.[264]

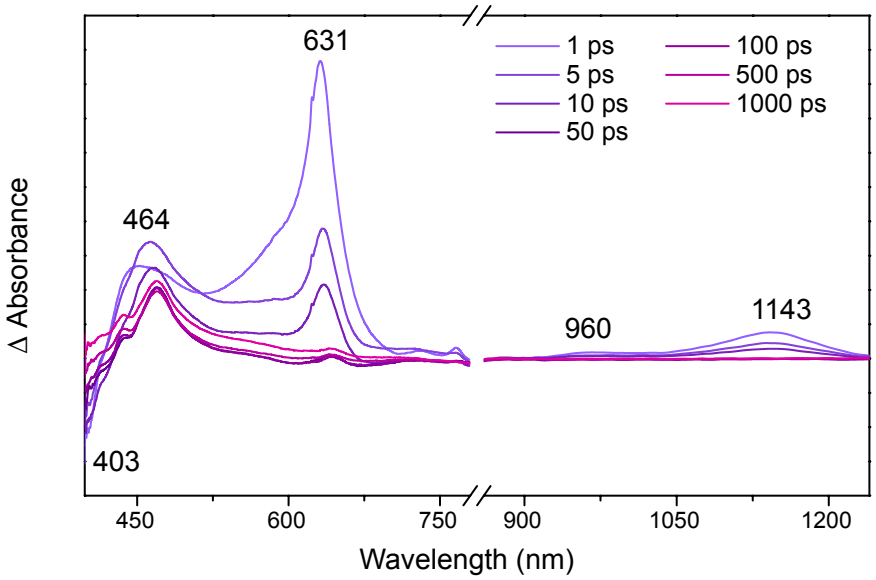


Figure 4.36: The picosecond transient absorption spectra of **NDI-1** in CH_2Cl_2 at a number of time-delays after photoexcitation at 380 nm.

The global analysis of the visible region of the data set generated the excited state spectra which can be seen in Figure 4.36. This shows the three different species are observed in the *ps*-TA, with the ^{1}NDI excited state at 460 and 631 nm, shown by the

black line. The second $NDI^{-\bullet}$ can be seen in red, with two distinct bands at 464 and 631 nm and a shoulder band at 550 nm. The final ^{3}NDI excited state can be seen in blue, with a sharp band a 464 nm with an additional band at higher energy *ca.* 440 nm and is indicative of a triplet state,[251] as well as a small band at 631 nm.

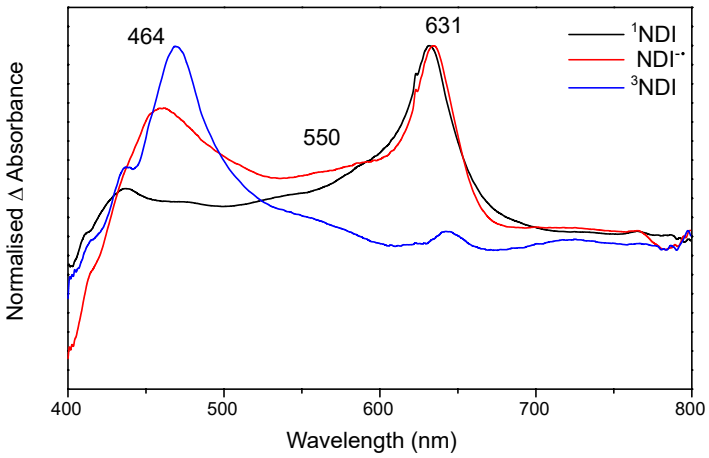


Figure 4.37: The normalised excited state spectra for the ^{1}NDI and ^{3}NDI excited state of **NDI-1**. This was a result of the global analysis of the *ps*-TRIR data set.

The kinetic information generated from global analysis showed a three process system, where the initial ^{1}NDI excited state has a lifetime of $\tau_1 = 0.6$ ps, followed by the $NDI^{-\bullet}$ state with a lifetime of $\tau_2 = 13$ ps and the final ^{3}NDI excited state having a long lifetime that lives beyond the experiment (4.5 ns). The kinetic plot generated from the global analysis can be seen in Figure 4.38 and shows the decay of the $NDI^{-\bullet}$ state to the ^{3}NDI state. The lifetime observed for the *ps*-TA support the observations made in the *ps*-TRIR for this complex.

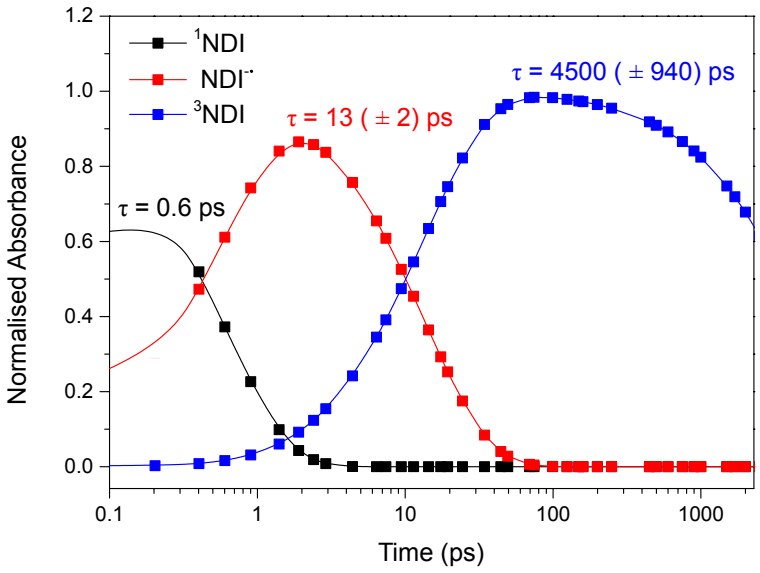


Figure 4.38: The kinetic plot for the three specices ^{1}NDI, NDI$^{-\bullet}$ and the ^{3}NDI excited state of **NDI-1** which was generated following the photoexcitation at 380 nm in CH_2Cl_2.

An illustration of decay process that occurs for **NDI-1** following an excitation at 380 nm is shown in Figure 4.39. Upon excitation a ^{1}NDI excited state is formed, which quickly decays to form a NDI$^{-\bullet}$ species. This NDI$^{-\bullet}$ species then decays to a ^{3}NDI excited state which is long lived, living beyond the experimental timeframe.

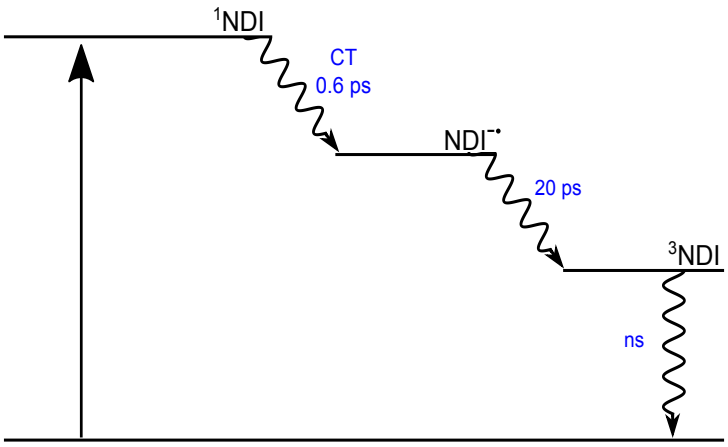


Figure 4.39: An illustration of decay process for **NDI-1** which occurs following the photoexcitation at 380 nm in CH_2Cl_2.

From the *ps*-TA for **PDI-1**, **PDI-2** and **NDI-1** there is a clear comparison with the observations seen for the *ps*-TRIR of the same complexes. Both the PDI monomers show the formation of a ^{1}PDI excited state, and the NDI monomers forming a NDI$^{-\bullet}$ state which decays to a long lived ^{3}NDI excited state. The lifetimes seen for all three complexes are very comparable with the *ps*-TRIR observations, where **PDI-2** has the shortest lifetime, which is likely due to the pilar-[5]-arene group quenching the ^{1}PDI excited state. The lifetimes seen for **PDI-1** and **NDI-1** are shorter then lifetimes reported in the literature but these observations are in line with the lifetimes seen for the *ps*-TRIR experiment. The lifetimes for all three monomers can be seen in Table 4.1. From the table, the lifetime of **PDI-2** is considerably shorter than **PDI-1** and **NDI-1** and significantly shorter than that reported for other NDI monomers in the literature.[262]

Table 4.1: The lifetimes of the excited states observed in *ps*-TRIR and *ps*-TA spectra for **1**, **2** and **H**. Where † indicates kinetics generated from global analysis of the data set.

	Nature of State	Band Position (cm^{-1})	τ (ps)	Band Position (nm)	τ (ps)
PDI-1	^{1}PDI	1647, 1623 1550, 1505	390 (± 50)	751, 939	625 (± 65)
PDI-2	^{1}PDI	1645, 1619 1550, 1587 1529, 1456	70 (± 20)	753, 949	55 (± 15)
NDI-1	^{1}NDI		0.6†	460, 631	0.6†
	$NDI^{-\bullet}$	1629, 1600 1516	24 (± 4)†	464, 550 631	13 (± 2)†
	^{3}NDI	1643, 1605	800 (± 24)†	436, 464 631	4500 (± 940)†

4.3.3 Time Resolved Investigation of the PDI and NDI Handcuff Complexes

The monomers that make up the handcuff complexes showed the formation of either a ^{1}PDI excited state or a ^{3}NDI excited state. Both the handcuff complexes are comprised of **PDI-2**, with either **PDI-1** forming **PDI/PDI-H** or **NDI-1** to give **PDI/NDI-H**. Both the handcuff complexes, **PDI/PDI-H** and **PDI/NDI-H** were excited at 520 nm in CH_2Cl_2 to see how the photophysical properties changed once the monomers were 'handcuffed' together.

4.3.3.1 Time Resolved Study of a PDI/PDI-H at 520 nm

The photophysical properties of the monomers that make up the handcuff complex **PDI/PDI** have already be discussed, but seeing how their photophysical properties change when they are 'handcuffed' together has been probed. The handcuff complex **PDI/PDI** is shown in Figure 4.40, where the two monomers that make up the complex can be seen.

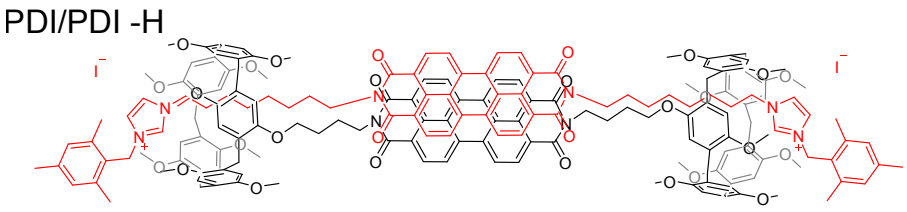


Figure 4.40: The structure of **PDI/PDI-H** which was probed at 520 nm in CH_2Cl_2 with *ps*-TRIR and *ps*-TA.

The *ps*-TRIR spectra of **PDI/PDI-H** can been seen in Figure 4.41. The parent bleaches are seen at 1700, 1665 and 1601 cm^{-1}, with transient excited state bands at 1650, 1585 and 1531 cm^{-1}. The *ps*-TRIR spectra of **PDI/PDI-H** shows bands that are consistent with both monomers **PDI-1** and **PDI-2**, however there are no new peaks that appear to be characteristic of **PDI/PDI-H**. In contrast to the *ps*-TRIR spectra for the monomers **PDI-1** and **PDI-2**, there is broadening of the C=O stretch at 1644 $cm^{-1}$for **PDI/PDI-H**. This broadening is due to the fact that the the C=O stretches are highly sensitive to their electronic environment, thus in the dimer there will be PDI interactions as well as solvent interaction, which will result in broadening of the C=O stretch. This broadening of the C=O stretch is consistent with the formation of an excimer, which has been observed in the literature.[211] As well as broadening of the C=O stretch, a band at *ca.* 1530 cm^{-1} is observed, which has been shown to be a band associated with the formation of an excimer.[210]

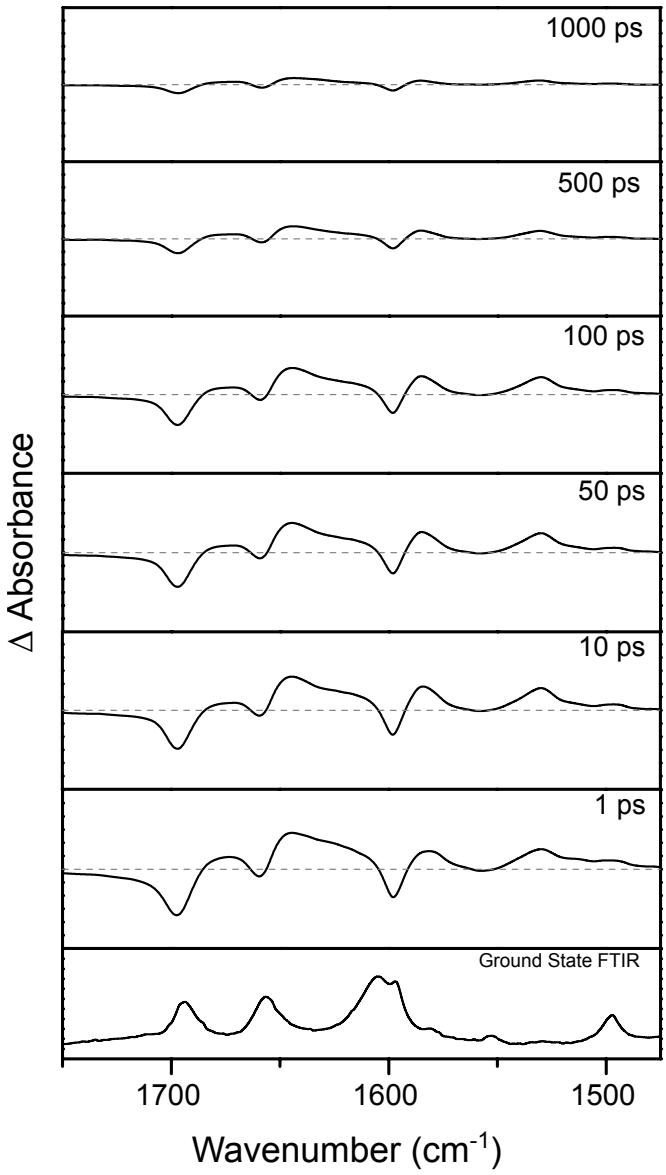


Figure 4.41: The *ps*-TRIR spectra of **PDI/PDI-H** in CH_2Cl_2 at a number of time-delays after photoexcitation at 520 nm.

The kinetic fit for the *ps*-TRIR of **PDI/PDI-H** indicates a three process system, where the lifetimes of the processes are τ_1 = 2.4 ps (± 0.9), τ_2 = 70 ps (± 10) and τ_3 = 640 ps (± 80). The first process can be assigned as excimer formation followed by

the subsequent geometric rearrangement of the excimer, with the final process being the decay of the excimer. The lifetime associated with the excimer of **PDI/PDI-H** is longer lived than the monomers, which is consistent with reports in the literature.[210] The lifetimes and the C=O broadening are consistent with the formation of an excimer, which has been reported for other PDI dimer complexes.[211] However, the lifetime of the excimer for **PDI/PDI-H** is much shorter lived compared to excimer reported in literature.[211] This decrease in lifetime could be due to the nature of the handcuff dimer, as well as the substituents on the handcuff complexes, which were seen to reduce the excited states lifetimes of the monomers. The observation of an excimer supports the emission spectrum observed for **PDI/PDI-H** which is attributed the emission to an excimer like state,[210] along with the DFT calculations reported for this complex.[173]

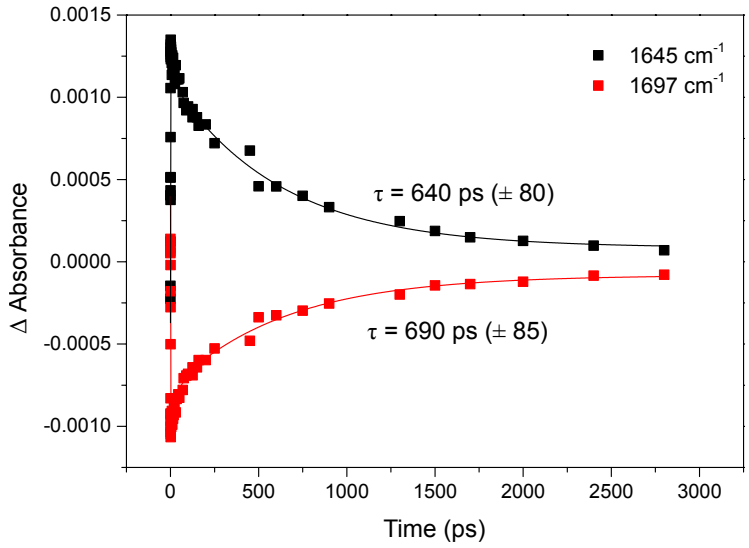


Figure 4.42: The kinetic plot for the decay of the excimer state of **PDI/PDI-H** which was generated following the photoexcitation at 520 nm in CH_2Cl_2.

The *ps*-TA spectra for the handcuff complex **PDI/PDI-H** can be seen in Figure 4.43, which shows ground state bleaches at 535 and 471 nm along with a broad

photoinduced state band at 620 nm and a narrow peak in the NIR at 961 nm. The excited state observed for **PDI/PDI-H** appears to be broader in the visible region compared to the excited states of **PDI-1** and **PDI-2**, with the broad peak seen at 620 nm to around 750 nm. The peak in the NIR at 961 nm starts to grow in at later time delays (100 ps). The broad feature that is initially centred at 694 nm, blue shifts to 620 nm in 9 ps, corresponding to the excimer formation between the two PDI cores.[165]

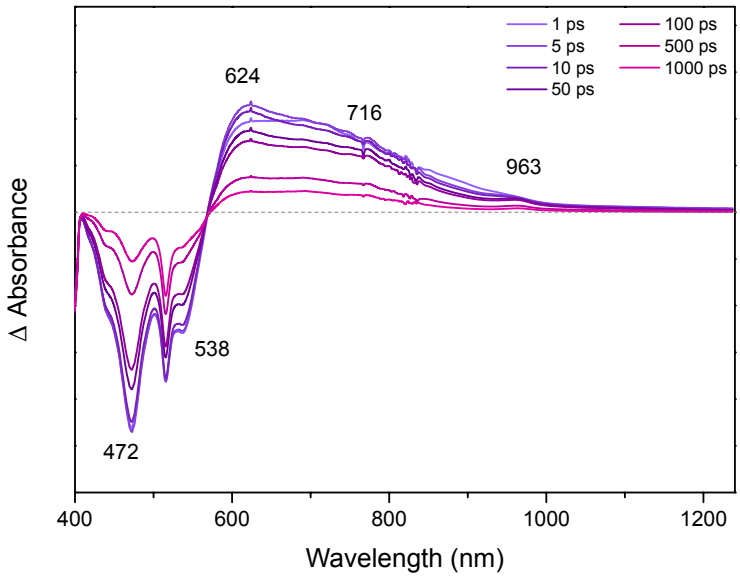


Figure 4.43: The picsosecond transient absorption spectra of **PDI/PDI-H** in CH_2Cl_2 at a number of time-delays after photoexcitation at 520 nm.

A kinetic fit of the bands indicated there are three processes, τ_1 = 9 ps (± 7) being the excimer formation, τ_2 = 110 ps (± 20), which can be attributed to the subsequent geometric rearrangement of the excimer state, and finally τ_3 = 850 ps (± 300) which is consistent with the decay of the excimer.[212] It is possible that the initial process is actually vibrational cooling of a hot excimer that is formed on the femosecond timescale.[165] The global analysis fit for **PDI/PDI-H** also shows three

processes, which is consistent with the kinetic fits for the *ps*-TA data. The first state shows the initial band at 694 nm decaying and the band at 620 nm growing in with a lifetime of 1 ps, which is likely the formation of an excimer. The second and third state observed in the global analysis show the broadening of the 620 nm band, which is consistent with the observation of an excimer state,[165,212] but also the DFT and spectroelectrochemical investigations for this complex.[173] The formation of a excimer seen from the *ps*-TA spectra is consistent with the observation seen in the *ps*-TRIR spectra of **PDI/PDI-H**, with lifetimes that are very comparable.

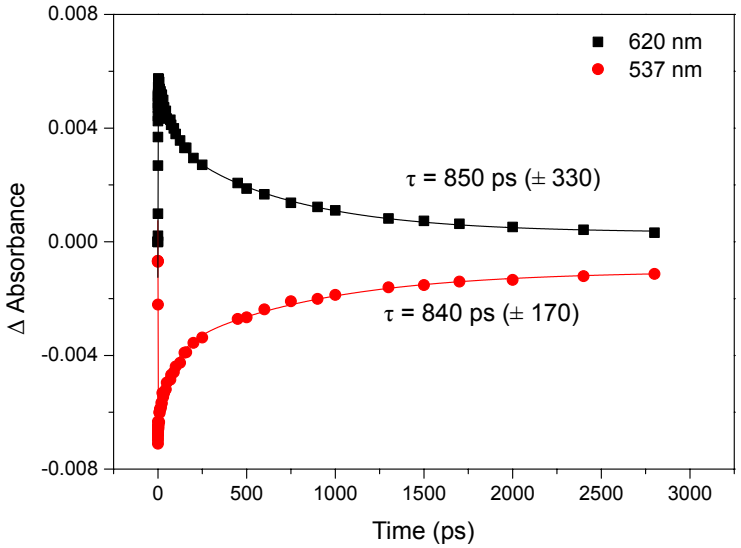


Figure 4.44: The kinetic plot for the decay of the excimer excited state of **PDI/PDI-H** which was generated following the photoexcitation at 520 nm in CH_2Cl_2.

4.3.3.2 Time Resolved Study of a PDI/NDI-H at 520 nm

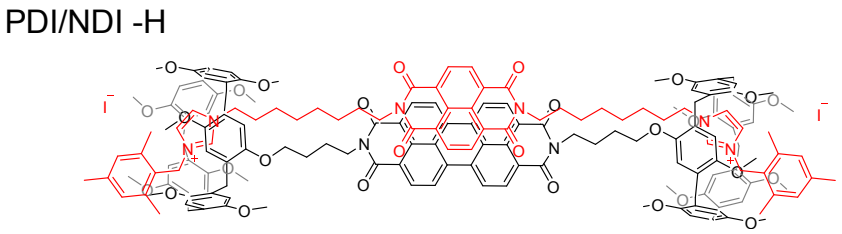


Figure 4.45: The structure of **PDI/NDI-H** which was probe at 520 nm in CH_2Cl_2 with *ps*-TRIR and *ps*-TA.

The other handcuff complex that was probed was **PDI/NDI-H**, which is made up of **NDI-1** and **PDI-2** is shown in Figure 4.45. There are not many dimers in the literature that have both a PDI and a NDI core, however the spectroelectrochemistry reported by Yang *et al.* may help elucidate the photophysical properties of **PDI/NDI-H**.[173] The *ps*-TRIR spectra for **PDI/NDI-H** can be seen in Figure 4.46, with broad transient band that grow in at 1636, 1589 and 1514 cm^{-1} following excitation. The parent bleaches were be observed at 1699, 1664 and 1597 cm^{-1}. From Figure 4.46, it appears the first initial state observed has bands at *ca.* 1636 and 1514 cm^{-1} which are consistent with observation made for both **NDI-1** and **PDI-2**. A third band grows in at 1531 cm^{-1}, which is consistent with observations made for both **PDI-2** and **PDI/PDI-H**. This observation suggests the initial state formed is based one of the units of the handcuff complex. There is also broadening of the C=O stretch at *ca.* 1630 cm^{-1}, similar to **PDI/PDI-H**, which indicates an interaction between the NDI and PDI unit. As the NDI and PDI units are not the same structure, this can not be the formation of an excimer, on the other hand it could be the formation of a charge transfer state. This charger transfer state could be the formation of an exciplex,

however proving the formation of an exciplex is challenging as the both an exciplex and an ion pair exhibit similar properties.[265] Global analysis was run on the *ps*-TRIR data to help distinguish the different species observed.

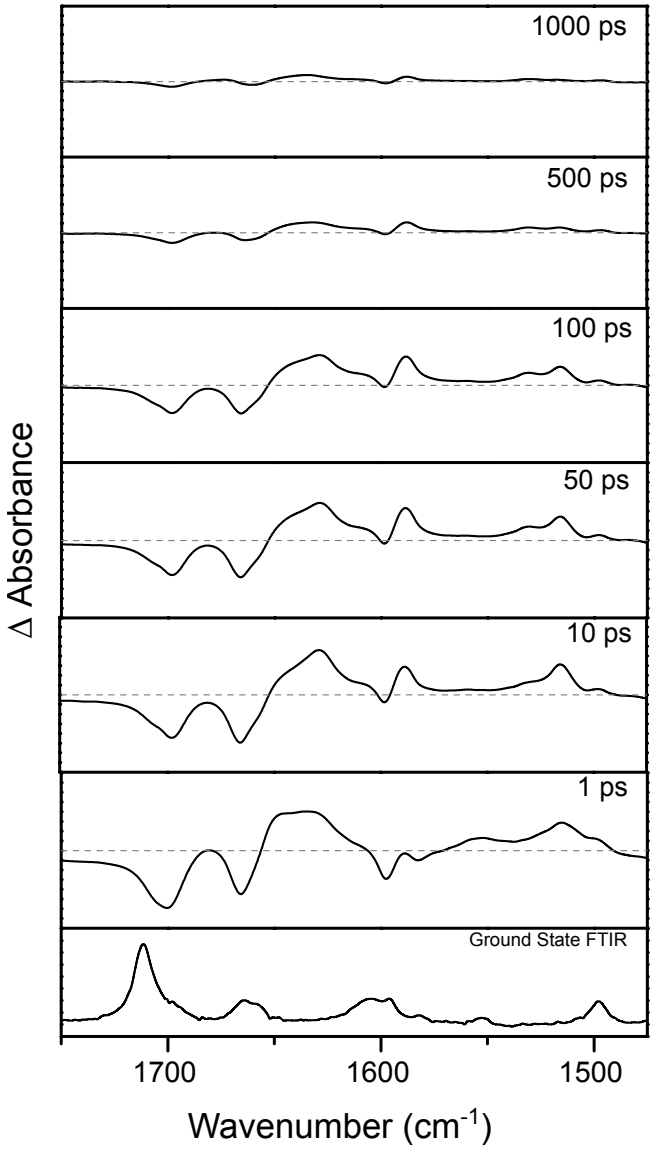


Figure 4.46: The *ps*-TRIR spectra of **PDI/NDI-H** in CH_2Cl_2 at a number of time-delays after photoexcitation at 520 nm.

A excited state spectra was generated for the different species observed in the *ps*-TRIR data of **PDI/NDI-H** shown in Figure 4.47. The first species observed has transient bands which are similar to the early transient bands observed for **PDI-2**, a ^{1}PDI excited state. The second species can be seen in black, which has three transient bands at 1629, 1587 and 1515 cm^{-1}, which is consistent with the observations made for **NDI-1** for the NDI$^{-\bullet}$ species. A second state is observed, with bands appearing at 1693, 1611, 1586 and 1531cm^{-1} which is represented by the red line in Figure 4.47. This is consistent with the PDI$^{-\bullet}$ species reported by Yang *et al.*,[173] which could suggest the formation of an ion pair.

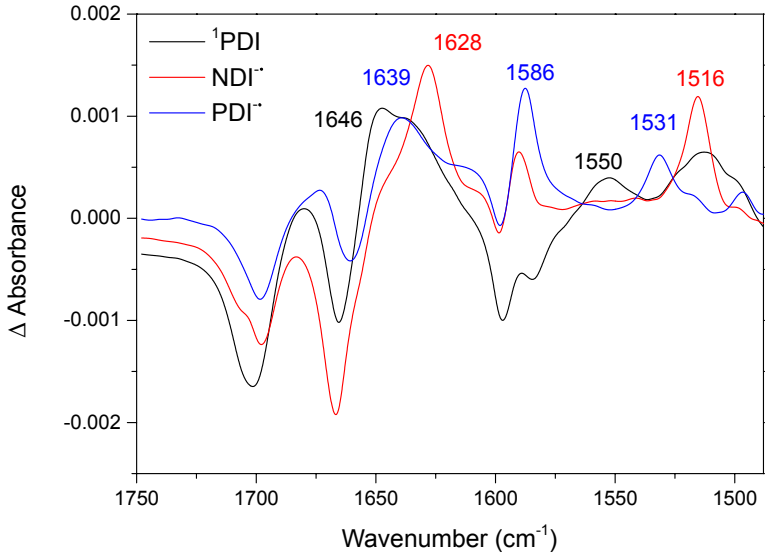


Figure 4.47: The normalised excited state spectra for **PDI/NDI-H**, which shows three species that are present in the *ps*-TRIR. This was generated by global analysis.

The lifetime of the ion pair that is observed in *ps*-TRIR spectra for **PDI/NDI-H** is seen to be decaying away by the 500 ps time delay. The decay of the NDI$^{-\bullet}$ species is faster (τ = 220 ps) than the decay of the PDI$^{-\bullet}$ species (τ = 970 ps). The global analysis suggests there are three processes occurring for **PDI/NDI-H**. The

first lifetime is very fast ($\tau = 1.3$ ps) and is the decay of the ^{1}PDI excited state, which goes on to form an ion pair as a result of CT from the pillar-[5]-arene ring. This results in either a $NDI^{-\bullet}$ and $PDI^{-\bullet}$ species. The $NDI^{-\bullet}$ state is seen to decay away after 190 ($\pm$ 15) ps, with the $PDI^{-\bullet}$ decay after 1000 ps ($\pm$ 185), which is very comparable with the lifetime observed for the *ps*-TRIR. The decay of the ^{1}PDI excited state and the formation of the ion pair can be seen in Figure 4.48. The global analysis suggests that there is 60:40 ration for the formation of $NDI^{-\bullet}$ *vs.* $PDI^{-\bullet}$.

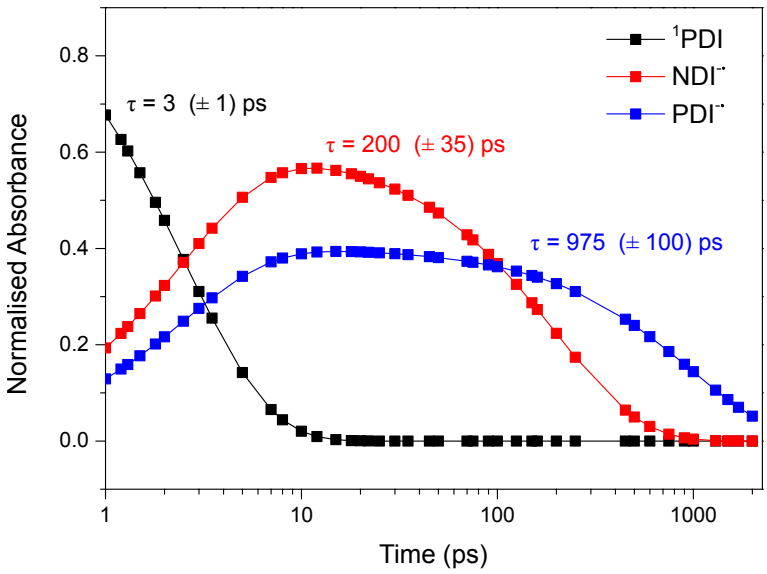


Figure 4.48: The kinetic plot for the decay of the ^{1}PDI excited state, of **PDI/NDI-H** which was generated following the photoexcitation at 520 nm in CH_2Cl_2. This kinetic plot was generated from global analysis of the data set.

The *ps*-TA spectra for **PDI/NDI-H** can be seen in Figure 4.49, where the parent bleaches are observed at 477 and 543 nm with the other parent bleach being obscured by the 520 nm excitation band. Following excitation, two transient bands can be seen at 750 and 948 nm, which matches up with the bands seen for **PDI-2**. These two bands then decay away as new three bands at 446, 622 and 957 nm are seen to

grow in. The broad band is similar to the observation for **PDI/PDI-H**, indicating the formation of a charge transfer state. This broad band is observed to be from *ca.* 620-800 nm, which is consistent with the dianionic species reported by Yang *et al.*[173] This suggests there is both a $NDI^{-\bullet}$ and the $PDI^{-\bullet}$, with the band at 446 nm being characteristic of a $NDI^{-\bullet}$ species. This is very comparable with the observations made for the *ps*-TRIR, which also indicated the formation of a charge transfer species. Both TA and TRIR spectra show the presence of a ^{1}PDI excited state, a $NDI^{-\bullet}$ and a $PDI^{-\bullet}$ species. It is likely that an ion pair is formed rather than an exciplex. This can be further supported by the luminescence data where just PDI emission is seen. Global analysis was also run on the data set to help identify the different states being observed.

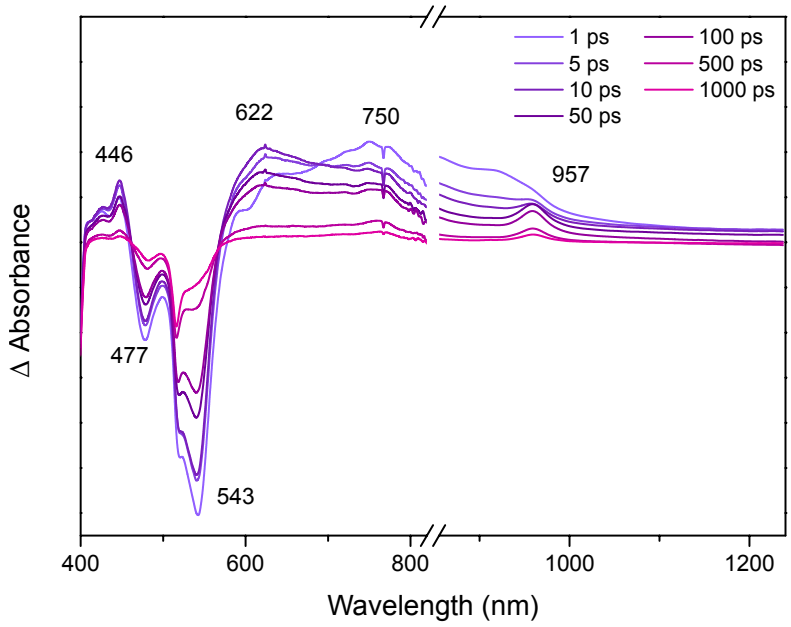


Figure 4.49: The picsosecond transient absorption spectra of **PDI/NDI-H** in CH_2Cl_2 at a number of time-delays after photoexcitation at 520 nm.

Figure 4.50 shows the normalised excited state spectra generated from the global analysis of **PDI/NDI-H** in the visible region. Three species are observed with the initial ^{1}PDI excited state shown in black with a band at 750 nm, which was also seen for the ^{1}PDI excited state of **PDI-2**. The second species is consistent with the formation of a NDI$^{-\bullet}$ state, with two bands at 446 and 622 nm. The broadening of the band at 622 nm suggests a charge transfer process, which is consistent with the formation of an ion pair. The final species seen is the presence of a PDI$^{-\bullet}$ species, similar to the *ps*-TRIR, but also supports the obeservations reported by Yang *et al.*[173]

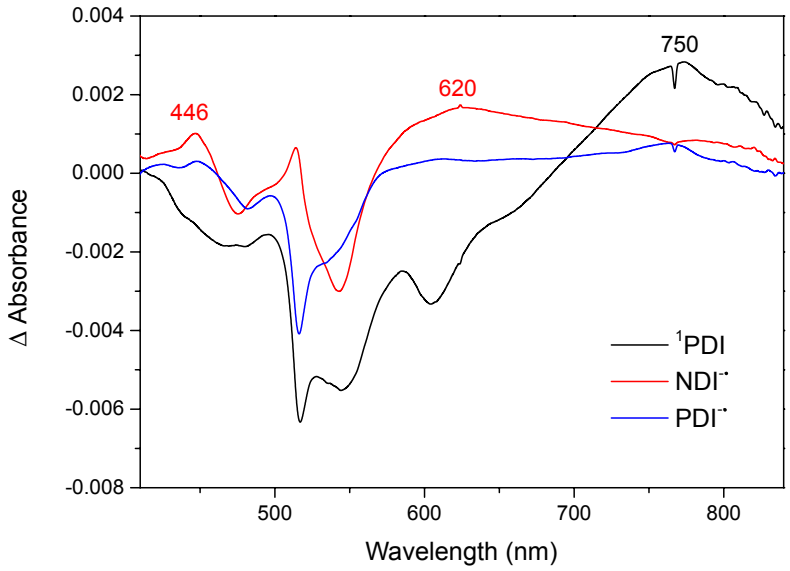


Figure 4.50: The normalised excited state spectra for the ^{1}PDI and NDI$^{-\bullet}$ state of **PDI/NDI-H**. This was a result of the global analysis of the *ps*-TRIR data set.

The kinetic plot for the decay of the ^{1}PDI excited state to the NDI$^{-\bullet}$ and PDI$^{-\bullet}$ state that was generated from the global analysis can be seen in Figure 4.51. This shows that following excitation the initial ^{1}PDI excited state decays after τ = 1.3 ps following CT from the pillar-[5]-arene. This results in either a NDI$^{-\bullet}$ or PDI$^{-\bullet}$ being formed. This initial excited state is very fast but can be seen in the *ps*-TA spectra.

The decay of the $NDI^{-\bullet}$ state had a lifetime of τ = 200 ($\pm$ 35) ps with the $PDI^{-\bullet}$ species having a lifetime of τ = 975 ($\pm$ 100) ps. The decay of the $NDI^{-\bullet}$ and $PDI^{-\bullet}$ for the *ps*-TA is comparable with the decay observed for the *ps*-TRIR. This further supports the possible formation of an ion pair over an exciplex.

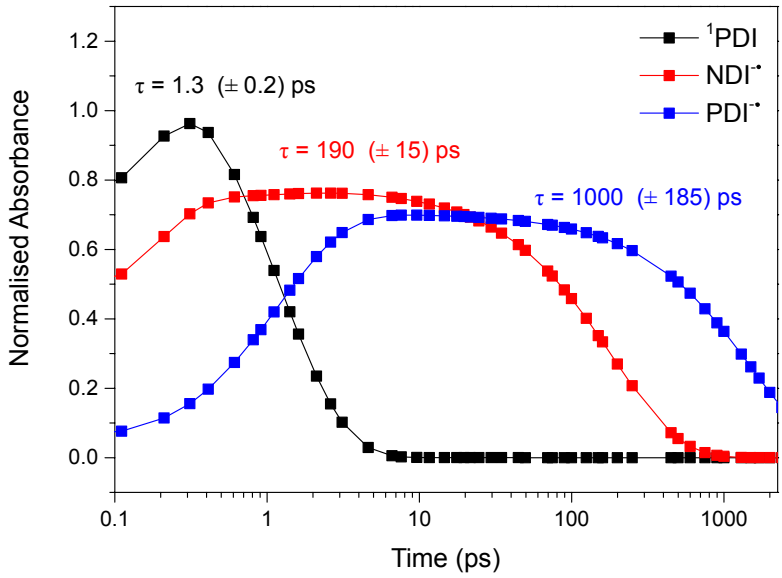


Figure 4.51: The kinetic plot for the decay of the excimer excited state of **PDI/NDI-H** which was generated following the photoexcitation at 520 nm in CH_2Cl_2.

The decay process that occurs for **PDI/NDI-H** following an excitation at 520 nm is shown in Figure 4.52. Where following excitation a ^{1}PDI excited state is formed, which quickly decays to form a $NDI^{-\bullet}$ and a $PDI^{-\bullet}$ species. The $NDI^{-\bullet}$ species decays back down to the ground state, with the $PDI^{-\bullet}$ species also decaying back down to the ground state with a longer lifetime than the $NDI^{-\bullet}$ species.

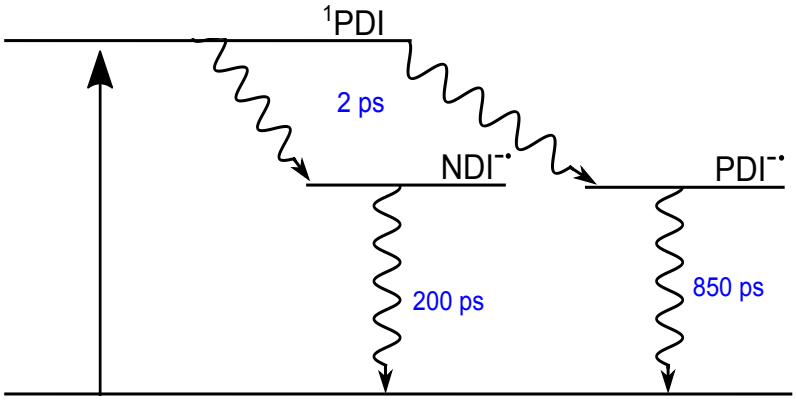


Figure 4.52: An illustration of decay process for **PDI/NDI-H** which occurs following the photoexcitation at 380 nm in CH_2Cl_2.

The observations seen in the *ps*-TA for both **PDI/PDI-H** and **PDI/NDI-H** are in very good agreement with the *ps*-TRIR and also the emission data. It is clear that following excitation **PDI/PDI-H** forms an excimer like state that has a lifetime of *ca.* 800 ps, which is shorter lived than other excimers seen in the literature for a PDI dimer. However, the nature of the substituents on the handcuff complex could explain this shorten lifetime. **PDI/NDI-H** clearly showed the formation of a charge transfer state, where the initial excited state is on the PDI unit, resulting in an ion pair with $NDI^{-\bullet}$ like state on the NDI unit and a $PDI^{-\bullet}$ on the PDI unit. The lifetimes for the *ps*-TA and *ps*-TRIR can be seen in Table 4.2.

Table 4.2: The lifetimes of the processes observed in psTRIR spectroscopy for **PDI/PDI-H** and **PDI/NDI-H**. Where † indicates kinetics generated from global analysis of the data set.

	Nature of State	Band Position (cm^{-1})	τ (ps)	Band Position (ps) (nm)	τ (ps)
PDI/PDI-H	Excimer (hot)		2.4 (± 6)	716	19 (± 9)
	(reorientation)		70 (± 60)		110 (± 20)
	Excimer	1650, 1585, 1531	640 (± 80)	624, 963	850 (± 300)
PDI/NDI-H	^{1}PDI	1649, 1616, 1552, 1507	2 (± 0.15) †	750, 948 6,	1.3 (± 0.2)†
	$NDI^{-\bullet}$	1628, 1588, 1515	190 (± 15)†	446, 622 957	200 (± 35)†
	$PDI^{-\bullet}$	1693, 1586, 1531	975 (± 100)†	750,	1000 (± 85)†

4.3.4 Time Resolved Investigation of a PDI Rotaxane

Another PDI complex that has been probed using both *ps*-TRIR and *ps*-TA is the novel PDI rotaxane complex, **PDI-rot**, which was synthesised by Dr Nicholas Pearce from the Champness group at The University of Nottingham. This **PDI-rot** complex is comprised of a PDI core that is bound to two long alkyl chains that have an imidazole group located at the end of the alkyl chain. What makes this complex different to the PDI monomers mentioned earlier in this chapter, is that fact that there are two pillar-[5]-arene ring which are sitting over the alkyl chain between the PDI core and the end imidazole substituent, illustrated in Figure 4.53. The *ps*-TRIR and *ps*-TA experiments mentioned in this section were run on the time-resolved system at The University of Nottingham with a 532 nm excitation wavelength.

4.3.4.1 Time Resolved Study of a PDI-rot at 532 nm

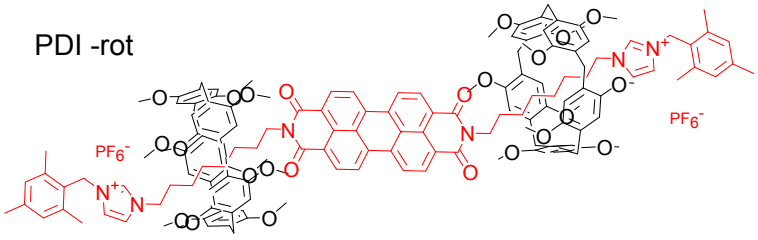


Figure 4.53: The structure of the **PDI-rot** complex.

The *ps*-TRIR spectra for **PDI-rot** is shown in Figure 4.54, with parent bleaches at 1695, 1659 and 1579 cm^{-1} and initial transient bands at 1645, 1617, and 1548 cm^{-1}. Two further bands grow in later at 1587 and 1526 cm^{-1}. The position of the initial transient species bands are consistent with excited state bands seen for the ^{1}PDI

excited state of **PDI-1**. This is to be expected as the PDI core of **PDI-rot** is bound to an alkyl chain with an imidazole substituent on the end which is very similar to that of **PDI-1**. The two bands that are seen to grown in at 1587 and 1526 cm^{-1} are not consistent with **PDI-1**. These bands are however, consistent with the reduced form of **PDI-2**, which was observed in the spectroelectrochemistry.[173] This suggests the formation of a $PDI^{-\bullet}$ species on the PDI core. The pillar-[5]-arene ring is very electron rich, so it is possible that the close proximity of the pillar-[5]-arene ring to the PDI core could be resulting in some CT to the PDI unit which then subsequently quenches the ^{1}PDI excited state, resulting in $PDI^{-\bullet}$ species. It has been reported in the literature that pillar-[5]-arene ring can result in a CT interactions,[266,267] so it is likely this is happening for **PDI-rot**.

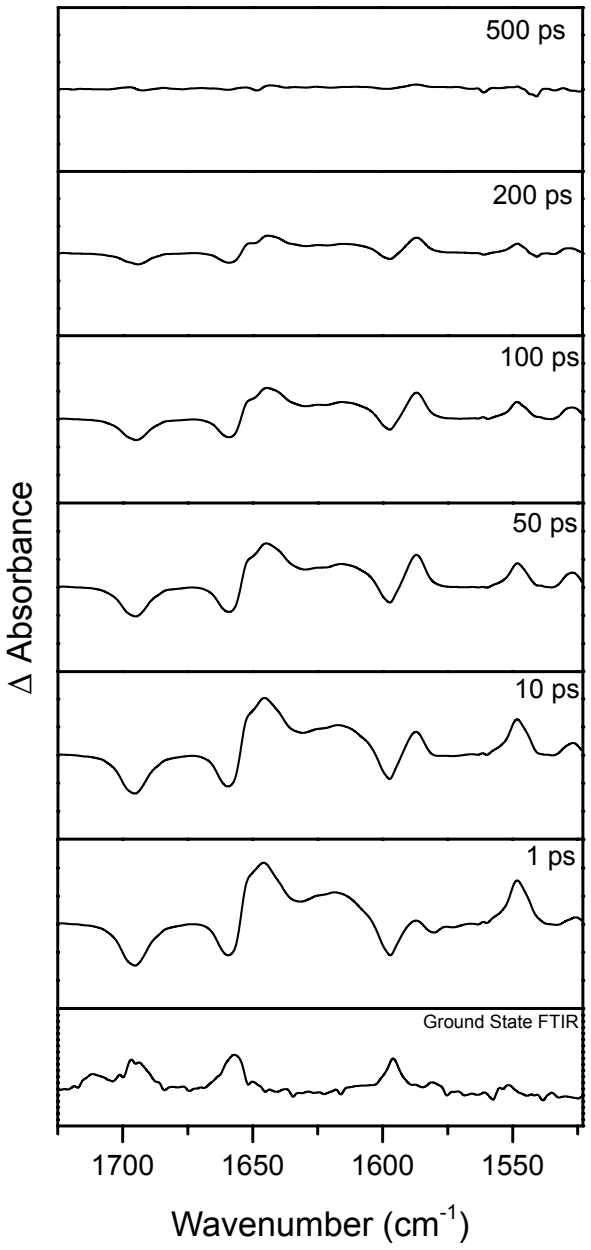


Figure 4.54: The *ps*-TRIR spectra of **PDI-rot** in CH_2Cl_2 at a number of time-delays after photoexcitation at 532 nm.

To help identify the bands growing in at 1587 and 1526 cm^{-1}, global analysis was run to aid the characterisation. The global analysis identified the presence of two species, which corresponds to the bands observed in the *ps*-TRIR. The normalised

excited state spectra for the two species identified by the global analysis is shown in Figure 4.55, where the initial state is shown in black, and the second state that grows in shown in red. The initial state has bands that are consistent with a ^{1}PDI excited state, therefore this state can be assigned to a singlet state located on the PDI unit. The second state clearly shows the bands associated with the reduced PDI$^{-\bullet}$ form, therefore it is thought to be PDI$^{-\bullet}$ species which quenches the ^{1}PDI excited state *via* electron donation from the pillar-[5]-arene ring.

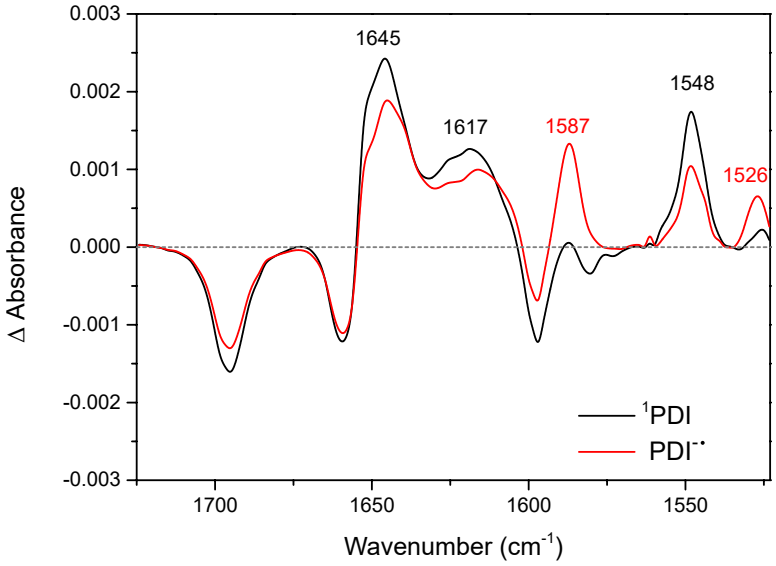


Figure 4.55: The excited state spectra for the ^{1}PDI excited state and charge transfer excited state of **PDI-rot** in CH_2Cl_2 which was generated using global analysis.

The initial ^{1}PDI excited state is very short lived with a lifetime of $\tau = 10$ ps. This is incredibly short lived for a ^{1}PDI excited state which usually have a lifetime of 1 - 2 ns.[262] The quenching of a ^{1}PDI excited state *via* CT has been reported before in the literature, where a ^{1}PDI excited state is seen to be quenched by a PDI$^{-\bullet}$ at a very fast rate, requiring *fs*-TA.[196] Therefore, the fast ^{1}PDI lifetime observed for **PDI-rot** is in

line with a CT process occurring. The kinetic plot for the decay of the ^{1}PDI excited state and the growth of the PDI$^{-\bullet}$ species is shown in Figure 4.56.

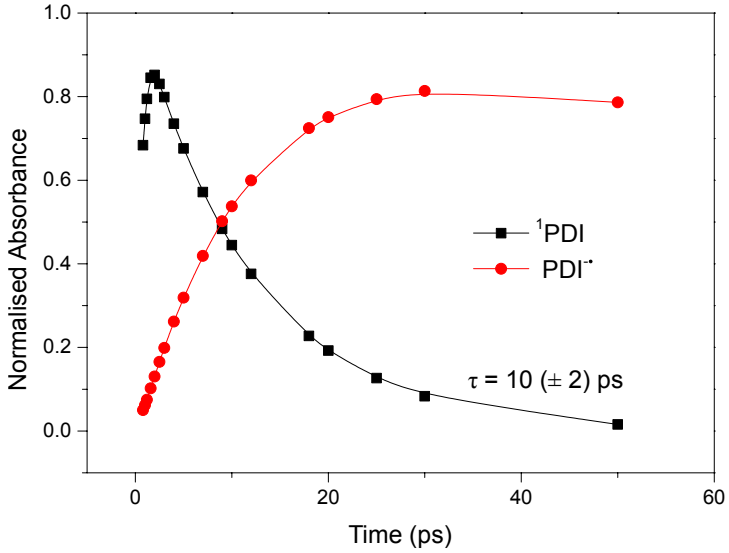


Figure 4.56: The kinetic plot for the decay of the ^{1}PDI excited state of **PDI-rot** in CH_2Cl_2 which was generated using global analysis.

The PDI$^{-\bullet}$ species that is seen to grow, decays on the picosecond timescale with a lifetime of $\tau = 170$ ps, along with the recovery of the parent species. The kinetic plot generated with global analysis can been seen in Figure 4.57, and shows the decay of the PDI$^{-\bullet}$ species. The *ps*-TRIR analysis has shown that by incorporation of a pillar-[5]-arene ring onto the alkyl chain between the PDI core and the end substituent results a CT process forming a PDI$^{-\bullet}$ species which quenches the ^{1}PDI excited state.

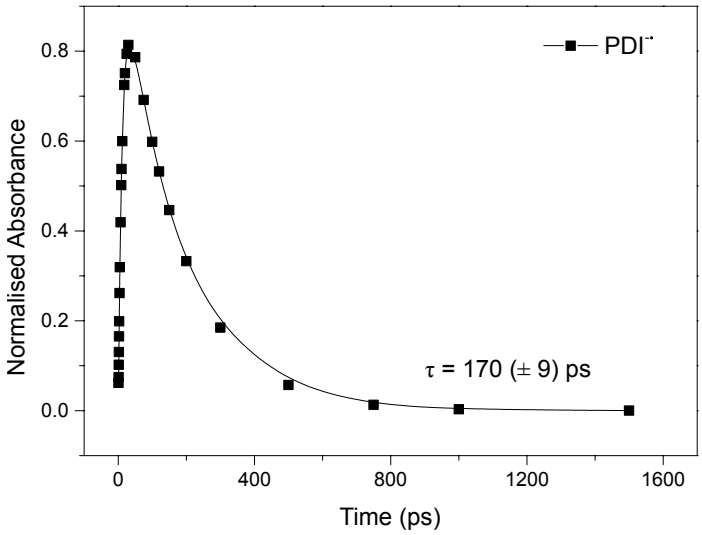


Figure 4.57: The kinetic plot for the decay of the charge transfer excited state of **PDI-rot** in CH_2Cl_2 which was generated using global analysis.

The *ps*-TA spectra for **PDI-rot** is shown in Figure 4.58. Upon excitation, one of parent bleaches of the ground state species can be observed at 488 nm, with the other two parent bleaches being obscured by the 532 nm excitation bleach. An additional bleach can be observed at 573 nm, which is consistent with the stimulated emission of the complex. A transient band is seen at 711 nm, which is the only transient band observed. The spectroelectrochemistry run by Dr Stephen Davies on **PDI-rot** indicated that the first reduced state of the complex had a strong absorption band at *ca.* 713 nm, which is consistent with transient band observed in the *ps*-TA spectra. This supports the assignment made from the *ps*-TRIR, where following a CT process a $PDI^{-\bullet}$ species is observed.

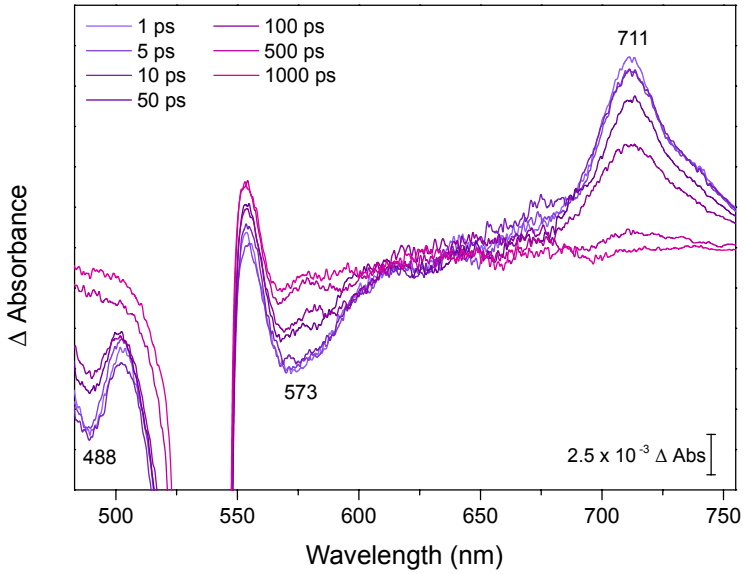


Figure 4.58: The *ps*-TA spectra of **PDI-rot** in CH_2Cl_2 at a number of time-delays after photoexcitation at 532 nm.

The $PDI^{-\bullet}$ species is seen to decay away on the picosecond timescale, similar to the *ps*-TRIR experiment. The single point kinetics only suggested there was one decay process, which was comparable for the decay of the $PDI^{-\bullet}$ species observed in the *ps*-TRIR data. The faster decay of the ^{1}PDI excited state was not observed, therefore global analysis was performed. It has been reported in the literature that the $PDI^{-\bullet}$ species and the ^{1}PDI excited state can overlap, and global analysis or target analysis is required to assign it.[268] But to the high intensity of the pump scatter band, the region 500 - 560 nm was zeroed to help with the global analysis. The global analysis suggested there were two species present, a fast process (9 ps) and a longer lived species (204 ps) which is comparable with the lifetimes observed in the *ps*-TRIR experiment. The excited state sprectrum generated from the global analysis is shown in Figure 4.59.

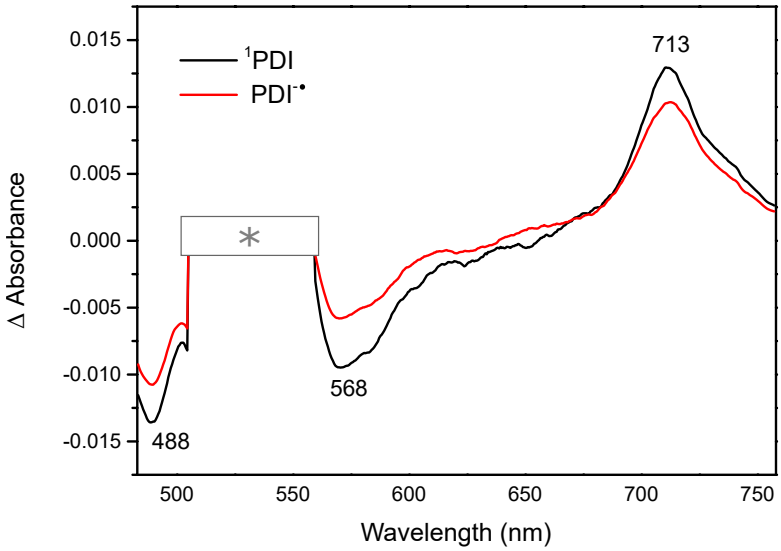


Figure 4.59: The excited state spectra for the ^{1}PDI excited state and charge transfer excited state of **PDI-rot** in CH_2Cl_2 which was generated using global analysis. The region that was zeroed to help with the global analysis is indicated by *.

The ^{1}PDI excited state is shown in black, with the stimulated emission of the excited state seen at 568 nm. The spectrum for $PDI^{-\bullet}$ species is in red, where the stimulated emission is still observed but there is a reduced intensity. The kinetic plot for the decay of ^{1}PDI excited state to the $PDI^{-\bullet}$ species can be seen in Figure 4.60, where the ^{1}PDI excited state has a lifetime of 9 ($\pm$ 1) ps.

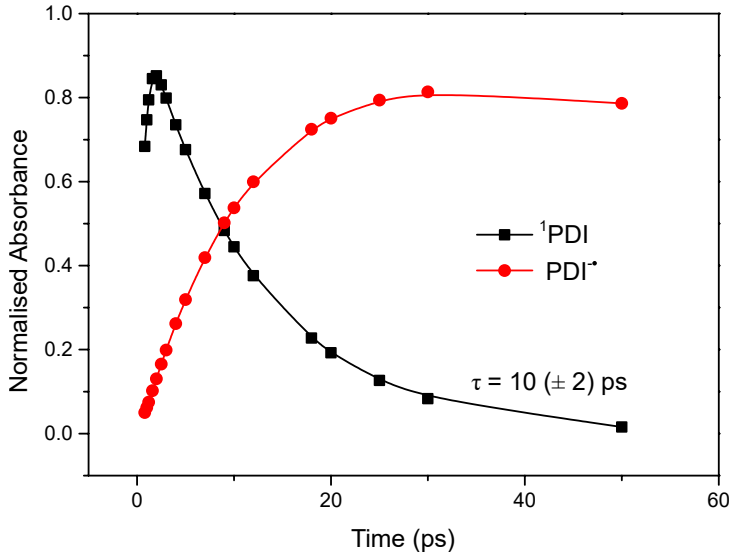


Figure 4.60: The kinetic plot for the decay of the ^{1}PDI excited state and the formation of PDI$^{-\bullet}$ of **PDI-rot** in CH_2Cl_2 which was generated by global analysis.

The decay of the PDI$^{-\bullet}$ species was also generated from the global analysis and can be seen in Figure 4.61. The PDI$^{-\bullet}$ species is seen to decay away with a lifetime of 204 (± 20) ps which is very similar to the lifetime of the PDI$^{-\bullet}$ observed in the *ps*-TRIR spectra. This supports the theory that there is CT process occurring shortly after excitation.

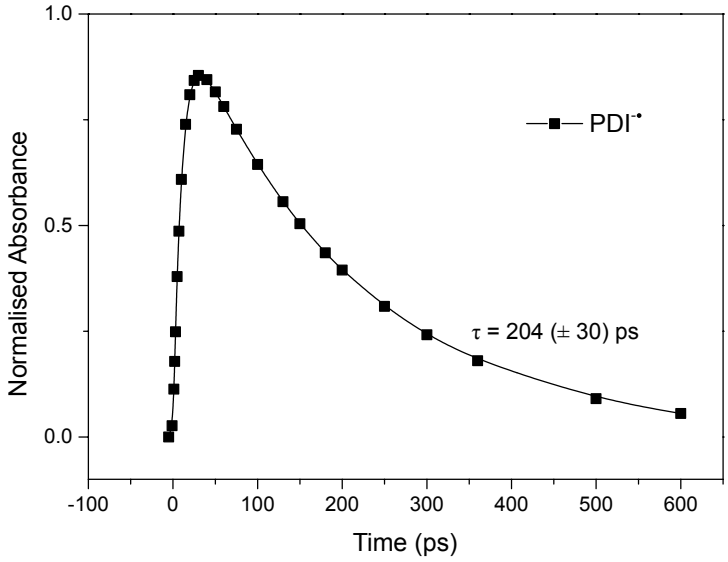


Figure 4.61: The kinetic plot for the decay of the $PDI^{-\bullet}$ species of **PDI-rot** in CH_2Cl_2 which was generated by global analysis.

It is clear from both the global analysis of the *ps*-TA and *ps*-TRIR data that there are still features of the ^{1}PDI excited state present. To investigate this further the single point kinetics of band at 1548 cm^{-1} where plotted which suggested a decay of 81 ps. This band was chosen due to that fact it is not characteristic of a $PDI^{-\bullet}$ species, therefore it must be a ^{1}PDI excited state band. This suggests there is not full conversion to the $PDI^{-\bullet}$ species, and in fact both a ^{1}PDI excited state and a $PDI^{-\bullet}$ species are being observed. The stimulated emission observed in the *ps*-TA also supports this theory as it appears longer lived than 10 ps. The recovery of the stimulated emission was plotted against the recovery of the parent to see how the two lifetimes compared. The stimulated emission is seen to recover after 85 ps, matching the decay of the band at 1548 cm^{-1} in the *ps*-TRIR. The recovery of the parent has a lifetime of 175 ps, which is comparable with the decay of the $PDI^{-\bullet}$ species, suggesting there is a dark state that is also contributing to the recovery of the parent bleach. The

kinetic plot of the recovery of the stimulated emission and the parent bleach is shown in Figure 4.62.

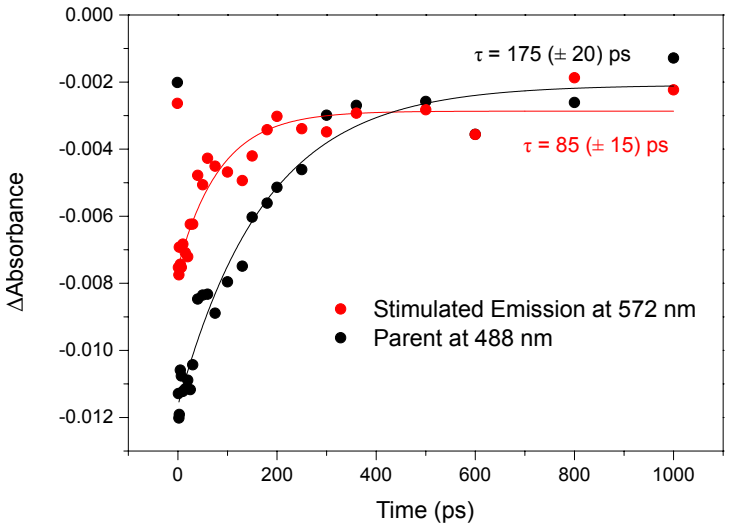


Figure 4.62: The kinetic plot for the recovery of the stimulated emission and the parent bleache of **PDI-rot** in CH_2Cl_2.

This suggests that following excitation a ^{1}PDI excited state is formed. Then some of this ^{1}PDI excited state decay to form a $PDI^{-\bullet}$ species as the result of a CT from the pillar-[5]-arene ring. The remainder of the ^{1}PDI excited state decays after 85 ps, with the $PDI^{-\bullet}$ species decaying away after 200 ps. The proposed decay process of **PDI-rot** can be seen in Figure 4.63.

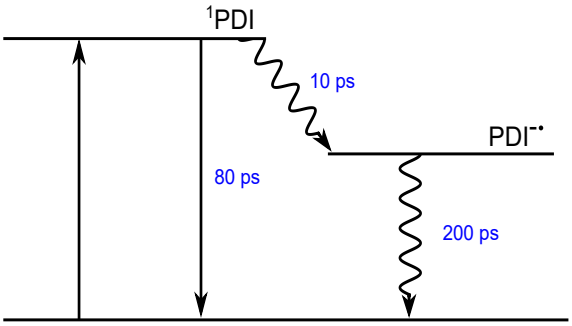


Figure 4.63: An illustration of the decay processes that occur for **PDI-rot** following an excitation at 532 nm in CH_2Cl_2.

Probing **PDI-rot** with both *ps*-TRIR and *ps*-TA has shown that by simply incorporating a pillar-[5]-arene ring onto a PDI monomer, which previously exhibited just a ^{1}PDI excited state, can results in a CT process forming a PDI$^{-\bullet}$ species. This change in the photophysical properties of this unique PDI rotaxane complex demonstrates how time-resolved techniques are needed to elucidate their photophysical properties, thus enabling future applications to be explored.

4.4 Conclusions

The *ps*-TA and *ps*-TRIR spectra and the global analysis for the monomers **PDI-1**, **PDI-2** and **NDI-1** have shown that for the PDI monomers a ^{1}PDI excited state is formed, whereas for **NDI-1** a ^{1}NDI excited state is observed, which decays *via* a $NDI^{-\bullet}$ species to form a ^{3}NDI excited state. For both **PDI-1** and **PDI-2** the formation of a ^{1}PDI excited state was observed following the cooling of the vibrationally hot states. The lifetime of the ^{1}PDI excited state of **PDI-1** (τ = 600 ps) was longer lived than **PDI-2** (τ = 80 ps) which is thought to be the result of the pillar-[5]-arene substituent group. The ^{1}PDI excited state lifetimes observed for both **PDI-2** and **PDI-1** are much shorter than what is reported in literature.[166,204,206,212,262] The NDI monomer exhibited different photophyscial properties to the PDI analogue. Following excitation, a ^{1}NDI excited state decays very quickly to form transient bands that are indicative of a $NDI^{-\bullet}$ species. This $NDI^{-\bullet}$ species then decays (τ = 25 ps) to form a ^{3}NDI excited state which has a lifetime of 890 ps. This decay pathway has been observed for NDI complexes, where the formation of $NDI^{-\bullet}$ species is the result of a charge transfer process.[254,257]

The handcuff dimers **PDI/PDI-H** and **PDI/NDI-H** exhibit very different photophysical properties. Following excitation, **PDI/PDI-H** forms an excimer, which is supported by observations from both the *ps*-TA and *ps*-TRIR spectroscopy as well as the *ps*-TRIR global analysis fits. The *ps*-TA spectra shows broadening of the excited state as well as small blueshift of the peak at early time delays, which is indicative of excimer formation. There is a three component process where first the excimer formation is being observed, followed by geometric rearrangement in the excimer state and finally the relaxation of the excimer, further supporting the formation of an ex-

cimer.[165,219] The lifetime of the excimer state was $\tau = 800$ ps, which is slightly shorter than what has been observed in literature for covalently bound dimers ($\tau \approx 1-4$ ns). In comparison, the **PDI/NDI-H** formed a ^{1}PDI excited state upon excitation which quickly decays to form either a NDI$^{-\bullet}$ or PDI$^{-\bullet}$ species as a result of CT from the electron rich pillar-[5]-arene. The *ps*-TA, *ps*-TRIR and global analysis of the data suggests the formation of an ion pair rather, than an exciplex, with the negative charged on the reduced PDI or NDI center, and the positive charge on the oxidised pillar-[5]-arene. The lifetime of the NDI$^{-\bullet}$ state is $\tau = 250$ ps, with the PDI$^{-\bullet}$ state having a lifetime of $\tau = 900$ ps which is comparable with the **PDI/PDI-H** dimer.

The *ps*-TA and *ps*-TRIR of **PDI-rot** indicated that the formation of a PDI$^{-\bullet}$ species following a CT process from the pillar-[5]-arene ring. In the *ps*-TRIR spectra, upon excitation a ^{1}PDI excited state is observed, and after 10 ps the formation of two bands at *ca.* 1580 and 1525 cm^{-1} are seen to grown in. These bands are indicative of a radical PDI species.[173,208] The *ps*-TA only saw two transient bands *via* the use of global analysis. The broad band at 710 nm corresponds to the PDI$^{-\bullet}$ spices and the ^{1}PDI excited state of the complex. It is clear that following excitation there is the formation of a ^{1}PDI excited state that undergoes CT to from a PDI$^{-\bullet}$ species, which decays with a lifetime of $\tau = 200$ ps. There is evidence of both the ^{1}PDI excited state and the PDI$^{-\bullet}$ species at later time delays, suggesting there is not full conversion to the PDI$^{-\bullet}$ species. However, it has shown that incorporating a pillar-[5]-arene ring onto the alkyl chain has induced a CT process.

The photophysical investigations have shown from both *ps*-TA and *ps*-TRIR that the monomers, handcuff complexes and the PDI rotaxane exhibit a range of photophysical properties, from singlet and triplet excited states, excimer states and CT processes. This is the first time the photophysics of these unique PDI monomers, NDI

monomer, handcuff complexes and a PDI rotaxance a have been probed, and it has shown that the substituent, orientation and nature of the rylene diimide core can have a significant affect on the photophysical properties.

Chapter 5

Investigation of Rhenium Tricarbonyl Perfluorinated Bipyridine Complexes

5.1 Introduction

In this Chapter, the photochemical and photophysical properties of rhenium tricarbonyl bipyridine complexes will be investigated and discussed. As previously mentioned, rhenium tricarbonyl α-diimine carbonyl complexes have been studied extensively due to their intense emission and photocatalytic properties. These desirable properties make them excellent compounds for photophysical and photochemical reactions for example, photo ligand substitution.[66,269] Hence rhenium tricarbonyl α-diimine carbonyl complexes are often used as photosensitisers.[269] This is because they posses an α-diimine ligand that is bound to the rhenium centre which acts as a chro-

mophore for photochemical electron transfer, which makes them desirable as photosensitive complexes.

Rhenium α-diimine complexes also have high quantum yields associated with the formation of a ^{3}MLCT or π-π^* excited state, which can result in a strong luminescence. As well as the luminescent properties, the complexes also exhibit relatively long lifetimes, on the order of several hundred nanoseconds, which are associated with the lowest energy excited state.[270] The energies of the empty π^* orbitals of the α-diimine ligand are lower due to the large conjugated π-systems and contribute to the strong luminescence observed for these complexes.[269] 2,2'-Bipyridine is an example of a α-diimine chelating ligand that complexes, to a variety of metal complexes including rhenium. The charge transfer associated with metal-bipyridine interaction is very intense and exhibits a strong, well-characterised MLCT making it an desirable ligand to study the photophysical and photochemical properties of.[271,272]

The energy of the luminescent excited state can also be influenced by the media the complex is in. Solvatochromism is defined by IUPAC as the pronounced change in the position and sometimes intensity of an electronic absorption or emission band, accompanying a change in polarity of the medium.[273] Positive solvatochromism corresponds to a red shift with increasing polarity. Therefore, a shift of the emission band to a lower energy corresponds to positive solvatochromism, illustrated in Figure 5.1. Most rhenium tricarbonyl α-diimine complexes exhibit positive solvatochromism.

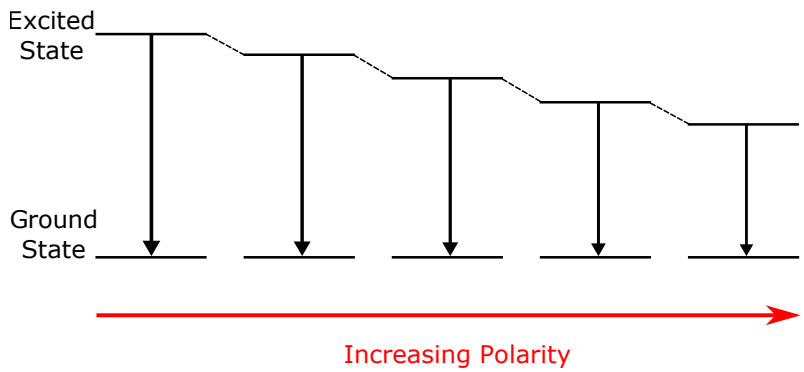


Figure 5.1: Illustration of electronic excited states that are stabilise at lower energy as the polarity of a solvent increases. This is associated with a red shift in energy of the emission band, thus corresponding to positive solvatochromism.

When a molecule has absorbed a photon of light, it promotes an electron from a low energy ground state to a higher energy excited state. This leads to the formation of a new electronic dipole, which in turn is stabilised or destabilised by the medium it is in, whereby a more polar solvent results in higher stability of the dipole. Following the excitation of the molecule resulting in the excited state, the solvent dipole reorientates around the excited state dipole, thus lowering the energy of the excited states.[274]

As well as positive solvatochromism, negative solvatochromism can also be observed however, this effect it is not as widely observed in rhenium carbonyl complexes as positive solvatochromism. Negative solvatochromism arises when the ground state is more polar then the excited state, and is stabilised by a polar solvent, thus the energy of the ground state is lowered.[275] This increases the energy gap between the ground state and the excited state, resulting in a shift of the emission wavelength. This is associated with a blue shift of the emission band with increasing polarity. Therefore, a shift of the emission band to higher energy corresponds to a negative solvatochromism, shown in Figure 5.2.

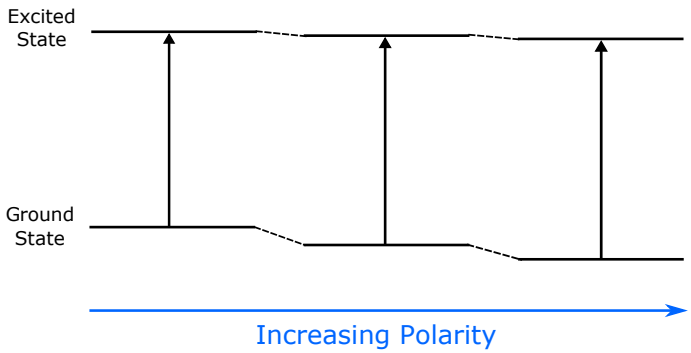


Figure 5.2: Illustration of the stabilisation of the ground state in a polar solvent showing a negative solvatochromism. This is causes a blue shift of the emission band as the polarity of the solvent increases.

5.1.1 Rhenium Tricarbonyl Bipyridine Complexes

Rhenium tricarbonyl bipyridine chloride, *fac*-[Re(CO)$_3$(bpy)(Cl)], has widely been explored due to its luminescent properties in solution at room temperature.[60,61,269,276] It has a well-studied triplet metal-to-ligand charge transfer excited state (^{3}MLCT).[60,61,276] Excitation into the singlet metal-to-ligand (^{1}MLCT) excited state leads to rapid inter-system crossing, as a result of the heavy metal spin coupling effect,[5] producing a ^{3}MLCT. It is the inter-system crossing that populates the emissive ^{3}MLCT excited state that is sufficiently long lived to be useful in catalysis.[276,277] These luminescent properties mean rhenium α-diimine complexes have potential applications for CO_2 reduction,[270,277–281] and as dyes for photosensitive solar cells.[51,53,282,283]

The photo ligand substitution has been reported for a variety of different metal bipyridine complexes, and they have been shown to generally proceed from the lowest vibrational level of the ^{3}MLCT excited state or from the triplet ligand-centred (^{3}LC) excited state.[68] In some cases the ^{3}LC results in the loss of a chloride ligand by thermal substitution of another ligand (pyridine, acetonitrile or phosphorus compounds) to

generate *fac*-[Re(CO)$_3$(bpy)(L)].[66] Photo ligand substitution of CO has been observed for rhenium complexes with phosphine groups in the axial position, these complexes can undergo ligand substitution following irradiation. Sato *et al.* reported the first observed photo ligand substitution of a *fac*-[Re(CO)$_3$(bpy)(Cl)] complex in 2007.[47] Previous to this publication, photo ligand substitution had not been seen for a *fac*-[Re(CO)$_3$(bpy)(Cl)] type complex. The chloride ligand can be thermally subsisted easily with other ligands in the presence of a silver cation, however the photodissociation of Cl^- or CO had not be observed. The first reported photo ligand substitution reaction was conducted in CH_3CN with a 313 nm excitation resulted in the formation of two dicarbonyl species. One species has the Cl^- and the CH_3CN groups respectively positioned in the *cis* and *trans* position to the bipyridine ligand with the second species being the reverse of this,[47] shown in Figure 5.4. However, the second species undergoes a interconversion between Cl^- and CO to give a third species. The TRIR of *fac*-[Re(CO)$_3$(bpy)(Cl) in CH_3CN can also be seen in Figure 5.3.

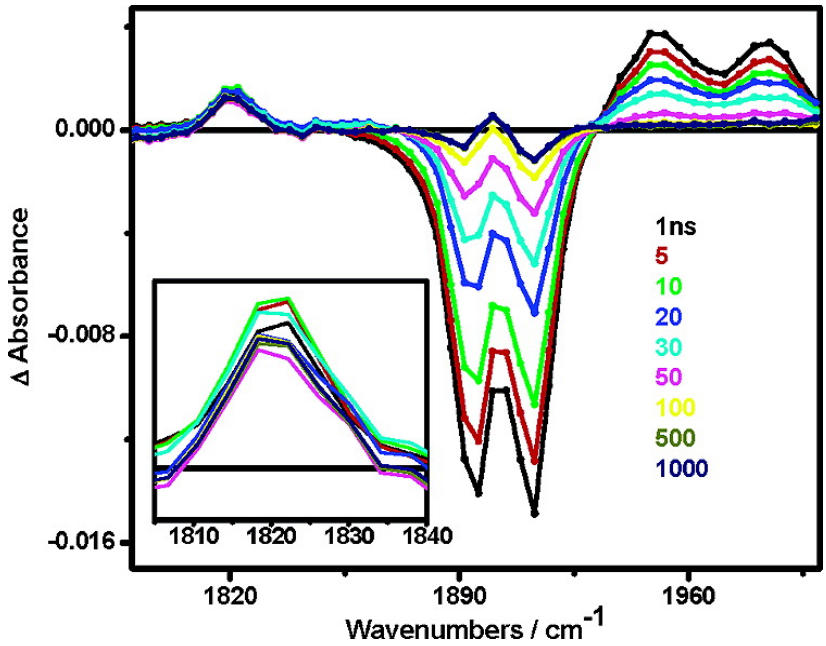


Figure 5.3: The *ns*-TRIR spectra of *fac*-[Re(CO)$_3$(bpy)(Cl)] in CH_3CN at selected time delays following a 266 nm excitation. The insert is an expansion of the low-wavenumber region which shows the band for the dicarbonyl photoproduct reported by Sato *et al.* Reproduced from reference 47.

The TRIR spectra showed that upon a 266 nm excitation a ^{3}MLCT was observed along with the parent bleaches shown in Figure 5.3. The band at 1824 cm^{-1}, that is assigned as the photoproduct, is first observed after 10 ps, with the second band at 1900 cm^{-1} emerging at later time delays as the ^{3}MLCT starts to decay away and the overlapping parent bleach recovers.[47] This observation showed that the photodissociation of CO is independent to the formation of the ^{3}MLCT excited state. It was concluded that following UV excitation, the photoproduct is vibrationally hot and relaxation of this state occurs on the picosecond time scale. This high energy excited state can then decay *via* two competitive processes; the intersystem crossing into the lowest ^{3}MLCT excited state or the photodissociation of CO.[47] Following these initial investigations the analysis was repeated by Sato *et al.* in tetrahydrofuran (THF).[66,68] The authors found that in the presence of THF *fac*-[Re(CO)$_3$(bpy)(Cl)] can either

populate a ^{3}MLCT excited state, which decays back down to the ground state, or a ^{3}LF state where CO loss occurs, followed by the coordination of THF to form the [Re(CO)$_2$(bpy)(THF)(Cl)] complex. Then the CO ligand flips and re-coordination of the CO occurs to afford the *mer*-[Re(CO)$_3$(bpy)(Cl)] complex. This shows that the photochemistry of just a simple *fac*-[Re(CO)$_3$(bpy)(Cl)] can be drastically altered by the solvent environment. The processes that occur following a UV excitation can be seen in Figure 5.4.

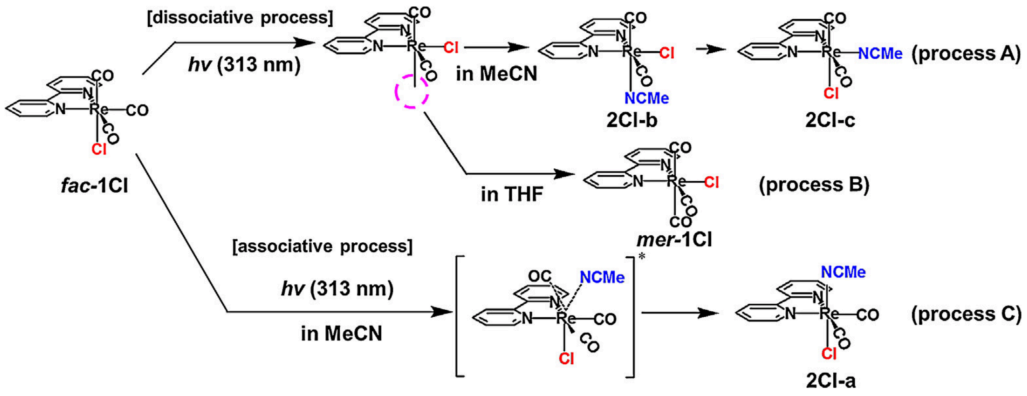


Figure 5.4: The mechanism involved in a photochemical reaction for a *fac*-[Re(CO)$_3$(bpy)(Cl) complex in CH$_3$CN and THF following a 313 nm which was reported by Sato *et al.* Reproduced from reference 68.

Calladine investigated whether a rhenium α-diimine complexes could form long-lived alkane complexes.[284] These alkane complexes are of particular interest as intermediates for C-H activation, as they have the ability to convert methane to methanol.[285] This conversation from a naturally abundant gas to a transportable liquid would make gas a viable energy source.[285] However, the issue with *fac*-[Re(CO)$_3$(bpy) (Cl)] is that they are insoluble in non-polar solvents like alkanes, so an alternative had to be found.[284] The solution was an alkyl substituted bipyridine; *fac*-[Re(CO)$_3$(bipyridine $-$R$_2$)(Cl)]. A few substituents were investigated, R = t-butyl, nonyl, CF$_3$ or ((CH$_2$)$_3$(CF$_2$)$_7$(CF$_3$)), but the most successful substituent was nonyl, where the α-diimine

used was 4,4'-dinonyl-2,2'-bipyrdine (dnb).[284] It was found that *fac*-$Re(CO)_3$(dnb)(Cl) was soluble in *n*-heptane which enabled the photophysics and photochemistry to be probed with TRIR.

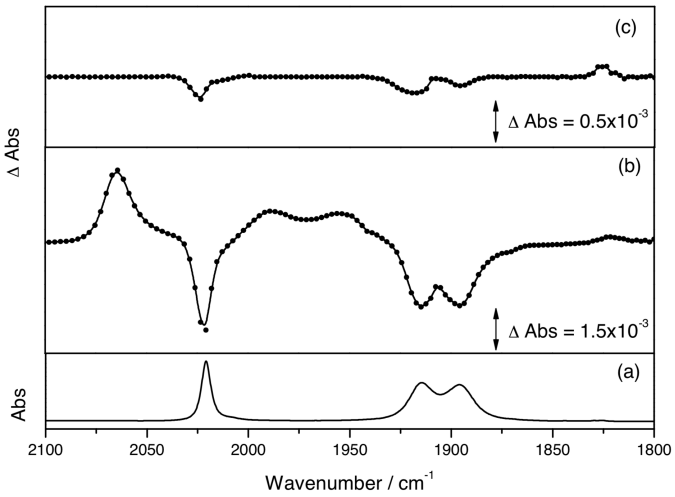


Figure 5.5: The FTIR spectrum of *fac*-$Re(CO)_3$(dnb)(Cl) in CH_3CN (a), the TRIR difference spectra (b) 10 and (c) 300 ns after 266 nm photolysis which shows the formation of the dicarbonyl species, *fac*-$Re(CO)_2$(dnb)(CH_3CN)(Cl) reported by Calladine. Reproduced from reference 284.

Both *ps* and *ns*-TRIR were carried out in CH_3CN and *n*-heptane to observe the photophysical properties. The *ps*-TRIR was implemented to observe the ^{3}MLCT state, which grew in with a lifetime of *ca.* 3 ps, this is associated with the vibrational cooling of the hot state. The lifetime of the ^{3}MLCT state was 41 ns in CH_3CN and 88 ns in *n*-heptane which is indicative behaviour following the energy gap law.[86] The dicarbonyl species in CH_3CN showed the generation of very distinct bands following an excitation of 266 nm, shown in Figure 5.5. However, in *n*-heptane these bands where more convoluted which could be due to the low solubility of the complex in *n*-heptane. It was difficult to assign the dicarbonyl species formed and it was thought that an organometallic alkane complex or an agostic complex involving the co-ordination of

the nonyl chain had formed. To help distinguish between the two dicarbonyl species generated following the excitation of 266 nm, the experiment was repeated in both cyclopentane and *n*-heptane under an atmosphere of CO. The rate of the reaction was measured a function of CO concentration, seen in Figure 5.6, which indicated that there was a second order rate constant ($k_c/_o$) for both *n*-heptane and cyclopentane.[284] This second order rate constant ruled out the formation of an organometallic alkane due to the fact previous work found there is a two-fold difference in $k_c/_o$ between the binding of *n*-heptane and cyclopentane.[284] This indicated that the nonyl chain was binding to the vacant site.

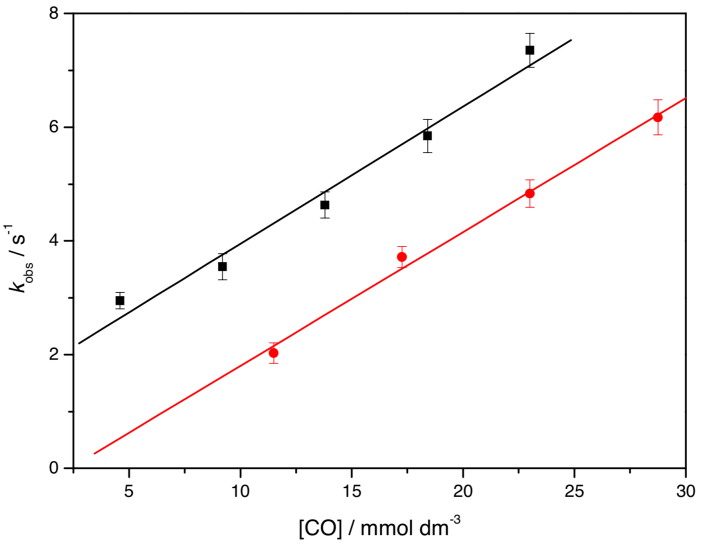


Figure 5.6: The kinetic plot for k_co *vs.* CO for the decay of the CO loss intermediate $[Re(CO)_2(dnb)Cl]$ after a 266 excitation in cyclopentane (black) and *n*-heptane (red), reported by Calladine. Reproduced from reference 284.

The methyl moiety on the end of the nonyl chain is co-ordinating to the vacant site poses a problem for the formation of organometallic alkane complexes. The nonyl chain is vital for the solubilisation of the complex into non-polar solvents, so an alternative approach to solubilise the complex in non-polar solvents is required. A po-

tential alternative to the nonyl chain is a previously studied perfluoroundecyl chain; $((CH_2)_3(CF_2)_7(CF_3))$.[286] This perfluorinated substituent could allow a rhenium complex to be investigated in a non-polar media, and if successful, a desired alkane could be doped into that media with the hope of forming an organometallic alkane complex. Broeke *et al.* noted that for a catalyst the anion requires 60 wt% of fluorine to achieve solubility in the fluorous phase.[287] It has been stated that the length and number of the perfluoroalkyl groups are important as they influence the solubility of the perfluoroalkylates compound in a fluorous solvent.[288] It is important that the perfluoroalkyl chain used as the substituent on the bipyridine has a spacer moiety. This is due to the strong electron-withdrawing properties of the perfluoroalkyl chain, which could have a dramatic effect on the catalyst and it's activity.[288] It has been reported that a three methyl spacers should be sufficient enough to insulate the bipyridine π system from the electron-withdrawing effect of the fluorinated alkyl chains.[279]

5.1.2 Perfluorinated Media

Another example of non-polar solvents is perfluorinated solvents, which are a potential alternative for solubilising the rhenium tricarbonyl complexes. Perfluorinated solvents are perfluorinated alkanes and cycloalkanes. Some examples of perfluorinated solvents include perfluoromethylcyclohexane (PFMCH) or perfluorohexane.[289] Perfluorinated solvents tend to have higher densities in comparison to their hydrocarbon counterparts, with their densities ranging from 1.7 to 1.9 g cm^{-3} and low permeabilites (ε_r 1-2).[289] They are also inert making them the perfect solvent for carrying out photochemical reactions. Perfluorinated solvents can also be doped with alkane and noble gases making photochemical substitution possible, as there is very little interaction between

the perfluorinated solvent and the metal centre. This can give rise to the photophysics of non-polar complexes being investigated in a very non-polar solvents.

As well as perfluorinated solvents, another perfluorinated media of interest is highly fluorinated hydrofluorocarbon (HFC) solvents. These which are commonly gas at room temperature but can have a low phase boundary enabling them to be liquid upon applying pressure or cooling. One example of a HFC reported in the literature is hexafluoropropane, which has been shown to dissolve a charged rhenium carbonyl complex.[290] Calculations found that hexafluoropropane would bind less favourably to a rhenium centre than an alkanes would.[290] Unlike perfluorinated solvents, hexafluoropropane is moderately polar, and has a similar dipole moment to CH_2Cl_2 (1.98 D *vs.* 1.14 D of CH_2Cl_2) making it a desirable media to solubilise a rhenium carbonyl complex.[291]

5.2 Aims

The aim of this Chapter was to investigate the photophysics and photochemistry of a rhenium tricarbonyl complex in a non-coordinating and non-polar medium. The first objective was to synthesise a functionalised bipyridine that could aid the solubility of a rhenium tricarbonyl complex in low polarity media. To help achieve this, two perfluorinated bipyridine ligands were synthesised and subsequently complexed the rhenium carbonyl complex, shown in Figure 5.7.

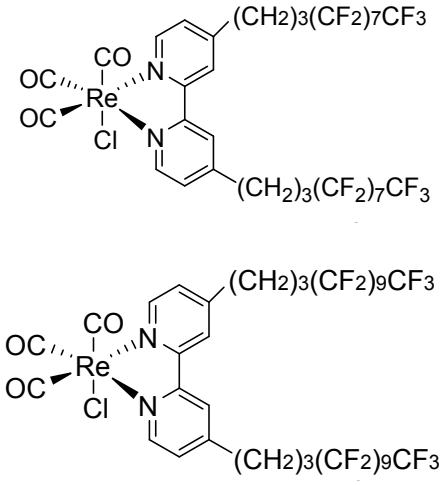


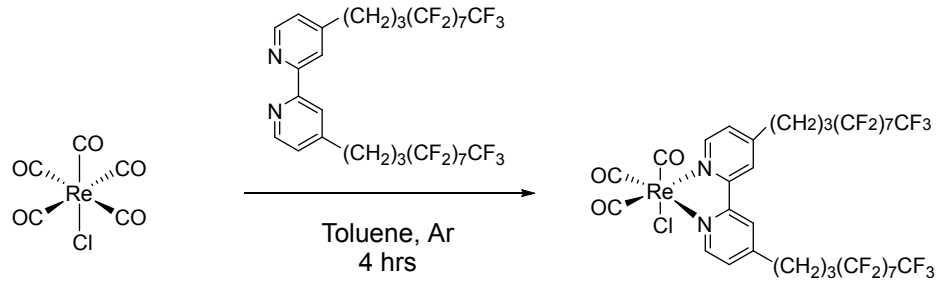
Figure 5.7: The structures of *fac*-$Re(CO)_3(bpy{-}R_F{}^8)Cl$ (top) and of *fac*-$Re(CO)_3(bpy{-}R_F{}^{10})Cl$ (bottom) which will be investigated within this Chapter.

To identify if the long perfluorinated chains had an effect on the photophysical properties of the complex, both luminescence and time-resolved infrared investigations were carried out. These investigations were compared to a non-fluorinated analogue, to fully understand the effect of the addition of the perfluorinated chains. The solubility of the rhenium bipyridine fluorinated tricabronyl complexes was also investigated to see if the addition of the perfluorinated bipyridine ligand aided the solubility of the complex.

5.3 Results

5.3.1 Synthesis of *fac*-Re(CO)$_3$(bpy–R$_F^n$)Cl Complexes

The synthesis of two rhenium bipyridine fluorinated tricabronyl species was carried out with the aim of probing a metal carbonyl complexes that is soluble in a non-polar solvent. The fluorinated rhenium bipyridine complex, *fac*-Re(CO)$_3$(bpy–R$_F^8$)Cl, was initially investigated to see if the addition of the long perfluorinated chain aided solubility of the species in a non-polar solvent. This complex was chosen due to the similarities to a non-fluorinated analogue which has previously been solubilised in an non-polar solvent.[284] The synthesis of *fac*-Re(CO)$_3$(bpy–R$_F^8$)Cl was conducted following similar synthetic preparations reported in literature,[279] the synthetic route can been seen in Scheme 5.1.



Scheme 5.1: The scheme for the synthesis of *fac*-Re(CO)$_3$(bpy–R$_F^8$)Cl following literature procedures in reference 279.

The synthesised *fac*-Re(CO)$_3$(bpy–R$_F^8$)Cl complex was characterised using ^{1}H NMR, ^{19}F NMR, FTIR, mass spectroscopy, elemental analysis and crystallography. The crystal structure obtained for *fac*-Re(CO)$_3$(bpy–R$_F^8$)Cl can be seen in Figure 5.8.

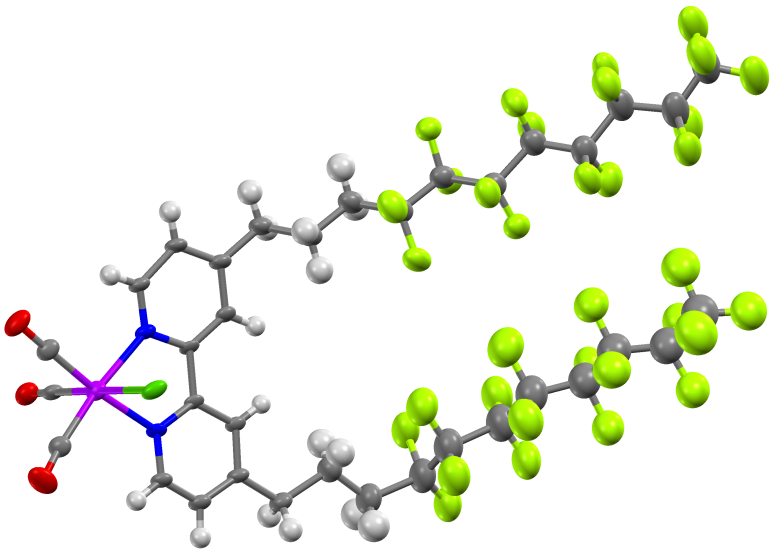


Figure 5.8: The single crystal structure of *fac*-Re(CO)$_3$(bpy−R$_F{}^8$)Cl.

From the crystallography measurements, the bond lengths were calculated and indicated that the C-C bond lengths of the propyl spacer between the bipyridine and the perfluoroundecane chain did not vary much. This suggests that the electron withdrawing effect of the perfluoroundecane chain is low. If there was an electron withdrawing effect, the C-C bond lengths would decrease for the carbon atom bound to the perfluoroundecane chain, which was not observed. Another observation to note from the crystallography is the solid state packing, this indicates that *fac*-Re(CO)$_3$(bpy−R$_F{}^8$)Cl packs *via* the perfluoroundecane chain with the fluorinated chain stacking above one another, shown in Figure 5.9. This solid state fluorinated chain stacking might result in the fluorinated chains aggregating once in solution.

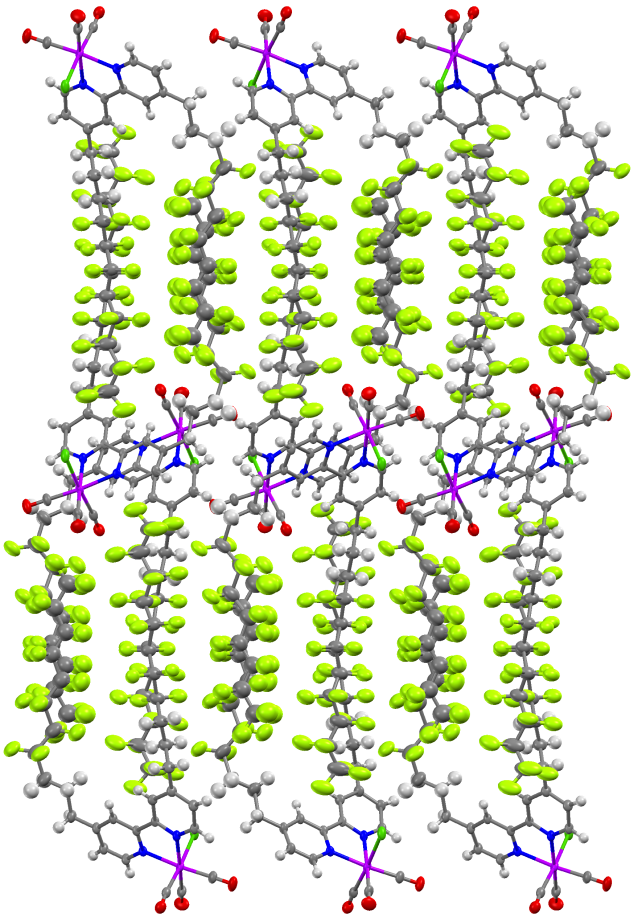
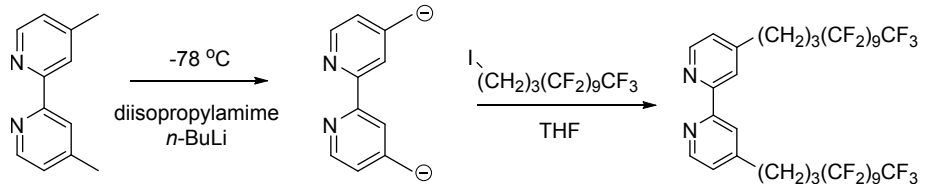


Figure 5.9: The solid state packing of *fac*-Re(CO)$_3$(bpy–R$_F{}^8$)Cl.

The solubility of *fac*-Re(CO)$_3$(bpy–R$_F{}^8$)Cl was investigated in a range of conventional solvents, and the addition of perfluoroundecane chain resulted in the solubility of *fac*-Re(CO)$_3$(bpy–R$_F{}^8$)Cl decreasing in solvents like tetrahydrofuran (THF) and choloform (CH_3Cl). Following this, the solubility was investigated in more non-polar solvents, such as *n*-heptane and perfluoromethylcyclohexane (PFCMH). It was found that *fac*-Re(CO)$_3$(bpy–R$_F{}^8$)Cl was insoluble in both, forming a suspension in PFMCH. To overcome this, the length of the perfluorinated chain was increased to see if this would aid the solubility in a non-polar solvents. It has been previously reported

in literature that increasing the fluorine percentage across the ligand by 2.5% can drastically improve the solubility in a perfluorinated solvent.[292] Therefore, a longer perfluorinated chain was bound to the bipyridine ligand. The synthesis of a longer perfluorinated bipyridine was conducted following a synthesis reported by Bennett *et al.*,[286] which can be seen in Scheme 5.2.



Scheme 5.2: The scheme for the synthesis of 4,4'-bis[1H, 1H, 2H, 2H, 3H, 3H-perfluorotridecyl]-2,2'-bipyridine following literature procedures from reference 286.

The synthesis of 4,4'-bis[1H, 1H, 2H, 2H, 3H, 3H-perfluorotridecyl]-2,2'-bipyridine, seen in Scheme 5.2, proved more difficult to synthesise than the shorter perfluorinated chain analogue. It was found that the key to isolating the 4,4'-bis[1H, 1H, 2H, 2H, 3H, 3H-perfluorotridecyl]-2,2'-bipyridine ligand was during the work up of experiment, where the use of perfluorotoluene as well as toluene was needed to separate the two mono and bis isomers.^{1}H NMR allowed for characterisation of the ligand as it was clear to identify the non substituted 4,4' position by the presence of a strong singlet from the CH_3 group. Due to the size and molecular weight of the ligand, it was difficult to identify 4,4'-bis[1H, 1H, 2H, 2H, 3H, 3H-perfluorotridecyl]-2,2'-bipyridine using mass spectrometry. However, using ^{1}H NMR allowed the successful characterisation. The 4,4'-bis[1H, 1H, 2H, 2H, 3H, 3H-perfluorotridecyl]-2,2'-bipyridine ligands was then complexed to the rhenium centre *via* the same synthetic method as *fac*-Re(CO)$_3$(bpy$-$R$_F{}^8$)Cl seen in Scheme 5.1. The solubility of *fac*-Re(CO)$_3$(bpy$-$R$_F{}^{10}$)Cl in non-polar solvents was investigated and will be discussed later in this Chapter.

5.3.2 Luminescence Spectroscopy of *fac*-Re(CO)$_3$(bpy−R)Cl

This Section will discuss the phosphorescence of two rhenium tricarbonyl bipyridine analogues which were measured to see if the energy of their luminescence changed as a result of the long perfluorinated chain on the 2,2'-bipyridine ligand. The emission study was conducted in a range of solvents to investigate any solvatochromic affects. To fully gauge whether the perfluorinated chain altered the luminescence, the non-fluorinated analogue *fac*-Re(CO)$_3$(dnb)Cl was probed as a direct comparison to *fac*-Re(CO)$_3$(bpy−R$_F$[8])Cl.

5.3.2.1 Emission Study of *fac*-Re(CO)$_3$(dnb)Cl

Initially, the luminescence of *fac*-Re(CO)$_3$(dnb)Cl was investigated to see how the polarity of a solvent altered the energy of the excited state. The phosphorescence of *fac*-Re(CO)$_3$(dnb)Cl was probed in CH_3CN (ε = 37.5), EtOH (ε = 24.6), CH_2Cl_2 (ε = 8.9), THF (ε = 7.6), toluene (ε = 2.3) and *n*-heptane (ε = 1.9). The position of the emission band in the different solvents is shown in Figure 5.10, where the wavelength of the emission peak has been plotted against the dielectric constant of the solvent.

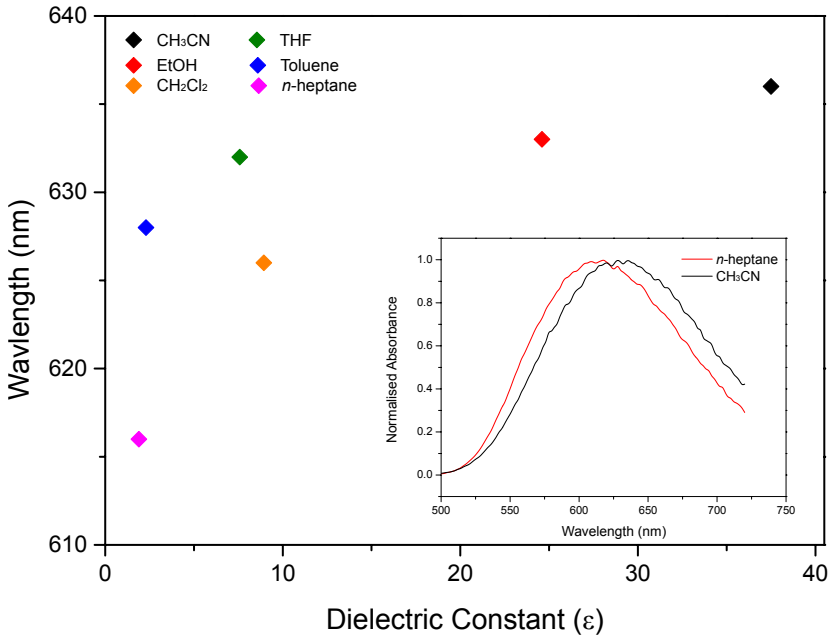


Figure 5.10: A plot of wavelength *vs* dielectric constant of the emission peaks to indicate how the polarity effects the energy of the excited state of *fac*-$Re(CO)_3(dnb)Cl$ in a range of solvents. The inset shows the emission spectra of *fac*-$Re(CO)_3(dnb)Cl$ in acetonitrile a polar solvent, and *n*-heptane a non-polar solvent, which indicates a blue shift of the emission band which is indicative of positive solvatochromism

From Figure 5.10 it can be seen that as the polarity of the solvent increases, the emission band is undergoing a red shift in energy, which is characteristic of positive solvatochromism. The energy of the emission band in *n*-heptane is *ca.* 616 nm, and as the polarity of the solvent is increased, a red shift is observed to 626 nm for CH_2Cl_2 ($\varepsilon = 8.9$) and then *ca.* 636 nm for CH_3CN. There is a slight discrepancy for toluene and THF as they do not fit this trend, however this could be due to the low solubility of *fac*-$Re(CO)_3(dnb)Cl$ in these solvents. If the position of the emission band in *n*-heptane and CH_3CN is compared, the red shift in more polar solvents can clearly been seen. The inset of Figure 5.10 shows the emission band of *fac*-$Re(CO)_3(dnb)Cl$ in *n*-heptane and CH_3CN, the position and shape of the bands indicate the excited state is a ^{3}MLCT excited state.

The luminescence of *fac*-Re(CO)$_3$(bpy–R$_F{}^8$)Cl was also probed in CH_3CN ($\varepsilon = 37.5$), EtOH ($\varepsilon = 24.6$), CH_2Cl_2 ($\varepsilon = 8.9$), THF ($\varepsilon = 7.6$) and toluene ($\varepsilon = 2.3$), where it was observed that the energy of the emission peak was shifted to lower energy in solvents of a lower polarity, which can be seen in Figure 5.11.

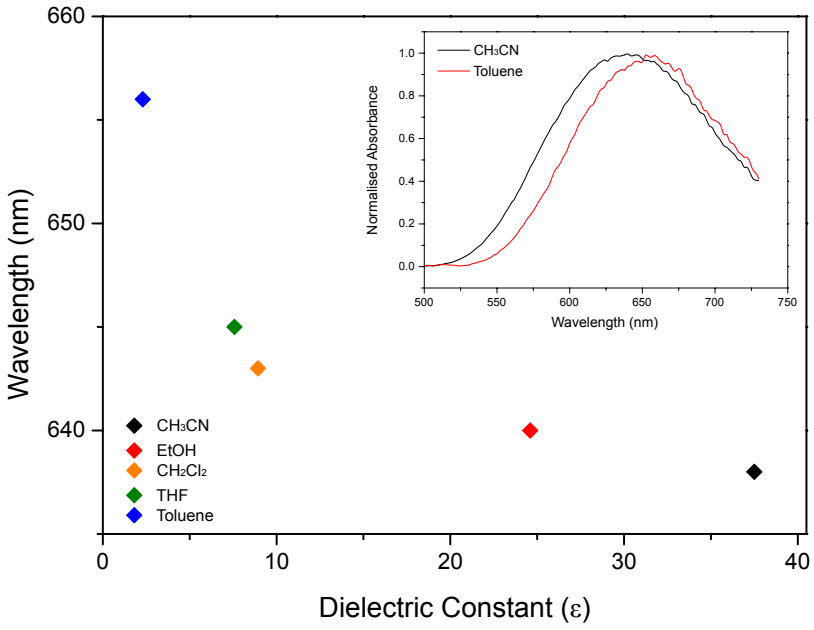


Figure 5.11: A plot of wavelength *vs* dielectric constant of the emission peaks to indicate how the polarity effects the energy of the excited state of *fac*-Re(CO)$_3$(bpy–R$_F{}^8$)Cl in a range of solvents. The inset shows the emission spectra of *fac*-Re(CO)$_3$(bpy–R$_F{}^8$)Cl in acetonitrile a polar solvent, and toluene a non-polar solvent, which indicates a blue shift of the emission band which is indicative of negative solvatochromism.

This shift observed in Figure 5.11 shows that as the polarity of the solvent decrease the emission band shifts to a lower energy, which is indicative of negative solvatochromism. As you increase the polarity, the energy of the excited state blue shifts from *ca.* 656 nm, to 643 nm, to 637 nm in toluene, CH_2Cl_2 and CH_3CN respectively, which is a result of the negative solvatochromic nature of the complex. There is better agreement for all the solvents in Figure 5.11 compared to that seen for *fac*-Re(CO)$_3$(dnb)Cl. Also due to *fac*-Re(CO)$_3$(bpy–R$_F{}^8$)Cl being insoluble in *n*-heptane,

the lowest polarity solvent investigated for *fac*-Re(CO)$_3$(bpy–R$_F{}^8$)Cl was toluene. The observation of negative solvatochromism for *fac*-Re(CO)$_3$(bpy–R$_F{}^8$)Cl is the opposite to that observed for *fac*-Re(CO)$_3$(dnb)Cl which exhibited positive solvatochromism. This suggests the addition of the long perfluorinated chain is having some affect on the energy of the excited state, which is seen by a change in the phosphorescence. The inset in Figure 5.11 shows the blue shift of the emission band in CH_3CN and toluene, which clearly indicates negative solvatochromism for *fac*-Re(CO)$_3$(bpy–R$_F{}^8$)Cl. The position and shape of the emissions bands also suggests this is the phosphorescence from a ^{3}MLCT excited state. The solid state crystal packing of *fac*-Re(CO)$_3$(bpy–R$_F{}^8$)Cl shows the complex packs *via* the perfluorinated chain, so it could be possible that the perfluorinated chain aggregating in solution, accounting for the switch from positive to negative solvatochromism.

This theory was investigated by probing of *fac*-Re(CO)$_3$(bpy–R$_F{}^8$)Cl at varying concentrations, to see if at a lower concentration the same solvatochromic effect was observed. To begin with the phosphorescence of *fac*-Re(CO)$_3$(bpy–R$_F{}^8$)Cl was probed in CH_3CN to see if a lower concentration would alter the energy of the ^{3}MLCT excited state. Figure 5.12 shows the emission spectra of *fac*-Re(CO)$_3$(bpy–R$_F{}^8$)Cl at a high and low concentration in CH_3CN, where it can be seen that upon dilution the energy of the excited state does not appear to change, with the emission band having an energy of *ca.* 640 nm.

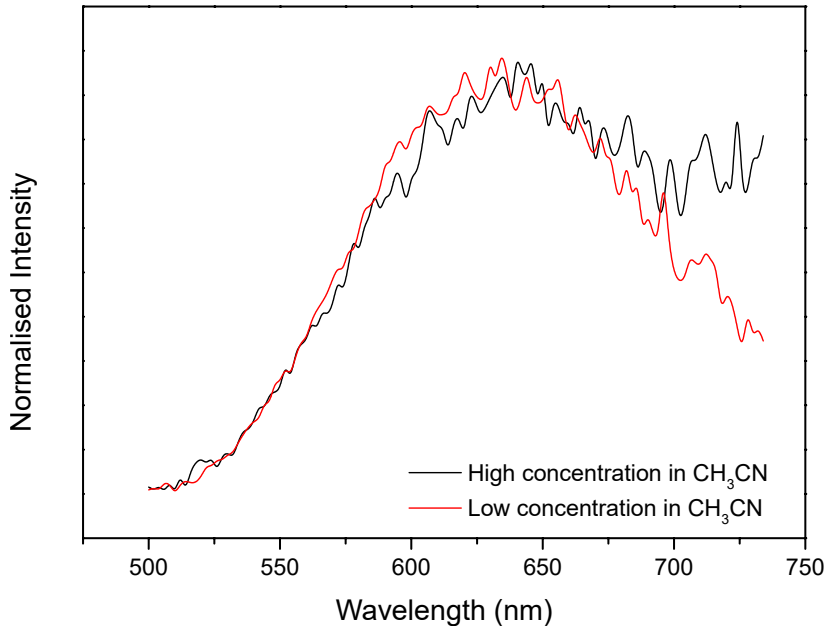


Figure 5.12: The emission spectra of *fac*-Re(CO)$_3$(bpy–R$_F$^{8})Cl in acetonitrile at a high and low concentration to probe the effect on the solvatochromism.

Following this observation, *fac*-Re(CO)$_3$(bpy–R$_F$^{8})Cl was probed in the non-polar solvent toluene, to see if like CH_3CN, the emission band would not shift. This would eliminate the theory that in solution the the perfluorinated chain were aggregating. From Figure 5.13 it is clear that that at lower concentrations in toluene there is a blue shift in the energy of the ^{3}MLCT excited state. The energy of the emission band is seen to shift to higher energy, with the lower concentration emission band having an energy of *ca.* 610 nm. The low concentration band in toluene is also at higher energy than the low concentration band in CH_3CN. This indicates that as the concentration of *fac*-Re(CO)$_3$(bpy–R$_F$^{8})Cl is lowered in both a polar or non-polar solvent, the solvatochromic affect is observed to switch from negative solvatochromism to positive solvatochromism.

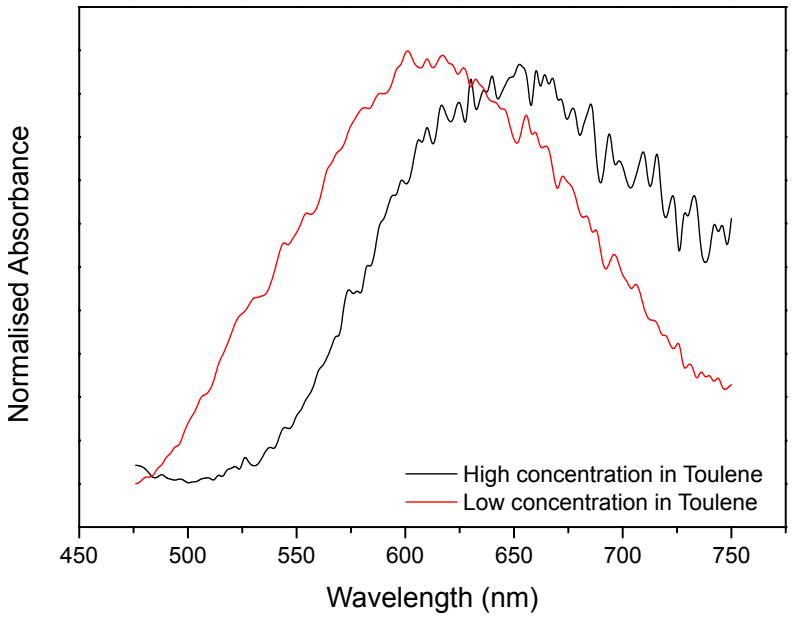


Figure 5.13: The emission spectra of *fac*-Re(CO)$_3$(bpy−R$_F$^{8})Cl in toluene at a high and low concentration to probe the effect on the solvatochromism.

This observation seen for the luminescence conducted at lower concentration suggested that in solution, the perfluorinated chain are aggregating together,[293] which has resulted in the observation of negative solvatochromism for *fac*-Re(CO)$_3$(bpy−R$_F$^{8})Cl. It is known from literature that the photochemistry of *fac*-[Re(CO)$_3$(bpy)Cl] complexes can vary depending on the solvent but also on the condition of the experiment, resulting in either CO loss of isomerisation.[66,68] Therefore if *fac*-Re(CO)$_3$(bpy−R$_F$^{8})Cl is aggregating in solution, the photochemistry could be altered.

5.3.3 Solubility Investigations of *fac*-Re(CO)$_3$(bpy−R$_F$^{n})Cl

The solubility of the two perfluorinated rhenium carbonyl complexes was probed in non-polar solvents. The aim of this Chapter was to synthesise a rhenium car-

bonyl complex that is soluble in a non-polar solvent in the hope of ultimately investigating its photophysics and photochemistry in a non-polar enivrionment. The two perfluorinated rhenium carbonyl complexes *fac*-Re(CO)$_3$(bpy–R$_F$^{8})Cl and *fac*-Re(CO)$_3$(bpy–R$_F$^{10})Cl were probed in perfluoromethylcyclohexane (PFMCH) and hexafluoropropane in both the gas and liquid phase.

Initially, the solubility of *fac*-Re(CO)$_3$(bpy–R$_F$^{8})Cl was investigated in PFMCH. From the luminescence spectroscopy, it was known that *fac*-Re(CO)$_3$(bpy–R$_F$^{8})Cl was insoluble in *n*-heptane. However, the addition of the perfluorinated chain should aid solubility in a perfluorinated solvent.[288] Figure 5.14 shows the FTIR spectra of *fac*-Re(CO)$_3$(bpy–R$_F$^{8})Cl in CH_2Cl_2. The spectrum shows three ν(CO) bands at 2022, 1918 and 1896 cm^{-1}, which clearly shows the complex has C$_s$ symmetry. This indicated the complex is soluble in CH_2Cl_2. When *fac*-Re(CO)$_3$(bpy–R$_F$^{8})Cl was solubilised in in PFMCH it had very sharp bands with a very low absorbance, which indicates that the complex is not very soluble in PFMCH, and was most likely forming a suspension. This suggests the addition of the perfluorodecyl chain was not sufficient in solubilising the complex in a non-polar, non-coordinating solvent.

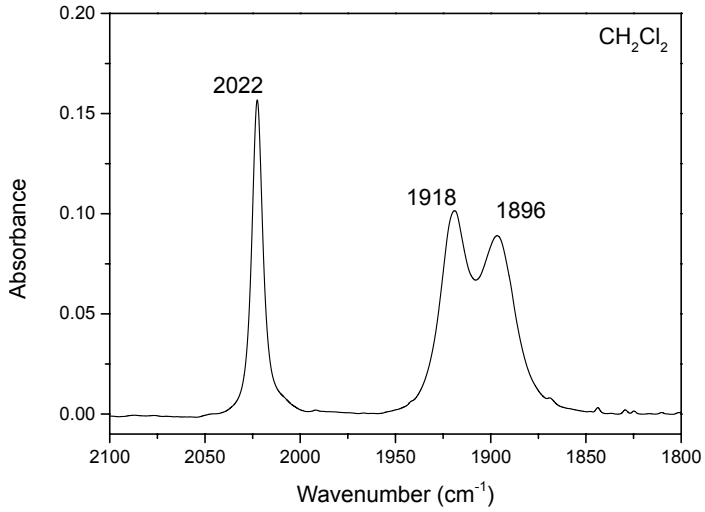


Figure 5.14: The FTIR spectrum of *fac*-Re(CO)$_3$(bpy–R$_F$^{8})Cl in CH_2Cl_2.

The longer perfluorododecyl chain of *fac*-Re(CO)$_3$(bpy–R$_F{}^{10}$)Cl resulted in the overall fluorine percentage across the complex to increase from 46.7 % to 50.43 %. This should improve the solubility of the complex in PFMCH, however it is not as high as the reported 60 % that is needed to fully solubilise a complex in the fluorous phase.[287] The solubility of *fac*-Re(CO)$_3$(bpy–R$_F{}^{10}$)Cl in PFMCH and CH_2Cl_2 can be seen in Figure 5.15.

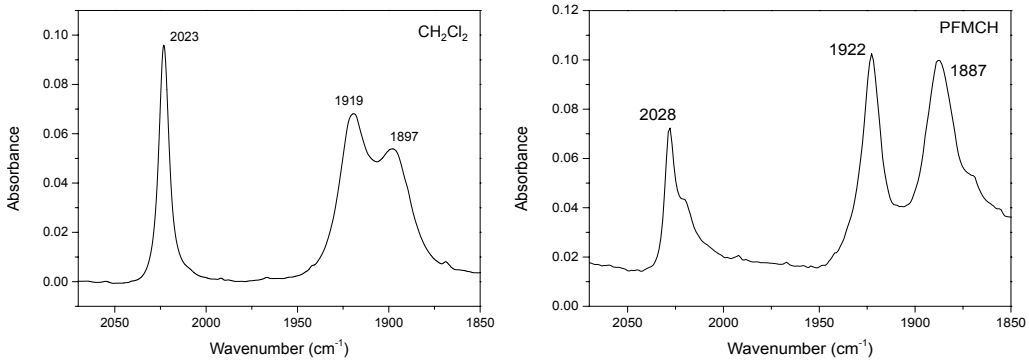


Figure 5.15: The FTIR spectrum of *fac*-Re(CO)$_3$(bpy–R$_F{}^{10}$)Cl in CH_2Cl_2 (left) and PFMCH (right).

Figure 5.15 shows the fully solubilised *fac*-Re(CO)$_3$(bpy–R$_F{}^{10}$)Cl in CH_2Cl_2 with bands at 2023, 1919 and 1987 cm^{-1}. It also shows the FTIR spectrum of *fac*-Re(CO)$_3$(bpy$^-$ R$_F{}^{10}$)Cl in PFMCH, which has much sharper bands at 2028, 1922 and 1887 cm^{-1}, which indicated that it is partially solubilised, and like *fac*-Re(CO)$_3$(bpy –R$_F{}^{8}$)Cl, it is forming a suspension in PFMCH. The solubility has improved by lengthening of the perfluorododecyl chain, however it is not long enough to sufficiently dissolve the complex in PFMCH. In an attempt to improved the solubility of *fac*-Re(CO)$_3$(bpy–R$_F{}^{10}$)Cl in PFMCH, a perfluorinated gas hexafluoropropane, was dissolved into PFMCH. Figure 5.16 shows the IR spectra of both the PFMCH and hexafluoropropane. Both the IR spectra have a lot of overlapping bands however,

hexafluoropropane has two bands distinct at 1410 and 1115 cm^{-1}, which were used monitor the solubility of hexafluoropropane in PFMCH.

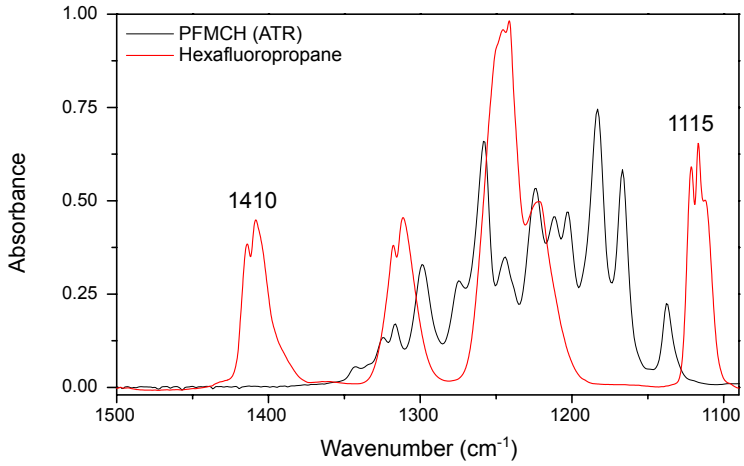


Figure 5.16: The IR spectra of PFMCH and hexafluoropropane gas.

Once hexafluoropropane was successfully solubilised in PFMCH, *fac*-Re(CO)$_3$(bpy–R_F[10])Cl was added to the mixture. The dielectric constant of hexafluoropropane is similar to that of CH_2Cl_2, therefore it should aid the solubility of the complex.[290] The FTIR spectrum of *fac*-Re(CO)$_3$(bpy–R_F[10])Cl in PFMCH and hexafluoropropane can be seen in Figure 5.17. Three ν(CO) bands are observed at 2038, 1918 and 1868 cm^{-1}, which are assigned to *fac*-Re(CO)$_3$(bpy–R_F[10])Cl. The main issue with this method is both PFMCH and hexafluoropropane absorb in the CO region, therefore in-order to obtain the FTIR a very small path-length was needed, and increasing the path-length resulted in the loss of the ν(CO) bands.

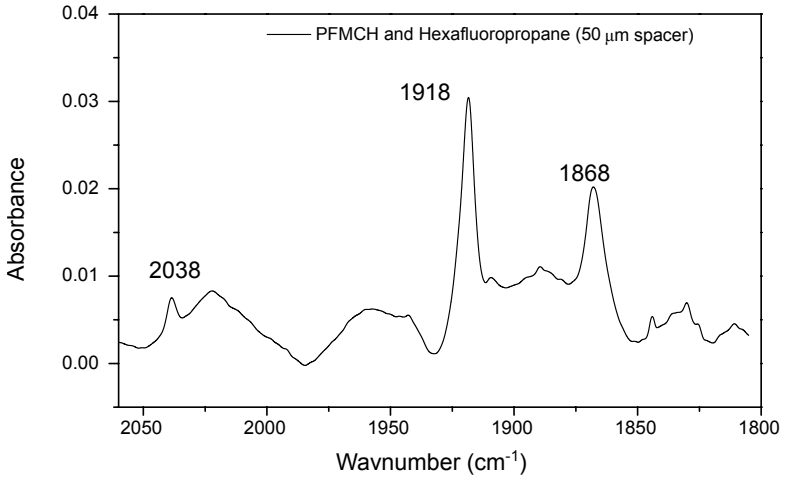


Figure 5.17: The FTIR spectra of *fac*-Re(CO)$_3$(bpy–$R_F{}^{10}$)Cl in CH_2Cl_2 in PFMCH doped with hexafluoropropane gas.

Following the bubbling of hexafluoropropane into the PFMCH solution, *fac*-Re(CO)$_3$ (bpy–$R_F{}^{10}$)Cl was dissolved directly into liquid hexafluoropropane to see if it would be soluble. The solubility of *fac*-Re(CO)$_3$(bpy –$R_F{}^{10}$)Cl in hexafluoropropane should be greater due to the increased dipole moment. The FTIR spectrum for *fac*-Re(CO)$_3$(bpy$^-$ $R_F{}^{10}$)Cl in hexafluoropropane is shown in Figure 5.18, with two visible bands at 2028 and 1906 cm^{-1}. There are still a large amout of hexafluoropropane bands which are highly absorbing in the CO region, however it is possible to observe two of the ν(CO) bands. Although a good solubility of *fac*-Re(CO)$_3$(bpy–$R_F{}^{10}$)Cl in hexafluoropropane is observed, the overlapping bands in the CO region do not make it a good solvent for further time-resolved spectroscopic techniques.

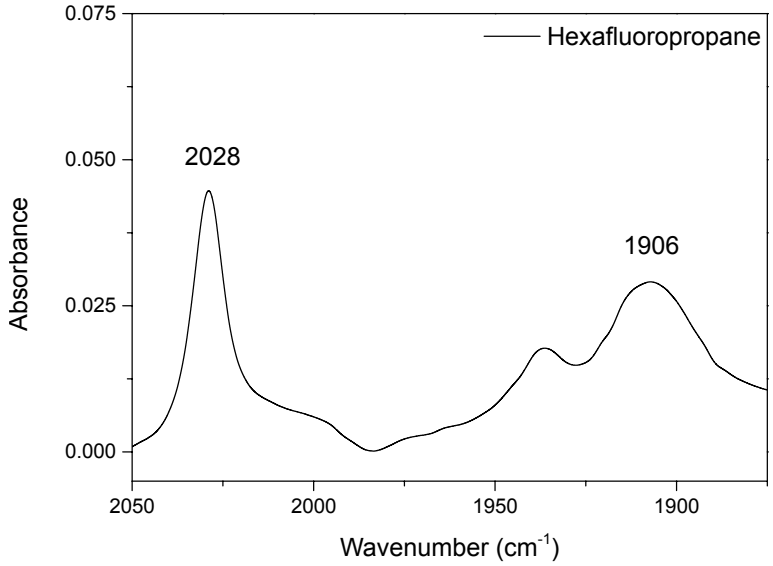


Figure 5.18: The FTIR spectra of *fac*-Re(CO)$_3$(bpy−R$_F$^{10})Cl in CH_2Cl_2 in liquid hexafluoropropane.

5.3.4 Time Resolved Infrared Investigation of *fac*-Re(CO)$_3$(bpy−R)Cl

Both *ps* and *ns*-TRIR was used to probe the photophysics of Re(CO)$_3$(bpy−R$_F$^{8})Cl and Re(CO)$_3$(dnb)Cl at 355 nm in CH_3CN. Following the improved solubility of Re(CO)$_3$(bpy−R$_F$^{10})Cl, the photochemistry of this complex was probed at 266 nm in CH_2Cl_2 to see if the perfluorinated chain alters the ability of the complex to undergo CO loss.

5.3.4.1 TRIR Investigation of *fac*Re(CO)$_3$(dnb)Cl

The *ps* and *ns*-TRIR spectra can be seen in Figure 5.19, where following excitation at 355 nm, the parent bleaches are clearly observed at 2014, 1909 and 1892 cm^{-1}. At

early time delays the transient species is seen at 2053, 1980 and 1946 cm^{-1} following the vibrational cooling of the hot state ($\tau = 4.5$ ps). The shift of the transient bands to higher energy is indicative of the formation of a ^{3}MLCT excited state, matching literature reports of non substituted bipyridine complexes, *fac*-$Re(CO)_3(bpy)Cl$.[66,294,295]

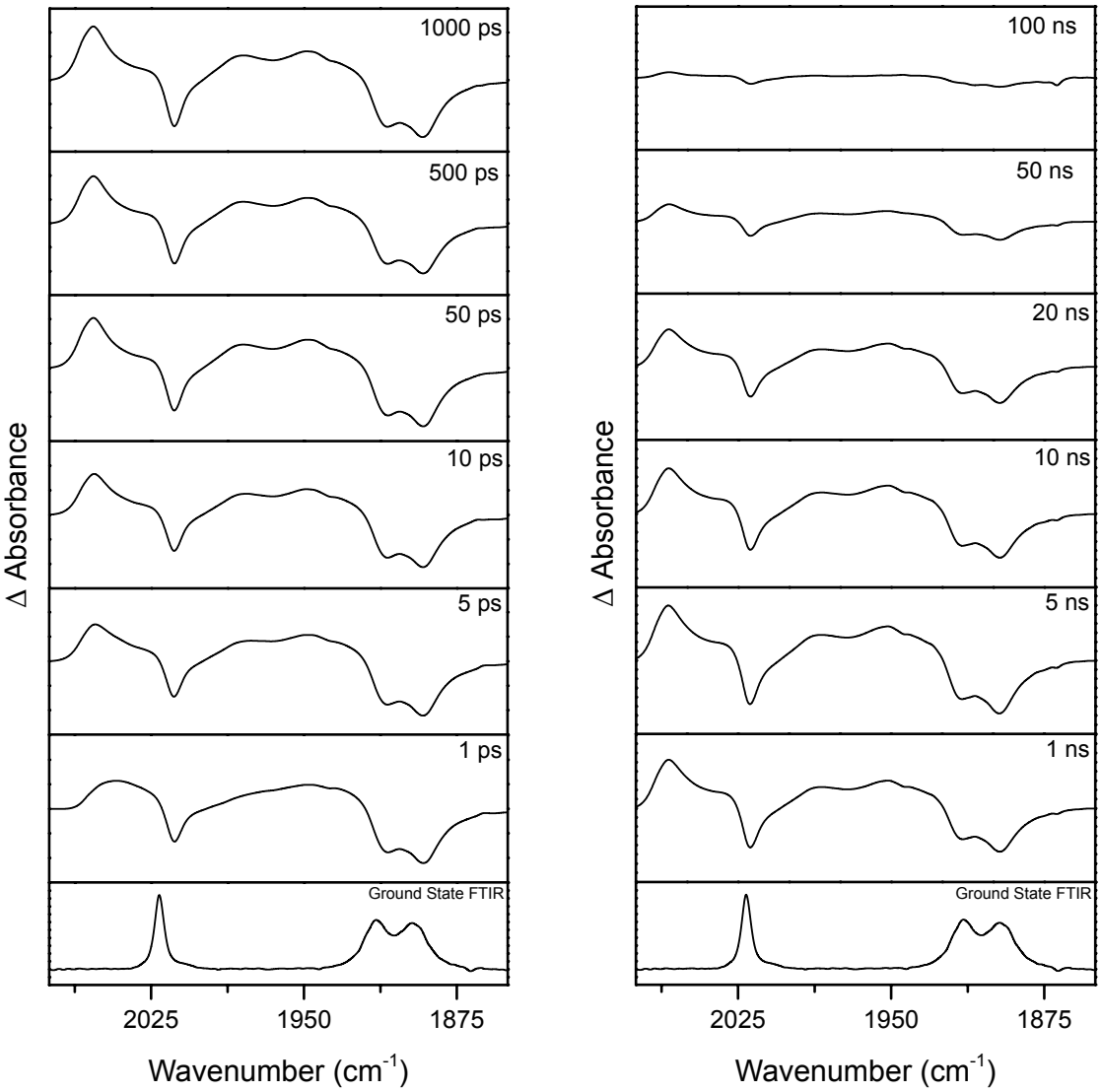


Figure 5.19: The *ps*-TRIR (left) and *ns*-TRIR of *fac*-$Re(CO)_3(dnb)Cl$ CH_3CN following a 355 nm excitation.

The ^{3}MLCT excited state, that is seen on the picosecond timescale, is long lived onto the nanosecond timescale where it is seen to decay. The ^{3}MLCT excited state can

be seen to decay back down to the ground state, which is accompanied by the recovery of the parent bleaches. The decay of the ^{3}MLCT excited state has a lifetime of *ca.* 40 ns, which is comparable to that of a rhenium tricarbonyl bipyridine complex.[66] The kinetic plot for the decay of the ^{3}MLCT excited state and the recovery of the parent can be seen in Figure 5.20. The observation of a ^{3}MLCT excited state is consistent with the luminescence measurements for *fac*-Re(CO)$_3$(dnb)Cl.

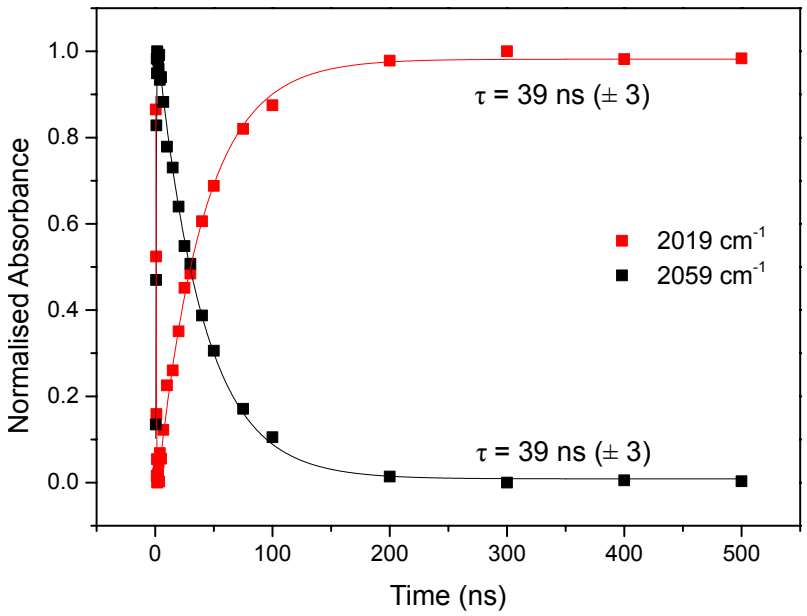


Figure 5.20: The kinetic plot for the decay of the ^{3}MLCT and the recovery of the parent of *fac*-Re(CO)$_3$(dnb)Cl following a 355 nm excitation in CH_3CN.

5.3.4.2 TRIR Investigation of *fac*-Re(CO)$_3$(bpy−R$_F{}^n$)Cl

The *ps* and *ns*-TRIR of *fac*-Re(CO)$_3$(bpy−R$_F{}^8$)Cl in CH_3CN is shown in Figure 5.21, where transient bands are observed at 2053, 1982 and 1948 cm^{-1}, along with parent bleaches at 2014, 1911 and 1891 cm^{-1}. The vibrational hot state is seen too cool with a lifetime of $\tau = 3$ ps. Again the transient bands shift to higher energy which indicates

the formation of a ^{3}MLCT excited state which supports the observation seen for the luminescence spectroscopy.

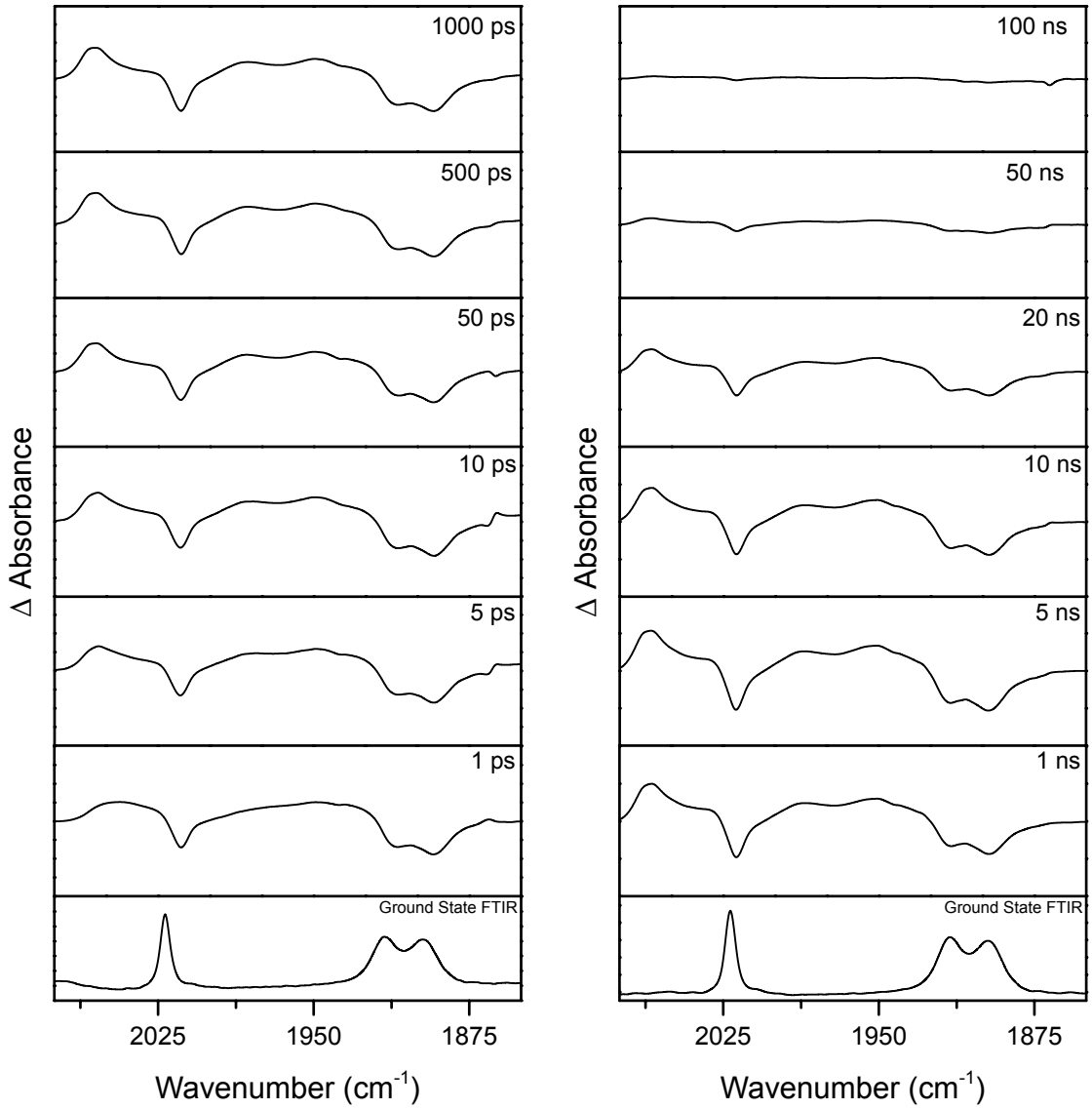


Figure 5.21: The *ps*-TRIR (left) and *ns*-TRIR of *fac*-Re(CO)$_3$(bpy−R$_F$^{8})Cl CH_3CN following a 355 nm excitation.

The decay of the ^{3}MLCT excited state can be seen in Figure 5.22. Similar to the decay observed for *fac*-Re(CO)$_3$(dnb)Cl, the ^{3}MLCT excited state of *fac*-Re(CO)$_3$(bpy−R$_F$^{8})Cl decays as the parents recovers, suggesting the ^{3}MLCT excited

state is decaying back down to the ground state. The decay of the ^{3}MLCT excited state appears to be slightly faster when comparing the *ns*-TRIR spectra of *fac*-Re(CO)$_3$(dnb)Cl and *fac*-Re(CO)$_3$(bpy–R$_F{}^8$)Cl. Figure 5.22 shows the kinetic plot for the decay of the ^{3}MLCT excited state and recovery of the parent, which indicates the ^{3}MLCT excited state has a lifetime of $\tau = 28$ ns. This is slightly faster than the lifetime observed for *fac*-Re(CO)$_3$(dnb)Cl (39 ns), which suggests the addition of the perfluorinated chains are having a very small effect on the lifetime, however it appears the propyl spacer is sufficiently insulting the bipyridine from the strong electron withdrawing effects.

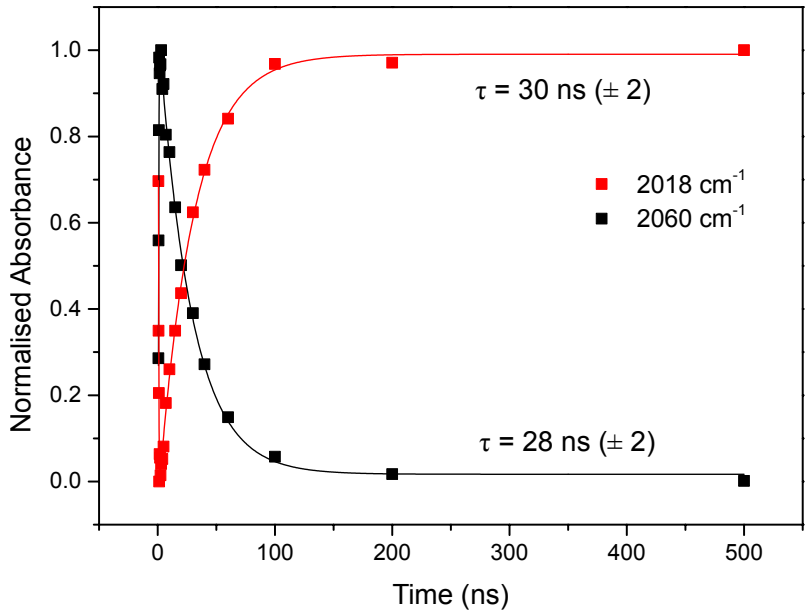


Figure 5.22: The kinetic plot for the decay of the ^{3}MLCT and the recovery of the parent of *fac*-Re(CO)$_3$(bpy–R$_F{}^8$)Cl following a 355 nm excitation in CH_3CN.

The *ns*-TRIR of *fac*-Re(CO)$_3$(bpy–R$_F{}^8$)Cl suggests the addition of the perfluorinated chain is not altering the photophysics of the ^{3}MLCT excited state. Following this the photochemistry of *fac*-Re(CO)$_3$(bpy–R$_F{}^{10}$)Cl was probed. Previous investigations show that when a *fac*-Re(CO)$_4$(bpy)Cl complexes are excited at a higher energy (266

nm), they can undergo CO loss.[47,68,284] The *ns*-TRIR for *fac*-Re(CO)$_3$(bpy–R$_F$^{10})Cl is shown in Figure 5.23.

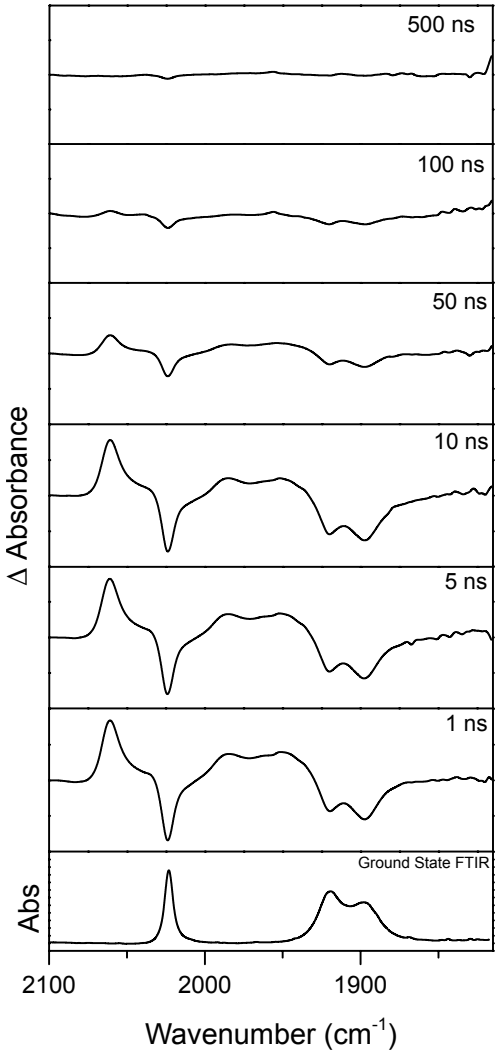


Figure 5.23: The *ns*-TRIR of *fac*-Re(CO)$_3$(bpy–R$_F$^{10})Cl CH_2Cl_2 following a 266 nm excitation.

Following the 266 nm excitation, the parent bleaches of *fac*-Re(CO)$_3$(bpy–R$_F$^{10})Cl can be seen at 2023, 1919 and 1986 cm^{-1}. Directly following excitation the transient bands are observed at 2061, 1986 and 1951 cm^{-1}, which suggests this state grows in on

the picosecond timescale. One thing to note is there only appears to be the presence of one transient species, which has bands that are shifted higher in comparison to the parent bands, which is characteristic of a ^{3}MLCT excited state. There are no ν(CO) bands shifted to lower energy which are indicative of the dicarbonyl species.[47] This indicates that the complex has not under gone CO loss. If the complex had undergone CO loss it would have most likely would have occurred on the picosecond timescale.[66] Following this a solvated species would of formed, which would of had to decay and recombine with CO. However, the experiment was not conducted in the presence of CO, therefore is it a very unlikely that there was CO recombination.

The most likely observation for the shift to higher energy of the three transient bands in the formation of a ^{3}MLCT excited state. It is known from the luminescence spectroscopy that the perfluorinated complexes exhibit negative solvatochromism at higher concentrations, therefore in CH_2Cl_2 ($\varepsilon = 8.9$) the energy of the ^{3}MLCT excited state could be shifted in relation to the ground state, which also may alter the energy of the ^{3}LF state required for the CO loss process. The kinetic plot of the decay of the excited state species seen in the *ns*-TRIR in Figure 5.24, which shows the excited state has a lifetime of $\tau = 57$ ns, this is consistent with the decay of a ^{3}MLCT excited state.[66] Both the kinetic decay and the *ns*-TRIR indicate the reformation of the parent bleaches which further supports the observation of a ^{3}MLCT excited state.

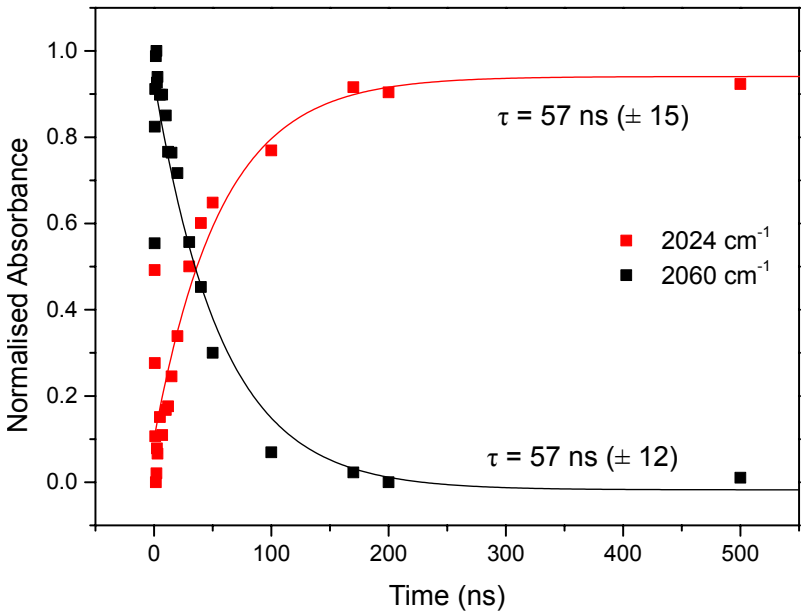


Figure 5.24: The kinetic plot for the decay of the ^{3}MLCT and the recovery of the parent of *fac*-Re(CO)$_3$(bpy–R$_F$^{10})Cl following a 355 nm excitation in CH_3CN.

The addition of the perfluorinated chains does not appear to alter the photophysics of the ^{3}MLCT excited state. The lifetime of *fac*-Re(CO)$_3$(bpy–R$_F$^{8})Cl was only affected slightly when compared to the non-perfluorinated analogue, *fac*-Re(CO)$_3$(dnb)Cl. Although *fac*-Re(CO)$_3$(bpy–R$_F$^{8})Cl has shorter lifetime, it is not significantly different, therefore it suggest the propyl spacer is insulating the bipyridine from the electron withdrawing effect of the perfluorinated chain. The same can not be said for the photochemistry, which appears to be affected by the presence of the perfluorinated chains. Upon excitation with 266 nm light the photodissociation of CO does not occur, instead the formation of a ^{3}MLCT excited state is observed for *fac*-Re(CO)$_3$(bpy–R$_F$^{10})Cl. It is possible that the negative solvatochromism effect, that is seen due to the perfluorinated chains aggregating, causes a shift in energy the ^{3}MLCT excited state and the ^{3}LF excited state, thus upon excitation with 266 nm light the population of the ^{3}MLCT is favoured over the ^{3}LF excited state. Further computational calculations

are needed to back up this theory. If this is the case then future investigations of *fac*-$Re(CO)_3(bpy-R_F{}^{10})Cl$ in non-polar and non-coordinating solvents could prove problematic as it appears the perfluorinated chains are inhibiting CO loss.

5.4 Conclusion

The aim of this Chapter was to see if it was possible to investigate the photophysical and photochemical properties of a rhenium tricarbonyl bipyridine complex in non-polar media, like PFMCH. To try and achieve this aim two perfluorinated functionalised bipyridines were synthesised, (bpy–$R_F{}^8$) and (bpy–$R_F{}^{10}$), and successfully complexed to a rhenium carbonyl centre. When the solubility of two fluorinated bipyridine complexes was investigated, it was found that the addition of a shorter perfluorinated chain did not improve the solubility of *fac*-$Re(CO)_3$(bpy–$R_F{}^8$)Cl in PFMCH. The longer chain saw a slight improvement, with *fac*-$Re(CO)_3$(bpy–$R_F{}^{10}$)Cl forming a suspension in PFMCH. Following this result, hexafluoropropane gas was added to PFMCH to aid solubility. The main issue with this PFMCH/hexafluoropropane mixture was the fact it is highly absorbing in the carbonyl region, which made it difficult to characterise the *fac*-$Re(CO)_3$(bpy–$R_F{}^{10}$)Cl, and would not be suitable for use in TRIR measurements. Liquid hexafluoropropane was subsequently tried and was found to be the best solvent at solubilising *fac*-$Re(CO)_3$(bpy–$R_F{}^{10}$)Cl, however liquid hexafluoropropane is still highly absorbing in the carbonyl region. It was found that substituting a perfluorinated chain onto the bipyridine ligand can result in the solubilisation of rhenium complex in a non-polar fluorinated solvent.

Although the solubility of *fac*-$Re(CO)_3$(bpy–$R_F{}^8$)Cl did not improve in a non-polar media, the photophysical properties were probed to ensure the addition of the perfluorinated chain did not change. When the luminescence was probed, it was shown that *fac*-$Re(CO)_3$(bpy–$R_F{}^8$)Cl exhibited negative solvatochromism, with the non-fluorinated analogue *fac*-$Re(CO)_3$(dnb)Cl exhibiting positive solvatochromism. This flip of the solvatochromic effect was therefore caused by the addition of the perfluo-

rinated chains. The solid-state packing of *fac*-Re(CO)$_3$(bpy–R$_F{}^8$)Cl was elucidated from the crystal structure obtained, where the complex is seen to stack *via* the perfluorinated chains. This led to the theory that the chains of *fac*-Re(CO)$_3$(bpy–R$_F{}^8$)Cl are aggregating in solution, thus affecting the energy of the excited state. This was investigated by lowering the concentration, *fac*-Re(CO)$_3$(bpy–R$_F{}^8$)Cl in a solution and probing the emission. It was found at lower concentrations *fac*-Re(CO)$_3$(bpy–R$_F{}^8$)Cl exhibited positive solvatochromism, supporting the theory of the aggregating chains. This made it clear the perfluorinated are somewhat problematic at higher concentrations.

TRIR was used to probe the excited state nature of *fac*-Re(CO)$_3$(bpy–R$_F{}^8$)Cl in CH_3CN, which was compared directly to *fac*-Re(CO)$_3$(dnb)Cl to better understand the influence of the perfluorinated chain. Both the *ps* and *ns*-TRIR showed the formation of a ^{3}MLCT, which was seen have a lifetime of *ca.* 40-30 ns for both complexes. The addition of the perfluorinated chain did not appear to drastically effect the lifetime or nature of the excited state observed. As well as the photophysical properties, the photochemical properties of the *fac*-Re(CO)$_3$(bpy–R$_F{}^n$)Cl complex was investigated. TRIR was used to probe *fac*-Re(CO)$_3$(bpy–R$_F{}^{10}$)Cl at 266 nm in CH_2Cl_2, which showed the formation of a ^{3}MLCT with no evidence for the formation of a CO loss product. It is likely that the negative solvatochromic effect observed at higher concentrations is contributing to this. This result was unexpected and identified that although the perfluorinated chain did not appear to affect the excited state lifetime of the complex, they are clearly having an effect on the photochemistry of the complex. The addition of the perfluorinated chain to a rhenium tricarbonyl bipyridine complex may not have yield the desired result. It did however, show how important it is to fully investigate the photophysical and photochemical properties of a complex.

Chapter 6

Conclusions and Future Work

This Chapter will summarise the findings that are reported within this Thesis and will outline the implications that have originated from the research. Furthermore, the future direction of the work and potential areas of investigations have been discussed.

6.1 Summary

The work within Chapters 2, 3 and 5 has focussed on the photophysical and photochemical properties of rhenium carbonyl α-diimine complexes. Chapter 2 and 3 probed the photochemical and photophysical properties of rhenium tetracarbonyl α-diimine complexes, where following a photophysical process, the photodissociation of a CO ligand was observed. The two complexes investigated were $[Re(CO)_4(bpy)][PF_6]$ and $[Re(CO)_4(dppz)][PF_6]$ Different photophysical and photochemical properties were observed depending on the α-diimine ligand, and the excitation wavelength. The photodissociation of a CO was observed for $[Re(CO)_4(bpy)][PF_6]$ with both a 355 and 266 nm excitation, and different photophysical properties were observed for each wave-

length. The different photophysical decay processes are shown in Figure 6.1. Whereas for $[Re(CO)_4(dppz)][PF_6]$, only photophysical properties were observed, with the exception of a photochemical process occurring for the higher energy excitation wavelength. The photophysical and photochemical properties of $[Re(CO)_4(dppz)][PF_6]$ were affected by the solvent and excitation wavelength a lot more than $[Re(CO)_4(bpy)][PF_6]$.

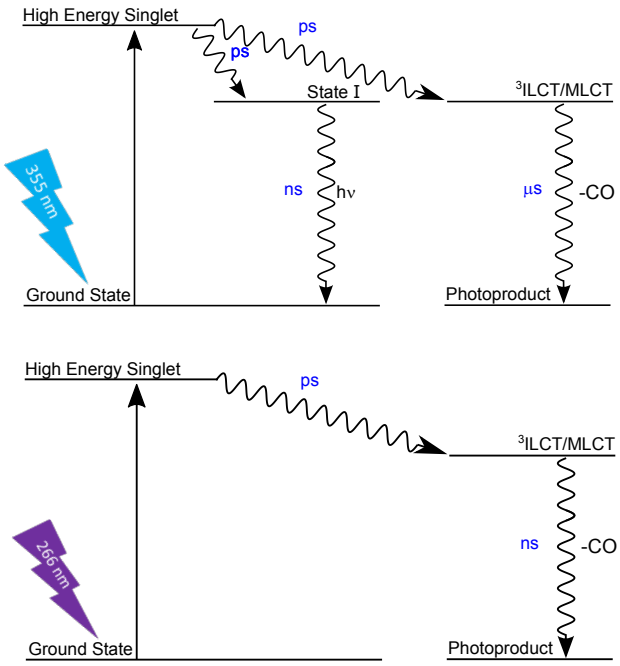


Figure 6.1: Illustration of the decay processes that occur for $[Re(CO)_4(bpy)][PF_6]$ in CH_2Cl_2 and CH_3CN when probed at 355 nm (top) and 266 nm (bottom).

This illustrates how easily the photophysical and photochemical properties of a complex can be altered simply by changing a ligand. This effect was also observed for another rhenium carbonyl α-diimine complex which was probed in Chapter 5. The photochemical properties of a rhenium tricarbonyl bipyridine complex were altered by the addition of a perfluorinated bipyridine ligand. When *fac*-$Re(CO)_3(bpy{-}R_F{}^{10})Cl$ was probed at 266 nm, only a photophysical process was observed, instead of the photodissociation of a CO, which was expected to occur. It has been shown by previous

studies that by exciting a *fac*-Re(CO)$_3$(bpy–R$_2$)Cl complex at 266 nm, the loss of CO is observed and a dicarbonyl species formed,[284] however this did not happen for *fac*-Re(CO)$_3$(bpy–R$_F$[10])Cl. Again, like the results observed in Chapters 2 and 3, by simply changing the ligand of the rhenium carbonyl α-diimine complex can drastically alter the photophysical and photochemical properties, with CO loss being inhibited for dppz and a perfluorinated bipyridine.

In Chapter 4 the photophysical properties of novel rylene diimide handcuff complexes were investigated. Prior to this work, the photophysical properties had not be probed. The monomer components of the handcuff complexes, along with the handcuff complexes and a rotaxane where investigated. The monomer complexes exhibited similar photophysical properties to those reported in the literature which had similar PDI or NDI cores. For the PDI monomers, **PDI-1** and **PDI-2**, the ^{1}PDI excited state observed was considerably shorter lived than other PDI monomers reported in the literature, $<$ 600 ps *vs.* 1-2 ns respectively. The NDI monomer, **NDI-1**, on the other hand exhibited the formation of a ^{1}NDI excited state that decayed *via* an NDI$^{-\bullet}$ species, forming a ^{3}NDI excited state. Again, the excited state of the ^{3}NDI excited state was shorter lived than other ^{3}NDI excited states reported in the literature. The ^{3}NDI exhibited a nanosecond lifetime rather than a mircosecond lifetime. It was proposed that the substituents on the monomers effected the lifetime of the excited states observed. The photophysical properties of the handcuff complexes showed the formation of a charge separated species, with **PDI/PDI** forming an excimer and **PDI/NDI** forming an ion pair. The formation of the excimer of **PDI/PDI** is likely due to the orientation of the two PDI units.

In comparison the rotaxane complex, **PDI-rot** saw the formation of a charged separated state which was the result of a CT process from the pilar-[5]-arene sub-

stituent located on the alkyl chain. The formation of a $PDI^{-\bullet}$ species was seen in both the *ps*-TA and *ps*-TRIR data, and was supported by spectroelectrochemical investigations. What is most interesting about **PDI-rot**, is the fact that the backbone of the rotaxane is comprised of the PDI monomer, **PDI-1**, which has the addition of a two pilar-[5]-arene sat on the alkyl chain either side of the PDI core. It is this pilar-[5]-arene substituent that is responsible for the CT process, illustrated in Figure 6.2. Incorporation of a pilar-[5]-arene onto the alkyl chain, that can interact with the PDI core, has altered the properties of the complex, resulting in **PDI-rot** exhibiting more desirable charge transfer photophysical properties.

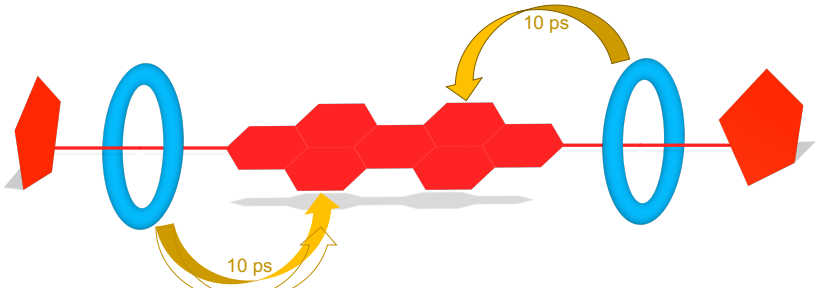


Figure 6.2: Illustration of the CT process that occurs from the pilar-[5]-arene ring onto the PDI core when **PDI-rot** is probed at 532 nm .

6.2 Implications and Future Work

The results observed in Chapters 2, 3 and 5 have shown that the photophysical and photochemical properties of a rhenium carbonyl α-diimine complex can be influenced by the α-diimine, exciation wavelength, and also the solvent environment. This results in implications when it comes to designing a rhenium carbonyl α-diimine complex for a specific application, especially a photochemical application. Being able to induce CO photodissociation is very desirable when investigating organometallic alkane complexes. This could lead to the formation of a long-lived alkane complex, which are

difficult to characterise at room temperature. This opens up a future area of research, where an alkane complex could be formed using rhenium tetracarbonyl bipyridine complex. So far, including this work and the literature reports, there have not been many investigations into the subsituents on the bipyridine ligand. A paper by Vanhelmont *et al.* reported the affect of an electron donor or acceptor subsituent on the bipyridine ligand,[296] and found the energy of the LUMO and HOMO orbitals can be influenced. This could open up avenue of research where you could tune the photodissciation of $[Re(CO)_4(bpy-R_2)]^+$ to either favour CO loss or inhibit CO loss. Along with investigating electron withdrawing and electron donating substituents on the bipyridine ligand, a TRIR study should be conducted in a range of solvents. This would allow for a further understanding of how the solvent environment affects the energy excited states.

Another area of research that should continue to be investigated, is the photodissoication of CO in non-polar media. This was attempted in Chapter 5, however the incorporation of the perfluorinated ligand inhibited the CO loss process. It has been shown from Chapter 2 that $[Re(CO)_4(bpy)][PF_6]$ undergoes CO loss following excitation at both 266 and 355 nm, therefore it is plausible that if the perfluorinated ligand was complexed to the tetracarbonyl center, CO loss is likely to occur. This could result in a rhenium carbonyl complex that is soluble in non-polar media, and can also undergo CO loss to form an alkane complex.

The photophysical properties of the unique rotaxane handcuff complexes were probed in Chapter 4, which demonstrated that the orientation and design of the rotaxane handcuff can alter their excited state nature. The desired photophysical property for these complexes was the observation of singlet fission or a charge separate state. The handcuff complex, **PDI/PDI-H**, saw the formation of an excimer state which is

a result of the two PDI unit being in close proximity to one another. This orientation inhibits singlet fission. Therefore, if the handcuff design was changed and the excimer is not formed, it could result in singlet fission. To achieve this, a slip-stacked orientation would be favourable, as singlet fission has been observed for other slip-stacked dimers.[213] Another area of research which could be investigated is probing their photophysical properties in another solvent. Photophyiscal investigations of other PDI dimers in toluene have yielded singlet fission. The charged nature of the handcuff complex makes them insoluble in toluene, however another solvent could alter their photophysical properties. Also probing the **NDI/NDI-H** handcuff analogue would also be of interest to see if it has similar photophysical properties to **PDI/PDI-H** handcuff, which resulted in an excimer.

Finally the PDI rotaxane, **PDI-rot**, saw the formation of a charge separated state which was the result of CT process from a pillar-[5]-arene wheel on the alkly chain. By incorporating the pillar-[5]-arene wheel, both a ^{1}PDI and PDI$^{-\bullet}$ species were formed. If the PDI rotaxane could be further substituted with other electron rich groups either on the PDI core or instead of the pillar-[5]-arene wheel, a more efficient CT process could arise that forms the PDI$^{-\bullet}$ species exclusively.

Chapter 7

Experimental

This Chapter describes the time-resolved techniques and apparatus which have been used for the work presented in this Thesis, this includes apparatus from both the University of Nottingham and the Rutherford Appleton Laboratory, Harwell Oxford. Other spectroscopic techniques and apparatus will be presented in this Chapter along with the description of synthetic Procedures and materials.

7.1 Time Resolved Spectroscopic Measurements

All the time-resolved measurements on the picosecond to the microsecond timescale were run on apparatus at the University of Nottingham and at the Rutherford Appleton Laboratory. The time-resolved infrared experiments in Chapter 2 and 3 were performed in collaboration with Dr Xue-Zhong Sun. The ultrafast-TRIR and TA experiments in Chapter 4 were performed on the ULTRA apparatus at Rutherford Appleton Laboratory. A description of the apparatus used within this Thesis is given here, as well as techniques used to analyse the data.

7.1.1 Nottingham TRIR Apparatus

Only a summary of the apparatus is given here as the ultrafast TRIR has been discusses elsewhere.[16] The laser pulse at 800 nm (2.3 mJ, 1 kHz, 140 fs) was produced by a combination of Ti:sapphire oscillator (MaiTai, Spectra Physics) and a regenerative amplifier system (Spitfire Pro, Spectra Physics), which is then split into two beams. One of the beams produces the pump pulse of 267 or 400 nm by harmonic generation (TimePlate Tripler, Minioptic Technology Inc.). The other beams goes on to produce the probe pulse which pumps a TOPAS-C optical parametric amplifier (Light Conversion), followed by a a difference frequency generator to produce a tuneable mid-IR pulses (180 cm^{-1}fwhm and *ca.* 2 μJ at 2000 cm^{-1}). The mid-IR pulses is then spit by a Ge beam splitter which sends one half to a single element MCT detector (Kolmar Technology) which is used as a reference beam, and the half is sent to probe the sample. To investigate a specific time delay, the pump pulse is optically delayed on a translation stage (LMA Actuator, Aerotech), which allows for time delays of up to *ca.* 2 ns to be recorded.

After passing through the sample, the transmitted IR probe is dispersed by a 250 nm IR monochromator (DK240, Spectra Products) with 150 L/mm gratings (giving *ca.* 4 cm^{-1}resolution) onto a 128-element MCT array detector (Infrared Associates). The signal is then amplified with a 144-channel amplifier (Infrared Associates Inc.) and digitalised with a 16-bit analogue to digital convertor (IR0144, Infrared Systems Development Corp.).

For *ns*-TRIR experiments, the output of a Q-switched Nd:YVO laser (1064 nm, 600 ps, Advanced Optical Technology) is frequency quadrupled to produce a 266 nm pump pulse or tripled to produce a 355 nm pump pulse. The pump and probe pulses

are synchronised and the delay is controlled using a pulse generator (DG535, Stanford Research Systems) allowing delays of 0.5 ns to 100 μs to be measured. The diameter of the pump beam (*ca.* 500 μm) is larger than the probe beam (*ca.* 200 μm) to ensure uniform spatial excitation of the sample.

For both the *ps* and *ns*-TRIR experiments the change in absorbance is measured by determining the ratio between the pump-on and pump-off IR intensity. The pump-off measurement is generated by an optical chopper (500 Hz) which blocks every second pump pulse. The sample is rastered in the x and y planes perpendicular to the pump and probe beam to avoid degradation and overheating of the sample. The sample is in continual flow through the cell with the use of a peristaltic pump.

7.1.2 Nottingham TA Apparatus

Transient Absorption Spectroscopy measurement is based on pump-probe method and has been described elsewhere.[16] In brief, the probe beam of white light continuum, is generated by focusing small amount of 800nm ($\sim$ 400nJ) laser beam into a 4 mm thick Sapphire disk. The picoseconds pump beam is obtained from a commercial Ti:sapphire oscillator / regenerative amplifier system (Spectra Physics, USA) and a TP-1 harmonic generator (TimePlate Tripler, Minioptic Technology, Inc) and the time difference (up to 3 ns) between the pump and probe pulses is controlled by an optical delay line. The nanosecond beam is produced with a Q-switched Nd:YVO laser (ACE-25QSPXHP/MOPA, Advanced Optical Technology, UK) which is electronically synchronised to the Spitfire Pro amplifier. Therefore, the delay between pump and probe pulses can be controlled with a pulse generator (DG535, Stanford Research System,USA) from 0.5 ns to 100 μs. The white light beam is split into two parts. One part passes through the sample and spatially overlapped with the pump beam.

Another part serves as a reference to the probe beam fluctuations. The polarization of the pump pulse is set at the magic angle (54.7 degree) relative to the probe pulse to recover the isotropic absorption spectrum. Both parts of probe beam are monitored by a duel array detector (512 pixels) (Cronin Camera, Spectronic device Ltd, UK). The detector is mounted in the focal plane of a 303 mm Acton spectrograph (Acton, USA) with a 150 g/mm grating. The pump beam size ($\sim$ 400μm diameter) is larger than the probe spot ($\sim$ 200μm diameter). A Harrick flowing solution cell with 2 mm thick CaF_2 windows is mounted on a motorized cell mount, which moves the cell in x and y dimensions rapidly and continuously.

7.1.3 TRIR Apparatus at the Rutherford Appleton Laboratory

Picosecond TRIR measurements were performed on the ultrafast-TRIR apparatus at the Rutherford Appleton Laboratory(ULTRA), as the ULTRA apparatus has been described in detail else where,[15] only a brief summary is given here. A Ti:sapphire laser amplifier (Thales Laser) generates the 800 nm laser pulse (0.8 mJ, 10 kHz, 50 fs) which is then split into two. The first part is sent to a harmonic generator which produces the UV pump pulse, and the second part is sent through an optical parametric amplifier (TOPAS, Light Conversion) to produce the tuneable mid-IR probe pulse. This IR probe beam is then split to pr oduce the reference beam and the IR probe beam. The diameter of the pump and probe beams were around 150 μm and 80 μm, respectively.

Once the IR probe beam has been passed through the sample, it is dispersed onto two linear 128-element MCT array detectors (Infrared Associates). A chopper is used to measure the intensity of the pump-off and pump-on probe which generates a

difference spectra. The reference beam of the IR probe pulse is sent to a 64 element MCT array detector (Infrared Associates), this provide a reference for beam intensity fluctuations. To avoid degradation of the samples, the cell is rastered perpendicular to the pump and pulse beams, with the sample being constantly refreshed with the use of a peristaltic pump and a flow pot system.

7.1.4 TA Apparatus at the Rutherford Appleton Laboratory

For the transient absorption (TA) spectroscopic measurements, the UV pump beam was generated in the same way as the ULTRA TRIR mentioned above. More detailed descriptions of the TA apparatus can be found in the literature.[297] For a TA experiment the probe pulse is a white light continuum (WLC) which is generated from the focusing the 800 nm seed laser onto a CaF_2 crystal. Like the ULTRA apparatus, the delay time is controlled with the use of an optical delay line for the picosecond measurements. The TA probe beam is *ca.* 50 μm in diameter.

7.1.5 TRIR and TA Data Analysis

For the TRIR and TA experiments time delays appropriate for the process being monitored were selected. Generally, the spectra were recorded at *ca.* 40 different time delays. A good signal-to-noise was achieved through the use of averaging, with *ca.* 5 second averaging and four cycles through each time delay. The ULTRA apparatus often only used a *ca.* 2 second averaging time due to the higher repetition rate. The data processing for the data recorded at Rutherford Appleton Laboratory was performed using custom software designed by M. R. Pollard and G. M. Greetham,

and custom software designed by Dr. Xue-Zhong Sun for data from the Nottingham setup.

Decay fitting was performed using Origin 9.0, with monoexponentials or biexponentials fitting modes applied to a single wavenumber points to produce a kinetic trace. The reported errors were obtained from the deviation from the exponential fit to the experimental data. In the cases where the kinetic data could not be obtained from the a single wavenumber points, global analysis was performed using Glotaran 1.5.1 software, a detailed description of the software can be found in the literature.[298]

7.2 Other Spectroscopic Measurements

7.2.1 Fourier Transform Infra-red Spectroscopy

All Fourier transform infra-red (FTIR) measurements were made using Thermo Nicolet FTIR spectrometer at 2cm^{-1}resolution, with a KBr detector. All IR solution cells (Harrick Corp) with calcium fluoride (CaF_2) windows (25x2 mm, Crystran) were typically used with a path length of *ca.* 390 μm.

7.2.2 UV/Visible Absorbance Spectroscopy

Absorption spectrum was taken using a Perkin Elmer Lambda 5 spectrometer in a quartz cuvette with 1cm spacing or an infra-red solution cell (Harrick Corp.) with CaF_2 windows (25x2 mm, Crystran) at a path length of 0.39 μm. An Hg-Arc lamp was used as the UV light source.

7.2.3 Luminescence Spectroscopy

All emission and excitation spectra were taken on an Edinburgh Instrument FLS920 combined fluorescence lifetime and steady state spectrometer. The excitation source used for all steady state emission and excitation was a xenon Arc lamp. All samples were taken using a quartz cuvette with a 1cm path length. All solutions exhibited absorbance of between 0.18-0.30 at the excitation wavelength. Emission lifetime experiments were run with a ps-diode laser (406 nm), with a freeze-pump-thaw degassed solution under Ar unless stated otherwise.

7.2.3.1 Single Crystal X-Ray Crystallography

Single crystals of $C_{35}H_{18}N_2O_3F_{34}ClRe$, *fac*-$Re(CO)_3(bpy-R_F{}^8)Cl$, were recrystallised in acetonitrile. A suitable crystal was selected and in fomblin film on a micromount on a GV1000, TitanS2 diffractometer. The crystal was kept at 120(2) K during data collection. Using Olex2,[299] the structure was solved with the ShelXS structure solution program using Direct Methods and refined with the ShelXL refinement package using Least Squares minimisation.[300,301]

Crystal Data for $C_{35}H_{18}N_2O_3F_{34}ClRe$ (M =1382.16 g/mol): orthorhombic, space group Pbca (no. 61), a = 10.8102(4) Å, b = 19.9384(7) Å, c = 40.1746(17) Å, V = 8659.1(6) Å^3, Z = 8, T = 120(2) K, μ(CuKα) = 7.833 mm^{-1}, Dcalc = 2.120 g/cm^3, 48009 reflections measured ($8.804° \leqslant 2\Theta \leqslant 133.184°$), 7595 unique ($R_{int}$ = 0.2065, R_{sigma} = 0.1349) which were used in all calculations. The final R_1 was 0.1665 ($I > 2\sigma(I)$) and wR_2 was 0.3796 (all data).

7.2.4 ^{1}H NMR Spectroscopy

^{1}H NMR spectra were recorded at 400 MHz in deuterated chloroform or deuterated methanol at room temperature using the JEOL ex400 NMR spectrometer. Shifts in peaks are due to changes in solvent were found in literature.

7.2.5 ^{19}F NMR Spectroscopy

^{19}F NMR spectra were recorded at 376 MHz in deuterated chloroform or deuterated methanol at room temperature using the JEOL ex400 NMR spectrometer. Shifts in peaks are due to changes in solvent were found in literature.

7.2.6 Mass Spectroscopy

All mass spectra were obtained with the Mass Spectrometry Service (University of Nottingham). Positive and neagtive ion electrospray mass spectra were recorded using an automated Micromass LCT spectrometer using ElectroSpray Ionisation. Measurements were performed in methanol or acetonitrile solutions.

7.2.7 Electrochemistry

All the electrochemical measurements were run here at The University of Nottingham, with all the bulk reductions being run in collaboration with Dr E. S. Davies.

For the electrochemical measurements in collaboration with Dr E. S. Davies the following experimental set up was used. The cyclic voltammetry measurements were

run in 1 mM degassed solutions in either CH_2Cl_2 or CH_3CN with [TBA][BF_4] as the supporting electrolyte. An Autolab PGSTAT20 potentiostat was used along with a glassy carbon working electrode, a Pt wire secondary electrode and a saturated calomel reference electrode. For the spectroelectrochemistry measurements a controlled potential electrode cell was used. This cell consisted of a Pt gauze basket which is seperated by a glass frit, from a secondary Pt gauze electrode. A test solution filled the working electrode compartment and was stirred rapidly for the duration of the electrolysis. The solution of the solvent and electrolyte filled the secondary electrode compartment. The saturated calomel reference electrode was bridged to test the solution through a vycor frit, oriented at the centre of the working electrode.

The other cyclic voltammetry measurements were made using a three electrode arrangement consisting of a glassy working electrode, a Pt sheet counter electrode and a Ag/AgCl reference electrode. A PGSTAT302N potentiostat was used, with the working electrode being thoroughly cleaned and polished prior to the experiment. All the solution were run either CH_2Cl_2 or CH_3CN with [TBA][BF_4] (1 mM) as the supporting electrolyte and purged with Ar for 5 minutes before the measurement was run. Ferrocene (Fc/Fc^+) was used as an internal standard for all CV spectra recorded.

The electrochemistry reported in Chapter 2 used both method mentioned above, with spectroelectrochemistry measurements being run in collaboration with Dr E. S. Davies. All the measurements meantion in Chapter 3 were run in collaboration with Dr E. S. Davies. All potential given in the text are converted from other reference electrodes to the Fc/Fc^+ reference.

7.3 DFT Calculations

DFT calculations was carried out using Gaussian 16 using CAM-B3LYP with 6-31G(d) basis set on the organic atoms and LanL2DZ basis set for the rhenium atom. A PCM solvent field was used, with the predefined solvent parameters used. Electronic transitions were modelled using TD-DFT.

7.4 Materials

All chemicals were used as supplied. Rhenium chloride pentacarbonyl, 4,4'-dimethyl-2,2'-bipyridine, diisopropylamine, *n*-BuLi, diethyl ether and dichloromethane, trifluorotoluene, lithium diisopropylamide were obtained from Sigma Aldrich. Acetonitrile, tetrahydrofuran, ethanol, methanol, 1,10-phen-5,6-dione, 1,2-diaminobenzene and silver trifluoromethanesulfonate were obtained from VWR international. Toluene, n-heptane, 2,2'-bipyridine and magnesium sulfate were obtained from Fischer scientific. 1-iodo-1H,1H,2H,2H-perfluorodecane, 1-iodo-1H,1H,2H,2H-perfluoroundodecane and ammonium hexafluorophosphate were obtained from Fluorochem. Rhenium bromide pentacarbonyl was obtained from Strem Chemicals.

7.5 Sample Preparation

The TRIR and TA solution samples were prepared under an Ar atmosphere using standard Schlenk line techniques. The solutions samples were made up to *ca.* 20 ml and degassed *via* freeze-pump-thaw before being run. All the samples were stored

under an Ar atmosphere. The solution set up used a Harrick transmission cell with two CaF_2 windows (25x2 mm, Crystran) with a telfon spacer to vary the path length. The path length was varied between 0.1 - 0.7 μm depending on the concentration of the solution. The concentration of the solution was selected such that the IR absorbance of the ν(CO) band were between 0.1 - 0.8, but also the UV absorbance of the excitation wavelength was was below 0.4. Due to the high repetition rates of the time-resolved experiments the samples were continually refreshed using a flow system which consists of a glass reservoir connected to the Harrick cell *via* two teflon pipes, with the sample being circulated *via* the use of a peristaltic pump.

7.6 Synthetic Procedures

All the synthetic procedures given here are based on literature methods. The synthesis of the PDI and NDI monomers, the PDI/PDI and PDI/NDI handcuff complexes were synthesised by Dr Lixu Yang and Dr Philipp Langer.[173] The PDI rotaxane was synthesised by Dr Nicholas Pearce, all of whom work for Professor Neil Champness at the University of Nottingham.

7.6.1 Synthesis of Diimine Ligands

7.6.1.1 Synthesis of Dipyridophenazines

1,10-Phenanthroline-5,6-dione (300 mg, 1.4 mmol) and 1,2-diaminobenzene (360 mg, 3.3 mmol) were dissolved in ethanol (75 ml) and refluxed for 1 hour. The solution was then cooled (0 °C) resulting in the formation of an orange precipitate. The precipitate was recrystallised with hot ethanol to yield the final product (380 mg, 94% yield). ^{1}H

NMR ($CDCl_3$, 400 MHz) δ= 9.87 (dd, J = 8.2, 1.5 Hz, 2H), 9.47 (dd, J = 5.2, 1.5 Hz, 2H), 8.46 (dd, J = 6.6, 3.4 Hz, 2H), 8.10 – 7.99 (m, 4H); m/z – 283.0986 $[C_{18}H_{11}N_4]^+$. See Appendix for ^{1}H NMR assignments.

7.6.1.2 Synthesis of 4,4'-bis[1H, 1H, 2H, 2H, 3H, 3H- perfluoroun decyl]-2,2'-bipyridine

To a flame dried 250 mL Schlenk flask under Ar,was added lithium diisoproplyamine (2.5 M) (3 mL) at -78 °C and stirred for 30 mins, after which 4,4'-dimethyl-2,2'-bipyridine (276 mg, 1.5 mmol) dissolved in THF (20 ml) was added *via* syringe and continued to stir for 3 hours whilst under argon. After 3 hours 1-iodo-1H, 1H, 2H, 2H-perfluordecane (1.34 g, 2.00 mmol) dissolved in THF (20 mL) was added *via* syringe. After an hour, the reaction mixture was allowed to warm slowly to ambient temperature overnight. The reaction was quenched with brine; the residue was extracted in Et_2O and dried over $MgSO_4$, solvent removal by rotary evaporation and subsequent recrystallisation of resulting solid in toluene afforded 2.47 g (30 % yield).^{1}H NMR ($CDCl_3$, 400 MHz) δ= 8.62 (d, 2H), 8.29 (s, 2H), 7.17 (dd, J = 4.97, 1.75 Hz, 2H), 2.83 (t, J = 7.53 Hz, 4H), 2.11 (m, 8H); ^{19}F NMR ($CDCl_3$, 376 MHz) δ= -126.1 (4F), -123.3 (4F), -122.7 (4F), -121.9 (8F), -126.6 (4F), -114.0 (4F), -80.7 (6F); m/z - 1077.09 $[C_{32}H_{18}N_2F_{34}]^+$H; Calculated: C (35.71 %), H (1.69 %), N (2.60 %); Found: C (36.38 %), H (1.39 %), N (2.29 %).[286,294] See Appendix for ^{1}H NMR assignments.

7.6.1.3 Synthesis of 4,4'-bis[1H, 1H, 2H, 2H, 3H, 3H- perfluorotri decyl]-2,2'-bipyridine

To a flame dried 250 mL Schlenk flask under Ar, was added diisopropylmaine (0.95 mL, 6.8 mmol) in THF (20 mL), the flask was cooled to -78 °C and *n*-Butyllithium (4.7 mL, 7.5 mmol)was added. The reaction was stirred at -78 °C for 20 mins, warmed to 0 °C and cooled to -78 °C again. 4,4'-dimethyl-2,2'-bipyridine (550 mg, 3.0 mmol) was dissolved in THF (15 ml) was added *via* syringe and continued to stir for 3 hours whilst under argon. After 3 hours 1-iodo-1H, 1H, 2H, 2H-perfluorododecane (3.68 g, 6.25 mmol) dissolved in THF (20 mL) was added *via* a cannula. After an hour, the reaction mixture was allowed to warm slowly to ambient temperature overnight. The reaction was quenched with brine; the residue was extracted in Et_2O and dried over $MgSO_4$, solvent removal by rotary evaporation and subsequent recrystallisation of resulting solid in toluene afforded 3.31 g (35 % yield)^{1}H NMR ($CDCl_3$, 400 MHz) δ= 8.63 (d, 2H), 8.30 (s, 2H), 7.20 (d, 2H), 2.84 (t, 4H), 2.11 (m, J = 22.0 Hz, 8H); .^{19}F NMR ($CDCl_3$, 376 MHz) δ= -126.1 (4F), -123.3 (4F), -122.7 (4F), -121.9 (8F), -126.6 (4F), -114.0 (4F), -80.7 (14F) ; m/z - 1277.09 $[C_{32}H_{18}N_2F_{42}]^+$H.[286] See Appendix for ^{1}H NMR assignments.

7.6.2 Synthesis of Rhenium Carbonyl Diimine Complexes

7.6.2.1 Sythesis of Rhenium Tetracarbonyl Bipyridines

To a flame dried 250 mL Schlenk flask under Ar and in the absence of light, was added rhenium pentacarbonyl bromide (203 mg, 0.5 mmol), silver trifluoromethane sulfonate (128 mg, 0.5 mmol) in CH_2Cl_2 (30 ml). The mixture was stirred at RT for

12 hours, afterwhich AgBr was filtered off and 2,2'-bipyridine (94 mg, 0.6 mmol) in CH_2Cl_2 (30 ml) was added. The mixture was stirred for a 16 hours under Ar and in the absence of light. Half the reaction mixed was removed under vacuum, and hexane (20 ml) was added to crash out the trifoliate analogue $[Re(CO)_4(bpy)][OTf]$ (*ca.* 220 mg). $[Re(CO)_4(bpy)][OTf]$ (220 mg, 0.36 mmol) and ammonium hexafluorophosphate (350 mg, 2.14 mmol) were dissolved in a H_2O/acetone (1:1) mixture, and stirred for 1 hour and then left to form a precipitate overnight. A yellow crystal was recovered (138 mg, 46% yield). ^{1}H NMR (CD_3CN, 400 MHz) δ = 9.02 (dd, J = 5.5, 1.5, 0.8 Hz, 2H), 8.50 (dd, J = 8.3, 1.1 Hz, 2H), 8.31 (t, J = 7.9, 1.5 Hz, 2H), 7.73 (dd, J = 7.7, 5.6, 1.3 Hz, 2H); m/z -455.0098 $[C_{14}H_8N_2O_4Re]^+$; Calculated: C (28.05 %), H (1.35 %), N (4. 67 %); Found: C (30.08 %), H (0.82 %), N (2.24 %).[71,77] See Appendix for ^{1}H NMR assignments.

7.6.2.2 Sythesis of Rhenium Tetracarbonyl Dipyridophenazines

To a flame dried 250 mL Schlenk flask under Ar and in the absence of light, was added rhenium pentacarbonyl bromide (203 mg, 0.5 mmol), silver trifluoromethane sulfonate (128 mg, 0.5 mmol) in CH_2Cl_2 (30 ml). The mixture was stirred at RT for 12 hours, afterwhich AgBr was filtered off and dipyridophenazines (170 mg, 0.6 mmol) in CH_2Cl_2 (30 ml) was added. The mixture was stirred for a 16 hours under Ar and in the absence of light. Half the reaction mixed was removed under vacuum, and hexane (20 ml) was added to crash out the trifoliate analogue $[Re(CO)_4(dppz)][OTf]$ (*ca.* 220 mg). $[Re(CO)_4(dppz)][OTf]$ (220 mg, 0.3 mmol) and ammonium hexafluorophosphate (350 mg, 2.14 mmol) were dissolved in a H_2O/acetone (1:1) mixture, and stirred for 1 hour and then left to form a precipitate overnight. A yellow powder was recovered (152 mg, 42% yield). ^{1}H NMR ($CDCl_3$, 400 MHz) δ = 9.68 (dd, J = 8.1, 1.8 Hz, 2H),

9.29 (dd, J = 4.5, 1.8 Hz, 2H), 8.39 (dd, J = 6.5, 3.4 Hz, 2H), 7.95 (dt, J = 6.6, 3.2 Hz, 2H), 7.81 (dd, J = 8.1, 4.4 Hz, 2H); m/z – 581.0262 $[C_{22}H_{10}N_4O_4Re]^+$; Calculated: C (38.15 %), H (2.13 %), N (7.42 %); Found: C (48.66 %), H (2.64 %), N (9.30 %).[71,77] See Appendix for ^{1}H NMR assignments.

7.6.2.3 Sythesis of Rhenium Tricarbonyl 4,4'-bis [1H, 1H, 2H, 2H, 3H, 3H-perfluoroundecyl] -2,2'-bipyridine Chloride

To a solution of rhenium pentacarbonyl chloride (15 mg, 0.04 mmol) in Toluene (5 mL) was added 4,4'-bis[1H, 1H, 2H, 2H, 3H, 3H- perfluorotridecyl]-2,2'-bipyridine (50 mg, 0.04 mmol). The solution was heated to reflux for 3 hours under an inert atmosphere in the absence of light. After 3 hrs the reaction was cooled to room temperature and cooled over ice. Precipitate was filtered and washed with cold toluene (10 mL) and recrystallised with EtOH to afford a yellow solid (63 %). ^{1}H NMR ($CDCl_3$, 400 MHz) δ = 8.98 (d, J = 5.55 Hz, 2H), 8.00 (s, 2H), 7.39 (d, J = 5.7 Hz, 2H), 2.95 (t, J = 7.16 Hz, 4H), 2.18 (m, 8H);^{19}F NMR ($CDCl_3$, 400 MHz) δ = -80.74 (6F), -113.94 (4F), -121.64 (8F), -121.89 (4F), -123.25 (4F), -126.08 (4F);m/z – 1494.9 $[C_{35}H_{18}F_{34}N_2O_3ClRe]Na^+$; Calculated: C (30.42 %), H (1.31 %), N (2.03 %) ; Found C (30.90 %), H (1.23 %), N (1.79 %). See Appendix for ^{1}H NMR assignments.

7.6.2.4 Sythesis of Rhenium Tricarbonyl 4,4'-bis[1H, 1H, 2H, 2H, 3H, 3H-perfluorotridecyl]-2,2'-bipyridinee Chloride

To a solution of rhenium pentacarbonyl chloride (15 mg, 0.04 mmol) in Toluene (5 mL) was added 4,4'-bis[1H, 1H, 2H, 2H, 3H, 3H- perfluorotridecyl]-2,2'-bipyridine (50 mg, 0.04 mmol). The solution was heated to reflux for 3 hours under an inert atmosphere

in the absence of light. After 3 hours the reaction was cooled to room temperature and solvent removed under reduced pressure. The crude product was crystallised with CH_3OH to obtain a yellow solid (44 %). ^{1}H NMR ($CDCl_3$, 400 MHz) δ = 8.97 (d, J = 5.7 Hz, 2H), 7.99 (s, 2H), 7.38 (d, J = 5.7 Hz, 2H), 2.94 (t, J = 7.8 Hz, 4H), 2.33 – 1.99 (m, 8H);^{19}F NMR ($CDCl_3$, 400 MHz) δ = -80.73 (CF_3 -6F), -113.96 (CF_2 -4F), -121.67 (CF_2 -20F), -122.69 (CF_2 -4F), -123.26 (CF_2 -4F), -126.9 (CF_2 -4F);FD-MS: 1581.99; Calculated: C (29.6 %), H (1.15 %), N (1.77 %);Found: C (30.26 %), H (1.32 %), N (1.48 %). See Appendix for ^{1}H NMR assignments.

Appendix A

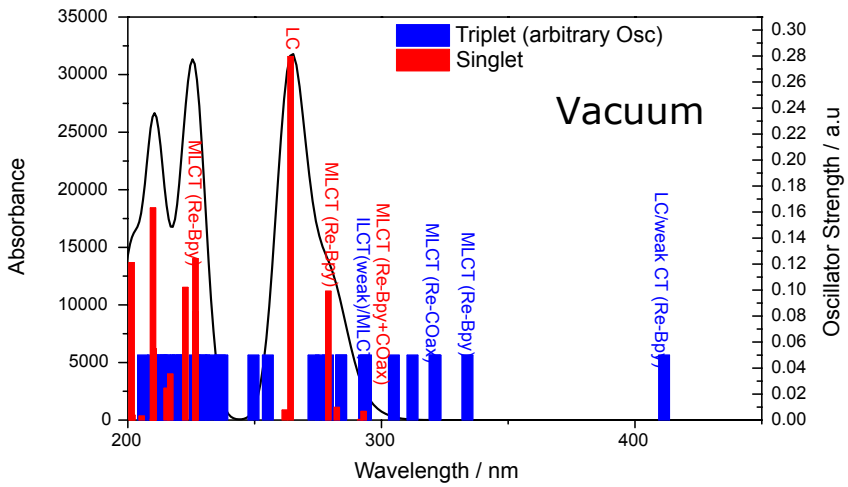


Figure A.1: The triplet (red) and singlet (blue) excited state transitions calculated for $[Re(CO)_4(bpy)]^+$ using TD-DFT in a vacuum.

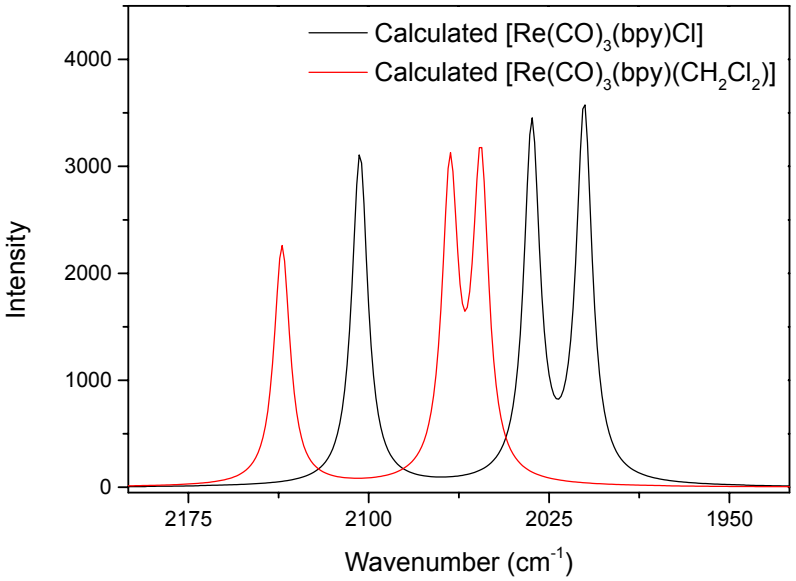


Figure A.2: The DFT calculated IR spectra for $[Re(CO)_3(bpy)(CH_2Cl_2)$ and $[Re(CO)_3(bpy)Cl$ to see how the $\nu(CO)$ bands shift when bound to CH_2Cl_2.

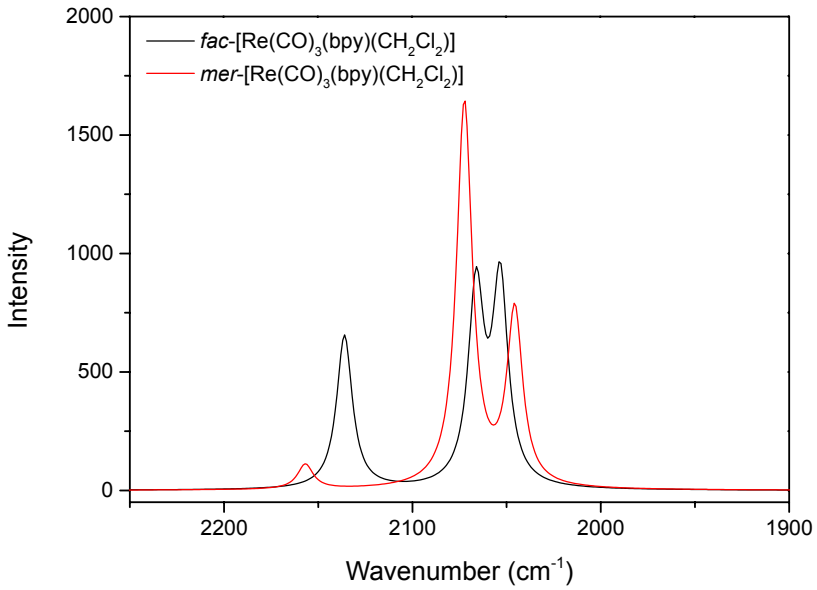


Figure A.3: The DFT calculated IR spectra for fac and mer isomers of $[Re(CO)_3(bpy)(CH_2Cl_2)$ and $[Re(CO)_3(bpy)Cl$ to help identify the solvated photoproduct of $[Re(CO)_4(bpy)][PF_6]$.

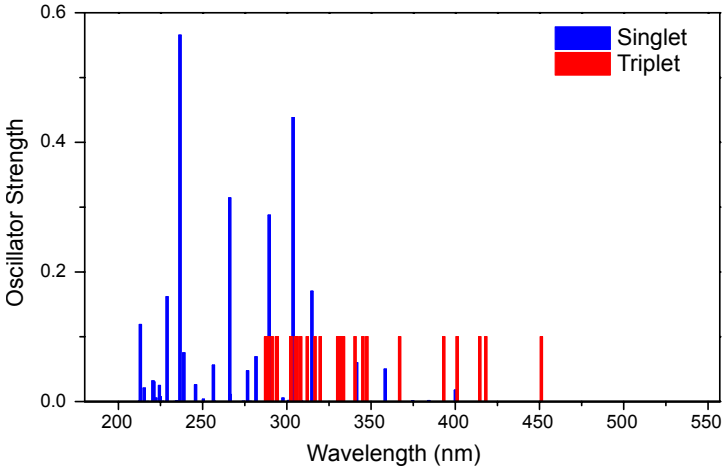


Figure A.4: The triplet (red) and singlet (blue) excited state transitions calculated for $[Re(CO)_4(dppz)]^+$ using TD-DFT in a vacuum.

Identification code	REKERA
Empirical formula	$C_{35}H_{18}N_2O_3F_{34}ClRe$
Formula weight	1382.16
Temperature/K	120(2)
Crystal system	orthorhombic
Space group	Pbca
a/Å	10.8102(4)
b/Å	19.9384(7)
c/Å	40.1746(17)
α/°	90
β/°	90
γ/°	90
Volume/Å^3	8659.1(6)
Z	8
ρ_{calc}g/cm^3	2.120
μ/mm^{-1}	7.833
F(000)	5312.0
Crystal size/mm^3	0.082 × 0.082 × 0.009
Radiation	CuKα (λ = 1.54184)
2Θ range for data collection/°	8.804 to 133.184
Index ranges	-11 ≤ h ≤ 12, -23 ≤ k ≤ 22, -47 ≤ l ≤ 47
Reflections collected	48009
Independent reflections	7595 [R_{int} = 0.2065, R_{sigma} = 0.1349]
Data/restraints/parameters	7595/1141/685
Goodness-of-fit on F^2	1.152
Final R indexes [I>=2σ (I)]	R_1 = 0.1665, wR_2 = 0.3623
Final R indexes [all data]	R_1 = 0.1939, wR_2 = 0.3796
Largest diff. peak/hole / e Å^{-3}	4.88/-1.92

Figure A.5: The crystallography data collected for *fac*-Re(CO)$_3$(bpy–R$_F{}^8$)Cl using single crystal crystallography.

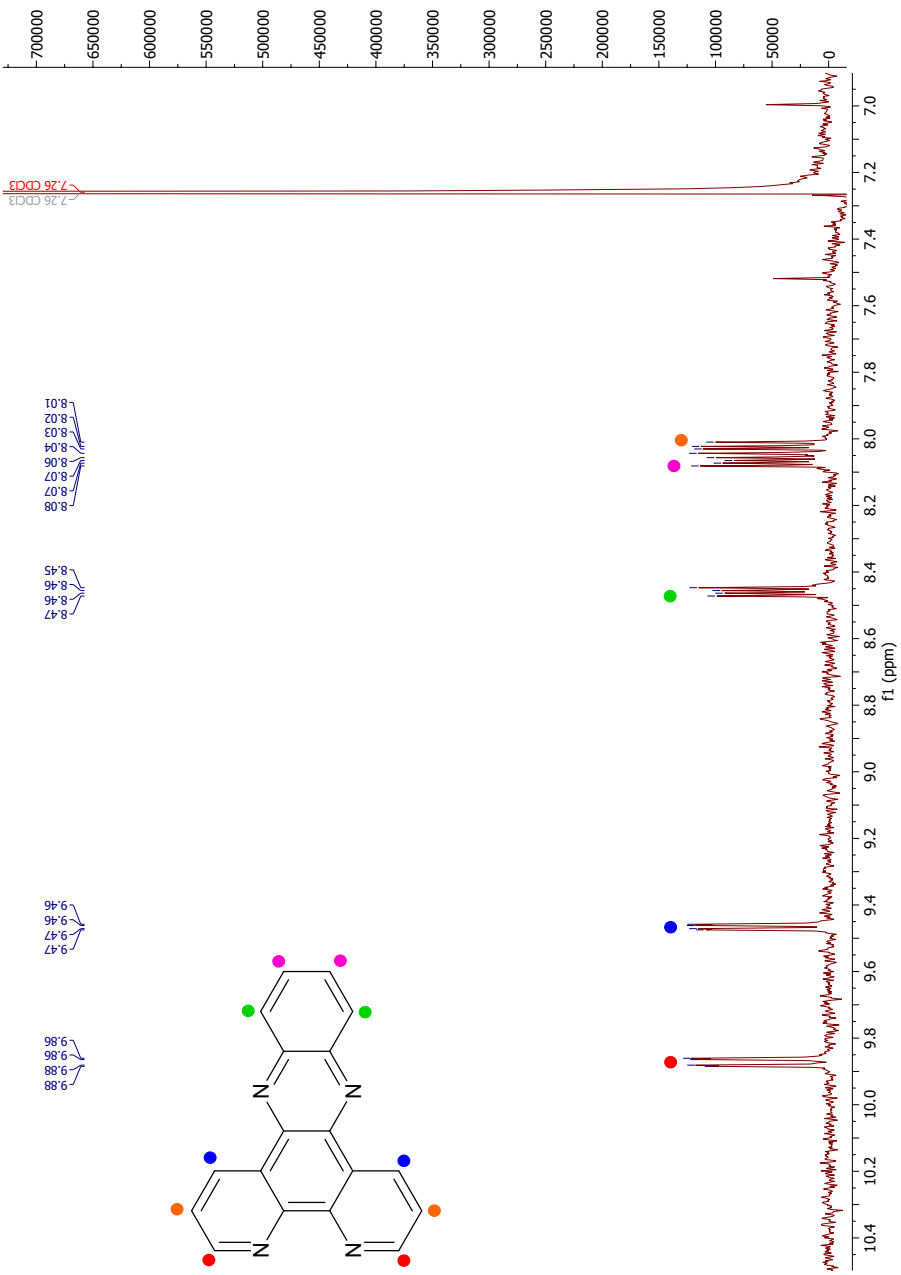


Figure A.6: The ^{1}H NMR of dipyridophenazines in $CDCl_3$ with the assignments of protons.

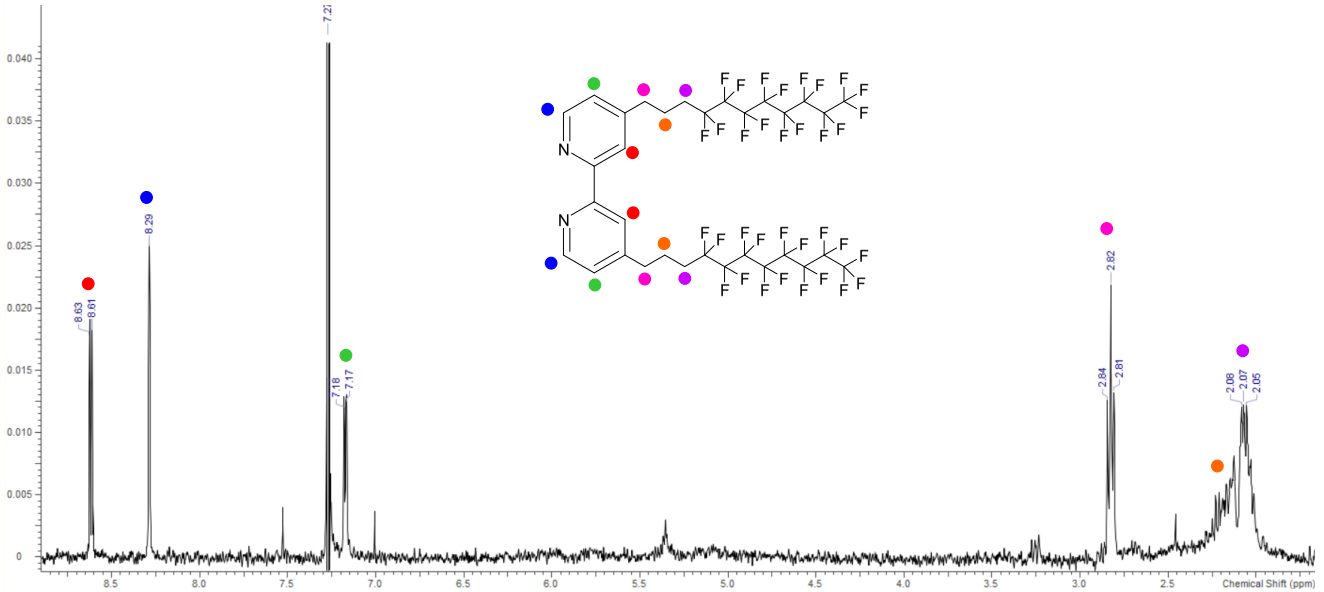


Figure A.7: The ^{1}H NMR of 4,4'-bis[1H, 1H, 2H, 2H, 3H, 3H-perfluoroundecyl]-2,2'-bipyridine in $CDCl_3$ with the assignments of protons.

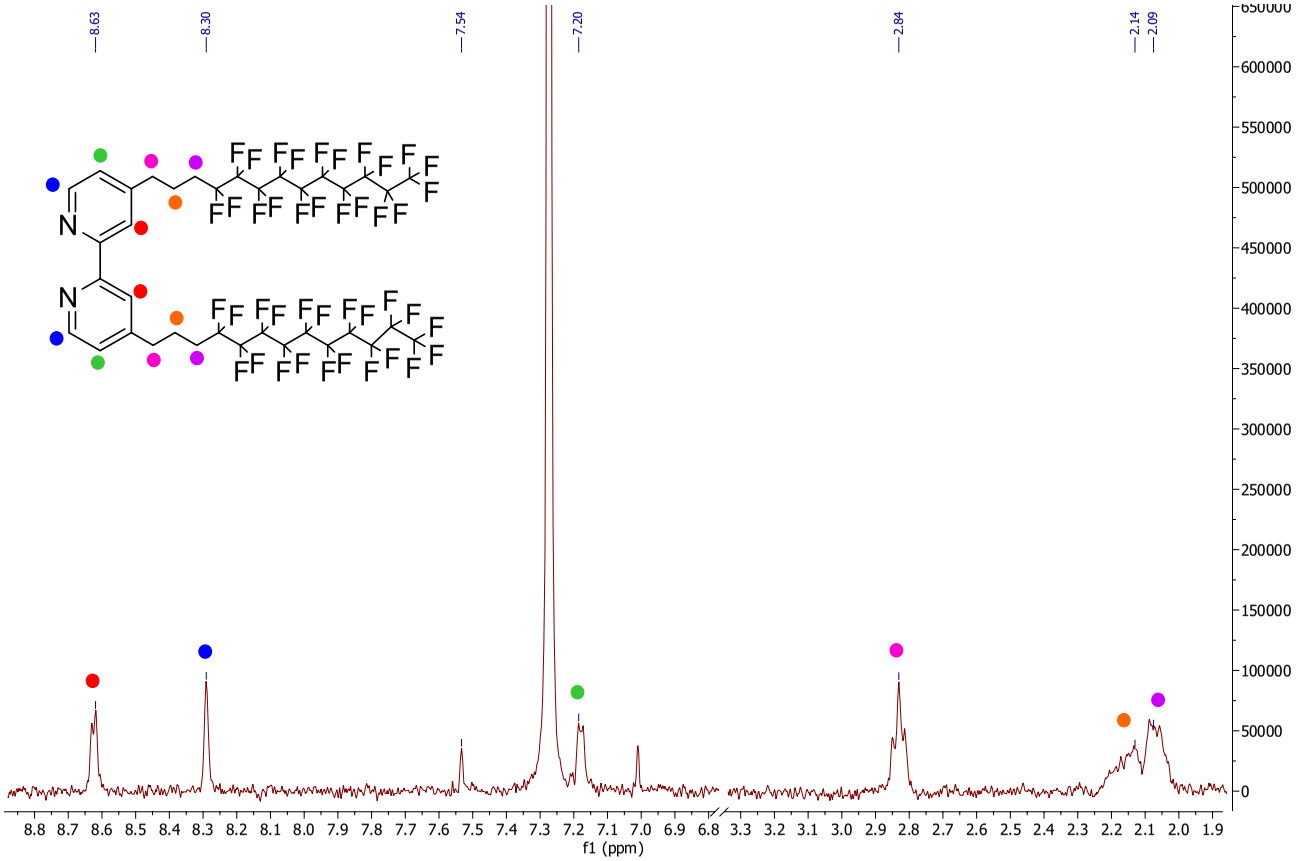


Figure A.8: The ^{1}H NMR of 4,4'-bis[1H, 1H, 2H, 2H, 3H, 3H-perfluorotridecyl]-2,2'-bipyridine in $CDCl_3$ with the assignments of protons.

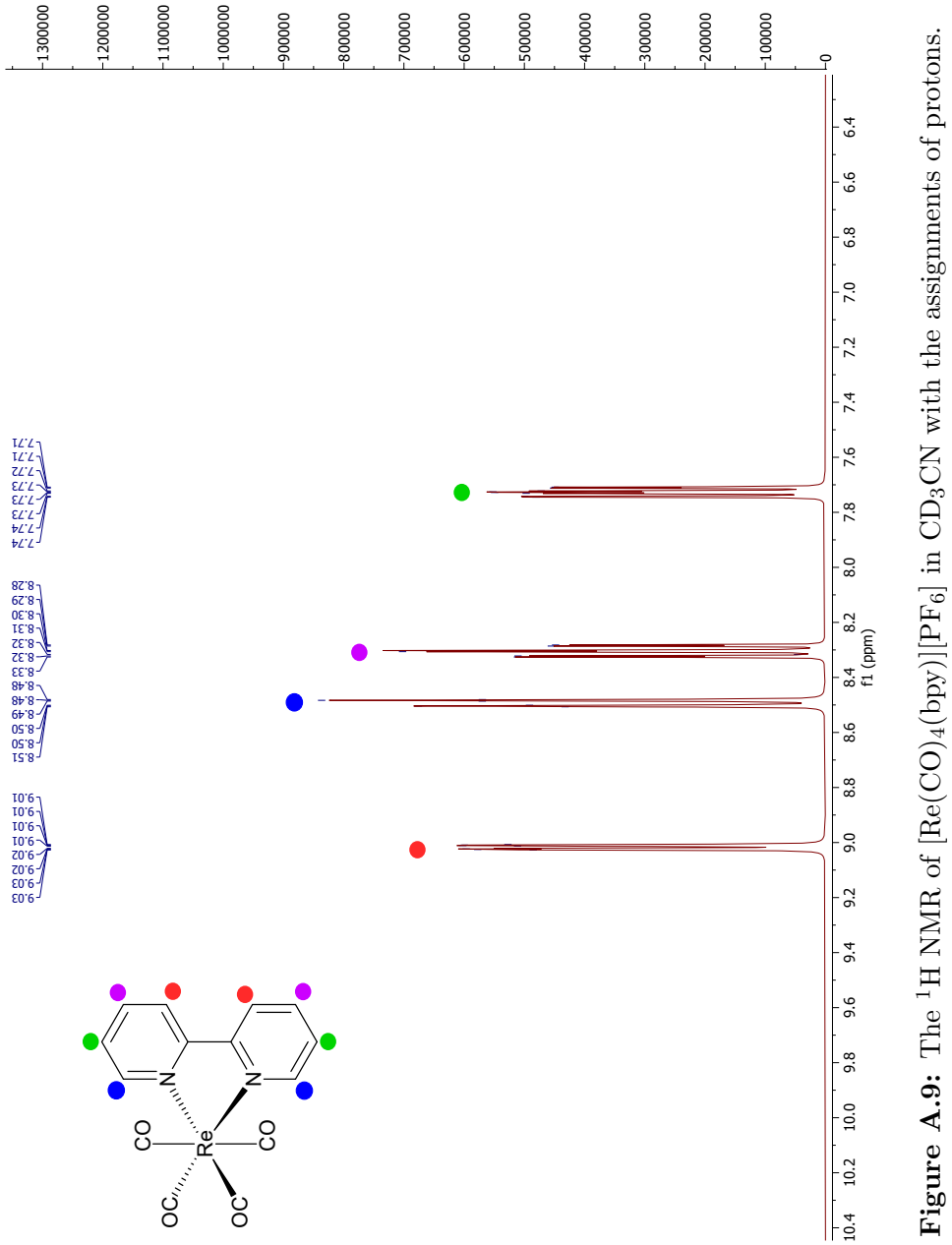


Figure A.9: The ^{1}H NMR of $[Re(CO)_4(bpy)][PF_6]$ in CD_3CN with the assignments of protons.

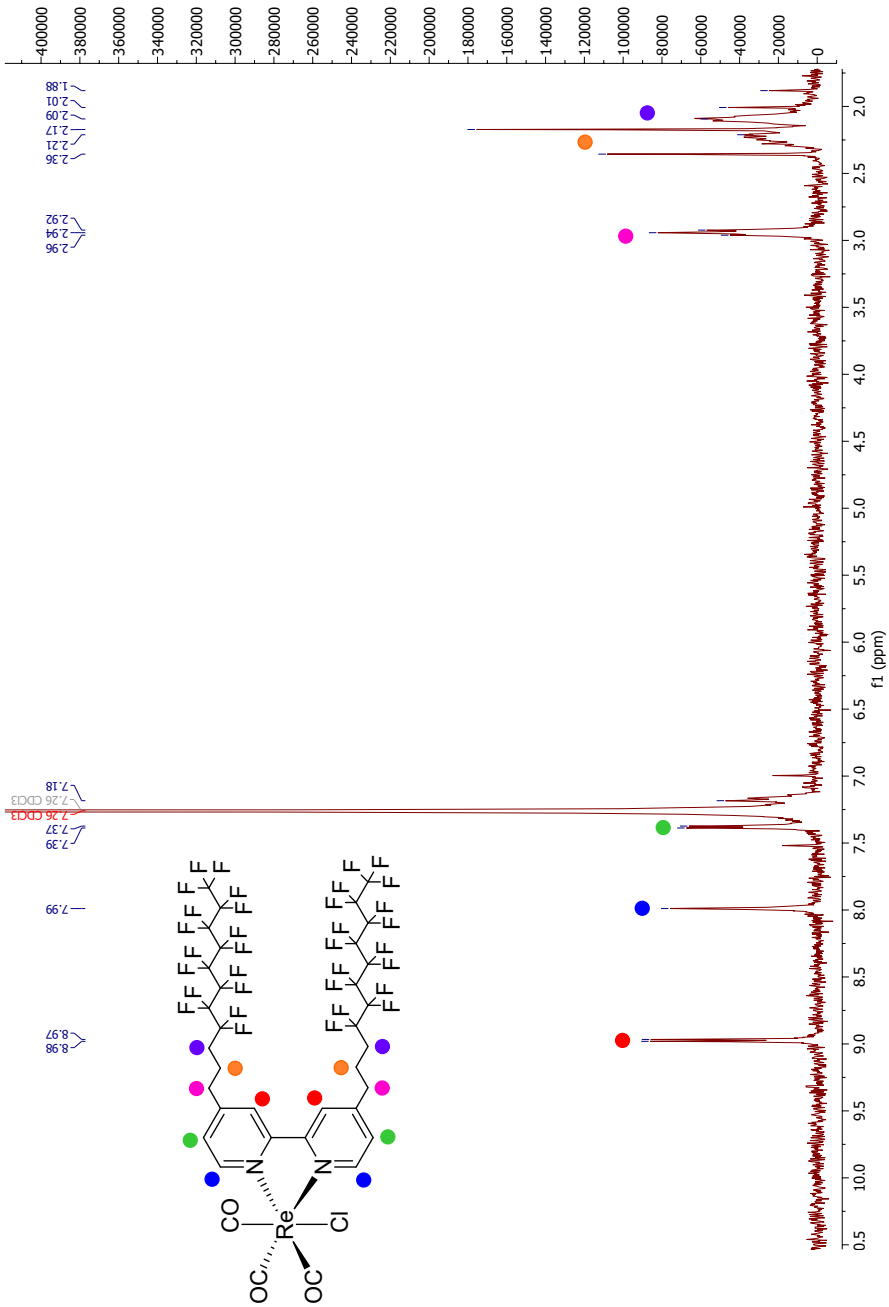


Figure A.10: The ^{1}H NMR of $[Re(CO)_4(dppz)][PF_6]$ in $CDCl_3$ with the assignments of protons.

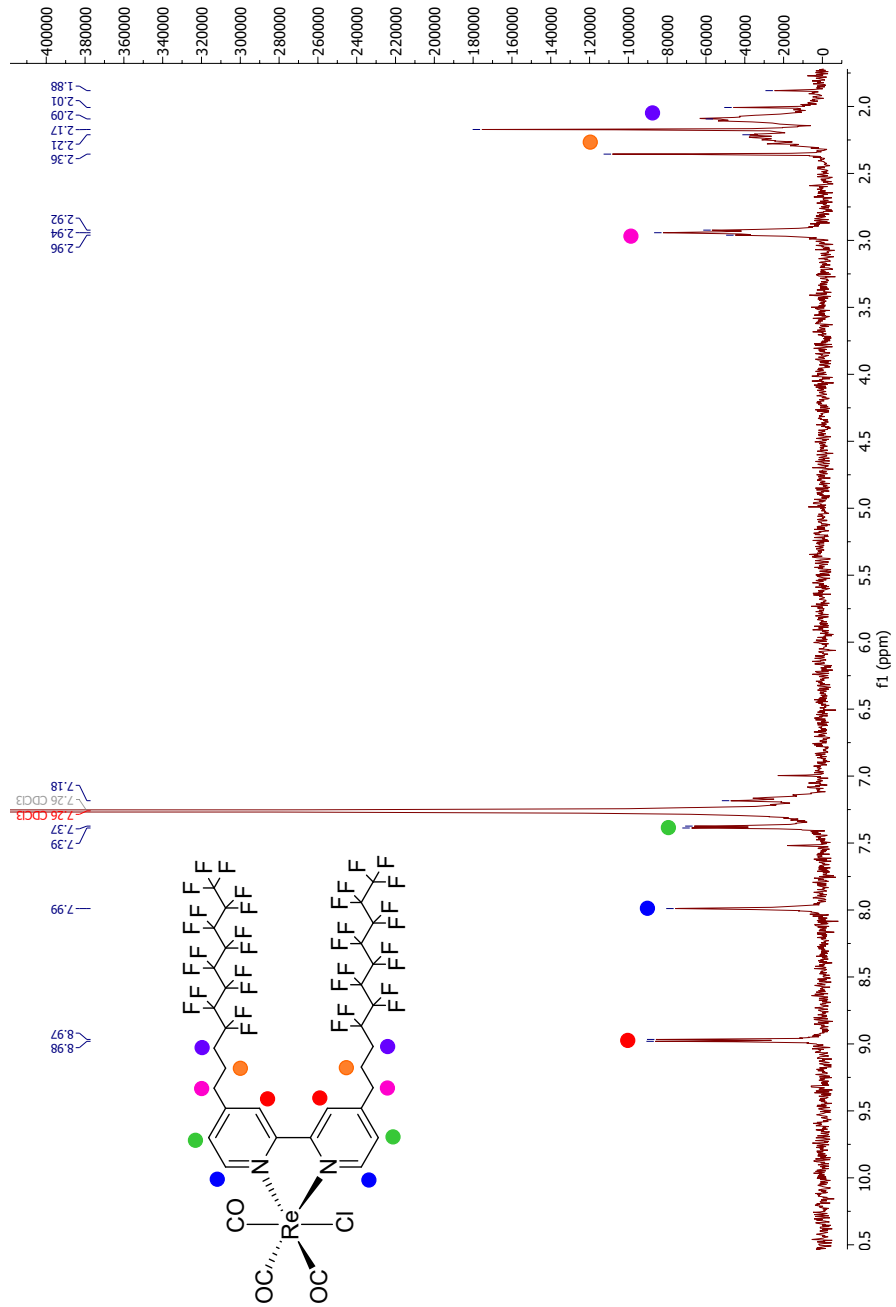


Figure A.11: The ^{1}H NMR of *fac*-Re(CO)$_3$(bpy–R$_F^8$)Cl in $CDCl_3$ with assignments of protons.

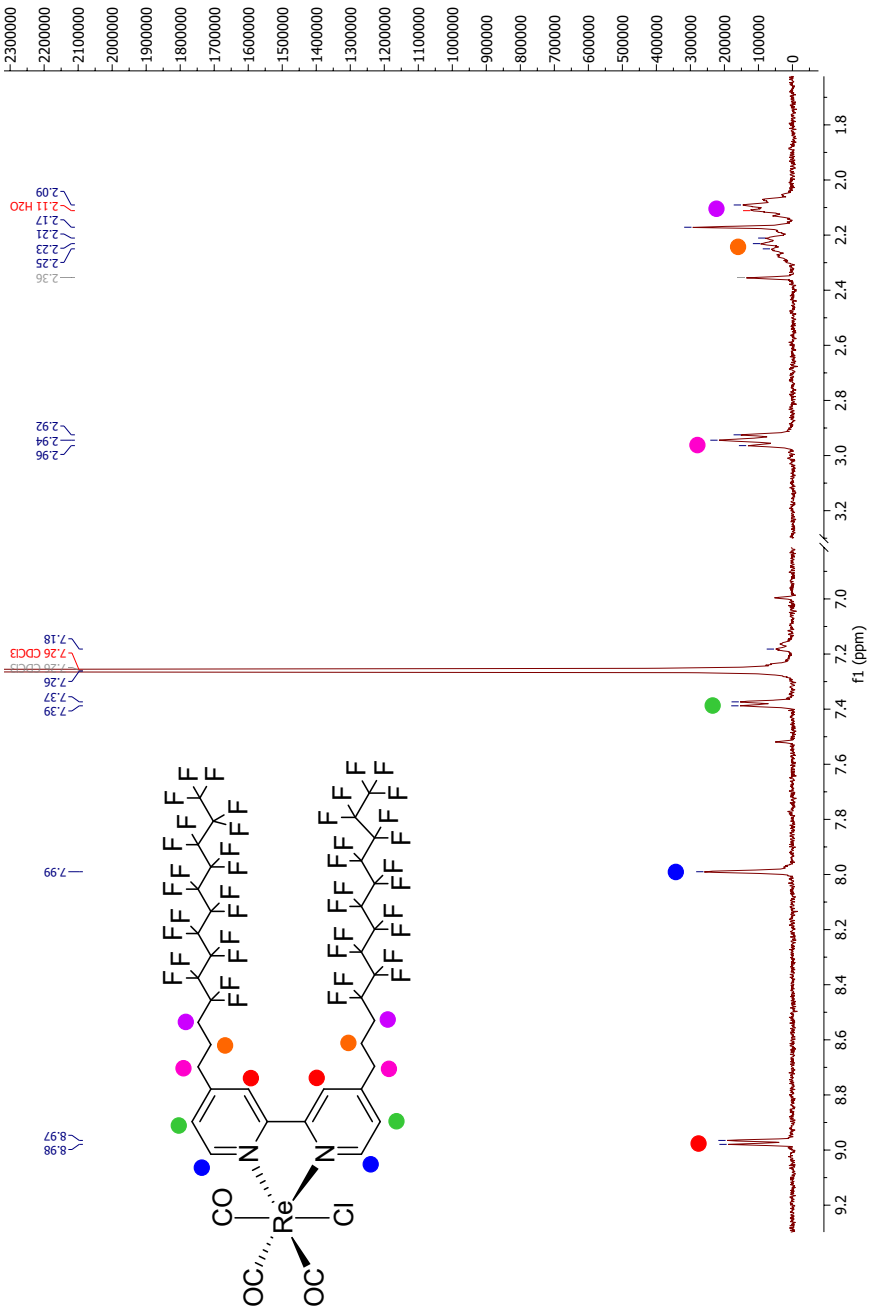


Figure A.12: The ^{1}H NMR of *fac*-Re(CO)$_3$(bpy$-$R$_F{}^{10}$)Cl in $CDCl_3$ with assignments of protons.

Bibliography

[1] J. A. Calladine, S. B. Duckett, M. W. George, S. L. Matthews, R. N. Perutz, O. Torres and K. Q. Vuong, *J. Am. Chem. Soc.*, 2011, **133**, 2303–2310.

[2] M. K. Kuimova, W. Z. Alsindi, J. Dyer, D. C. Grills, O. S. Jina, P. Matousek, A. W. Parker, P. Portius, X. Z. Sun, M. Towrie *et al.*, *Dalton Trans.*, 2003, 3996–4006.

[3] K. McFarlane, B. Lee, J. Bridgewater and P. C. Ford, *J. Organomet. Chem.*, 1998, **554**, 49–61.

[4] B. Wardle, *Principles and Applications of Photochemistry*, John Wiley & Sons Ltd, England, 2009.

[5] C. E. Wayne and R. P. Wayne, *Photochemistry*, Oxford University Press, Oxford, 1996.

[6] B. A. Thrush, *Photochem. Photobiol. Sci.*, 2003, **2**, 453–454.

[7] G. Porter, *Proc. R. Soc. London, Ser. A.*, 1950, **200**, 284–300.

[8] R. G. W. Norrish and G. Porter, *Nature*, 1949, **164**, 658.

[9] J. N. Schrauben, K. L. Dillman, W. F. Beck and J. K. McCusker, *Chem. Sci.*, 2010, **1**, 405–410.

[10] J. M. Butler, M. W. George, J. R. Schoonover, D. M. Dattelbaum and T. J. Meyer, *Coord. Chem. Rev.*, 2007, **251**, 492–514.

[11] J. A. Calladine, K. Q. Vuong, X. Z. Sun and M. W. George, *Pure Appl. Chem.*, 2009, **81**, 1667–1675.

[12] M. W. George and J. J. Turner, *Coord. Chem. Rev.*, 1998, **177**, 201–217.

[13] T. Johnson, A. Simon, J. Weil and G. Harris, *Appl. Spec.*, 1993, **47**, 1376–1381.

[14] M. W. George, M. Poliakoff and J. J. Turner, *Analyst*, 1994, **119**, 551–560.

[15] G. M. Greetham, P. Burgos, Q. A. Cao, I. P. Clark, P. S. Codd, R. C. Farrow, M. W. George, M. Kogimtzis, P. Matousek, A. W. Parker, M. R. Pollard, D. A. Robinson, Z. J. Xin and M. Towrie, *Appl. Spectrosc.*, 2010, **64**, 1311–1319.

[16] M. Towrie, D. C. Grills, J. Dyer, J. A. Weinstein, P. Matousek, R. Barton, P. D. Bailey, N. Subramaniam, W. M. Kwok, C. S. Ma, D. Phillips, A. W. Parker and M. W. George, *Appl. Spectrosc.*, 2003, **57**, 367–380.

[17] G. Greetham, D. Sole, I. Clark, A. Parker, M. Pollard and M. Towrie, *Rev. Sci. Instrum.*, 2012, **83**, 103107.

[18] S. F. Sousa, P. A. Fernandes and M. J. Ramos, *J. Phys. Chem. A.*, 2007, **111**, 10439–10452.

[19] C. J. Cramer and D. G. Truhlar, *Phys. Chem. Chem. Phys.*, 2009, **11**, 10757–10816.

[20] H. Wang, F. Cai, D. Feng, L. Zhou, D. Li, Y. Wei, Z. Feng, J. Zhang, J. He and Y. Wu, *J. Mol. Struct.*, 2019, **1194**, 157–162.

[21] I. Maisuls, F. M. Cabrerizo, A. G. Lappin, G. T. Ruiz and G. J. Ferraudi, *J. Photochem. Photobiol. A.*, 2018, **364**, 169–176.

[22] J. F. Martinez, N. T. La Porte, S. Chaudhuri, A. Sinopoli, Y. J. Bae, M. Sohail, V. S. Batista and M. R. Wasielewski, *J. Phys. Chem. C*, 2019, **123**, 10178–10190.

[23] L. S. Matos, R. C. Amaral and N. Y. Murakami Iha, *Inorg. Chem.*, 2018, **57**, 9316–9326.

[24] J. Wang, Y. Lu, W. McCarthy, R. Conway-Kenny, B. Twamley, J. Zhao and S. M. Draper, *Chem. Commun.*, 2018, **54**, 1073–1076.

[25] A. Woźna and A. Kapturkiewicz, *Phys. Chem. Chem. Phys.*, 2015, **17**, 30468–30480.

[26] A. Carreño, M. Gacitúa, J. Fuentes, D. Páez-Hernández, J. Peñaloza, C. Otero, M. Preite, E. Molins, W. Swords, G. Meyer *et al.*, *New J. Chem.*, 2016, **40**, 7687–7700.

[27] M. Fumanal and C. Daniel, *J. Phys. Chem. A*, 2016, **120**, 6934–6943.

[28] A. Juris, V. Balzani, F. Barigelletti, S. Campagna, P. l. Belser and A. v. von Zelewsky, *Coord. Chem. Rev.*, 1988, **84**, 85–277.

[29] R. A. Krause, in *Coordination Compounds: Synthesis and Medical Application*, Springer, 1987, pp. 1–52.

[30] T. J. Meyer, *Pure Appl. Chem.*, 1986, **58**, 1193–1206.

[31] N. Sutin and C. Creutz, *Pure Appl. Chem.*, 1980, **52**, 2717–2738.

[32] T. J. Meyer, *Acc. Chem. Res.*, 1989, **22**, 163–170.

[33] R. Leasure, L. Sacksteder, D. Nesselrodt, G. Reitz, J. Demas and B. DeGraff, *Inorg. Chem.*, 1991, **30**, 3722–3728.

[34] P. Chen, R. Duesing, D. K. Graff and T. J. Meyer, *J. Phys. Chem.*, 1991, **95**, 5850–5858.

[35] C. Creutz, M. Chou, T. L. Netzel, M. Okumura and N. Sutin, *J. Am. Chem. Soc.*, 1980, **102**, 1309–1319.

[36] E. J. Lee and M. S. Wrighton, *J. Am. Chem. Soc.*, 1991, **113**, 8562–8564.

[37] L. Cooley, S. Larson, C. Elliott and D. Kelley, *J. Phys. Chem.*, 1991, **95**, 10694–10700.

[38] O. Ishitani, I. Namura, S. Yanagida and C. Pac, *J. Chem. Soc., Chem. Commun.*, 1987, 1153–1154.

[39] O. Ishitani, M. W. George, T. Ibusuki, F. P. Johnson, K. Koike, K. Nozaki, C. Pac, J. J. Turner and J. R. Westwell, *Inorg. Chem.*, 1994, **33**, 4712–4717.

[40] A. O. T. Patrocinio and N. Y. Murakami Iha, *Inorg. Chem.*, 2008, **47**, 10851–10857.

[41] A. O. T. Patrocinio, M. K. Brennaman, T. J. Meyer and N. Y. Murakami Iha, *J. Phys. Chem. A*, 2010, **114**, 12129–12137.

[42] A. S. Polo, M. K. Itokazu, K. M. Frin, A. O. de Toledo Patrocínio and N. Y. M. Iha, *Coord. Chem. Rev.*, 2006, **250**, 1669–1680.

[43] M. Kayanuma, C. Daniel, H. Köppel and E. Gindensperger, *Coord. Chem. Rev.*, 2011, **255**, 2693–2703.

[44] A. Vlček Jr, in *Photophysics of Organometallics*, Springer, 2009, pp. 115–158.

[45] D. Striplin and G. Crosby, *Coord. Chem. Rev.*, 2001, **211**, 163–175.

[46] A. Vogler and H. Kunkely, *Coord. Chem. Rev.*, 2000, **200**, 991–1008.

[47] S. Sato, A. Sekine, Y. Ohashi, O. Ishitani, A. M. Blanco-Rodriguez, A. Vlček Jr, T. Unno and K. Koike, *Inorg. Chem.*, 2007, **46**, 3531–3540.

[48] H.-Y. Li, J. Wu, X.-H. Zhou, L.-C. Kang, D.-P. Li, Y. Sui, Y.-H. Zhou, Y.-X. Zheng, J.-L. Zuo and X.-Z. You, *Dalton Trans.*, 2009, 10563–10569.

[49] A. Boulay, A. Seridi, C. Zedde, S. Ladeira, C. Picard, L. Maron and E. Benoist, *Eur. J. Inorg. Chem.*, 2010, **2010**, 5058–5062.

[50] Y. Li, Y. Liu, J. Guo, F. Wu, W. Tian, B. Li and Y. Wang, *Synth. Met.*, 2001, **118**, 175–179.

[51] A. S. Polo, M. K. Itokazu and N. Y. Murakami, *Coord. Chem. Rev.*, 2004, **248**, 1343–1361.

[52] N. P. Liyanage, W. Yang, S. Guertin, S. S. Roy, C. A. Carpenter, R. E. Adams, R. H. Schmehl, J. H. Delcamp and J. W. Jurss, *Chem. Commun.*, 2019, **55**, 993–996.

[53] F. P. A. Johnson, M. W. George, F. Hartl and J. J. Turner, *Organometallics.*, 1996, **15**, 3374–3387.

[54] F. Cecchet, M. Alebbi, C. A. Bignozzi and F. Paolucci, *Inorg. Chim. Acta*, 2006, **359**, 3871–3874.

[55] P. Lang, R. Giereth, S. Tschierlei and M. Schwalbe, *Chem. Commun.*, 2019, **55**, 600–603.

[56] V. Balzani, A. Juris, M. Venturi, S. Campagna and S. Serroni, *Chem. Rev.*, 1996, **96**, 759–834.

[57] K. S. Schanze and K. A. Walters, *Molecular and Supramolecular Photochemistry*, 1998, **2**, 75–128.

[58] D. Stufkens, *Comments Inorg. Chem.*, 1992, **13**, 359–385.

[59] M. Wrighton and D. L. Morse, *J. A. Chem. Soc.*, 1974, **96**, 998–1003.

[60] A. J. Lees, *Chem. Rev.*, 1987, **87**, 711–743.

[61] D. J. Stufkens and A. Vlček Jr, *Coord. Chem. Rev.*, 1998, **177**, 127–179.

[62] G. Stor, D. Stufkens and A. Oskam, *Inorg. Chem.*, 1992, **31**, 1318–1319.

[63] D. Rossennar, B. D. Stufkens and A. Vlček Jr, *Inorg. Chem.*, 1996, **35**, 2902–2909.

[64] A. Kumar, S.-S. Sun and A. J. Lees, *Photophysics and Photochemistry of Organometallic Rhenium Diimine Complexes*, Springer, 2009, pp. 37–71.

[65] L. Sacksteder, A. P. Zipp, E. A. Brown, J. Streich, J. Demas and B. DeGraff, *Inorg. Chem.*, 1990, **29**, 4335–4340.

[66] S. Sato, Y. Matubara, K. Koike, M. Falkenstrom, T. Katayama, Y. Ishibashi, H. Miyasaka, S. Taniguchi, H. Chosrowjan, N. Mataga, N. Fukazawa, S. Koshihara, K. Onda and O. Ishitani, *Chem. Eur. J.*, 2012, **18**, 15722–34.

[67] K. Koike, N. Okoshi, H. Hori, K. Takeuchi, O. Ishitani, H. Tsunbaki, I. P. Clark, M. W. George, F. P. A. Johnson and J. J. Turner, *J. Am. Chem. Soc.*, 2002, **124**, 11448–11455.

[68] S. Sato and O. Ishitani, *Coord. Chem. Rev.*, 2015, **282-283**, 50–59.

[69] R. J. Shaver, D. P. Rillema and C. Woods, *J. Chem. Soc., Chem. Commun.*, 1990, 179–180.

[70] R. Sahai, D. Rillema, R. Shaver, S. Van Wallendael, D. Jackman and M. Boldaji, *Inorg. Chem.*, 1989, **28**, 1022–1028.

[71] R. J. Shaver and D. P. Rillema, *Inorg. Chem.*, 1992, **31**, 4101–4107.

[72] S. Van Wallendael, R. J. Shaver, D. P. Rillema, B. Yoblinski, M. Stathis and T. F. Guarr, *Inorg. Chem.*, 1990, **29**, 1761–1767.

[73] P. J. Giordano and M. S. Wrighton, *J. Am. Chem. Soc.*, 1979, **101**, 2888–2897.

[74] S. M. Fredericks, J. C. Luong and M. S. Wrighton, *J. Am. Chem. Soc.*, 1979, **101**, 7415–7417.

[75] W. K. Smothers and M. S. Wrighton, *J. Am. Chem. Soc*, 1983, **105**, 1067–1069.

[76] D. M. Manuta and A. J. Lees, *Inorg. Chem.*, 1986, **25**, 1354–1359.

[77] G. F. Strouse, H. U. Guedel, V. Bertolasi and V. Ferretti, *Inorg. Chem.*, 1995, **34**, 5578–5587.

[78] G. F. Strouse and H. U. Güdel, *Inorganica Chim. Acta*, 1995, **240**, 453–464.

[79] S. Bernhard, K. M. Omberg, G. F. Strouse and J. R. Schoonover, *Inorg. Chem.*, 2000, **39**, 3107–3110.

[80] K. A. Grice, N. X. Gu, M. D. Sampson and C. P. Kubiak, *Dalton Trans.*, 2013, **42**, 8498–8503.

[81] A. Klein, C. Vogler and W. Kaim, *Organometallics*, 1996, **15**, 236–244.

[82] J. M. Smieja, E. E. Benson, B. Kumar, K. A. Grice, C. S. Seu, A. J. Miller, J. M. Mayer and C. P. Kubiak, *Proc. Natl. Acad. Sci. U. S. A.*, 2012, **109**, 15646–15650.

[83] D. Miholova and A. Vlček Jr, *J. Organomet. Chem.*, 1985, **279**, 317–326.

[84] B. Olbrich-Deussner and W. Kaim, *J. Organomet. Chem.*, 1988, **340**, 71–91.

[85] S. P. Schmidt, J. Nitschke, W. C. Trogler, S. I. Huckett and R. J. Angelici, in *Manganese(I) and Rhenium(I) Pentacarbonyl(Trifluoromethanesulfonato) Complexes*, John Wiley & Sons, Ltd, 1989, vol. 26, ch. 20, pp. 113–117.

[86] R. Englman and J. Jortner, *J. Lumin.*, 1970, **1**, 134–142.

[87] M. Grätzel, *Comments Inorg. Chem.*, 1991, **12**, 93–111.

[88] M. K. Nazeeruddin, A. Kay, I. Rodicio, R. Humphry-Baker, E. Müller, P. Liska, N. Vlachopoulos and M. Grätzel, *J. Am. Chem. Soc.*, 1993, **115**, 6382–6390.

[89] M. Arkin, E. Stemp, C. Turro, N. Turro and J. Barton, *J. Am. Chem. Soc.*, 1996, **118**, 2267–2274.

[90] J. R. Lakowicz, H. Malak, I. Gryczynski, F. N. Castellano and G. J. Meyer, *Biospectroscopy*, 1995, **1**, 163–168.

[91] X.-Q. Guo, F. N. Castellano, L. Li and J. R. Lakowicz, *Biophys. Chem.*, 1998, **71**, 51–62.

[92] A. Kirsch-De Mesmaeker, J.-P. Lecomte and J. M. Kelly, in *Electron Transfer II*, Springer, 1996, pp. 25–76.

[93] Q. Cao, C. M. Creely, E. S. Davies, J. Dyer, T. L. Easun, D. C. Grills, D. A. McGovern, J. McMaster, J. Pitchford, J. A. Smith *et al.*, *Photochem. Photobiol. Sci.*, 2011, **10**, 1355–1364.

[94] V. Sathish, E. Babu, A. Ramdass, Z.-Z. Lu, T.-T. Chang, M. Velayudham, P. Thanasekaran, K.-L. Lu, W.-S. Li and S. Rajagopal, *RSC Adv.*, 2013, **3**, 18557–18566.

[95] T. Morimoto, T. Nakajima, S. Sawa, R. Nakanishi, D. Imori and O. Ishitani, *J. Am. Chem. Soc*, 2013, **135**, 16825–16828.

[96] Y. Tamaki, K. Watanabe, K. Koike, H. Inoue, T. Morimoto and O. Ishitani, *Faraday Discuss.*, 2012, **155**, 115–127.

[97] J. Agarwal, E. Fujita, H. F. Schaefer III and J. T. Muckerman, *J. Am. Chem. Soc.*, 2012, **134**, 5180–5186.

[98] J. J. Concepcion, J. W. Jurss, M. K. Brennaman, P. G. Hoertz, A. O. T. Patrocinio, N. Y. Murakami Iha, J. L. Templeton and T. J. Meyer, *Acc. Chem. Res.*, 2009, **42**, 1954–1965.

[99] N. Song, C. J. Gagliardi, R. A. Binstead, M.-T. Zhang, H. Thorp and T. J. Meyer, *J. Am. Chem. Soc.*, 2012, **134**, 18538–18541.

[100] L. Tong, A. K. Inge, L. Duan, L. Wang, X. Zou and L. Sun, *Inorg. Chem.*, 2013, **52**, 2505–2518.

[101] K. J. Young, L. A. Martini, R. L. Milot, R. C. Snoeberger III, V. S. Batista, C. A. Schmuttenmaer, R. H. Crabtree and G. W. Brudvig, *Coord. Chem. Rev.*, 2012, **256**, 2503–2520.

[102] K. E. Erkkila, D. T. Odom and J. K. Barton, *Chem. Rev.*, 1999, **99**, 2777–2796.

[103] C. Moucheron, A. Kirsch-De Mesmaeker and J. M. Kelly, in *Less Common Metals in Proteins and Nucleic Acid Probes*, Springer, 1998, pp. 163–216.

[104] M. K. Kuimova, X. Z. Sun, P. Matousek, D. C. Grills, A. W. Parker, M. Towrie and M. W. George, *Photochem. Photobiol. Sci.*, 2007, **6**, 1158–1163.

[105] J. Dyer, C. M. Creely, J. C. Penedo, D. C. Grills, S. Hudson, P. Matousek, A. W. Parker, M. Towrie, J. M. Kelly and M. W. George, *Photochem. Photobiol. Sci.*, 2007, **6**, 741–748.

[106] R. Horvath and K. C. Gordon, *Inorg. Chim. Acta.*, 2011, **374**, 10–18.

[107] M. K. Kuimova, W. Z. Alsindi, A. J. Blake, E. S. Davies, D. J. Lampus, P. Matousek, J. McMaster, A. W. Parker, M. Towrie, X.-Z. Sun *et al.*, *Inorg. Chem.*, 2008, **47**, 9857–9869.

[108] G. Ruiz, M. Juliarena, R. Lezna, M. Feliz and G. Ferraudi, *J. Photochem. Photobiol., A.*, 2006, **179**, 289–297.

[109] A. W. McKinley, P. Lincoln and E. M. Tuite, *Coord. Chem. Rev.*, 2011, **255**, 2676–2692.

[110] A. E. Friedman, J. C. Chambron, J. P. Sauvage, N. J. Turro and J. K. Barton, *J. Am. Chem. Soc.*, 1990, **112**, 4960–4962.

[111] C. Hiort, P. Lincoln and B. Norden, *J. Am. Chem. Soc.*, 1993, **115**, 3448–3454.

[112] R. M. Hartshorn and J. K. Barton, *J. Am. Chem. Soc.*, 1992, **114**, 5919–5925.

[113] A. E. Friedman, C. V. Kumar, N. J. Turro and J. K. Barton, *Nucleic Acids Res.*, 1991, **19**, 2595.

[114] E. Sabatani, H. D. Nikol, H. B. Gray and F. C. Anson, *J. Am. Chem. Soc.*, 1996, **118**, 1158–1163.

[115] E. Olson, D. Hu, A. Hörmann, A. Jonkman, M. Arkin, E. Stemp, J. Barton and P. Barbara, *J. Am. Chem. Soc.*, 1997, **119**, 11458–11467.

[116] V. W.-W. Yam, K. K.-W. Lo, K.-K. Cheung and R. Y.-C. Kong, *J. Chem. Soc., Chem. Commun.*, 1995, 1191–1193.

[117] C. G. Coates, J. Olofsson, M. Coletti, J. J. McGarvey, B. Önfelt, P. Lincoln, B. Norden, E. Tuite, P. Matousek and A. W. Parker, *J. Phys. Chem. B*, 2001, **105**, 12653–12664.

[118] M. K. Brennaman, J. H. Alstrum-Acevedo, C. N. Fleming, P. Jang, T. J. Meyer and J. M. Papanikolas, *J. Am. Chem. Soc.*, 2002, **124**, 15094–15098.

[119] M. K. Brennaman, T. J. Meyer and J. M. Papanikolas, *J. Phys. Chem. A*, 2004, **108**, 9938–9944.

[120] J. R. Schoonover and G. F. Strouse, *Chem. Rev.*, 1998, **98**, 1335–1356.

[121] H. D. Stoeffler, N. B. Thornton, S. L. Temkin and K. S. Schanze, *J. Am. Chem. Soc.*, 1995, **117**, 7119–7128.

[122] J. R. Schoonover, W. D. Bates and T. J. Meyer, *Inorg. Chem.*, 1995, **34**, 6421–6422.

[123] J. R. Schoonover, G. F. Strouse, R. B. Dyer, W. D. Bates, P. Chen and T. J. Meyer, *Inorg. Chem.*, 1996, **35**, 273–274.

[124] V. W.-W. Yam, K. K.-W. Lo and R. Y.-C. Kong, *J. Chem. Soc., Dalton Trans.*, 1997, 2067–2072.

[125] J. J. McGarvey, P. Callaghan, C. G. Coates, J. R. Schoonover, J. M. Kelly, L. Jacquet and K. C. Gordon, *J. Phys. Chem. B*, 1998, **102**, 5941–5942.

[126] J. Dyer, W. J. Blau, C. G. Coates, C. M. Creely, J. D. Gavey, M. W. George, D. C. Grills, S. Hudson, J. M. Kelly, P. Matousek *et al.*, *Photochem. Photobiol. Sci.*, 2003, **2**, 542–554.

[127] J. R. Schoonover, G. F. Strouse, P. Chen, W. D. Bates and T. J. Meyer, *Inorganic Chemistry*, 1993, **32**, 2618–2619.

[128] M. K. Kuimova, D. C. Grills, P. Matousek, A. W. Parker, X.-Z. Sun, M. Towrie and M. W. George, *Vib. Spectrosc.*, 2004, **35**, 219–223.

[129] S. Sousa, R. Sampaio, N. B. Neto, A. Machado and A. Patrocinio, *Photochem. Photobiol. Sci.*, 2014, **13**, 1213–1224.

[130] P. Xiao, J. Huang, Y. Yu, J. Yuan, D. Luo, B. Liu and D. Liang, *Appl. Sci.*, 2018, **8**, 1449.

[131] J. M. Hancock, A. P. Gifford, Y. Zhu, Y. Lou and S. A. Jenekhe, *Chem. Mater.*, 2006, **18**, 4924–4932.

[132] M.-T. Lee, C.-H. Liao, C.-H. Tsai and C. H. Chen, *Adv. Mater.*, 2005, **17**, 2493–2497.

[133] T.-C. Chao, Y.-T. Lin, C.-Y. Yang, T. S. Hung, H.-C. Chou, C.-C. Wu and K.-T. Wong, *Adv. Mater.*, 2005, **17**, 992–996.

[134] S.-J. Yeh, M.-F. Wu, C.-T. Chen, Y.-H. Song, Y. Chi, M.-H. Ho, S.-F. Hsu and C. H. Chen, *Adv. Mater.*, 2005, **17**, 285–289.

[135] Z.-h. Cui, A. J. Aquino, A. C.-H. Sue and H. Lischka, *Phys. Chem. Chem. Phys.*, 2018, **20**, 26957–26967.

[136] T. Qian, F. Chen, Y. Chen, Y.-X. Wang and W. Hu, *Chem. Commun.*, 2017, **53**, 11822–11825.

[137] M. R. Wasielewski, *Acc. Chem. Res.*, 2009, **42**, 1910–1921.

[138] F. J. M. Hoeben, P. Jonkheijm, E. W. Meijer and A. P. H. J. Schenning, *Chem. Rev.*, 2005, **105**, 1491–1546.

[139] J. Wang, A. Kulago, W. R. Browne and B. L. Feringa, *J. Am. Chem. Soc.*, 2010, **132**, 4191–4196.

[140] P. M. Beaujuge and J. M. J. Fréchet, *J. Am. Chem. Soc.*, 2011, **133**, 20009–20029.

[141] S.-G. Chen, P. Stradins and B. A. Gregg, *J. Phys. Chem. B*, 2005, **109**, 13451–13460.

[142] B. A. Gregg, *J. Phys. Chem. B*, 2003, **107**, 4688 – 4698.

[143] E. E. Neuteboom, S. C. Meskers, P. A. Van Hal, J. K. Van Duren, E. Meijer, R. A. Janssen, H. Dupin, G. Pourtois, J. Cornil, R. Lazzaroni *et al.*, *J. Am. Chem. Soc.*, 2003, **125**, 8625–8638.

[144] B. A. Gregg and R. A. Cormier, *J. Am. Chem. Soc.*, 2001, **123**, 7959–7960.

[145] J. J. Dittmer, E. A. Marseglia and R. H. Friend, *Adv. Mater.*, 2000, **12**, 1270–1274.

[146] S. Ferrere, A. Zaban and B. A. Gregg, *J. Phys. Chem. B*, 1997, **101**, 4490–4493.

[147] C. W. Tang, *Appl. Phys. Lett.*, 1986, **48**, 183–185.

[148] Y. Zeng, J. Chen, T. Yu, G. Yang and Y. Li, *ACS Energy Lett.*, 2017, **2**, 357–363.

[149] S. Prathapan, S. I. Yang, J. Seth, M. A. Miller, D. F. Bocian, D. Holten and J. S. Lindsey, *J. Phys. Chem. B*, 2001, **105**, 8237–8248.

[150] S. I. Yang, S. Prathapan, M. A. Miller, J. Seth, D. F. Bocian, J. S. Lindsey and D. Holten, *J. Phys. Chem. B*, 2001, **105**, 8249–8258.

[151] K.-y. Tomizaki, R. S. Loewe, C. Kirmaier, J. K. Schwartz, J. L. Retsek, D. F. Bocian, D. Holten and J. S. Lindsey, *J. Org. Chem.*, 2002, **67**, 6519–6534.

[152] K. Muthukumaran, R. S. Loewe, C. Kirmaier, E. Hindin, J. K. Schwartz, I. V. Sazanovich, J. R. Diers, D. F. Bocian, D. Holten and J. S. Lindsey, *J. Phys. Chem. B*, 2003, **107**, 3431–3442.

[153] M. A. Miller, R. K. Lammi, S. Prathapan, D. Holten and J. S. Lindsey, *J. Org. Chem.*, 2000, **65**, 6634–6649.

[154] G. Li, Y. Chen, Y. Qiao, Y. Lu and G. Zhou, *J. Org. Chem.*, 2018, **83**, 5577–5587.

[155] A. Benito-Hernández, M. T. El-Sayed, J. T. L. Navarrete, M. C. R. Delgado and B. Gómez-Lor, *Org. Chem. Front.*, 2018, **5**, 1748–1755.

[156] A. Agosti, E. Kuna and G. Bergamini, *Eur. J. Inorg. Chem.*, 2019, **2019**, 577–584.

[157] W. E. Ford and P. V. Kamat, *J. Phys. Chem.*, 1987, **91**, 6373–6380.

[158] F. Würthner, C. Thalacker and A. Sautter, *Adv. Mater.*, 1999, **11**, 754–758.

[159] H. Langhals and S. Saulich, *Chem. Eur. J.*, 2002, **8**, 5630–5643.

[160] A. P. Schenning, J. v. Herrikhuyzen, P. Jonkheijm, Z. Chen, F. Würthner and E. Meijer, *J. Am. Chem. Soc.*, 2002, **124**, 10252–10253.

[161] C. Kirmaier, E. Hindin, J. K. Schwartz, I. V. Sazanovich, J. R. Diers, K. Muthukumaran, M. Taniguchi, D. F. Bocian, J. S. Lindsey and D. Holten, *J. Phys. Chem. B*, 2003, **107**, 3443–3454.

[162] A. Y. Rybkin, A. Y. Belik, O. Kraevaya, E. Khakina, A. Zhilenkov, N. Goryachev, D. Volyniuk, J. Grazulevicius, P. Troshin and A. Kotelnikov, *Dyes Pigm.*, 2019, **160**, 457–466.

[163] A. M. Levine, S. Biswas and A. B. Braunschweig, *Nanoscale Adv.*, 2019, **1**, 3858–3869.

[164] X.-F. Chen, M. E. El-Khouly, K. Ohkubo, S. Fukuzumi and D. K. Ng, *Chem. Eur. J.*, 2018, **24**, 3862–3872.

[165] E. A. Margulies, L. E. Shoer, S. W. Eaton and M. R. Wasielewski, *Phys. Chem. Chem. Phys.*, 2014, **16**, 23735–23742.

[166] K. M. Lefler, K. E. Brown, W. A. Salamant, S. M. Dyar, K. E. Knowles and M. R. Wasielewski, *J. Phys. Chem. A*, 2013, **117**, 10333–10345.

[167] N. Aratani, A. Osuka, H. S. Cho and D. Kim, *J. Photo. Photobiol. C*, 2002, **3**, 25–52.

[168] D. Holten, D. F. Bocian and J. S. Lindsey, *Acc. Chem. Res.*, 2002, **35**, 57–69.

[169] D. Gust, T. A. Moore and A. L. Moore, *Acc. Chem. Res.*, 2001, **34**, 40–48.

[170] M. R. Wasielewski, *Chem. Rev.*, 1992, **92**, 435–461.

[171] M. N. Paddon-Row, *Aust. J. Chem.*, 2003, **56**, 729–748.

[172] N. Meher and P. K. Iyer, *Nanoscale*, 2019, **11**, 13233–13242.

[173] L. Yang, P. Langer, E. S. Davies, M. Baldoni, K. Wickham, N. A. Besley, E. Besley and N. R. Champness, *Chem. Sci.*, 2019, **10**, 3723–3732.

[174] C. W.-T. Chan, H.-K. Cheng, F. K.-W. Hau, A. K.-W. Chan and V. W.-W. Yam, *ACS Appl. Mater. Interfaces*, 2019, **11**, 31585–31593.

[175] B. A. DeHaven, D. W. Goodlett, A. J. Sindt, N. Noll, M. De Vetta, M. D. Smith, C. R. Martin, L. González and L. S. Shimizu, *J. Am. Chem. Soc.*, 2018, **140**, 13064–13070.

[176] I.-W. Hwang, H. S. Cho, D. H. Jeong, D. Kim, A. Tsuda, T. Nakamura and A. Osuka, *J. Phys. Chem. B*, 2003, **107**, 9977–9988.

[177] P. H. Dinolfo and J. T. Hupp, *Chem. Mater.*, 2001, **13**, 3113–3125.

[178] D. Reinhoudt and M. Crego-Calama, *Science*, 2002, **295**, 2403–2407.

[179] F. Würthner, C. R. SahaMöller, B. Fimmel, S. Ogi, P. Leowanawat and D. Schmidt, *Chem. Rev.*, 2015, **116**, 962 – 1052.

[180] P. Spenst and F. Würthner, *J. Photochem. Photobiol. C*, 2017, **31**, 114–138.

[181] H. Liu, L. Shen, Z. Cao and X. Li, *Phys. Chem. Chem. Phys.*, 2014, **16**, 16399–16406.

[182] A. Issac, R. Hildner, D. Ernst, C. Hippius, F. Würthner and J. Köhler, *Phys. Chem. Chem. Phys.*, 2012, **14**, 10789–10798.

[183] F. Schlosser, M. Moos, C. Lambert and F. Würthner, *Adv. Mater.*, 2013, **25**, 410–414.

[184] P. Spenst and F. Würthner, *Angew. Chem. Int. Ed.*, 2015, **54**, 10165–10168.

[185] S. Yagai, T. Seki, T. Karatsu, A. Kitamura and F. Würthner, *Angew. Chem. Int. Ed.*, 2008, **47**, 3367–3371.

[186] S. Yagai, *Bull. Chem. Soc. Jpn.*, 2014, **88**, 28–58.

[187] T. Seki, A. Asano, S. Seki, Y. Kikkawa, H. Murayama, T. Karatsu, A. Kitamura and S. Yagai, *Chem. Eur. J.*, 2011, **17**, 3598–3608.

[188] T. van der Boom, R. T. Hayes, Y. Zhao, P. J. Bushard, E. A. Weiss and M. R. Wasielewski, *J. Am. Chem. Soc.*, 2002, **124**, 9582–9590.

[189] M. J. Ahrens, L. E. Sinks, B. Rybtchinski, W. Liu, B. A. Jones, J. M. Giaimo, A. V. Gusev, A. J. Goshe, D. M. Tiede and M. R. Wasielewski, *J. Am. Chem. Soc.*, 2004, **126**, 8284–8294.

[190] D. Ambrosek, H. Marciniak, S. Lochbrunner, J. Tatchen, X.-Q. Li, F. Würthner and O. Kuhn, *Phys. Chem. Chem. Phys.*, 2011, **13**, 17649–17657.

[191] J. E. Bullock, R. Carmieli, S. M. Mickley, J. Vura-Weis and M. R. Wasielewski, *J. Am. Chem. Soc.*, 2009, **131**, 11919–11929.

[192] T. E. Kaiser, I. G. Scheblykin, D. Thomsson and F. Würthner, *J. Phys. Chem. B*, 2009, **113**, 15836–15842.

[193] T. Kaiser, H. Wang, V. Stepanenko and F. Würthner, *Angew. Chem. Int. Ed.*, 2007, **46**, 5541–5544.

[194] X. Li, L. E. Sinks, B. Rybtchinski and M. R. Wasielewski, *J. Am. Chem. Soc.*, 2004, **126**, 10810–10811.

[195] H. Marciniak, X.-Q. Li, F. Würthner and S. Lochbrunner, *J. Phys. Chem. A*, 2011, **115**, 648–654.

[196] B. Rybtchinski, L. E. Sinks and M. R. Wasielewski, *J. Phys. Chem. A*, 2004, **108**, 7497–7505.

[197] J. Zhang, F. J. M. Hoeben, M. J. Pouderoijen, A. P. H. J. Schenning, E. W. Meijer, F. C. De Schryver and S. De Feyter, *Chem. Eur. J.*, 2006, **12**, 9046–9055.

[198] F. Würthner, *Chem. Commun.*, 2004, 1564–1579.

[199] M. J. Ahrens, M. J. Fuller and M. R. Wasielewski, *Chem. Mater.*, 2003, **15**, 2684–2686.

[200] C. Huang, S. Barlow and S. R. Marder, *J. Org. Chem.*, 2011, **76**, 2386–2407.

[201] H. Langhals and R. Ismael, *Eur. J. Org. Chem.*, 1998, **1998**, 1915–1917.

[202] M. R. Wasielewski, *J. Org. Chem.*, 2006, **71**, 5051–5066.

[203] T. A. Zeidan, R. Carmieli, R. F. Kelley, T. M. Wilson, F. D. Lewis and M. R. Wasielewski, *J. Am. Chem. Soc.*, 2008, **130**, 13945–13955.

[204] D. Veldman, S. M. A. Chopin, S. C. J. Meskers, M. M. Groeneveld, R. M. Williams and R. A. J. Janssen, *J. Phys. Chem. A*, 2008, **112**, 5846–5857.

[205] S. Long, Y. Wang, S. Vdovic, M. Zhou, L. Yan, Y. Niu, Q. Guo and A. Xia, *Phys. Chem. Chem. Phys.*, 2015, **17**, 18567–18576.

[206] J. M. Lim, P. Kim, M.-C. Yoon, J. Sung, V. Dehm, Z. Chen, F. Würthner and D. Kim, *Chem. Sci.*, 2013, **4**, 388–397.

[207] J. J. Gassensmith, J. M. Baumes and B. D. Smith, *Chem. Commun.*, 2009, 6329–6338.

[208] K. E. Brown, B. S. Veldkamp, D. T. Co and M. R. Wasielewski, *J. Phys. Chem. Lett.*, 2012, **3**, 2362–2366.

[209] D. Gosztola, M. P. Niemczyk, W. Svec, A. S. Lukas and M. R. Wasielewski, *J. Phys. Chem. A*, 2000, **104**, 6545–6551.

[210] E. R. Kennehan, C. Grieco, A. N. Brigeman, G. S. Doucette, A. Rimshaw, K. Bisgaier, N. C. Giebink and J. B. Asbury, *Phys. Chem. Chem. Phys.*, 2017, **19**, 24829–24839.

[211] C. M. Mauck, R. M. Young and M. R. Wasielewski, *J. Phys. Chem. A*, 2017, **121**, 784–792.

[212] K. E. Brown, W. A. Salamant, L. E. Shoer, R. M. Young and M. R. Wasielewski, *J. Phys. Chem. Lett.*, 2014, **5**, 2588–2593.

[213] E. A. Margulies, C. E. Miller, Y. Wu, L. Ma, G. C. Schatz, R. M. Young and M. R. Wasielewski, *Nat. Chem.*, 2016, **8**, 1120–1125.

[214] J. M. Giaimo, J. V. Lockard, L. E. Sinks, A. M. Scott, T. M. Wilson and M. R. Wasielewski, *J. Phys. Chem. A*, 2008, **112**, 2322–2330.

[215] J. M. Giaimo, A. V. Gusev and M. R. Wasielewski, *J. Am. Chem. Soc.*, 2002, **124**, 8530–8531.

[216] A. Schubert, V. Settels, W. Liu, F. Würthner, C. Meier, R. F. Fink, S. Schindlbeck, S. Lochbrunner, B. Engels and V. Engel, *J. Phys. Chem. Lett.*, 2013, **4**, 792–796.

[217] A. Schubert, M. Falge, M. Kess, V. Settels, S. Lochbrunner, W. T. Strunz, F. Würthner, B. Engels and V. Engel, *J. Phys. Chem. A*, 2014, **118**, 1403–1412.

[218] R. F. Kelley, W. S. Shin, B. Rybtchinski, L. E. Sinks and M. R. Wasielewski, *J. Am. Chem. Soc.*, 2007, **129**, 3173–3181.

[219] B. Walker, H. Port and H. C. Wolf, *Chem. Phys.*, 1985, **92**, 177–185.

[220] I. A. Howard, F. Laquai, P. E. Keivanidis, R. H. Friend and N. C. Greenham, *J. Phys. Chem. C*, 2009, **113**, 21225–21232.

[221] R. F. Fink, J. Seibt, V. Engel, M. Renz, M. Kaupp, S. Lochbrunner, H.-M. Zhao, J. Pfister, F. Würthner and B. Engels, *J. Am. Chem. Soc.*, 2008, **130**, 12858–12859.

[222] J. Sung, A. Nowak-Król, F. Schlosser, B. Fimmel, W. Kim, D. Kim and F. Würthner, *J. Am. Chem. Soc.*, 2016, **138**, 9029–9032.

[223] R. Katoh, S. Sinha, S. Murata and M. Tachiya, *J. Photochem. Photobiol. A*, 2001, **145**, 23–34.

[224] V. Settels, W. Liu, J. Pflaum, R. F. Fink and B. Engels, *J. Comput. Chem.*, 2012, **33**, 1544–1553.

[225] H.-M. Zhao, J. Pfister, V. Settels, M. Renz, M. Kaupp, V. C. Dehm, F. Würthner, R. F. Fink and B. Engels, *J. Am. Chem. Soc.*, 2009, **131**, 15660–15668.

[226] Z. Chen, U. Baumeister, C. Tschierske and F. Würthner, *Chem. Eur. J.*, 2007, **13**, 450–465.

[227] Z. Chen, V. Stepanenko, V. Dehm, P. Prins, L. Siebbeles, J. Seibt, P. Marquetand, V. Engel and F. Würthner, *Chem. Eur. J.*, 2007, **13**, 436–449.

[228] J. Ferguson, *J. Chem. Phys.*, 1966, **44**, 2677–2683.

[229] Y. Wu, M. Frasconi, D. M. Gardner, P. R. McGonigal, S. T. Schneebeli, M. R. Wasielewski and J. F. Stoddart, *Angew. Chem., Int. Ed.*, 2014, **53**, 9476–9481.

[230] M. E. Ozser, D. Uzun, I. Elci, H. Icil and M. Demuth, *Photochem. Photobiol. Sci.*, 2003, **2**, 218–223.

[231] F. Matino, G. Schull, F. Köhler, S. Gabutti, M. Mayor and R. Berndt, *Proc. Natl. Acad. Sci. U. S. A.*, 2011, **108**, 961–964.

[232] R. E. Dawson, A. Hennig, D. P. Weimann, D. Emery, V. Ravikumar, J. Montenegro, T. Takeuchi, S. Gabutti, M. Mayor, J. Mareda *et al.*, *Nat. Chem.*, 2010, **2**, 533.

[233] M. Kaik and J. Gawroński, *Org. Lett.*, 2006, **8**, 2921–2924.

[234] M. Borgström, N. Shaikh, O. Johansson, M. F. Anderlund, S. Styring, B. Åkermark, A. Magnuson and L. Hammarström, *J. Am. Chem. Soc.*, 2005, **127**, 17504–17515.

[235] O. Johansson, H. Wolpher, M. Borgström, L. Hammarström, J. Bergquist, L. Sun and B. Åkermark, *Chem. Comm.*, 2004, 194–195.

[236] X. Guo, Z. Gan, H. Luo, Y. Araki, D. Zhang, D. Zhu and O. Ito, *J. Phys. Chem. A*, 2003, **107**, 9747–9753.

[237] L. Flamigni, M. R. Johnston and L. Giribabu, *Chem. Eur. J.*, 2002, **8**, 3938–3947.

[238] S. E. Miller, A. S. Lukas, E. Marsh, P. Bushard and M. R. Wasielewski, *J. Am. Chem. Soc.*, 2000, **122**, 7802–7810.

[239] S. Guo, W. Wu, H. Guo and J. Zhao, *J. Org. Chem.*, 2012, **77**, 3933–3943.

[240] C. Röger and F. Würthner, *J. Org. Chem.*, 2007, **72**, 8070–8075.

[241] L. Tan, G. Zhang, D. Zhang and D. Zhu, *J. Org. Chem.*, 2011, **76**, 9046–9052.

[242] X. Gao, W. Qiu, X. Yang, Y. Liu, Y. Wang, H. Zhang, T. Qi, Y. Liu, K. Lu, C. Du *et al.*, *Org. Lett.*, 2007, **9**, 3917–3920.

[243] C. Thalacker, C. Röger and F. Würthner, *J. Org. Chem.*, 2006, **71**, 8098–8105.

[244] R. S. Kishore, V. Ravikumar, G. Bernardinelli, N. Sakai and S. Matile, *J. Org. Chem.*, 2008, **73**, 738–740.

[245] M. Lista, J. Areephong, N. Sakai and S. Matile, *J. Am. Chem. Soci.*, 2011, **133**, 15228–15231.

[246] L. Shen, X. Lu, H. Tian and W. Zhu, *Macromolecules*, 2011, **44**, 5612–5618.

[247] S. V. Bhosale, C. H. Jani and S. J. Langford, *Chem. Soc. Rev.*, 2008, **37**, 331–342.

[248] M. Supur, M. E. El-Khouly, J. H. Seok, K.-Y. Kay and S. Fukuzumi, *J. Phys. Chem. A*, 2011, **115**, 14430–14437.

[249] N. Banerji, A. Fürstenberg, S. Bhosale, A. L. Sisson, N. Sakai, S. Matile and E. Vauthey, *J. Phys. Chem. B*, 2008, **112**, 8912–8922.

[250] J. F. Penneau, B. J. Stallman, P. H. Kasai and L. L. Miller, *Chem. Mater.*, 1991, **3**, 791–796.

[251] B. M. Aveline, S. Matsugo and R. W. Redmond, *J. Am. Chem. Soc.*, 1997, **119**, 11785–11795.

[252] B. Abraham, S. McMasters, M. A. Mullan and L. A. Kelly, *J. Am. Chem. Soc.*, 2004, **126**, 4293–4300.

[253] J. E. Rogers, S. J. Weiss and L. A. Kelly, *J. Am. Chem. Soc.*, 2000, **122**, 427–436.

[254] P. Ganesan, J. Baggerman, H. Zhang, E. J. R. Sudhölter and H. Zuilhof, *J. Phys. Chem. A*, 2007, **111**, 6151–6156.

[255] S. Green and M. A. Fox, *J. Phys. Chem.*, 1995, **99**, 14752–14757.

[256] T. C. Barros, S. Brochsztain, V. G. Toscano, P. Berci Filho and M. J. Politi, *J. Photochem. Photobiol. A*, 1997, **111**, 97–104.

[257] I. V. Sazanovich, M. A. Alamiry, J. Best, R. D. Bennett, O. V. Bouganov, E. S. Davies, V. P. Grivin, A. J. Meijer, V. F. Plyusnin, K. L. Ronayne *et al.*, *Inorg. Chem.*, 2008, **47**, 10432–10445.

[258] G. Andric, J. F. Boas, A. M. Bond, G. D. Fallon, K. P. Ghiggino, C. F. Hogan, J. A. Hutchison, M. A.-P. Lee, S. J. Langford, J. R. Pilbrow *et al.*, *Aust. J. Chem.*, 2004, **57**, 1011–1019.

[259] Y. Ofir, A. Zelichenok and S. Yitzchaik, *J. Mater. Chem.*, 2006, **16**, 2142–2149.

[260] M. Kasha, H. Rawls and M. Ashraf El-Bayoumi, *Pure Appl. Chem.*, 1965, **11**, 371–392.

[261] S. Archer and J. A. Weinstein, *Coord. Chem. Rev.*, 2012, **256**, 2530 – 2561.

[262] B. G. Alberding, S. E. Brown-Xu, M. H. Chisholm, A. J. Epstein, T. L. Gustafson, S. A. Lewis and Y. Min, *Dalton Trans.*, 2013, **42**, 5275–5280.

[263] S. W. Eaton, L. E. Shoer, S. D. Karlen, S. M. Dyar, E. A. Margulies, B. S. Veldkamp, C. Ramanan, D. A. Hartzler, S. Savikhin, T. J. Marks and M. R. Wasielewski, *J. Am. Chem. Soc.*, 2013, **135**, 14701–14712.

[264] T. Šolomek, N. E. Powers-Riggs, Y.-L. Wu, R. M. Young, M. D. Krzyaniak, N. E. Horwitz and M. R. Wasielewski, *J. Am. Chem. Soc.*, 2017, **139**, 3348–3351.

[265] M. Koch, G. Licari and E. Vauthey, *J. Phys. Chem. B*, 2015, **119**, 11846–11857.

[266] S. Wang, Y. Wang, Z. Chen, Y. Lin, L. Weng, K. Han, J. Li, X. Jia and C. Li, *Chem. Commun.*, 2015, **51**, 3434–3437.

[267] X. Zeng, H. Deng, X. Jia, L. Cui, J. Li, C. Li and J. Fang, *Chem. Communications*, 2018, **54**, 11634–11637.

[268] C. Hippius, I. H. van Stokkum, E. Zangrando, R. M. Williams and F. Würthner, *J. Phys. Chem. C*, 2007, **111**, 13988–13996.

[269] H. Takeda, K. Kokie, T. Morimoto, H. Inumaru and O. Ishitani, *Advances in Inorganic Photochemistry*, Elsevier Inc, USA, 2011, vol. 64.

[270] H. Takeda, K. Kokie, H. Inoue and O. Ishitani, *J. Am. Chem. Soc.*, 2008, **130**, 2023–2031.

[271] D. W. Thompson, A. Ito and T. J. Meyer, *Pure. Appl. Chem.*, 2013, **85**, 1257–1305.

[272] P. Kurz, B. Probst, B. Springler and A. R., *Eur. J. Inorg. Chem.*, 2006, **15**, 2966–2974.

[273] A. D. McNaught and I. Wilkinson, *Compendium of Chemical Terminology*, Blackwell Scientific Publications, Oxford, 2nd edn., 1997.

[274] J. R. Lakowicz, *Principles of Fluorescence Spectrscopy*, Kluwer Academic/Plenum Publishers, New York, 2nd edn., 1999.

[275] K. Ahmed, A. Auni, G. Ara, M. M. Rahman, M. Y. A. Mollah and M. A. B. H. Susan, *J. Bangladesh. Chem. Soc.*, 2012, **25**, 146–158.

[276] L. A. Worl, R. Duesing, P. Chen, L. D. Ciana and T. J. Meyer, *J. Chem. Soc. Dalt. Trans.*, 1991, 849–858.

[277] M. W. George, F. P. A. Johnson, J. R. Westwell, P. M. Hodges and J. J. Turner, *J. Chem. Soc. Dalt. Trans*, 1993, 2977.

[278] P. Atkins, T. Overton, J. Rourke, M. Weller and F. Armstrong, *Shriver & Atkins' Inorganic Chemistry*, Oxford University Press, Oxford, 5th edn., 2010.

[279] M. D. Doherty, D. C. Grills and E. Fujita, *Inorg. Chem.*, 2009, **48**, 1796–1798.

[280] F. Franco, C. Cometto, C. Garino, C. Minero, F. Sordello, C. Nervi and R. Gobetto, *Eur. J. Inorg. Chem.*, 2015, **2015**, 296–304.

[281] E. E. Benson, K. A. Grice, J. M. Smieja and C. P. Kubiak, *Polyhedron*, 2013, **58**, 229–234.

[282] S. G. Sun, X. J. Peng, Y. Q. Xu, Y. L. Gao and L. C. Sun, *Chem. J. Chinese. U.*, 2004, **25**, 67–70.

[283] G. M. Hasselmann and G. J. Meyer, *J. Phys. Chem. B.*, 1999, **103**, 7671–7675.

[284] J. A. Calladine, *Thesis*, University of Nottingham, 2010.

[285] R. H. Crabtree, *J. Chem. Soc., Dalton Trans.*, 2001, 2437–2450.

[286] B. L. Bennett, K. A. Robins, R. Tennant, K. Elwell, F. Ferri, I. Bashta and G. Aguinaldo, *J. Fluor. Chem.*, 2006, **127**, 140–145.

[287] J. van den Broeke, B. J. Deelman and G. van Koten, *Tetrahedron Lett.*, 2001, **42**, 8085–8087.

[288] E. d. Wolf, G. v. Koten and B.-J. Deelman, *Chem. Soc. Rev.*, 1999, **28**, 37–41.

[289] D. J. Adams, P. J. Dyson and S. J. Tavener, *Chemistry In Alternative Reaction Media*, John Wiley & Sons Ltd, England, 2004.

[290] H. M. Yau, A. I. McKay, H. Hesse, R. Xu, M. He, C. E. Holt and G. E. Ball, *J. Am. Chem. Soc.*, 2015, **138**, 281–288.

[291] A. Goodwin and J. Mehl, *Int. J. Thermodyn.*, 1997, **18**, 795–806.

[292] R. Saladino, M. C. Ginnasi, D. Collalto, R. Bernini and C. Crestini, *Adv. Synth. Catal.*, 2010, **352**, 1284–1290.

[293] J. Blatchford, T. Gustafson, A. Epstein, D. V. Bout, J. Kerimo, D. Higgins, P. Barbara, D.-K. Fu, T. M. Swager and A. MacDiarmid, *Physical Review B*, 1996, **54**, R3683.

[294] M. P. Aarnts, D. J. Stufkens, M. P. Wilms, E. J. Baerends, A. Vlček Jr, I. P. Clark, M. W. George and J. J. Turner, *Chem. Eur. J.*, 1996, **12**, 1556– 1565.

[295] I. P. Clark, M. W. George, F. P. A. Johnson and J. J. Turner, *Chem. Commun.*, 1996, 1587–1588.

[296] F. W. M. Vanhelmont, M. V. Rajasekharan, H. U. Güdel, S. C. Capelli, J. Hauser and H.-B. Bürgi, *J. Chem. Soc., Dalton Trans.*, 1998, 2893–2900.

[297] C. J. Wood, M. Cheng, C. A. Clark, R. Horvath, I. P. Clark, M. L. Hamilton, M. Towrie, M. W. George, L. Sun, X. Yang *et al.*, *J. Phys. Chem. C*, 2014, **118**, 16536–16546.

[298] J. Snellenburg, S. Laptenok, R. Seger, K. Mullen and I. Van Stokkum, *J. Stat. Softw.*, 2012, **49**, 1–22.

[299] O. V. Dolomanov, L. J. Bourhis, R. J. Gildea, J. A. Howard and H. Puschmann, *J. Appl. Cryst.*, 2009, **42**, 339–341.

[300] G. M. Sheldrick, *Acta Cryst. A*, 2008, **64**, 112–122.

[301] G. M. Sheldrick, *Acta Cryst. C*, 2015, **71**, 3–8.